UNIVERSITY OF CAPE TOWN

DEPARTMENT OF MECHANCIAL ENGINEERING

RONDEBOSCH, CAPE TOWN, SOUTH AFRICA

Research and Development of a Rescue Robot End-Effector

Prepared by Michael Rieger

Robotics and Agents Research Laboratory

University of Cape Town

Supervised by Stephen Marais

Robotics and Agents Research Laboratory

University of Cape Town

February 2013

The financial assistance of the National Research Foundation (NRF) towards this research is hereby acknowledged. Opinions expressed and conclusions arrived at, are those of the author and are not necessarily to be attributed to the NRF.

UNIVERSITY OF CAPE TOWN

Research and Development of a Rescue Robot End-Effector

Robotics and Agents Research Laboratory

Michael Rieger
Wednesday, 15 May 2013

The financial assistance of the National Research Foundation (NRF) towards this research is hereby acknowledged. Opinions expressed and conclusions arrived at, are those of the author and are not necessarily to be attributed to the NRF.

Summary

Introduction to Urban Search and Rescue Robotics

This report details the research, design, development and testing of an end-effector system for use on an **U**rban **S**earch **a**nd **R**escue (**USAR)** robot which is in development in the **R**obotics and **A**gents **R**esearch **L**aboratory (**RARL**) at the **U**niversity of **C**ape **T**own (**UCT**). This is the 5th generation **M**obile **R**obot **P**latform (**MRP**) that UCT has developed. Figure 0-1, below, presents the fully developed design codenamed '**Ratel**'.

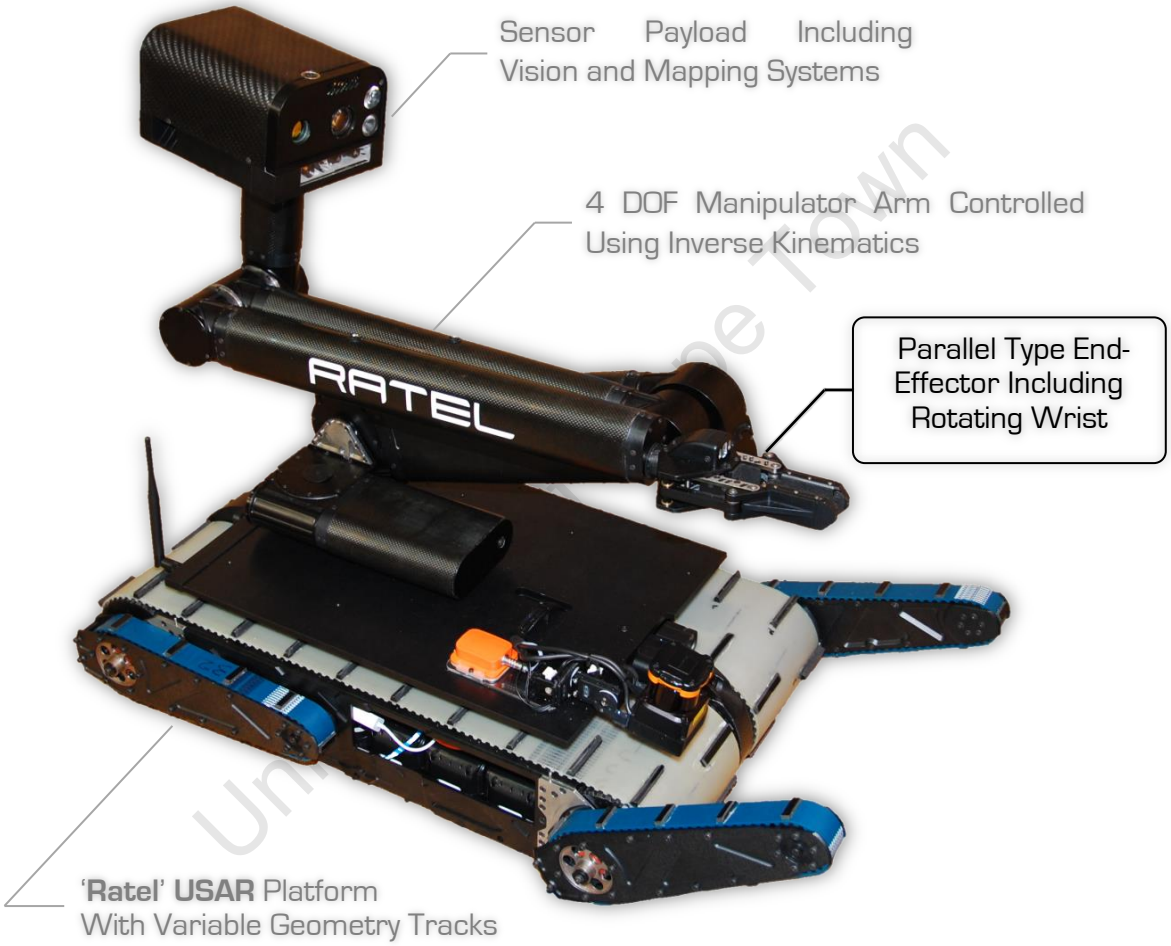

Figure 0-1: UCT's USAR Robot Developed in the Robotics and Agent Research Laboratory [1]

Mobile **USAR** robots have been used successfully to aid rescue workers in a wide range of disaster environments including mining accidents, earthquakes, tsunamis, urban disasters, hostage situations and bomb disposals. It is vital to be prepared to deal with these unpredictable events in order to reduce the number of casualties of both victims and rescue personnel.

The Ratel **MRP,** shown on the previous page, is made up of a combination of electro-mechanical modules. In the design of the platform, emphasis was placed on developing a system that could be robust, flexible and modular; whilst remaining intuitive to control. The platform designer, MSc student Eugene Dreyer [2], based the design around a central spine onto which system components could be mounted. This was done with the intention to improve modularity as well as serviceability in the future.

Additionally, the robot was equipped with a variety of sensors including five cameras (including a thermal camera), a CO2 sensor, a speaker and microphone, an Asus Xtion Pro Live 3D camera and a Hokuyo laser scanner. Together, these provide high sensing capabilities to perform operations such as victim identification, non-contact victim interaction and area mapping.

USAR robots used to be mainly of the observation type, but new robots (including UCT's **Ratel MRP)** are being developed to deal with inherently dynamic, complex and unpredictable disaster response situations, particularly related to object manipulation and gripping. In order to actively interact with the environment, a flexible and robust gripping system is vital. Figure 0-2, below, presents the end-effector solution that was developed for the **Ratel** manipulator arm to fulfil these functions.

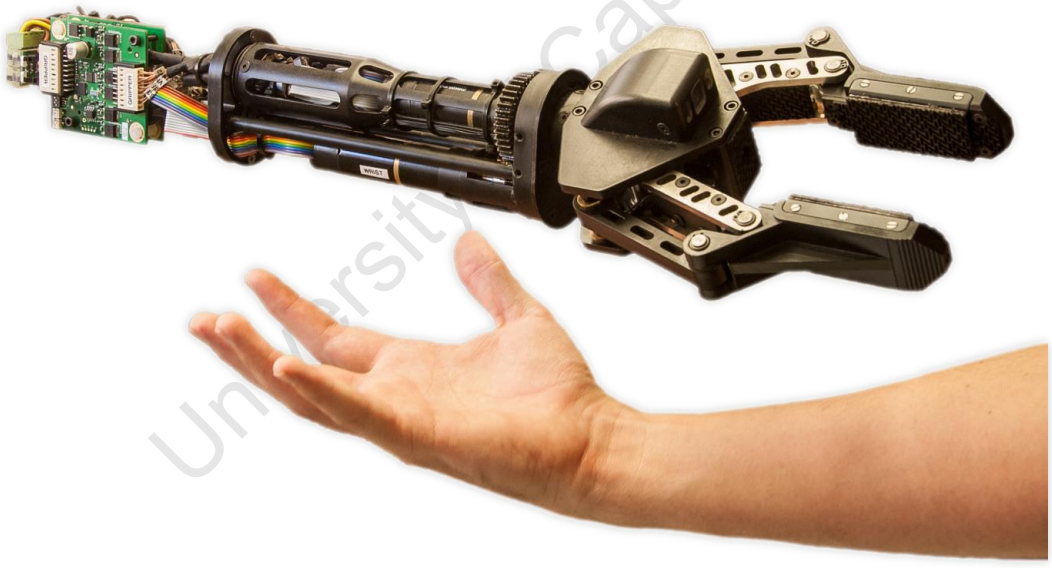

Figure 0-2: Completed End-Effector System Including Parallel Gripper, Wrist and Control Electronics

The Ratel End-Effector

The following system characteristics and properties were deemed important for a suitable **USAR** end-effector solution:

- The gripping system should potentially be deployable in real world USAR environments that are both hazardous and unpredictable.
- The system must therefore be robust, flexible, dextrous and highly reliable.
- The system should be as compact, cost-effective and light-weight as possible.

- The system should be modular where possible, allowing for swappable prehension force sensors that can be selected based on the manipulation task
- The system should be highly controllable, utilise sensors that are sensitive yet durable and employ a user-friendly interface.
- **DFMA** (**D**esign **f**or **M**anufacture and **A**ssembly) principles should be applied throughout the design process to ease manufacture and simplify assembly and maintenance

The design of the end-effector was broken down into four main subsystems to simplify the overall analysis. These were **1. Gripper Subsystem, 2. Wrist Subsystem, 3. Electrical and Electronics Subsystem** and **4. Programming and System Control**.

1. **Gripper Subsystem**

As can be seen from Figure 0-2, the end-effector utilises a parallel four-bar linkage mechanism and was primarily manufactured from Aluminium and Stainless Steel. The majority of the components were machined in the UCT Mechanical Engineering Workshop. Actuation was provided by a M12 lead screw coupled to a 40W Maxon EC22 brushless DC motor providing an estimated gripper prehension force of 200N.

Multiple sensory functions were incorporated into the design including **FSR** (**F**orce **S**ensing **R**esistor) sensors, Weiss Robotics tactile sensor arrays, object presence sensors, a micro VGA colour CMOS camera and LED lighting. These systems were driven by a custom designed embedded controller running a Freescale MC9S08GT16A processor.

2. **Wrist Subsystem**

The gripper itself is attached to a wrist that encloses both the gripper drive motor and the wrist rotation motor (also a 40W Maxon EC22). With the use of a 30-way slip-ring, continuous rotation was made possible. This enabled the potential use of tools such as drills or screwdrivers for specific applications. The maximum wrist torque that was achieved was 5.2Nm.

3. **Electrical and Electronics Subsystem**

The primary controller board was custom-designed in collaboration with Tracy Booysen, a scientific officer within the department of mechanical engineering at UCT, and students from the RARL. The PCB was designed according to dimensions specified by the cross-section of the manipulator arm. A NI LabView ARM Embedded Tier-1 compatible Cortex-M3 LM3S8962 processor was selected to perform system control and monitoring. The advantage of this processor was the inclusion of two quadrature encoder modules that could accept position information from both of the Maxon EC22 motors.

Due to the need for high resolution current sensing (an attempt was to be made to derive the gripper force from the current draw), a custom-developed dual current sensor was developed for deployment throughout the MRP.

This PCB featured two Allegro ACS712 Hall Effect ICs fed into a differential amplifier with variable gain and a selectable inverting input. Two versions were created. A 5A version was used in the gripper subsystem with 20A configurations deployed throughout the robot platform.

4. Programming and System Control

LabView was used as the standard development suite for this project as well as others throughout the RARL. The idea was to standardise a platform across all systems to speed up development time and to make collaboration easier. Figure 0-3, below, presents the LabView GUI running on the operator control station. An attempt was made to make the GUI as clear, responsive, natural, attractive and efficient as possible whilst retaining important features. This GUI was jointly developed with MSc student Bradley Springer, responsible for inverse kinematic control of the manipulator arm.

Figure 0-3: Manipulator Arm Control GUI Section with Relevant End-Effector Section Highlighted in Green [3]

Concluding Remarks

Once the system had been manufactured and assembled, various benchmarking tests were performed to gauge the actual performance against the design specifications that were set at the start of the project. Overall the end-effector performed very well, meeting the design requirements that were set and receiving positive comments in the operator user tests. Of the primary specifications that were set, the overall mass of the gripper and wrist was one of the only targets that was exceeded by 17%.

Suggested improvements that could be made to the system include further weight reductions, remanufacturing of some faulty parts, replacement of the motor speed controllers with position controllers and improving the sensory capabilities of the gripper subsystem.

Plagiarism Declaration

This thesis is submitted in complete fulfilment of a M.Sc. (Mechanical Engineering) at the University of Cape Town.

I know the meaning of plagiarism and declare that all of the work in the document, save for that which is properly acknowledged, is my own. Each contribution to, and quotation in, this document from the work(s) of other people has been attributed, and has been cited and referenced according to the style for IEEE Transactions.

I have not allowed, and will not allow anyone to copy my work with the intention of passing it off as their own.

Michael Rieger
Wednesday, 15 May 2013

Acknowledgments

This project would not have been possible without the assistance and support of several key individuals. I owe great thanks to:

Stephen Marais, who supervised the project and provided continuous guidance and support throughout its development. Stephen was always willing to offer his assistance and time in trying to solve any issues that arose. Also, thank you for giving us all the opportunity to travel to Mexico City and take part at RoboCupRescue 2012 - it was an eye-opening experience and much appreciated.

Tracy Booysen, who was always willing to provide assistance and answers to, often dim-witted, questions. Thank you for the patience, enthusiasm and good humour.

The workshop staff and particularly Glen Newins, who was always friendly and answered questions and requests with interest and a keen sense of wit.

To my family and friends that supported me throughout these two long years, thank you.

Finally, to the students in the robotics lab including Brad, Julian, Justin, Richard and David. Thank you guys for the humour filled atmosphere, as well as the continuous support that was provided by anyone that was in the vicinity when problems arose.

Table of Contents

List of Figures

List of Tables

List of Acronyms

µP	-	**Micro**processor
ADC	-	**A**nalog-to-**D**igital **C**onverter
ASTM	-	**A**merican **S**ociety for **T**esting and **M**aterials
BDM	-	**B**ackground **D**ebug **M**ode
CNC	-	**C**omputer **N**umerical **C**ontrol
CPT	-	**C**ounts **p**er **T**urn
CPU	-	**C**entral **P**rocessing **U**nit
DAC	-	**D**igital-to-**A**nalog **C**onverter
DFMA	-	**D**esign **f**or **M**anufacture and **A**ssembly
DOF	-	**D**egrees **O**f **F**reedom
EOD	-	**E**xplosive **O**rdnance **D**isposal
FEA	-	**F**inite **E**lement **A**nalysis
FOS	-	**F**actor **o**f **S**afety
FSR	-	**F**orce **S**ensing **R**esistor
GUI	-	**G**raphical **U**ser **I**nterface
HazMat	-	**Haz**ardous **Mat**erials
I2C	-	**I**nter-**I**ntegrated **C**ircuit
IR	-	**I**nfra**r**ed
MRP	-	**M**obile **R**obot **P**latform
NI	-	**N**ational **I**nstruments
NIST	-	**N**ational **I**nstitute for **S**tandards and **T**echnology
PCB	-	**P**rinted **C**ircuit **B**oard
PVC	-	**P**oly**v**inyl **C**hloride
PWM	-	**P**ulse **W**idth **M**odulation
RARL	-	**R**obotics and **A**gents **R**esearch **L**aboratory
ROS	-	**R**obot **O**perating **S**ystem
SPI	-	**S**erial **P**eripheral **I**nterface
SWAT	-	**S**pecial **W**eapons **a**nd **T**actics
TCP	-	**T**ransmission **C**ontrol **P**rotocol
TDP	-	**T**eam **D**escription **P**apers
UART	-	**U**niversal **A**synchronous **R**eceiver/**T**ransmitter
UCT	-	**U**niversity of **C**ape **T**own
UGV	-	**U**nmanned **G**round **V**ehicle
USAR	-	**U**rban **S**earch **a**nd **R**escue

Chapter 1. Introduction

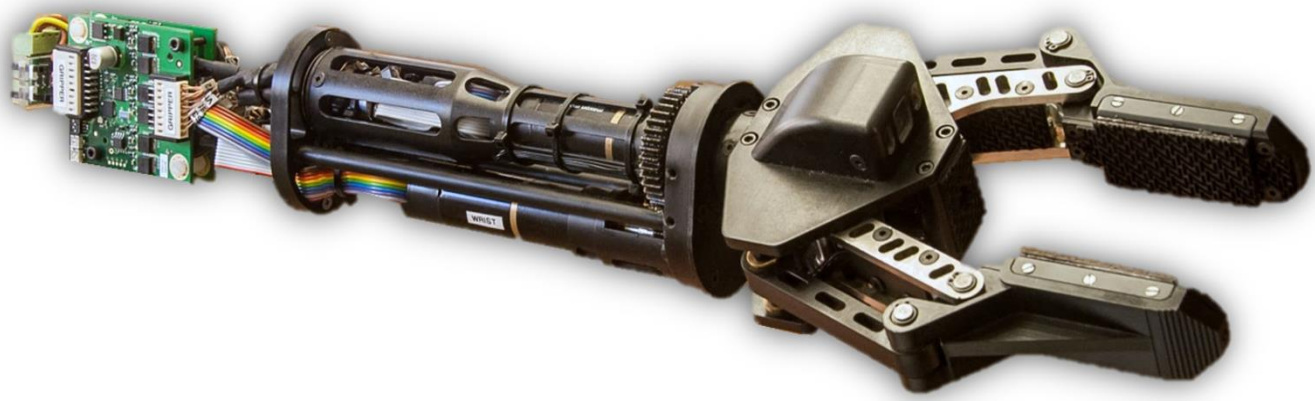

Figure 1-1: The End-Effector Developed for UCT's US&R Robot

In 322 BC, Aristotle wrote:

> ***"If every tool, when ordered, or even of its own accord, could do the work that befits it... then there would be no need either of apprentices for the master workers or of slaves for the lords."*** [4]

This statement rings as true today as it did more than 2300 years ago and captures the essence of robotics and the underpinning of its relentless development, especially over the past decade.

To some, the field of robotics may appear to be a relatively new one but in actual fact it has been around for millennia. Archytas built the first known robot, a mechanical steam-powered pigeon, around 350BC. From these humble beginnings the field of robotics has developed immensely. It is a field that has fascinated inventors including the likes of Leonardo da Vinci [5] and Nikola Tesla [6] amongst numerous others.

Shown in Figure 1-2 is a remote control boat that was developed by Tesla in New York, 1898. For its time, it was a remarkable achievement.

Figure 1-2: Nikola Tesla's remote control boat (1898), **displayed in Madison Square Gardens** [6]

The field of robotics now includes various disciplines ranging from the development of mobile and service robots, including industrial and manufacturing machines, to swarm robotics and robots that explore our universe. However, within the last decade a new robotics field has emerged to satisfy the ever increasing need to assist humans with tedious, challenging and hazardous tasks. This field is referred to as **'Rescue Robotics'**.

In its most basic form, a 'rescue robot' is a robot that has been designed to aid **U**rban **S**earch **a**nd **R**escue (**USAR**) units that have been deployed in disaster areas. Such perilous environments may be found following tragedies such as the World Trade Centre attacks of 2001, hurricane Katrina in 2005 or the Fukushima Daiichi nuclear disaster of 2011 (Figure 1-3). Robots that are deployed in such environments need to be suitably equipped to deal with the dynamics, complexity and unpredictability that these disaster response situations demand.

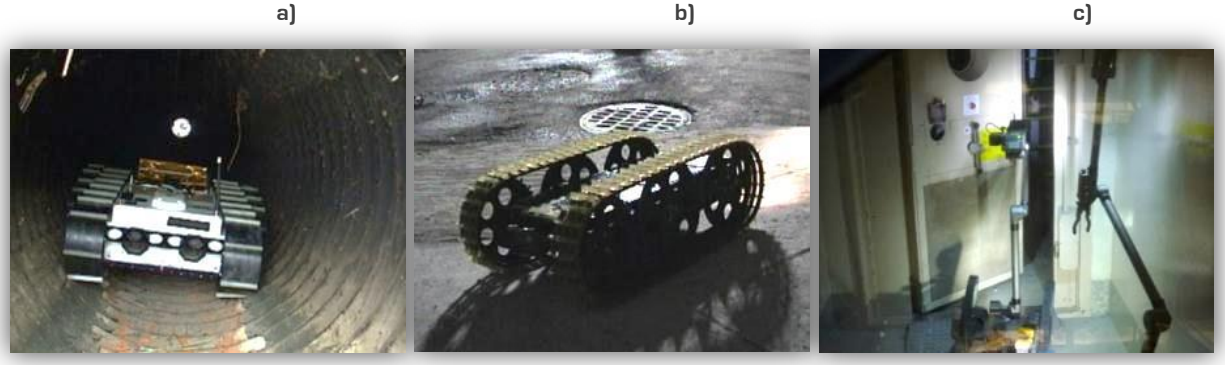

Figure 1-3: Rescue robots deployed in real-world environments
a) World Trade Centre [7] **b) Hurricane Katrina** [8] **c) Fukushima Daiichi nuclear plant** [9]

Within this relatively new field of rescue robotics, the **R**obotics and **A**gents **R**esearch **L**aboratory (**RARL**) at the **U**niversity of **C**ape **T**own **(UCT)** has been developing a **M**obile **R**obot **P**latform (**MRP)** of its own. The latest 5th generation rescue robot platform is shown in Figure 1-4, below, and has been named the **Ratel** (honey badger).

Figure 1-4: Photograph of UCT's USAR Platform at RoboCup Rescue 2012 [1]

Although **UCT**'s **MRP** has been designed to deal primarily with **USAR** scenarios, it could additionally be deployed to assist with **E**xplosive **O**rdnance **D**isposal (**EOD**), **S**pecial **W**eapons **a**nd **T**actics (**SWAT**) support, military reconnaissance, industrial accidents, **H**azardous **M**aterials (**HazMat**) and counter terrorism incidents. One of the **UCT**'s **USAR** platform key features is its ability to physically interact with its immediate environment through the use of an inverse kinematic controlled manipulator arm.

For rescuers and first responders this ability is vital and requires a manipulator arm end-effector that is versatile, robust and simple to operate. Figure 1-5, below, depicts two iRobot robot platforms (Warrior 710 and PackBot 510) equipped with different end-effector solutions.

a) b)

Figure 1-5: a) iRobot 710 Warrior [10], **b) iRobot 510 PackBot** [11] **with Parallel/Angular Type Grippers**

In order to fully design and test a suitable end-effector for **UCT**'s **MRP** platform, the **RoboCupRescue Robot League** [12] was specifically used as a driving platform and test bed. As such, the end-effector and other sub-systems would have to meet and, more importantly, exceed the requirements of this competition if a multi-purpose, all-terrain rescue vehicle was to be designed.

The completed end-effector system is shown in Figure 1-1 and Figure 1-6 and can be broken down into three distinct subsystems. These are the parallel gripper, the wrist and the electrical and electronics systems. Newly developed functionality includes a high sensory capability (tactile sensing, object presence detectors, integrated LED lighting, gripper camera, current sensing) driven by high performance control circuitry in the form of a custom designed 50MHz ARM Cortex-M3 embedded controller coupled with an effective and robust mechanical structure. The parallel gripper was actuated through the use of a M12 power screw and mounted to the wrist with full 360° continuous rotation capability.

a) b)

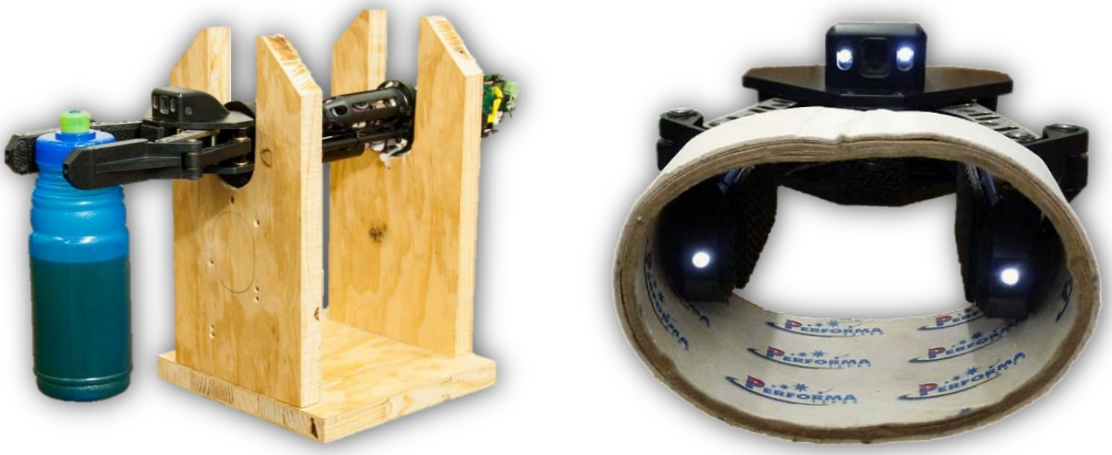

Figure 1-6: End-Effector Gripping a) Water Bottle [1], **b) Roll of Duct Tape**

The report that follows will illustrate the research, design and development process that was followed in developing the Ratel's end-effector system.

First, background research will be presented including evaluations of commercial and research based end-effector solutions followed by a detailed list of overall system specifications and their design justifications. Then a system overview will be provided analysing the three subsystem modules detailed above.

Each module will demonstrate individual design processes including conceptual designs, relevant calculations, and mechanical and/or electrical subsystems that were developed. Thereafter, the overall system programming and control interfaces will be presented and detailed testing of the system components will be demonstrated. Finally, conclusions will be drawn, and recommendations made, relating to individual modules and the end-effector system as a whole.

Chapter 2. Background Research

In order to develop an end-effector system that was functional, practical and potentially deployable in the real world, significant background research needed to be conducted into past and present mobile robotics end-effector systems, projects and studies. These sources included journal papers, books, research papers, industrial documents, online catalogues and RoboCupRescue **T**eam **D**escription **P**apers (**TDP**). After performing in-depth reviews of the selected literary materials, conclusions were drawn on how best to proceed with the development of the project.

The following sections will provide an overview of the subsequent topics that were studied in order to provide answers to some key questions:

- **Brief Overview of RoboCupRescue Robot League**
  - What is RoboCupRescue and why is it useful?
  - What are the manipulation challenges?
  - How do these challenges test the capabilities of the end-effector?
- **Gripper Theory and Categories**
  - Which elements make up a complete end-effector system?
  - What are the most common types of grippers?
  - What is the difference between a fully- and an under-actuated mechanism?
  - What types of prehension techniques exist?
  - Which prehension methods would be suitable for a rescue robot end-effector?
- **A Selection of Research/Commercial Mobile Robot Grippers**
  - What types of end-effectors are commercially available?
  - What types of end-effectors have been developed by research institutions and how do they differ from commercial versions?
  - Which end-effectors has UCT developed?
  - What specifications do these systems exhibit?
  - Have any of these end-effector technologies been proven to be effective in real-world disaster situations?
- **Sensors and Electronics Systems**
  - What types of sensors are required for US&R environments?
  - What is the difference between kinaesthetic and cutaneous sensing and how can these be applied to an end-effector system?
  - What is sensor fusion and why should it be applied to a manipulator system?
  - What types of tactile sensors technologies exist and what are their performance characteristics?

In order to assess and verify the performance of the **MRP** and its various subsystems, some type of test bed was required. This presented itself in the form of the RoboCupRescue Robot League [12], which was specifically used as a driving platform for the research, development and deployment of **UCT**'s **USAR** robot. As such, the end-effector and other sub-systems had to meet and, more importantly, exceed the requirements of this competition if a multi-purpose, all-terrain rescue vehicle was to be designed. The following section will briefly outline the RoboCupRescue competition, focussing on test areas that involve the manipulator arm and end-effector.

2.1 Brief Overview of RoboCupRescue Robot League

RoboCup is an international competition that is hosted annually with participants competing from institutions and universities around the world. It has been selected by the **N**ational **I**nstitute for **S**tandards and **T**echnology (**NIST**) in order to test and verify **A**merican **S**ociety for **T**esting and **M**aterials (**ASTM**) standard test methods for response robots [13].

In 2011 the competition was held in Istanbul, Turkey, with the 2012 event taking place in Mexico City. Of the many events that take place during the main competition, the RoboCupRescue Robot League was chosen by the **RARL** as the primary competition platform [12]. As such, the rules specified by the governing body were used as initial guidelines for the design of the end-effector [14]. The following sections will briefly describe the 2011 rules followed by the additions and changes that were made in 2012.

2.1.1 Summary of RoboCupRescue Blue Arena Rules (2011)

The RoboCupRescue competition consists of various colour-coded arenas which test specific components and features of **USAR** robots. Points are awarded for tasks of varying difficulty levels. For the end-effector sub-system, the Blue Arena provides the most relevant and challenging objectives. It is described as challenging 'robots with manipulator grasping and precision placement capabilities in complex terrain' [14]. A blue arena subsection is shown in Figure 2-1 below.

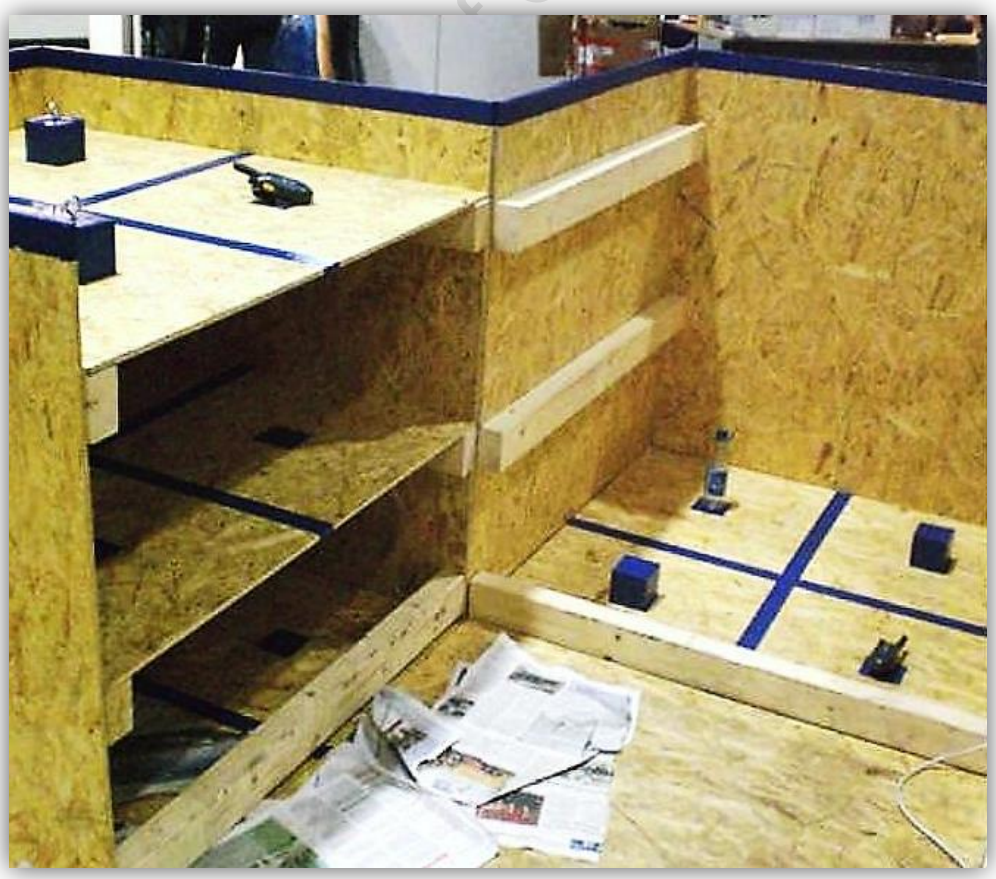

Figure 2-1: RoboCup Rescue Blue Arena [14]

The Blue Arena requires precision grasping and placement of objects that are initially located at different height levels (0m, 0.5m, 1m) and at various depths (0.3m, 0.6m). The particular objects that are to be manipulated are illustrated in Figure 2-2. These include:

- 100mm wood cube covered in duct tape with a Ø20mm eye-bolt
- Full 500ml water bottle
- Small hand-held radio

20 Points are awarded to a team if three of these objects can be successfully placed in a located victim box. The rules also specify that points can be deducted if objects (or any arena elements) are damaged or need to be replaced.

Figure 2-2: Blue Arena – Objects To Be Manipulated [14]

From these rules, the following initial end-effector design criteria were realised. The end-effector would need to:

1. Grasp a variety of different objects (sizes and weights)
2. Pick and place objects weighing in excess of 500g
3. Place objects in victim boxes (i.e. demonstrate manoeuvrable / dexterity)
4. Provide a form of force feedback to the user/controller to avoid damaging objects

2.1.2 Summary of RoboCupRescue Manipulation Areas (2012)

In June 2012 the **RARL USAR** team travelled to Mexico City to compete at RoboCupRescue 2012 together with a wide range of other universities from around the world. A number of alterations had been made to the rules compared to the previous years' competitions.

In comparison to the 2011 rules, there were no longer multiple objects placed on levels at varying depths, but only water bottles placed within horizontal and vertical **P**oly**v**inyl **C**hloride (**PVC**) tubes. In order to score points, a water bottle needed to be removed from a tube and placed in a victim box. Figure 2-3 on the following page shows a manipulation zone within the rescue arena. As can be seen in the image, the **PVC** tubes were approximately 100mm in diameter with varying depths and arrangements. Furthermore, pipe stars were introduced to test manipulator dexterity and manoeuvrability for both object manipulation and inspection (See Figure 2-4).

Figure 2-3: RoboCupRescue 2012 Manipulation Zone [15]

As can be seen in Figure 2-3 and Figure 2-4, dextrous manipulation and inspection operations within the arena were non-trivial and would require certain functional elements to be present in the end-effector system to be successfully overcome. These would possibly include a gripper camera, continuous gripper rotation and a suitable control interface.

Figure 2-4: Pipe Stars as Part of NIST's Standard Test Methods [16]

2.2 Gripper Theory and Categories

Robot end-effectors, but more specifically robotic grippers, are "active links between the handling equipment and the work piece" [17]. They can be found in a wide area of robotics applications including process control and automation, numerical control, mobile robotics amongst others.

Various prehension techniques (the act of grasping) exist, with many applications requiring specific prehension methods. Often a combination of techniques may be required for a particular application. This may be particularly relevant to end-effectors deployed in **USAR** scenarios as environments are inherently unstructured and dynamic, and require an end-effector that is versatile and flexible, yet robust and easy to maintain.

2.2.1 Gripper Elements

Figure 2-5, below, illustrates a general mechanical gripper containing various sub-systems, each playing an essential role in the overall operation of an end-effector. Key sub-systems include suitable sensors, a kinematic and drive system as well as a control system to interface with a user/autonomous controller.

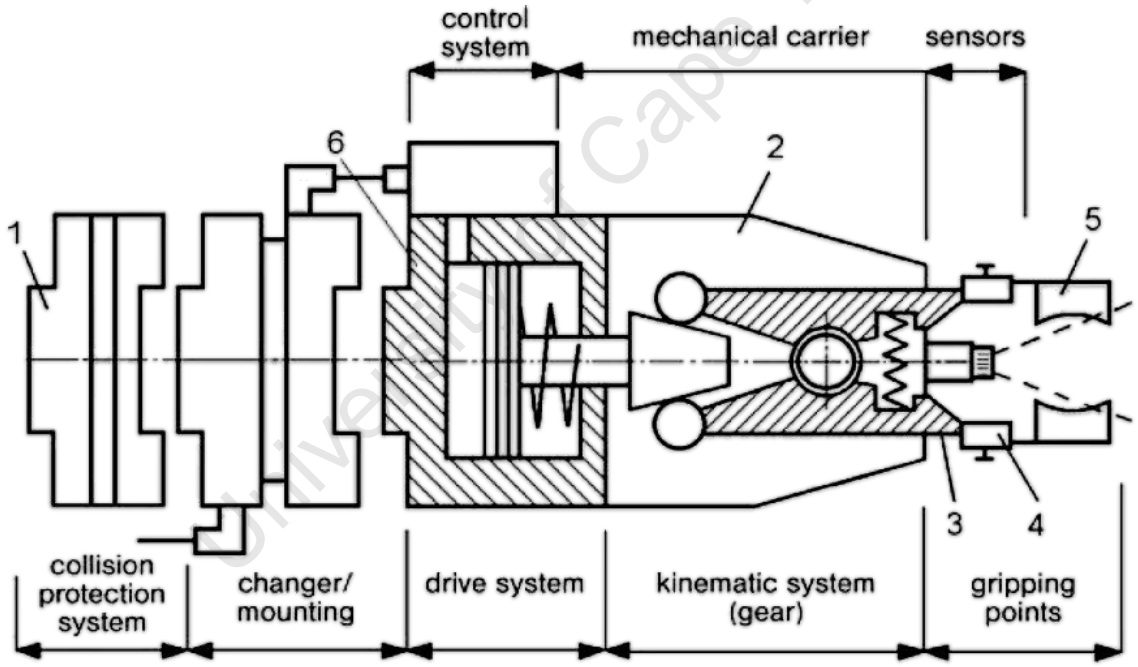

Figure 2-5: Mechanical Gripper Subsystems [17]

2.2.2 Actuation Architectures: Fully Versus Under-Actuated Mechanisms

Mechanical mechanisms can be divided into three categories based on the relationship between the number of actuators and the respective **D**egrees **O**f **F**reedom (**DOF**) [18]. These are:

- Fully Actuated: $n_{DOF} = n_{ACT}$
- Redundantly Actuated: $n_{DOF} < n_{ACT}$
- Underactuated: $n_{DOF} > n_{ACT}$

Full actuation implies that each joint (or **DOF**) has its own actuator and that there are no passive or underactuated joints. This results in a mechanism or linkage system that can be fully controlled. This is often the case with angular or parallel grippers. Basic angular and parallel arrangements are presented in Figure 2-6 a) and b) below.

The study of underactuated mechanisms, where mechanical systems have more degrees of freedom than actuators, is a relatively old research field in robotics but has recently received renewed interest [18]. It is used in a large variety of robotic applications, although designers often do not take full advantage of the system by completing a full analysis or optimisation.

The idea behind underactuation in grasping is that, by utilising mechanical mechanisms intelligently, an end-effector is able to adapt to the shape of an object dynamically with the use of only one actuator [18]. These types of grippers are often described as adaptable or adaptive grippers (See Figure 2-6 c)). Adaptive grippers are ideal in a wide range of applications where the exact shape, dimensions and orientation of an object may be unknown. This ability would make such a gripper ideal in USAR applications, where environments and conditions are often inherently unpredictable. Further advantages include their light weight, low cost and low energy consumption [19].

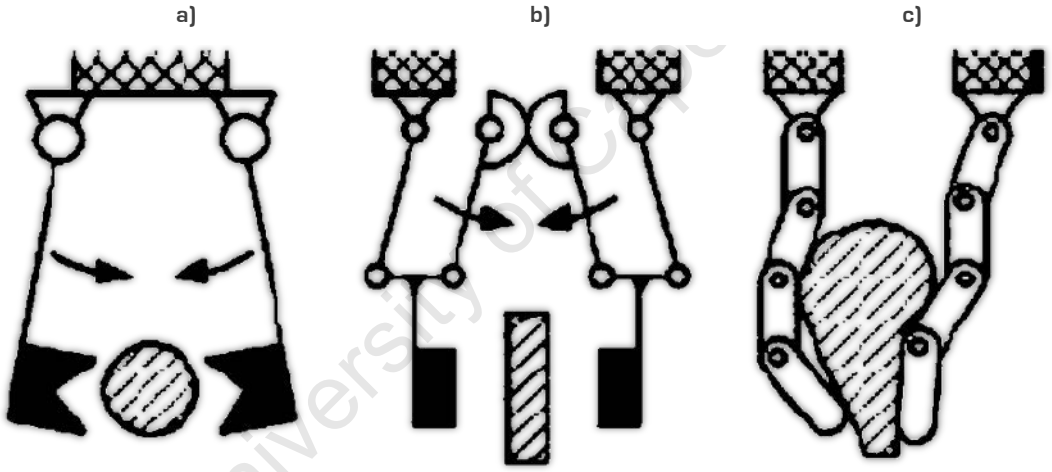

Figure 2-6: Sketches of Common Grippers a) Angular Gripper b) Parallel Gripper c) Adaptive Gripper [17]

2.2.3 Prehension techniques

Four types of gripper prehension methods exist, each being efficient at performing certain tasks. The information contained within the following section has been primarily extracted from the book "Robot Grippers" by Monkman, Hesse, Steinmann and Schunk [17].

2.2.3.1 Impactive

Impactive (or friction) end-effectors are the most frequently employed gripper type and can support a variety of technical configurations depending on the application. They are characterised by their ability to physically grasp objects by applying direct impact pressure onto the work piece. In other words, impactive prehension is achieved and maintained by forces exerted against two or more surfaces on the same object.

These types of grippers exhibit high reliability, large and adjustable prehension forces, as well as good adaptability to a diverse range of applications. These characteristics make such grippers ideal for use in rescue robotics applications. Frequently, designs will also incorporate other prehension techniques such as those described in the sections below. An example of such a combination is illustrated in Figure 2-7 below.

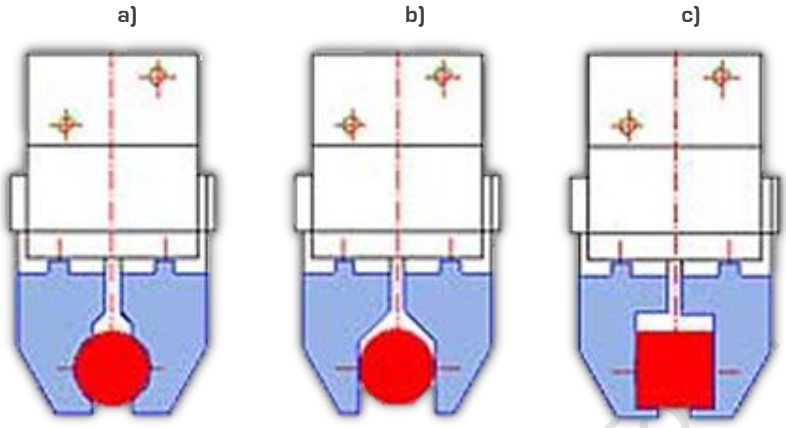

Figure 2-7: a) Encompassing b) Friction c) Retention Prehension Techniques[20]

2.2.3.2 Ingressive

An ingressive manipulator differs from an impactive type in that the work piece is permeated in some way to achieve prehension. Often this is in the form of some type of ingressive pin or hooking tool. Ingressive grippers are usually found in industrial environments, particularly for pick and place operations, and often operate on soft materials such as textiles, carbon fibre, fibre glass etc.

At first, this type of prehension may appear to be too inflexible for use on a mobile rescue robot due to the unpredictable nature of disaster scenarios. However, combining such a gripping method with an impactive gripper could aid in the manipulation of certain objects. As such, integration of some type of ingressive behaviour into the final gripper should be considered. Figure 2-8, below, is an example of a 'pinch' type ingressive manipulator that uses a knurled wheel and foot to pull a single sheet of fabric from a stack [17].

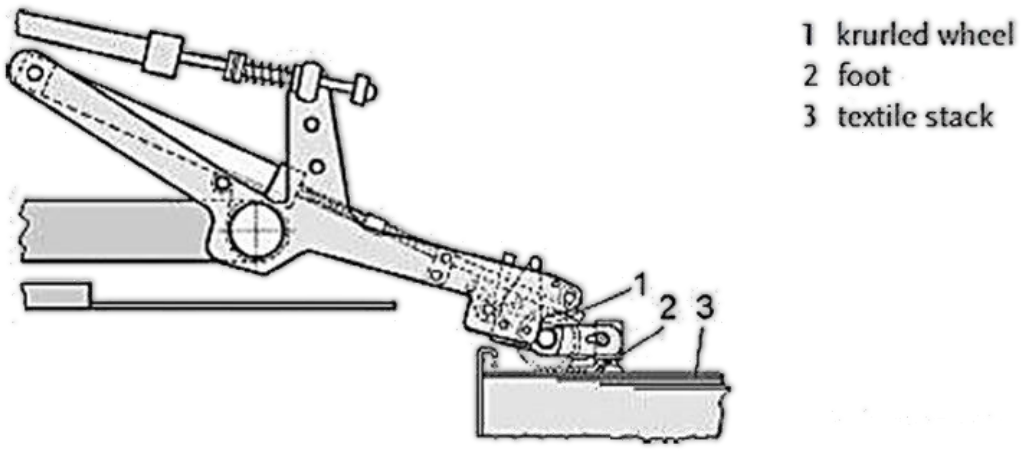

Figure 2-8: The CluPicker Ingressive End-Effector by Jet-Sew Parts Fabric Sheets [17]

2.2.3.3 Astrictive

Astrictive gripper types are included here for completeness, but are unlikely to be integrated into a mobile robotics platform. This gripping technique is most commonly found in industrial and automation applications, making use of vacuum suction, magneto-adhesion and electro-adhesion. Due to the dependence on some type of continuous energy supply for object retention, their use in mobile robotics is limited. An example of a composite vacuum gripper created by Schmalz GmbH is shown below.

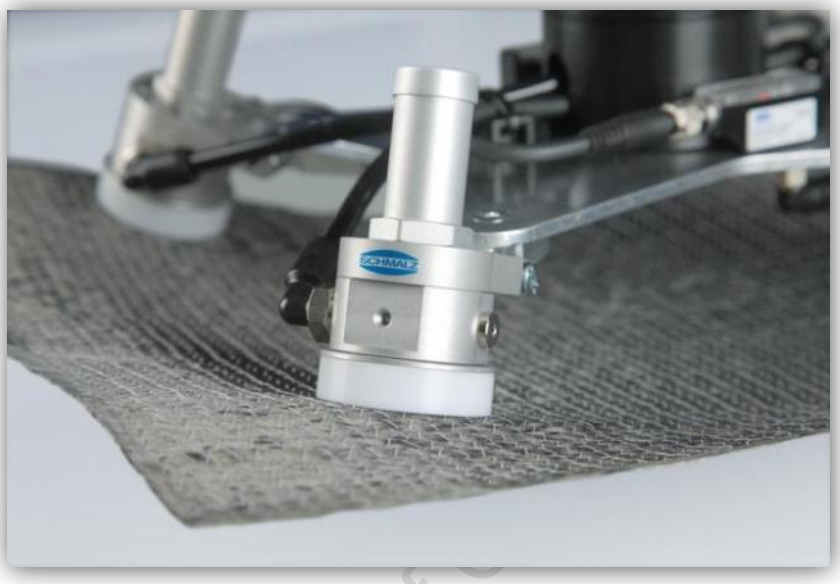

Figure 2-9: Schmalz's Vacuum Gripper for Handling Porous, Non-Rigid and Unstable Components [21]

2.2.3.4 Contigutive

Contigutive grippers, like astrictive types, are rarely found in mobile robotics. They achieve prehension through direct contact with objects and exert their holding force through chemical, thermal or surface tension techniques. These manipulators are therefore quite inflexible and are usually suited to a specific activity. As such, their use in rescue robot applications might not be recommended. Figure 2-10, illustrates a contigutive tape feeding end-effector that uses chemo-adhesion to manipulate a flat object [17].

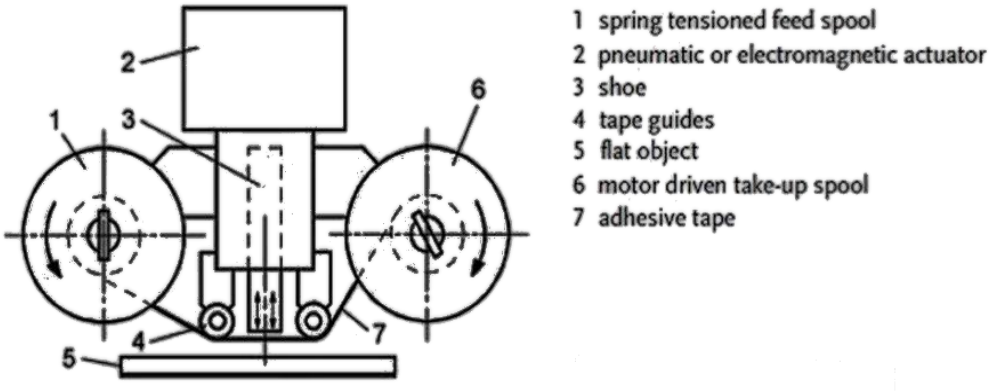

Figure 2-10: Basic schematic of an adhesive tape feeding end-effector [17]

2.2.3.5 Conclusions

Based on the requirements of an end-effector for use in a mobile rescue robotics scenario, the following conclusions may be drawn from the various gripper prehension techniques that were presented:

- Impactive prehension is the most prevalent prehension method (principally in mobile robotics) as it offers excellent flexibility, controllability and reliability
- Ingressive gripping, although not directly useful in a rescue robotics environment as a stand-alone solution, may be combined with an impactive prehension gripper to provide great versatility and adaptability. This could prove particularly useful in the manipulation of certain objects that have hooks, holes and eye-bolts

2.3 A Selection of Research/Commercial Mobile Robot Grippers

With **USAR** type **MRP**s becoming extremely popular within the last decade (spurred on particularly by the U.S. military), companies such as iRobot and Northrop Grumman have developed commercially viable platforms such as those being deployed in Iraq and Afghanistan[1].

2.3.1 iRobot 510 'Packbot' and 310 SUGV

iRobot is probably one of the most widely known commercial mobile robotics manufacturers. The company has developed multiple platforms that can share a variety of end-effector types. The two platforms shown below are the 510 PackBot and the 310 Small **U**nmanned **G**round **V**ehicle (**UGV**), demonstrating iRobot's angular (left) and parallel (right) end-effectors.

Figure 2-11: iRobot 510 PackBot with Angular Gripper [22] **and 310 SUGV with Parallel Gripper** [23]

[1] In 2007 nearly 5000 robots were deployed in Afghanistan and Iraq compared with about 150 in 2004 [74]

The following table presents some of the specifications of both the parallel [24] and angular [25] type grippers extracted from online iRobot catalogues.

Table 2-1: iRobot End-Effector Specifications

Gripper Type	Angular / Parallel	Parallel
Jaw Opening	180°	≈ 127mm (5")
Grip Force	N/A	≈ 156N (35lbs)
Maximum Lift Capacity	13.6 kg	6.8 kg
Adjustable Fingers	Yes	No
Wrist Roll	Continuous 360°	Continuous 360°
Power Type	Electric	Electric

2.3.2 Kraft Predator and Raptor Manipulators

Kraft TeleRobotics specialises in the design and development of multi-purpose manipulators (with gripper end-effectors) for a variety of applications including deep sea exploration, nuclear power plant decommissioning and **UGV** operations. Although many of the manipulators operate using hydraulics, electric varieties are also available.

Together with a Kraft manipulator, the 'Kraft Force Feedback Mini-Master' control interface (Figure 2-12) makes arm control simple and intuitive for an operator. In addition to providing this helpful control interface, it is capable of providing proportional control of the prehension force. This is particularly useful for autonomous and remote operation of the arm and simplifies the core control of the rescue robot for the user.

Figure 2-12: Kraft Force Feedback 'Mini-Master' [26]

Table 2-2 illustrates comparisons of various gripper and wrist specifications provided by Kraft TeleRobotics. It should be noted that the grippers are not specific to any particular manipulator and can be selected based on the application.

Table 2-2: Kraft Tele-robotics End-Effector Comparison

	Parallel	Angular	Angular – Four Finger Intermeshing
	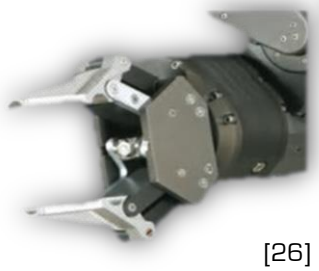 [26]	 [27]	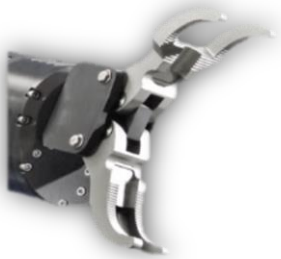 [28]
Arm Type	Predator	Viper	Raptor
DOF (Wrist)	2	1	2
Wrist Pitch	200°	180°	200°
Wrist Yaw	200°	-	200°
Wrist Roll	340° @ 0 - 40rpm	Continuous	340° @ 0 - 40rpm
Wrist Torque	135Nm	-	135Nm
Jaw Opening	≈ 100mm (4")	≈ 100mm (4")	≈ 220mm (8.75")
Grip Force	1334N	-	1334N
Material	Anodized Aluminium (Fingers – Heat Treated SS)	Anodized Aluminium	Anodized Aluminium (Fingers – Heat Treated SS)
Tool Ability	3/4" T-Handle Interface	N/A	3/4" T-Handle Interface
Grooved Jaws	Yes	Yes	Yes
Control	Proportional Grip Force or Closure Rate	Proportional Grip Force or Closure Rate	Proportional Grip Force or Closure Rate
Power Type	Hydraulic	24VDC Electric	Hydraulic

2.3.3 Remotec Andros Series

Remotec, a subsidiary of the global security company Northrop Grumman, is a global leader in **UGV**s and provides a versatile set of robots for military and commercial use. Their mobile robotic platforms are commonly employed for **EOD**, **USAR**, **HazMat** disposal, Law Enforcement (including **SWAT**) and military applications [29].

Within the Remotec Andros family of **UGV**s it would appear that standard parallel gripper and wrist sections are used for each robot type even though each robot is designed for diverse target markets and applications. This would lead one to believe that Remotec has confidence in this type of end-effector and that it is both versatile and adaptable.

Figure 2-13 shows a Remotec parallel gripper with indented gripping fingers mounted on the Andros Wolverine platform.

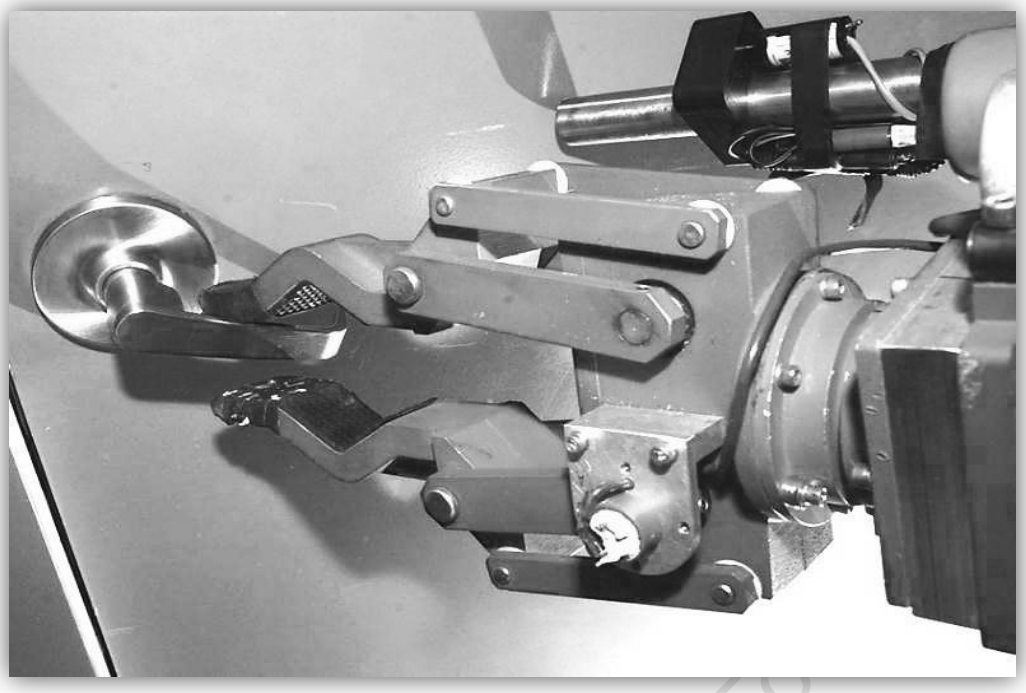

Figure 2-13: Remotec Wolverine Parallel Gripper [30]

2.3.4 The SMD Harvard Hand

This underactuated four fingered gripper was developed at Harvard University by A. Dollar and R. Howe and is commonly referred to as the "Harvard Hand" [31].

At the design inception, objectives were set to incorporate passive adaptive behaviour (i.e. adaptive behaviour due to mechanical design and not due to active control) and to develop a system that was robust, simple and easy to control, particularly in unstructured environments.

The gripper is actuated with a single motor that drives the four fingers. Tendons, along with viscoelastic flexure joints, provide the adaptive behaviour of the system. Figure 2-14, below, demonstrates the ability of the gripper to grasp a variety objects [32].

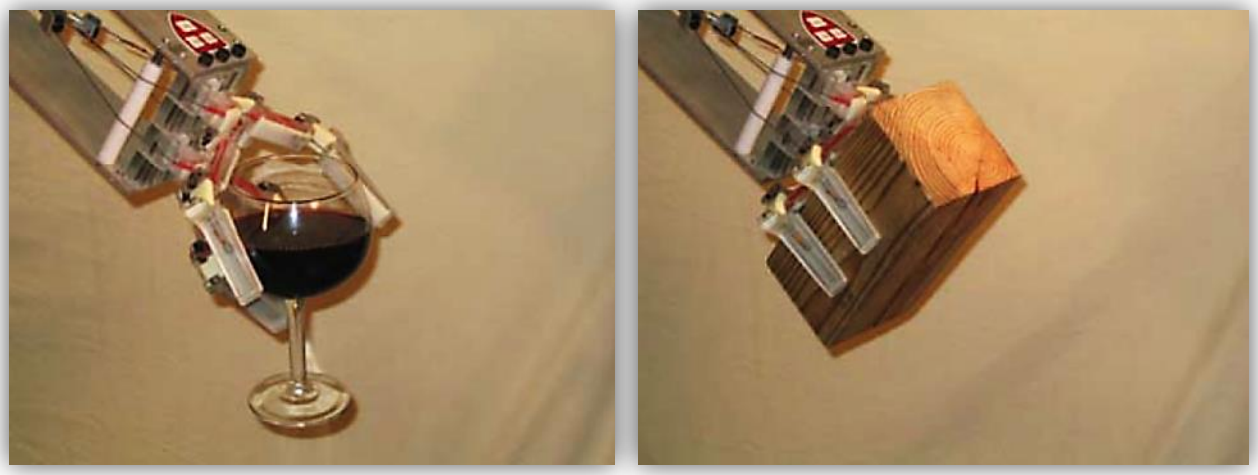

Figure 2-14: The SMD Harvard Gripper Holding a Wine Glass / Wood Block [31]

Figure 2-15, below, displays the internal schematic of the gripping mechanism.

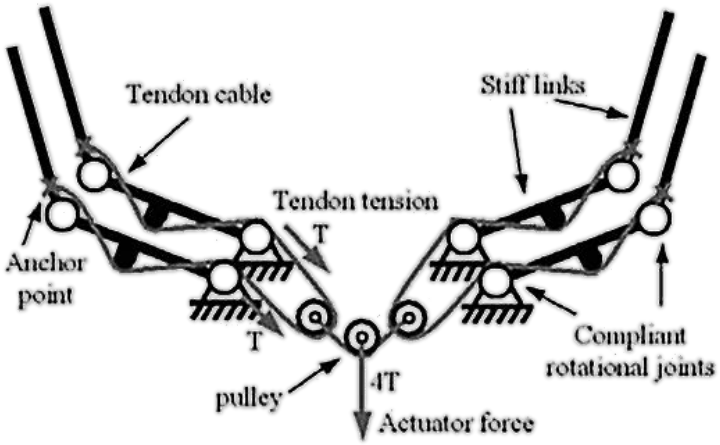

Figure 2-15: Diagram illustrating actuation of the hand with tendons [31]

Results of performance tests indicated that the gripper could grasp various objects with large position errors without any form of tactile sensor feedback. Using the passive adaptability of the fingers, the DC motor was simply run until it stalled. Although this type of gripper has many appealing features, the whole configuration appears bulky. If this type of mechanism were to be implemented on a mobile robotics platform, it would need to be improved to make it more robust and compact.

2.3.5 Four Fingered Helios VIII Gripper

The Helios VIII rescue robot, designed by the Tokyo Institute of Technology, is one of only a few **USAR** robots to include an adaptive type gripper. The four fingered gripper driven by a single 20W DC actuator is presented in Figure 2-16, below.

The underactuated tendon-type mechanism utilises a single wire for both tightening and extending the fingers. Together with pulleys located on every phalanx (finger section) and a spring mechanism to take up wire stretch, the gripper is extremely flexible and adaptable.

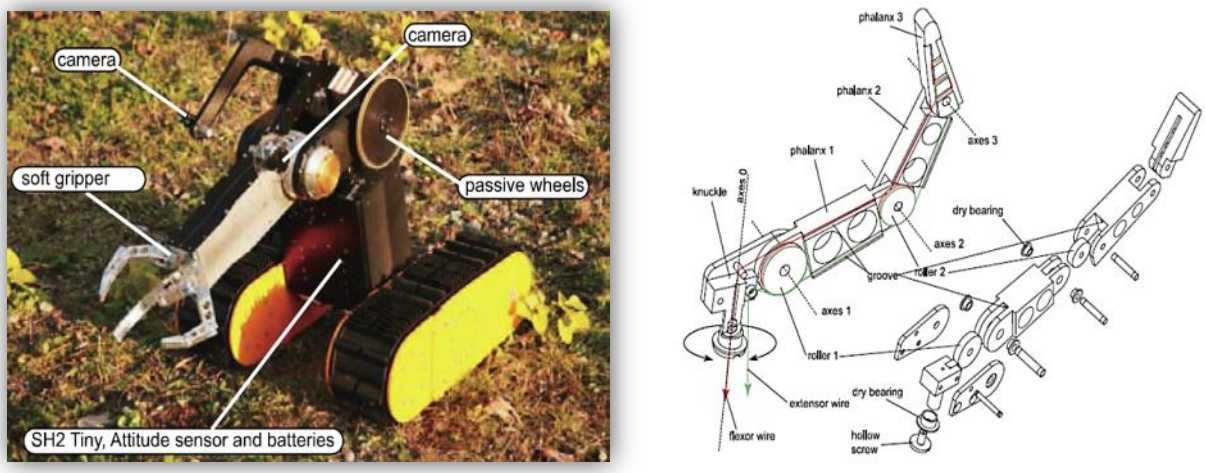

Figure 2-16: Helios VIII Rescue Robot [33]

A unique feature of the Helios gripper is its ability to fully retract its fingers back onto the arm manipulator, thus shielding the fingers when not in use. Although exact specifications are not provided, images and video footage indicate that the fingers exert more than enough force to lift a 500ml water bottle and other similarly weighted objects. Furthermore, tactile sensors do not appear to be present, but force sensing may be achieved through current monitoring of the DC actuator as all fingers are driven using coupled tendons.

2.3.6 Previous Undergraduate Projects

From 2010 to 2011 three undergraduate projects were run in the **RARL** at **UCT** with the objective to develop prototype end-effectors for use on the rescue robot platform. The project undertaken by Marten Cross involved the development of an angular gripper [34], whilst Terry Scott was tasked with the design of a parallel jaw gripper [35]. Each of these projects included the additional requirement to design a wrist for the end-effector that could interface with the manipulator arm. Both of these grippers were actuated using 90W Maxon EC22 4-Pole motors coupled to Maxon DEC50/5 speed controllers.

Stephen Walker's project [36] involved the development of an underactuated gripper as a "proof of concept" design with the aim to assess its viability for use in rescue robotics. This six **DOF** gripper was actuated using a 40W EC22 Maxon motor coupled to a DEC 24/3 speed controller. The three end-effector designs are presented below.

Figure 2-17: M. Cross's 'Viper' Angular Gripper [34], **T. Scott's 'Brachyuran' Parallel Jaw Gripper** [35]

Figure 2-18: S.Walker's Adaptive Gripper Mounted on a Carbon Fibre Arm Section [36]

Table 5-2, in the **Initial Design Development** section of **Chapter 5. Gripper Subsystem**, provides a more detailed breakdown of the individual projects and summarises the advantages and disadvantages of each including some important desired specifications that were achieved.

2.4 Sensors and Electronics Systems

In robotics manipulation research, the attempt has always been made to emulate the capabilities of humans, both in terms of artificial tactile sensing and enhancing a robot's control capabilities. According to Howe [37], in order to reliably and consistently handle objects in unstructured environments, such as those encountered in **USAR**, the control of contact forces and the motion of the gripper fingers through tactile sensing is vital.

Howe presents two types of contact sensing, namely kinaesthetic and cutaneous sensing. Kinaesthetic or proprioceptor sensing describes the "perception of limb motion and forces" through internal parameters. For a robot this may include torque, force, current or position sensors from motors or internal measuring devices. Cutaneous or exteroceptor sensing provides contact information directly from sensors located on contact surfaces such as tactile sensors.

Howe further suggests that studies have shown that, due to transmission effects such as friction, backlash and inertia, using kinaesthetic sensing alone will not provide enough sensor information to accurately sense and control an end-effector effectively. As a result one can conclude that some type of sensor fusion of both kinaesthetic and cutaneous sensors should be included in the design requirements of the end-effector system.

2.4.1 Piezoresistive Sensors

Piezoresistive sensors utilise the properties of specific semiconductor materials to alter their electrical resistance when they experience mechanical strain or deformation. This is in contrast to piezoelectric sensors that actually generate an electrical potential. Two types of piezoresistive sensors are commonly found, those utilising a conductive elastomer between two measuring plates and those using a thin conductive polymer substrate material.

Figure 2-19, below, illustrates a piezoresistive sensor utilising elastomer foam as the compressive material. When a force is applied to the foam, the particle density changes and a variation in resistance can be measured. The resistance usually decreases when the conductive material is compressed.

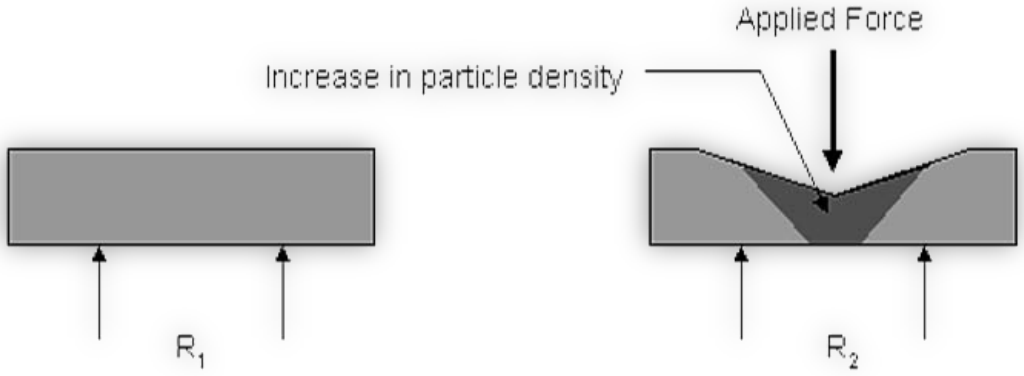

Figure 2-19: Particle Density Change in an Elastomer with an Applied Force [38]

Crowder [38] explains that piezoresistive sensors are very popular in robotic systems due to their simplicity, straightforward interface and their ability to provide decent resolution tactile image data when used in an array. Disadvantages include the highly non-linear behaviour of the resistive elastomer foam, the long non-linear time constant in both compression and expansion and the poor long term reliability due to permanent deformation and fatigue that may occur with cyclic use.

Figure 2-20 illustrates an Interlink Electronics [39] **F**orce **S**ensing **R**esistor (**FSR**) utilising a conductive polymer substrate. The thin (less than 0.5mm) polymer film decreases its resistance as a force is applied to it. As with elastomer force resistors, advantages include a simple interface and low cost. However, force sensing accuracy ranges from 5% to 25% depending on the applied force (and temperature variations) resulting in relatively low precision and thus making the sensor unsuitable for precision measurements. [40]

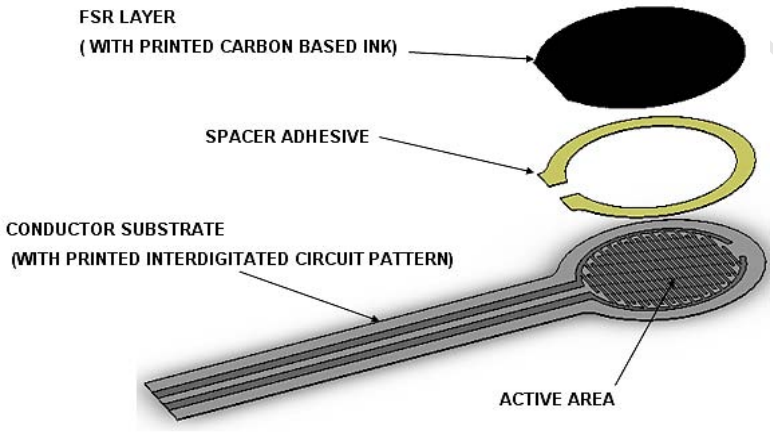

Figure 2-20: Construction of a Force Sensing Resistor [41]

Force sensing resistors are often arranged in an array to provide improved object image resolution. Figure 2-21, below, illustrates an 84 cell Weiss Robotics piezoresistive force sensor array with an integrated sensor controller. Such a device could act as a suitable cutaneous sensor providing flexibility, robustness and good tactile image resolution.

Figure 2-21: Weiss Robotics DSA9205i Intelligent Sensor Module [42]

2.4.2 Capacitive Sensors

Capacitive sensors operate on the simple principle that the capacitance between two parallel plates can be derived using $C = \frac{\varepsilon * A}{d}$ [2]. These types of sensors therefore require an applied force to either change the distance between the plates or their overlapping surface area. The dielectric material used for these sensors is often used as the elastomer material as well, providing specific force-capacitance characteristics. Figure 2-22 illustrates the principle behind a typical point-force sensor [38].

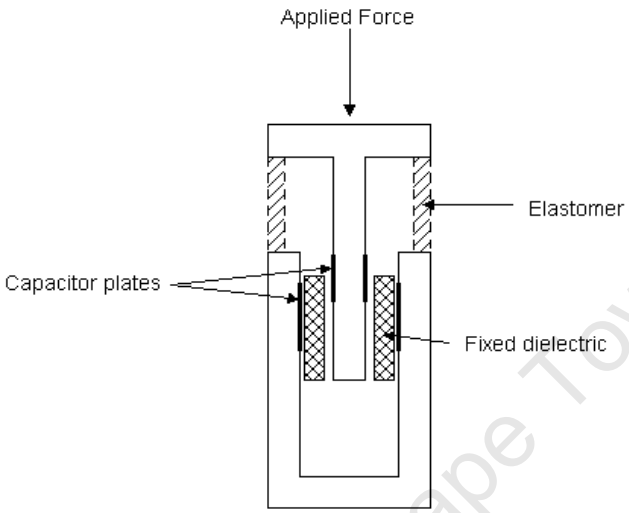

Figure 2-22: Example of a Capacitive Force Sensor [38]

As with piezoresistive sensors, capacitive sensors are rarely used individually and are often part of a tactile sensing array. These types of sensors are one of the oldest and most common types of pressure sensors with many commercially available solutions available. They provide good sensitivity, but have the disadvantages that complex post signal processing circuitry is required and that hysteresis might affect the performance over time [44]. Figure 2-23, right, illustrates the construction of such a sensor as described by Pressure Profile Systems Inc. [45]. The array consists of row and column electrodes with an elastomeric dielectric wedged between them. By using two multiplexers, the corresponding row/column cells can be scanned and the local pressure measured at that point.

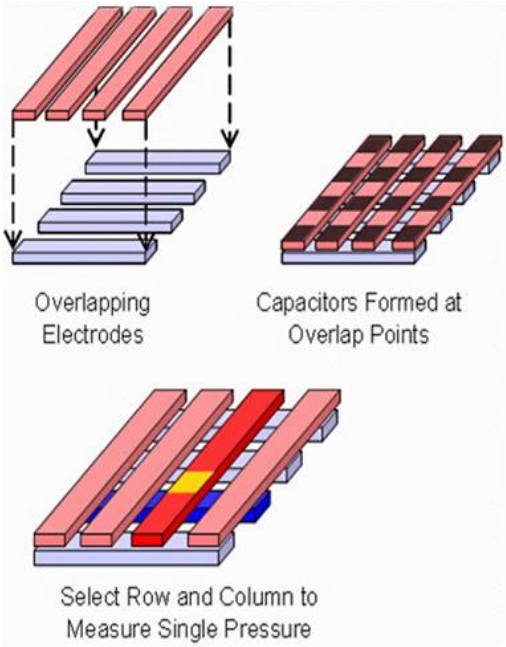

Figure 2-23: Capacitance based tactile sensing array construction [45]

[2] C = Capacitance, ε = Dielectric constant, A = Area of overlap between plates, d = Distance between plates

2.4.3 Optical Sensors

Optical force sensors are available in a wide variety of different configurations. An example of an optical proximity sensor developed by the Man-Machine Systems Laboratory at MIT [46] is shown in Figure 2-24, below. By using a light source that reflects off a moving surface onto which a force has been applied, the intensity of the light reflections can be measured using a photosensor. With known photosensor characteristics, the relevant force information can be extracted from the data. This is the fundamental principle behind most optical sensors.

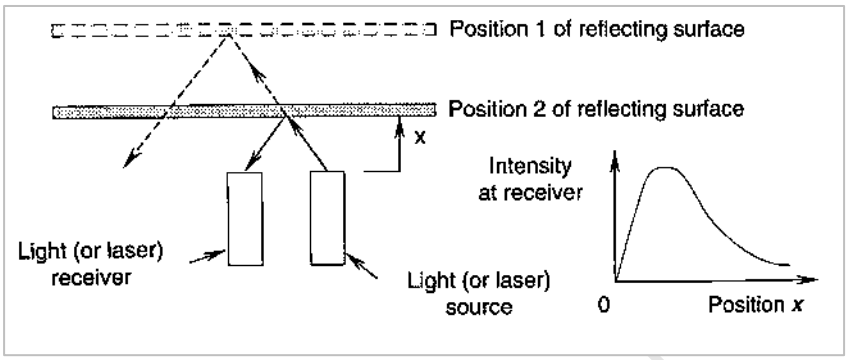

Figure 2-24: Optical proximity sensor developed by MIT [46]

A prototype (shown below) utilising this optical force sensing principle was developed at the *Seconda Università degli studi di Napoli* by S. Pirozzi [47]. This 16 cell array is made up of surface mount **I**nfra**r**ed (**IR**) LEDs and **IR** phototransistors that output a voltage related to the applied force. Of particular interest is the sensor's ability to not only detect normal stresses, but shear stresses as well. This is accomplished by monitoring neighbouring sensor cells for negative and positive deformations in order to deduce how a force has been applied (Figure 2-25, Left).

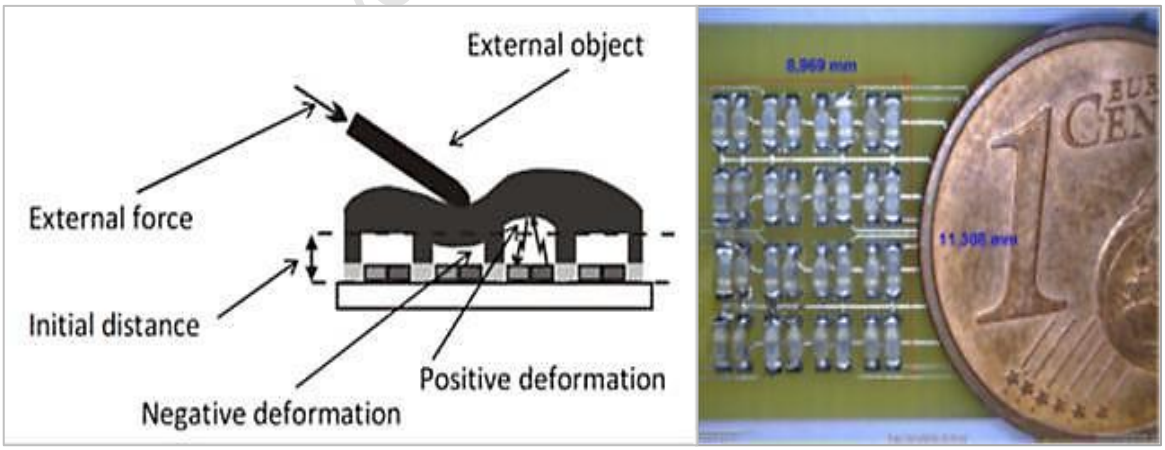

Figure 2-25: Optical sensor array by S. Pirozzi [47]

This type of sensor could potentially be designed on a customised basis with off the shelf surface mount components, thus providing a low cost and compact, yet flexible and easy to integrate, sensing system when compared with commercial force sensing array solutions.

Another type of optical force sensor using an alternative mechanical actuation system is shown below.

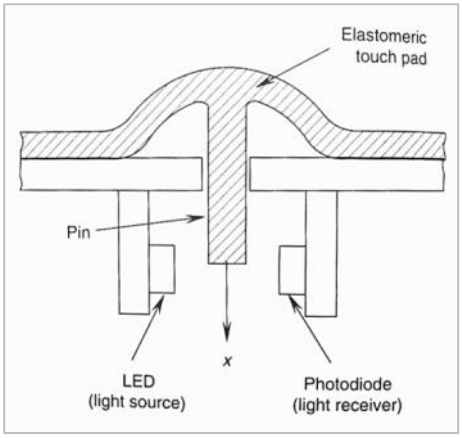

Figure 2-26: Optical tactile sensor with localised light source [46]

Using a type of elastomeric touch pad with an attached pin, an LED light source can be used, together with a photodiode or phototransistor, to measure the light obstructed by the pin. By measuring the tactile deflection of the pin using the photo sensor, the tactile force can be determined. Such a sensor would be very cost effective and reliable and, by using surface mount components, it could be made extremely compact. Commercial versions of this specific sensor were not found.

2.4.4 Conclusions

The following conclusions were drawn from the information detailed in this section:

- By utilising a combination of both dynamic (piezoelectric/transduction) and static (capacitive/resistive) sensors, control of a gripper could be greatly improved.
- FSR and elastomer based piezoresistive sensors are cheap, easy to interface and can be easily installed, but suffer from inaccuracy, hysteresis effects, frailness (if they are not protected) and temperature sensitivity.
- Piezoelectric force sensors are dynamic in nature and can only provide static force information after signal processing. However, they can be very useful to improve closed loop control by reducing overshoot and step rise times.
- Capacitive sensors provide good sensitivity, but suffer from moderate hysteresis (depending on the elastomer material) and the need for relatively complex circuitry and signal processing.
- Optical sensors can be cost effective, simple to implement, compact and robust, but they are not widely commercially available thus requiring a custom design. A great benefit is that they can be used to infer tangential forces as well as normal forces. It should be noted that other types of sensor arrays (dependant on their construction) may also provide this capability.
- Sensor arrays (piezoresistive/ capacitive/ optical) can provide excellent force distribution images with possible slip detection and offer the robot/operator a highly improved sensing ability (even small arrays e.g. 4x4 cells) with improved grasp stability. Although commercially available products are costly, an optical or piezoresistive sensing array could provide a simple and reliable sensing solution.

2.5 Concluding Remarks

The gripper systems presented in the sections above are by no means an exhaustive list, with many more having been identified while performing literature research. Extracting from these sources, the following deductions may be drawn:

- Important gripper characteristics include high reliability, robustness and controllability, while retaining good flexibility and dexterity as well as being cost-effective and light-weight.
- Most angular and parallel grippers are not as well equipped to cope with the uncertainty and unpredictability inherent in **USAR** environments when compared to adaptive types. However, they offer high reliability and robustness and can be relatively compact. Furthermore, their control is simple with sensors being easy to install and utilise.
- Adaptive grippers can be flexible and highly dexterous whilst remaining relatively lightweight and easy to control. However, due to their increased actuation complexity when compared to angular or parallel systems, their reliability and robustness have not yet been proven in the field. All adaptive grippers that were investigated were still in their research stages, with no known grippers being deployed in real-world **USAR** environments.
- Many gripper systems suffer from reduced sensing ability, with only proprioceptive sensing of torque and position available. These include commercial grippers as well as grippers developed in research institutions. The use of exteroceptive sensors, as well as sensor fusion, is crucial to a high performance and effective end-effector system.
- Rescuers would prefer a gripper with reduced functionality but increased reliability and simplicity (particularly related to the control of the system) to increase their confidence in the manipulator system.

Based on the conclusions drawn above, the following chapter will present the primary system specifications that were selected including justification on why these choices were made.

Chapter 3. Primary Specifications

The previous **Background Research** chapter detailed some of the existing solutions and future challenges associated with the design of an **USAR** end-effector. Drawing from this information, this chapter establishes some design requirements which will guide the project through the various phases of the design process. These specifications also form the basis for the test requirements which the end-effector will be evaluated against and from which performance characteristics will be gauged. Justifications for all primary specifications have been provided to substantiate the selections that were made.

The following table details the specifications of the overall end-effector system. These shall hereafter be referred to as the **Primary System Specifications**. Subsequently, each subsystem chapter will present individual detailed specifications related to the specific system and will be known as **Subsystem Specifications**.

Table 3-1: Primary Specifications and Requirements of the Overall System

Location	Design Requirement	Desired Value
3.1 Physical Specifications		
3.1.1	Gripper Type	Parallel Type
3.1.2	Number of Gripping Fingers	2
3.1.3	Minimum Gripper Stroke (Open)	130mm
3.1.4	Overall Mass (Excluding Motors and Controllers)	800g
3.1.5	Overall Maximum Length	480mm
3.2 Functional Specifications		
3.2.1	Ability to Grip a Large Variety of Objects	Yes
3.2.2	Primary Communications Protocol	I2C
3.2.3	Built In Gripper CAM for Close Range Manipulation	Yes
3.2.4	Suitable Lighting for Close Range Manipulation	Yes
3.2.5	System Supply Voltage	5V, 12V, 18V
3.3 Performance Specifications		
3.3.1	Minimum Achievable Prehension Force	100N
3.3.2	Minimum Achievable Wrist Torque	5Nm
3.3.3	Minimum Gripper Open/Close Time	5s
3.3.4	Maximum Allowable Power Draw	90W
3.3.5	Continuous Rotation of the Wrist Section	Yes
3.3.6	Minimum Wrist Rotational Speed	60 RPM
3.4 Software Specifications		
3.4.1	Control Software	LabView

3.1 Physical Specifications

3.1.1 Gripper Type

In previous years, adaptive, parallel and angular gripper projects have been undertaken, of which the parallel end-effector has proven the most promising. For a detailed review of the past end-effector projects, please see **Chapter 5**. **Gripper Subsystem**.

3.1.2 Number of Gripping Fingers

As a parallel type gripper has been selected for development, a minimum of two gripping fingers are required to provide one degree of freedom for the end-effector. More gripping fingers increase complexity but may increase flexibility for gripping certain objects.

3.1.3 Maximum Gripper Stroke

Due to the nature of objects that will be manipulated (e.g. 100mm Cube in RoboCupRescue) the grip stroke for the gripper has been chosen to be 130mm. This should aid in the flexibility and adaptability of the system and allow the end-effector to handle a large variety of objects that could be encountered in a disaster area.

3.1.4 Overall Mass (Excluding Motors and Controllers)

The overall mass of the gripper and wrist sections may not exceed a total of 800g excluding motors and additional electronics. This value was specified by Peter Henson, an MSc student who designed the Ratel manipulator arm.

3.1.5 Overall Dimensions

The combined lengths of the gripper and wrist should be minimised as far as possible to keep the end-effector compact and manoeuvrable, while allowing sufficient room for the motors, motor controllers and additional electronics to be installed.

3.2 Functional Specifications

3.2.1 Ability to Grip a Large Variety of Objects

During rescue robot operations, the gripper is the only device that gives the robot the ability to physically interact with its environment. These surroundings can be dynamic and unpredictable and require an end-effector that can operate efficiently under varying conditions and manipulate a diverse range of objects.

3.2.2 Primary Communications Protocol

The primary communications protocol to the manipulator arm was pre-selected by Peter Henson as I2C. Bradley Springer, an MSc student developing the control system for the manipulator, will test and evaluate this communications protocol and may make modifications if necessary.

3.2.3 Built In Gripper CAM for Close Range Manipulation

As the gripper is located at the end of the rescue robot arm, it may be advantageous to include a low resolution camera to aid in exploring areas that may be difficult to reach or inaccessible to the sensor payload.

3.2.4 Suitable Lighting for Close Range Manipulation

USAR environments are often not well illuminated and would require artificial lighting to aid the operator to perform visual inspections. Although the Ratel sensor payload already houses a powerful LED lighting solution, it may be advantageous to install additional lighting into the end-effector to improve the gripper camera image and to make inspections of small openings easier.

3.2.5 System Supply Voltage

Three voltage rails supplying the end-effector system were pre-selected by Peter Henson, namely 5V, 12V and 18V lines.

3.3 Performance Specifications

3.3.1 Minimum Achievable Prehension Force

The minimum achievable prehension force of the gripper was established to be 100N. This is the approximate prehension force that a human can exert using one hand, as deduced by testing various persons from the **RARL** with a spring gauge.

3.3.2 Minimum Achievable Wrist Torque

Disaster areas are unpredictable and may require the end-effector to utilise tools such as screwdrivers or drills and may include activities such as moving rubble and debris. A rough estimate was that a normal human can exert a torque of between 5Nm to 10Nm by hand. The wrist should then at least be able to match the minimum of 5Nm exerted by a human, if not exceed it. As a comparison, a Metabo 400W DRILLBE4006 can exert approximately 6Nm of torque.

3.3.3 Minimum Gripper Open/Close Time

In real world scenarios the gripper should be able to operate within its prehension force boundaries while staying dextrous and manoeuvrable enough to be easy to control by an operator. Based on the data acquired from the three prototype end-effector versions, a minimum opening and closing time of approximately 5s was shown to provide suitable speed and control characteristics.

3.3.4 Maximum Allowable Power Draw

The maximum power draw of the system at high load operating conditions should not exceed 90W. This allows 40W each per motor and 10W for additional control and sensor circuitry.

3.3.5 Continuous Rotation of the Wrist Section

The gripper should be able to rotate continuously through 360° to enable the use of tools such as screwdrivers or drill attachments. A 30way slip-ring was pre-selected by Peter Henson to facilitate this function.

3.3.6 Minimum Wrist Rotational Speed

A rotational speed of 60RPM should be more than sufficient for normal gripper manoeuvres as well as tool operations such as low-speed drilling. The speed was, in part,

dictated by the Maxon EC22 40W motors that were pre-selected for the project, but also by data collected while operating the prototype end-effector versions.

3.4 Software Specifications

3.4.1 Control Software

The LabView programming environment was selected by the **RARL** as the primary interface and embedded programming software package for use on all projects. The packages to be utilised in this project may include the LabView Arm Embedded Module, LabView Vision Acquisition Module as well as the standard LabView base package.

3.5 Summary

The primary specifications and design justifications for the end-effector system were detailed above. These specifications were arrived at by performing background research into various commercial and research based end-effectors as well as studying different sensory systems.

The following chapter will examine the design of the overall end-effector by analysing the gripper, wrist and electronic subsystems separately. Each module will illustrate the design process from the initial design development stage to a final solution. Within each chapter, module specific specifications, calculations and design justifications will be demonstrated followed by a subsystem summary.

Chapter 4. System Development

Figure 4-1: Overall End-Effector System

The overall end-effector system (shown above) was subdivided into three major subsystems that were examined individually. This was done as each subsystem had module specific criteria and desired features that were unique to that system. Furthermore, the system breakdown simplified the analysis and design of the overall system. Figure 4-2, below, displays the system breakdown into the three end-effector subsystems. Figure 4-3, on the following page, illustrates the interconnections between these subsystems.

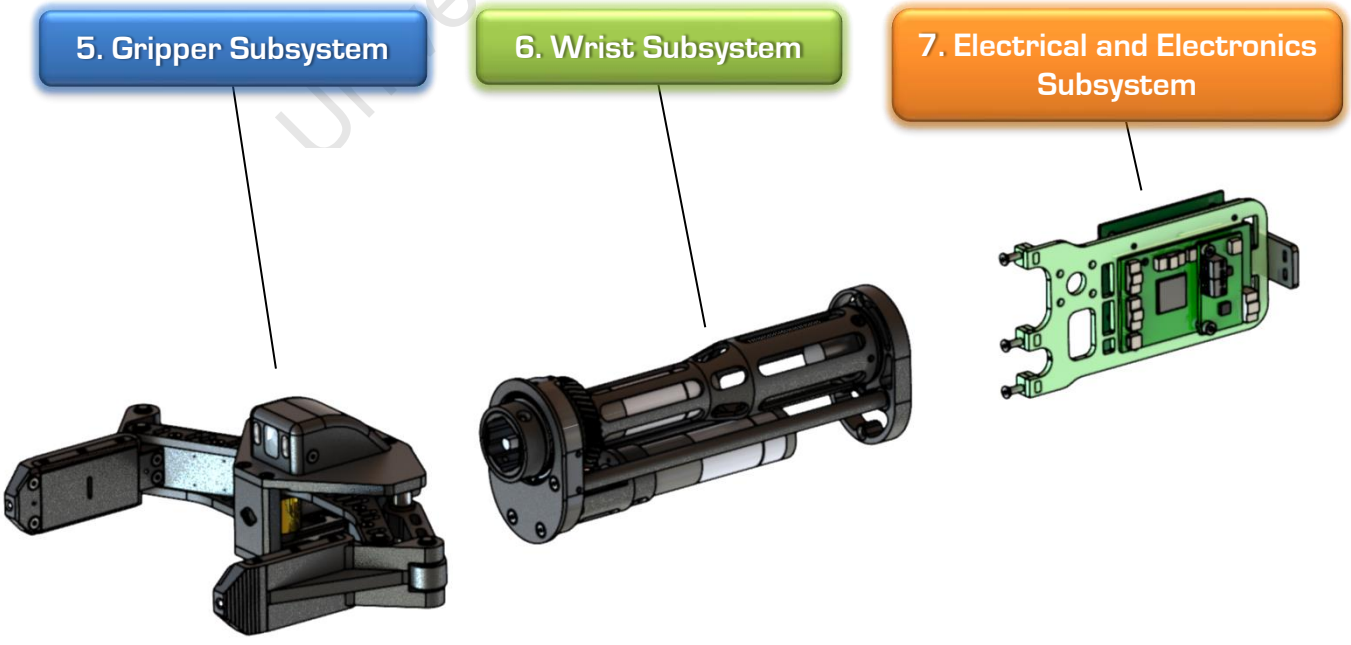

Figure 4-2: End-Effector System Breakdown

Figure 4-3: Basic Interconnections Between Subsystems

Gripper Subsystem

The parallel gripper subsystem is made up of a combination of mechanical, electrical and software components that, once integrated, function as a stand-alone system. The following features and functionality have been included:

- Four-bar parallel linkage mechanism driven by an M12x1.75mm lead screw
- Quick release gripper/wrist interface for easy removal or exchange of the gripper
- Integrated adjustable KX-1 VGA camera with high bright LED lighting
- Object presence detection capabilities located at the rear/front of the gripper fingers
- Modular force and pressure sensors for easy removal and exchange
- Digital Hall effect limit switches as non-mechanical end-stops
- Custom gripper embedded controller with a Freescale MC9S08GT16A microprocessor
- Communications to the end-effector primary controller via SPI

Wrist Subsystem

The wrist subsystem connects the gripper module to the electrical and electronics module (both mechanically and electrically) and has been designed to be mounted to the end of the Ratel manipulator arm. The subsystem houses the two Maxon EC22 40W 157:1 drive motors for actuation of the parallel gripper as well as the wrist itself. A 2:1 spur gearbox provides a theoretical maximum torque of 6Nm during tool handling operations. Additionally, the module is fitted with a 30-way slip ring to facilitate continuous rotation of the gripper as well as Hall Effect sensors for position control and calibration. Temperature sensing has been included to monitor the motors during high load operations.

Electrical and Electronics Subsystem

The electrical and electronics module provides control, monitoring and processing functionality to the end-effector system. Additional features include power regulation and communications with the Ratel manipulator arm. It is connected to the wrist module and consists of two Maxon DEC24/3 speed controllers, a custom designed ARM Cortex-M3 LM3S8962 embedded controller, a custom dual current sensor as well as a connection distribution board.

Figure 4-4, below, presents an overview of the overall end-effector system with minimum and maximum system dimensions for when the gripper is opened and closed.

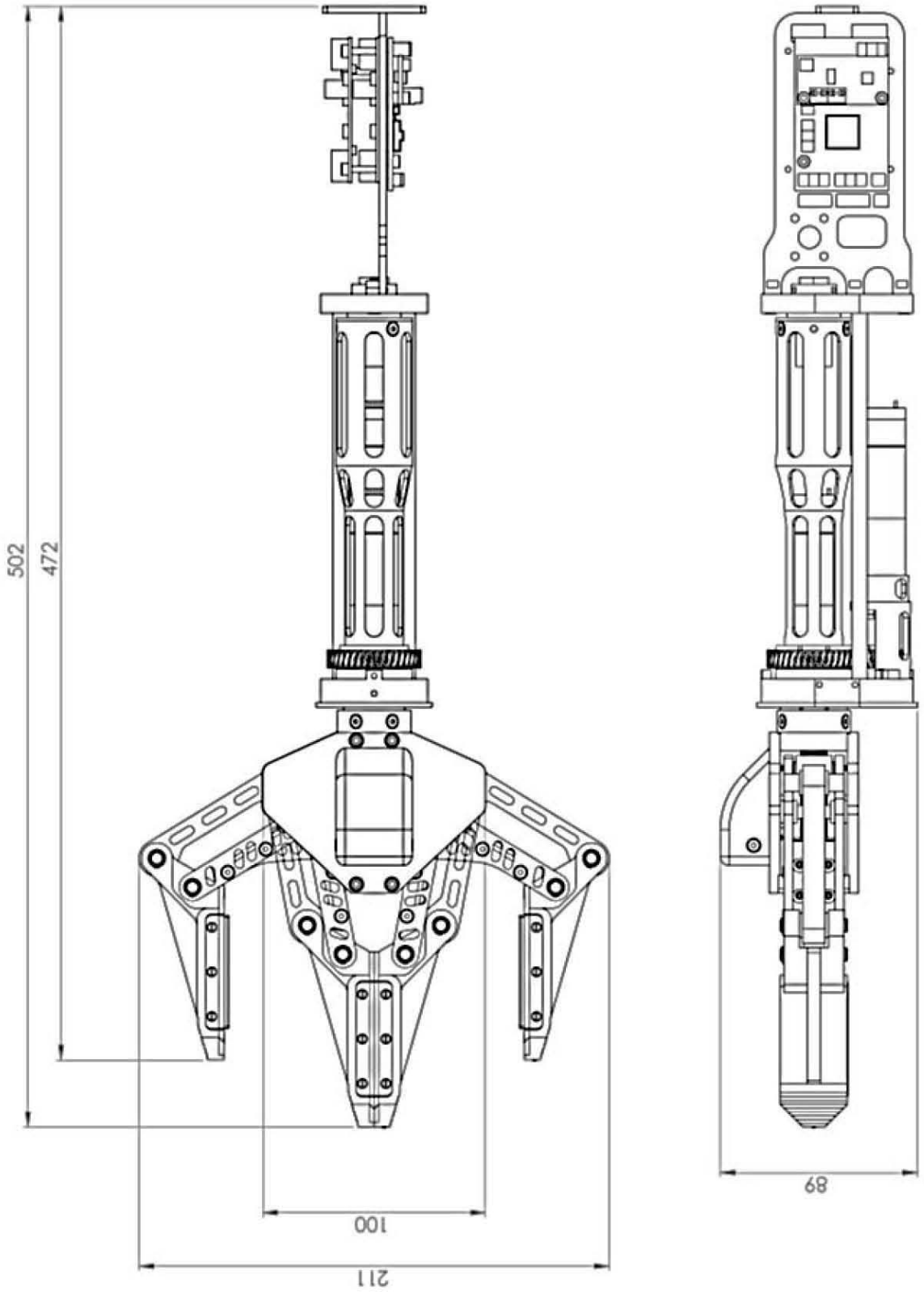

Figure 4-4: Overall Dimensions of the End-Effector System

Summary

The final end-effector consisted of three primary modules, each contributing to the overall performance and operability of the system. **DFMA** principles were utilised throughout the design processes in an attempt to simplify assembly and future maintenance. In total, only four tools were required to assemble or dissemble the entire system, these being a small flat screwdriver, Circlip pliers and a set of 2mm/2.5mm Allen keys.

The following three chapters will detail the unique development processes that were followed for each electro-mechanical system including generating subsystem specific specifications and design requirements, initial design developments, production of detailed design solutions and evaluation of the manufactured components. Conclusions and recommendations will also made at the end of each subsystem chapter.

Chapter 5. Gripper Subsystem

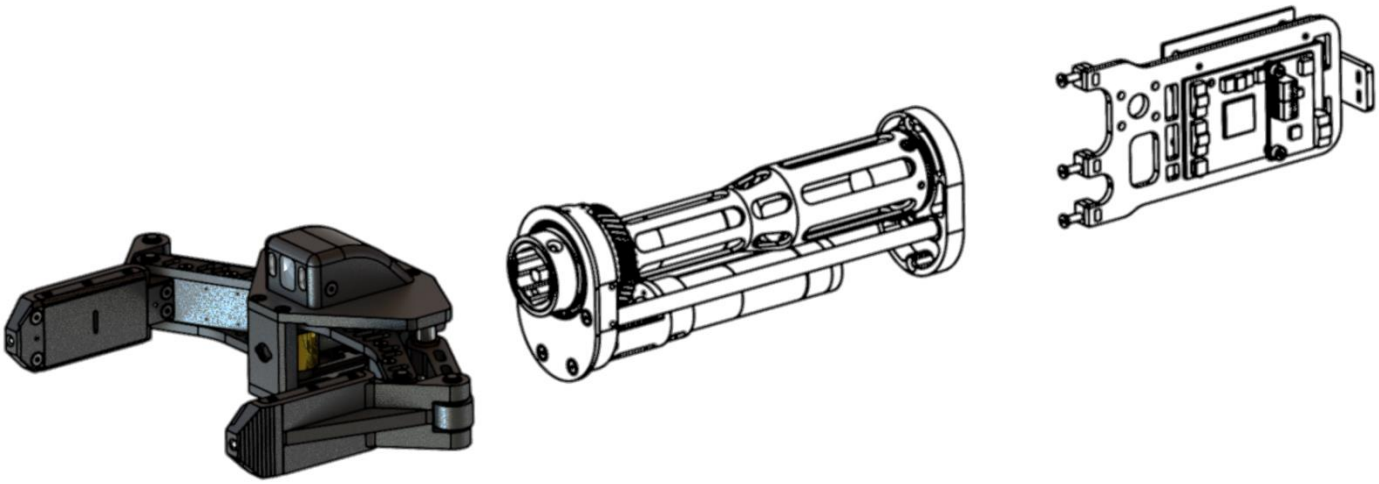

Figure 5-1: Highlighted Gripper Subsystem as Part of the Overall End-Effector

The gripper subsystem is made up of a combination of mechanical, electrical and software components that, once integrated, function as a stand-alone system. Figure 5-1, above, presents the gripper subsystem as part of the overall end-effector. Functionality incorporated in the system includes a VGA camera, integrated lighting, object presence detection sensors as well as interchangeable force and pressure sensors. Figure 5-2, below, shows the final manufactured design.

Figure 5-2: Manufactured End-Effector Parallel Gripper Subsystem

This chapter will detail the complete design process and development of this module, as well as describe its interaction with the rest of the end-effector system. Focus will be placed on the following key areas:

- **Specifications and Design Criteria**
- **Initial Design Development**
- **Material Selection and Manufacturing Methods**
- **Four-Bar Parallel Linkage Mechanism**
- **Lead Screw Actuation**
- **Gripper-Wrist Interface**
- **Gripper Fingers**
- **Camera, Lighting and Sensors**
- **Gripper Embedded Microcontroller**
- **Gripper Controller Software**

The chapter starts by presenting module specific detailed specifications of the gripper subsystem including design justifications.

5.1 Module Specific Specifications

The following detailed gripper specifications are rooted in the primary specifications presented in Chapter 3. Critical and non-critical design requirements are presented that will be validated against when full module testing is performed. After presenting the detailed module specifications below, justifications are provided to clarify the design choices that were made.

Table 5-1: Gripper Specific Module Specifications

Location	Design Requirement	Desired Value
Physical Specifications		
5.1.1	Gripper Type	Parallel Type
5.1.1	Minimum Gripper Stroke	130mm
5.1.2	Minimum Gripper Finger Length	70mm
5.1.2	Gripper Finger Width	30mm
5.1.2	Maximum Gripper Length	180mm
5.1.3	Gripper Mass	500g
Functional and Performance Specifications		
5.1.1	Number of Gripping Fingers	2
5.1.1	Minimum Achievable Prehension Force	100N
5.1.4	Actuation System	Lead Screw (Non back-driveable)
5.1.5	Gripper Motor and Gearbox	Maxon EC22 40W 157:1 GP22HP
5.1.6	Tool Handling Capability	Yes
5.1.7	Gripper Finger Serrations	Yes
5.1.8	Modular Gripping Fingers	Yes
5.1.1	Minimum Gripper Open/Close Time	5s
Electrical and Electronic Specifications		
5.1.9	Current Sensor Feedback	25mA Resolution
5.1.10	Gripper Finger Position Feedback	512 CPT Maxon Quad Encoder
5.1.5	Gripper Motor Controller	Maxon DEC24/3
5.1.11	Integrated Camera and Lighting	Yes
5.1.12	Gripper Limit Sensors	Digital Hall Effect
5.1.13	Object Presence Perception	IR LED Light Bridges
5.1.14	Prehension Tactile Force Feedback	Weiss Robotics 9205i
5.1.15	Integrated Gripper Controller	Freescale MC9S08GT16A µP
5.1.16	Gripper Module Communications Protocol	Serial Peripheral Interface (SPI)

Justifications of Gripper Specifications

5.1.1 Please see **Chapter 3. Primary Specifications** section for detailed justifications on these main system specifications.

5.1.2 The gripping fingers should be large enough to comfortably grip most objects that may be found in disaster areas including items such as rocks, pieces of wood, water bottles etc. The maximum length of the gripper was defined by MSc student, Peter Henson.

5.1.3 A maximum mass of 800g was specified for the overall end-effector excluding electronics systems. Constituting this overall mass, 500g has been assigned to the gripper section.

5.1.4 As was observed in Terry Scott's parallel- and Marten Cross's angular-gripper, the ability of the end-effector to be self-locking could greatly simplify the control, user interface and power requirements of the system (actuation will only need to be provided during actual motion).

5.1.5 Maxon 24V 40W EC22 (Nr: 386658) motors were pre-selected for this project due to their high quality and reliability, as well as their good weight (85g) to power (19.7mNm @ 31900rpm) output. This motor was matched to a Maxon 157:1 GP22HP (Nr: 370786) planetary gearbox and a Maxon DEC 24/3 speed controller to provide a potential 3Nm torque @ 200rpm of the output shaft.

5.1.6 When operating the **MRP** in the field, the ability to utilise tools without modifying the robot may be very advantageous to an operator. Possible tools that may prove useful include screwdrivers, hex sockets and drills.

5.1.7 Serrations on the exterior of the gripping fingers would improve outward gripping and simplify manipulation of some objects such as pipes and tubes.

5.1.8 As each rescue scenario may present unique challenges for the end-effector, it may prove advantageous to have gripping fingers that could be modified 'on the go' as necessary. Depending on the scenario this could, for example, include exchanging an advanced sensor, such as the Weiss Robotics 9205i, for a more robust and durable **FSR** solution.

5.1.9 In order to achieve a stable and reliable sensor feedback system sensor fusion, including tactile sensor feedback as well as motor current monitoring, should be implemented. Due to the fact that the Maxon DEC 24/3 controllers do not offer integrated motor current sensing, an external board should be developed to provide high resolution current measurements.

5.1.10 Position feedback for the gripper will be provided by a pre-selected, factory fitted 512 **C**ounts **p**er **T**urn (**CPT**) Maxon MR Quadrature Encoder (Order Nr: 201940). Together with the integrated quadrature decoder module on the proposed LM3S8962 primary controller, high resolution position feedback would be available.

5.1.11 As the gripper is located at the end of the Ratel manipulator, it may be advantageous to include a low resolution camera and LED lighting solution to aid in exploring difficult to reach areas that may be inaccessible to the sensor payload.

5.1.12 The Maxon MR quadrature encoders are relative shaft encoders and need to be recalibrated upon power up of the system. During this calibration process, digital Hall Effect switches could act as ideal non-contact end stops.

5.1.13 Visual identification of objects and precise control of the gripping system may prove difficult for an operator working off a camera feed alone. Object proximity sensors would aid in identifying when an object is fully enclosed in the gripper and would greatly improve the chances of a successful manipulation operation.

5.1.14 Object manipulation activities may include interfacing with humans; therefore a form of force feedback would be essential. An advanced tactile sensing array would be optimal for this task. The Weiss Robotics 9205i 84 cell piezoresistive tactile sensing array with integrated control circuitry provides high resolution force distribution images of objects being manipulated, as well as a simple control interface. As an alternative and possibly more robust solution, the use of force sensing resistors should also be investigated.

5.1.15 The Freescale MC9S08GT16A was selected as the integrated gripper controller due to its wide use in the **RARL**, as well as its ease of use and minimal power requirements.

5.1.16 The **S**erial **P**eripheral **I**nterface (**SPI)** bus was chosen as a communications protocol due to its speed, ease of use and its availability on the MC9S08GT16A integrated gripper controller.

5.2 Initial Design Development Process

From the background research that was performed and the detailed specifications listed in the previous section, the following investigation into conceptual designs was undertaken.

In previous years, three undergraduate end-effector projects were run to assess gripper concept designs and should be regarded as precursors to the current research being conducted. These included an adaptive gripper created by Stephen Walker [36] (Figure 5-3), an angular gripper designed by Marten Cross [34] (Figure 5-4) and a parallel end-effector produced by Terry Scott [35] (Figure 5-5).

These projects were run to identify which end-effector should be chosen for further development and implementation on the rescue robot platform. Careful evaluation and practical testing was carried out on all projects. Figure 5-6 presents an additional adaptive gripper finger prototype that was based on the Robotiq Three Finger Adaptive Gripper [48] as a proof of concept design.

Figure 5-3: Adaptive Gripper Concept

Figure 5-4: Angular Gripper Concept

Figure 5-5: Parallel Gripper Concept

Figure 5-6: Prototype Adaptive Gripper Finger

The following table provides a brief overview of the various key performance indicators that were achieved by the three main end-effector concepts. These characteristics were determined by carefully analysing and evaluating key system elements and performing tests on some of these to verify the data specified in the undergraduate reports.

Table 5-2: Summary of Key Performance Indicators of Past Gripper Projects

Desired Specification	**Angular**	**Parallel**	**Adaptive**
Prehension Force (100N)	+- 230N	300N	Not Specified
Grip Stroke	230mm	110mm	165mm
Overall Mass (G+W) (800g)	1745g	1130g	548g + Wrist
Sensors and Feedback	- 2 x Hall effect - Current feedback - No encoder feedback	- Hall effect switches - Current feedback - Quadrature encoding	- Current feedback (External)
Control Unit	Freescale MC9S08GT16A	Freescale MC9S08GT16A	Freescale MC9S08GT16A
Tool Change/Cutter	Tool Change	None	None
Key Advantages	- Large prehension force - Excellent grip stroke - Great adaptability to environments	- Large prehension force possible - Low backlash - Simple sensor mounting - Self-blocking	- Great adaptability - Fewer sensors required - Single small motor sufficient - Versatile - Lightweight
Key Disadvantages	- Large backlash - Difficult to manufacture - Difficult sensor mounting - Precision gripping more difficult - Heavyweight	- Limited grip stroke - Reduced versatility - Gripper misalignment possible	- Small prehension forces - Complicated design - Large/bulky - Reverse driving - Limited grip stroke

From Table 5-2 it was concluded that many objectives were realised, but that some crucial specifications were not. This is understandable as these projects were only run over four months with limited funding available.

Of the specifications that were exceeded, the overall masses were probably the most critical. The angular gripper surpassed the weight specification by more than 120% and the parallel gripper by 40%. This was mainly due to the fact that the grippers were overdesigned to exert a prehension force in excess of the 100N proposed above and also that motors were pre-selected for the projects.

Furthermore, all the end-effectors had a highly reduced set of sensing capabilities. Force and touch sensing was largely proprioceptive and only the internal parameters of the grippers were sensed (e.g. current draw and quadrature encoding). Furthermore, no additional features such as a gripper camera or object perception sensing had been

implemented. This would have made these end-effectors very difficult to control if they were to be used on the **MRP** remotely.

Figure 5-6 shows a three phalanx gripping finger that was manufactured on the UCT Perspex laser cutter. The aim of creating this prototype was to test how much complexity this type of mechanism would introduce over a single **DOF** angular or parallel system. Having tested the finger by simulating gripping a variety of objects, the realisation was made that a differential gearbox was needed at the base of the finger for the two-linkage system mechanism to work effectively. Upon this realisation, it was concluded that this type of end-effector would most likely be too complicated to be realistically used for rescue operations, but that other types of adaptive grippers should be investigated further. As a result, Stephen Walker's adaptive gripper was produced and can be seen as a continuation of this concept.

Based on the conclusions that were drawn in Table 5-2, the parallel gripper by Terry Scott was selected for further development. Principal advantages over the other systems included low backlash characteristics, high prehension force capabilities, simple mounting for sensors and its self-locking ability. The compactness of the lead-screw arrangement also made this an attractive actuation technique, compared with a worm gear drive as found in Marten Cross's angular gripper.

Figure 5-7, below, illustrates the initial basic concept that was developed. Using an iterative design process, features and functionality were added incrementally. Throughout the development process, **DFMA** principles were used to guide design iterations.

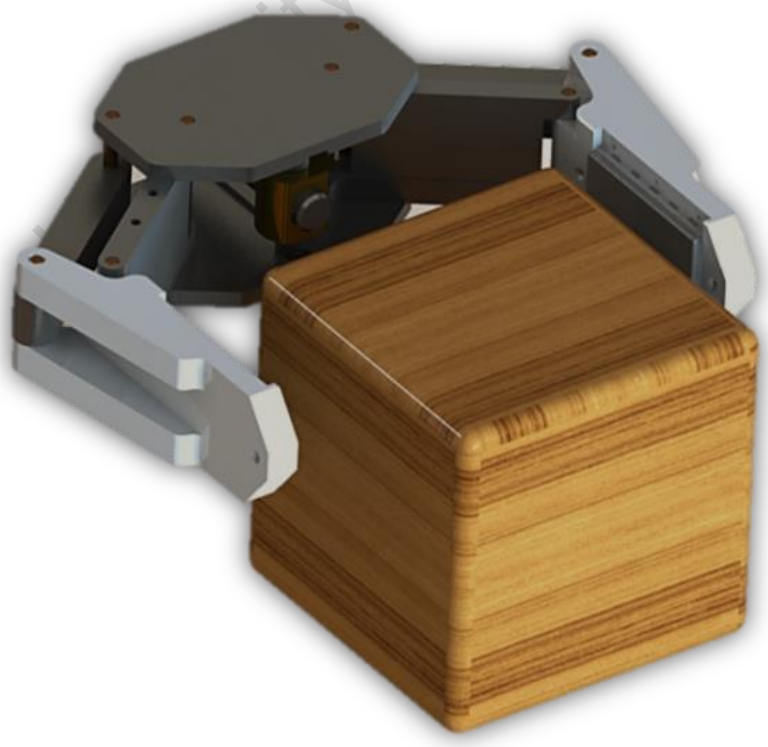

Figure 5-7: Initial Parallel Type Gripper Concept Based on Terry Scott's Project

Using the basic concept above as a starting point, various additions and alterations were made to the design including adding a gripper camera and embedded microcontroller housing, modifying the gripping fingers to facilitate internal wiring, improving the parallel link mechanism and adding light bridge sensors. These modifications are illustrated in Figure 5-8 below.

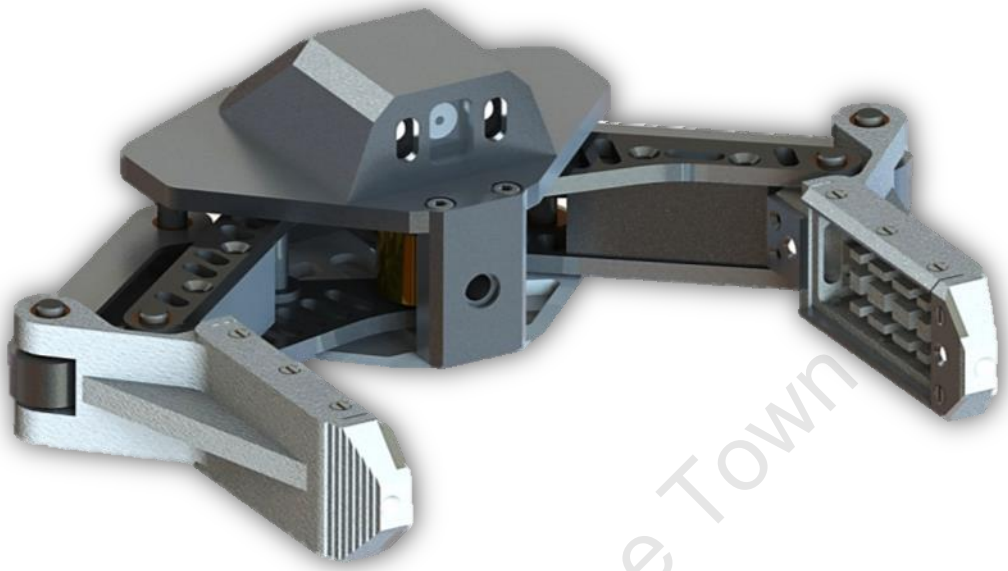

Figure 5-8: Gripper Design After Some Additions

At this stage, the design was presented to the workshop to receive advice on which parts should be altered to simplify manufacture. Recommended modifications included simplifying the camera and microcontroller housing, adding different strengthening supports to the gripper fingers and modifying the gripper/wrist interface for simplified manufacture on the **CNC** (**C**omputer **N**umerical **C**ontrol) mill. Some of these modifications can be seen in Figure 5-9.

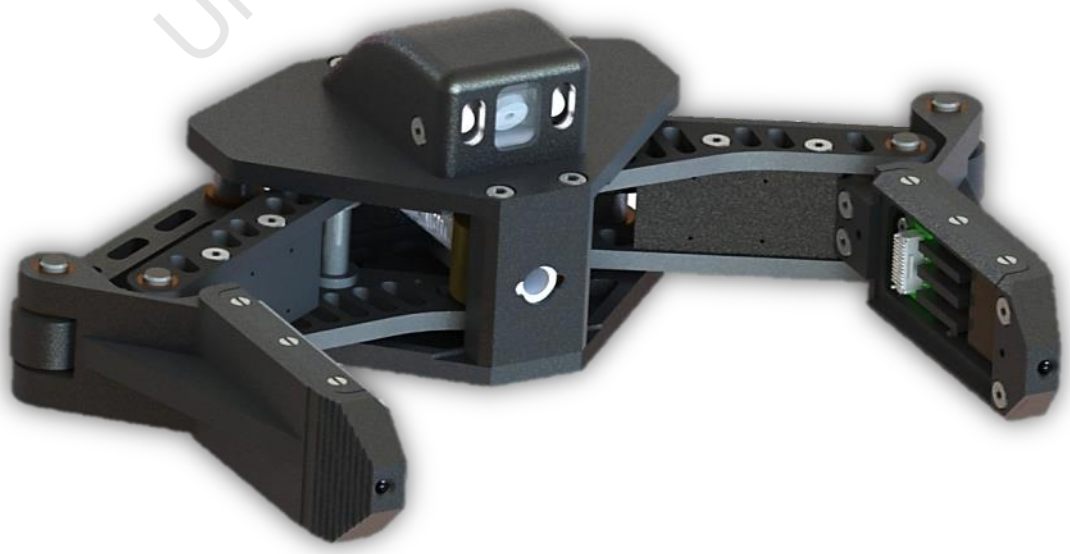

Figure 5-9: The Final Gripper Design After Multiple Design Iterations

5.3 Detailed Mechanical Design

The conceptual design process that was presented was critical to the detailed design that is presented in this chapter. The undergraduate projects allowed for practical investigations into what functioned effectively and what did not. Utilising the knowledge gained from these concepts, prototypes and the conclusions drawn from Chapter 2, the following full detailed design was developed.

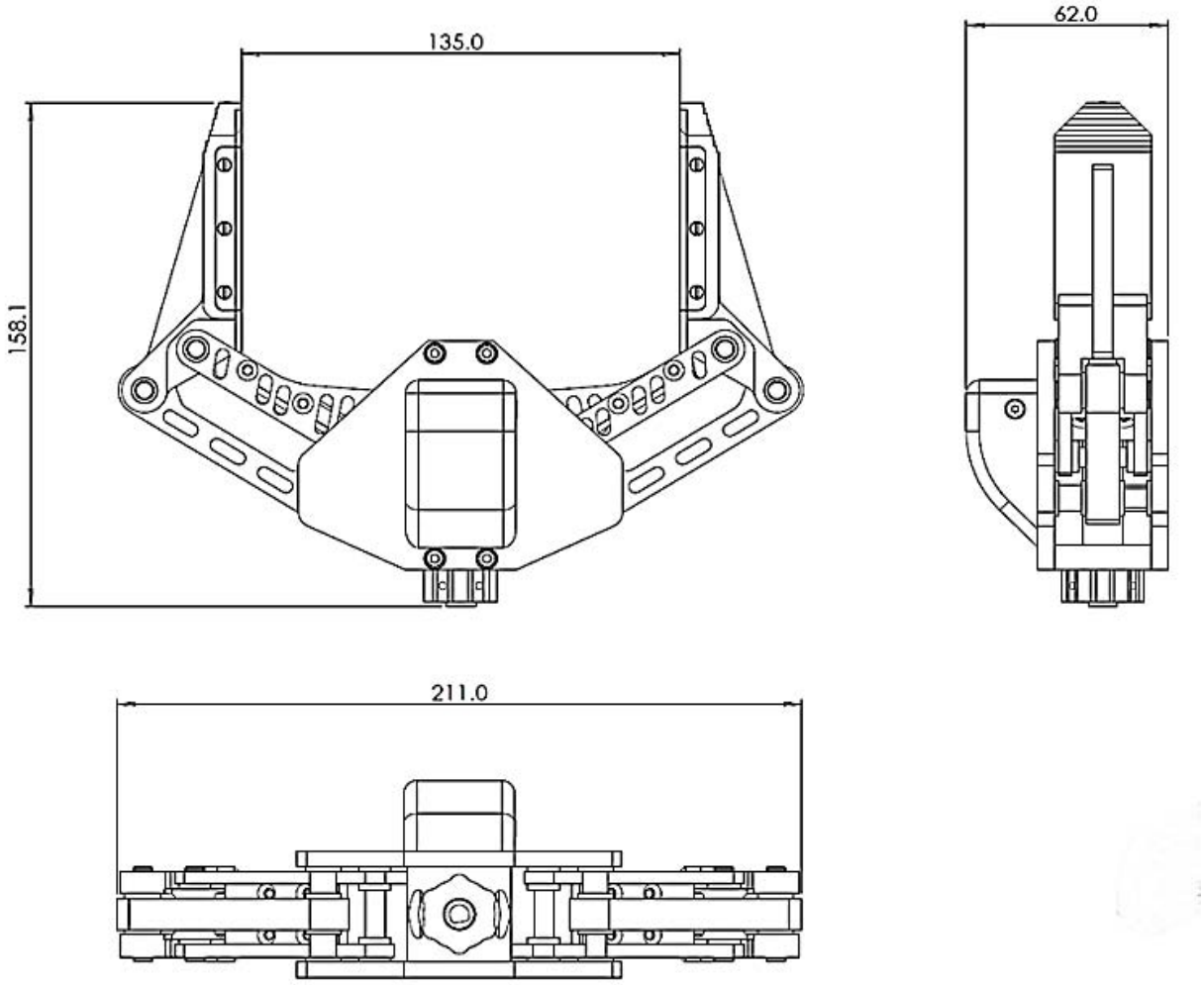

Figure 5-10: Physical Dimensions of the End-Effector Gripper Subsystem

Figure 5-10 shows the overall physical dimensions of the final mechanical design of the gripper subsystem. The module consists of four principal mechanical sections that were analysed separately. These are:

- **Four-Bar Parallel Linkage Mechanism and Journal Bearings**
- **Lead Screw Actuation**
- **Gripper-Wrist Interface**
- **Gripper Fingers**
- **Gripper Electronics Housing**

The subsequent figures highlight some of the key features of the final gripper design.

The following SolidWorks renders show the final gripper subsystem from the front and the rear:

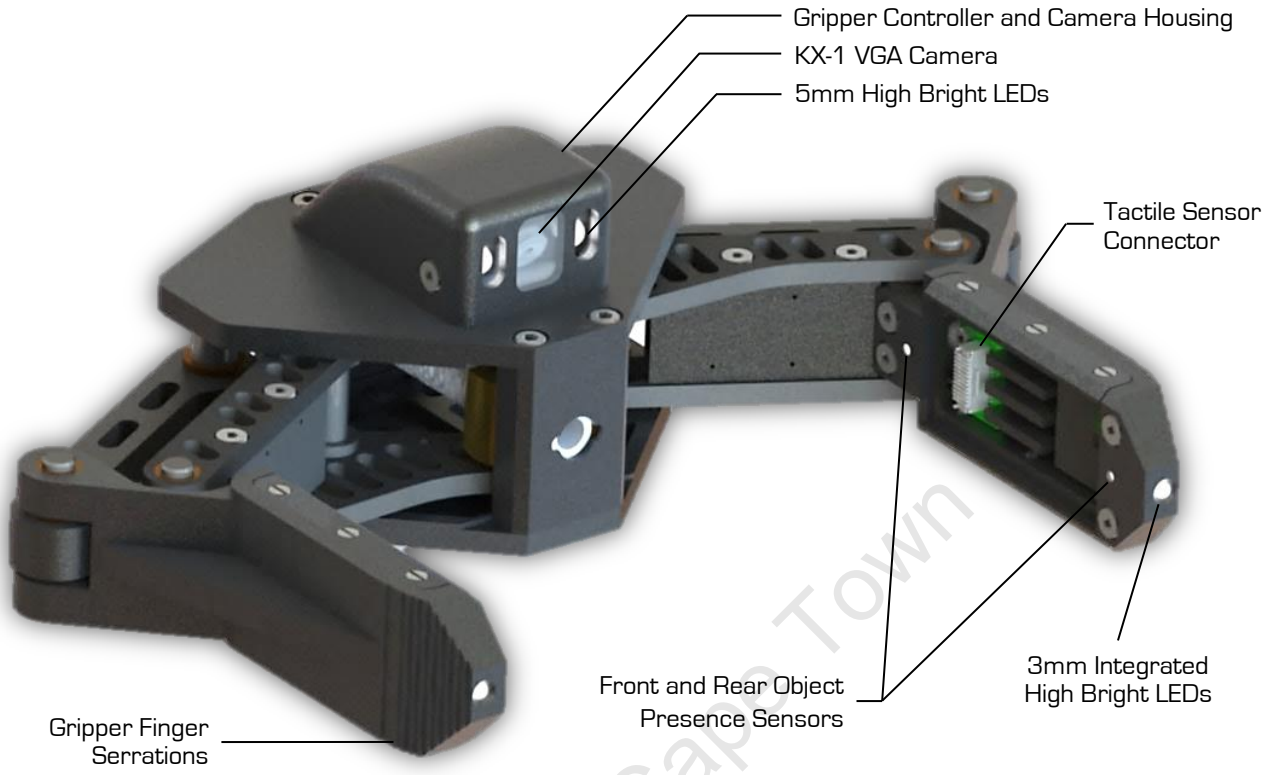

Figure 5-11: Solidworks Render of the Final Gripper Subsystem (Front)

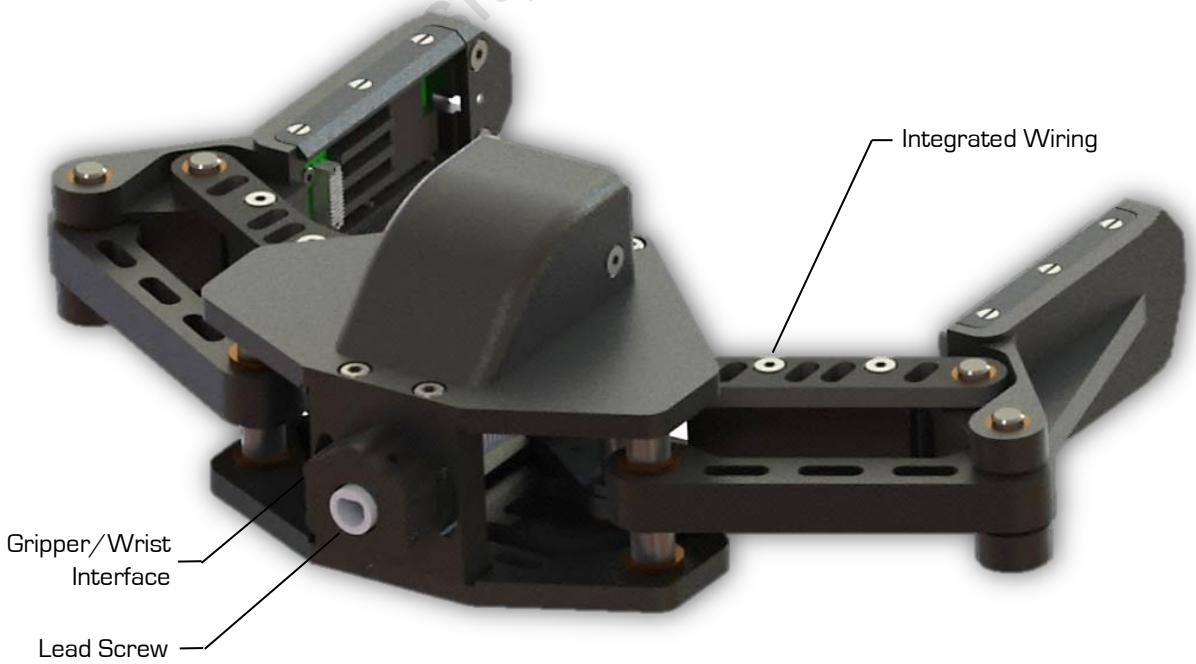

Figure 5-12: Solidworks Render of the Final Gripper Subsystem (Rear)

The following figure illustrates the manufactured gripper components before assembly.

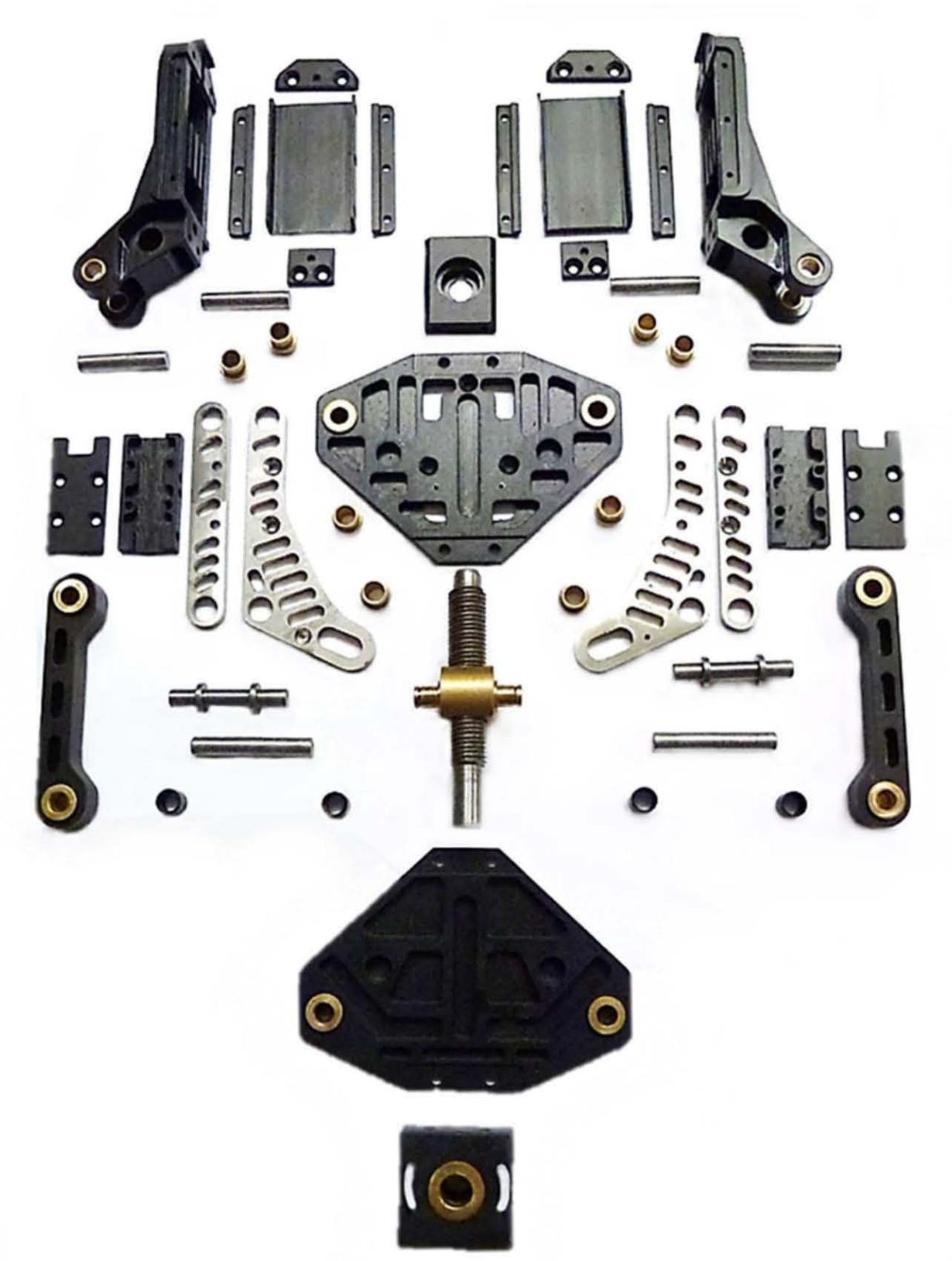

Figure 5-13: Gripper Subsystem Parts Before Assembly

The system shown in Figure 5-14, below, highlights the various critical components of the gripper module. The following sections will expand on the mechanical aspects of these components.

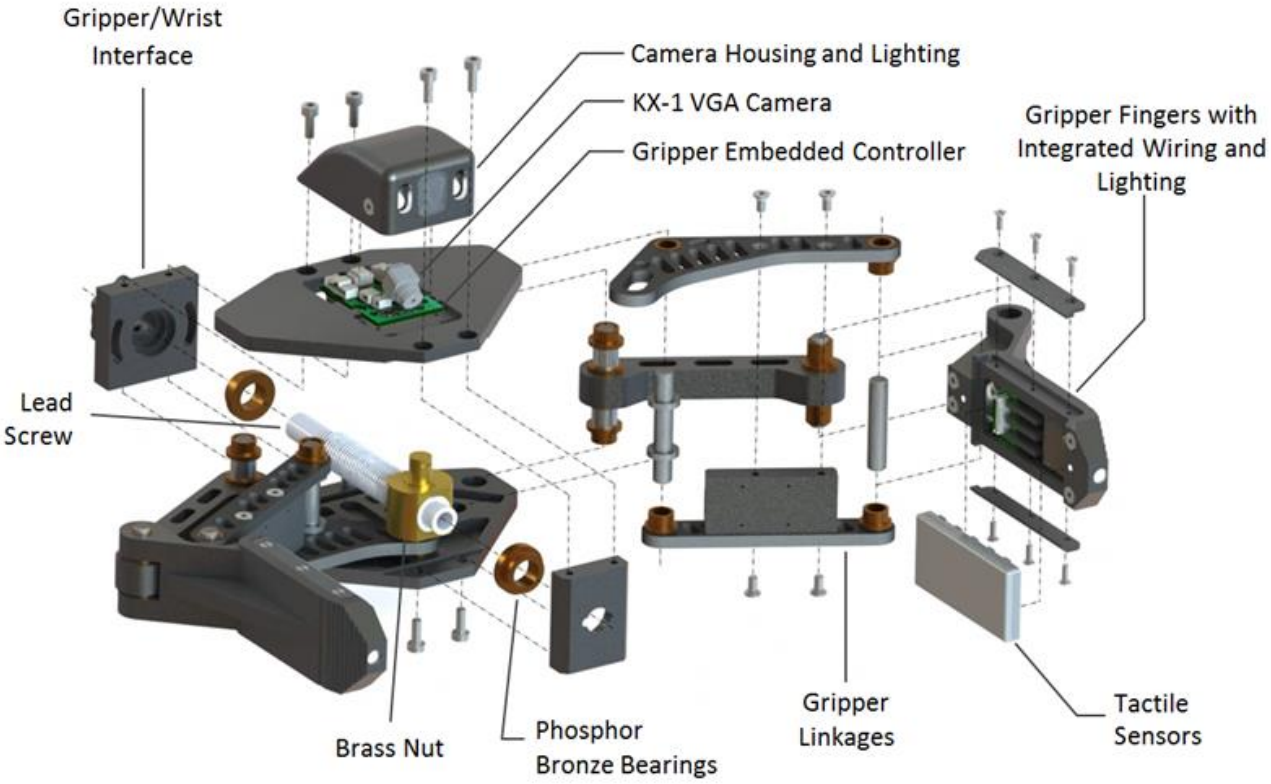

Figure 5-14: Exploded View of the Gripper Module

Material Selections

The rescue robot platform may be deployed in a wide variety of disaster environments. Thus, in order to realise the manoeuvrability, robustness and maintainability of the system, the material choice for certain components was critical. For the gripper subsystem the following selections were made:

1. Overall Body: Due to its high strength-to-weight properties, corrosion resistance and its ability to be easily machined, *Aluminium 6061* was selected as the primary material for the body and some links of the gripper. All *Aluminium* parts were hard black anodised to add further protection to the components.

2. Mid Link / Bent Lever: *Stainless Steel* was selected, instead of plain carbon steel, for the main force transmission links because of its corrosion resistant properties and its higher strength properties over *Aluminium*. Furthermore, these components could potentially be laser cut at Vulcan Steel [49].

3. Lead Screw and Nut: *Silver Steel* was selected for the M12x1.75 (double start) lead screw based on recommendations by the workshop staff. The lead screw nut was manufactured out of *Brass* due its low-friction characteristics as well as its acceptable strength properties.

5. Bearings: *Phosphor Bronze* was selected for the plain bearings used throughout the gripper. This alloy is noted for its low coefficient of friction, toughness and good strength properties.

6. Linkage Pins: *Silver Steel* was selected for the pin linkages due to its high strength properties, its moderate corrosion resistance as well as its machinability.

Utilising these materials, the overall gripper mass excluding electronics was found to be 615g (See **Chapter 9. Testing and Results**, section **9.1.1 Mass Measurement Tests**).

Fabrication

Almost all of the components were designed with the intention that they would be manufacured in UCT's Mechanical Engineering Workshop. The machining facilities available in the workshop include CNC mills and lathes, as well as hand-turning and milling. Due to the intricacies that were added to save weight, the primary drive links were laser cut externally by Vulcan Steel [49].

Figure 5-15, on the next page, shows the gripper camera housing during manufacturing (left) and the completed housing before anodising (right). A R5 coin illustrates the relative size of the proposed KX-1 CMOS camera that would be mounted within this housing.

Figure 5-15: Gripper Camera Housing Being Manufactured (Left) and Completed (Right)

Some of the more complex parts to manufacture, the gripping fingers, are shown below during various stages of machining.

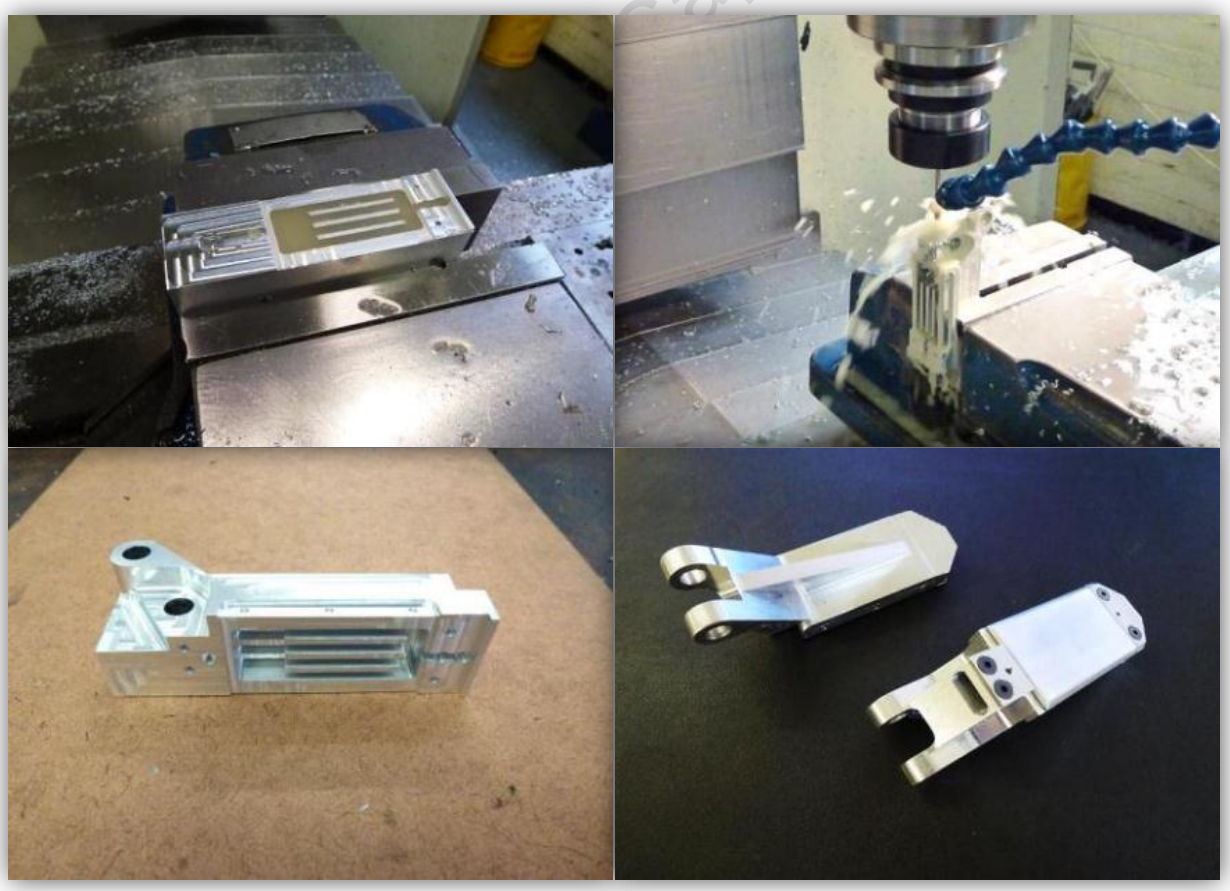

Figure 5-16: Gripper Fingers During the Machining Process

Four-Bar Parallel Linkage Mechanism and Journal Bearings

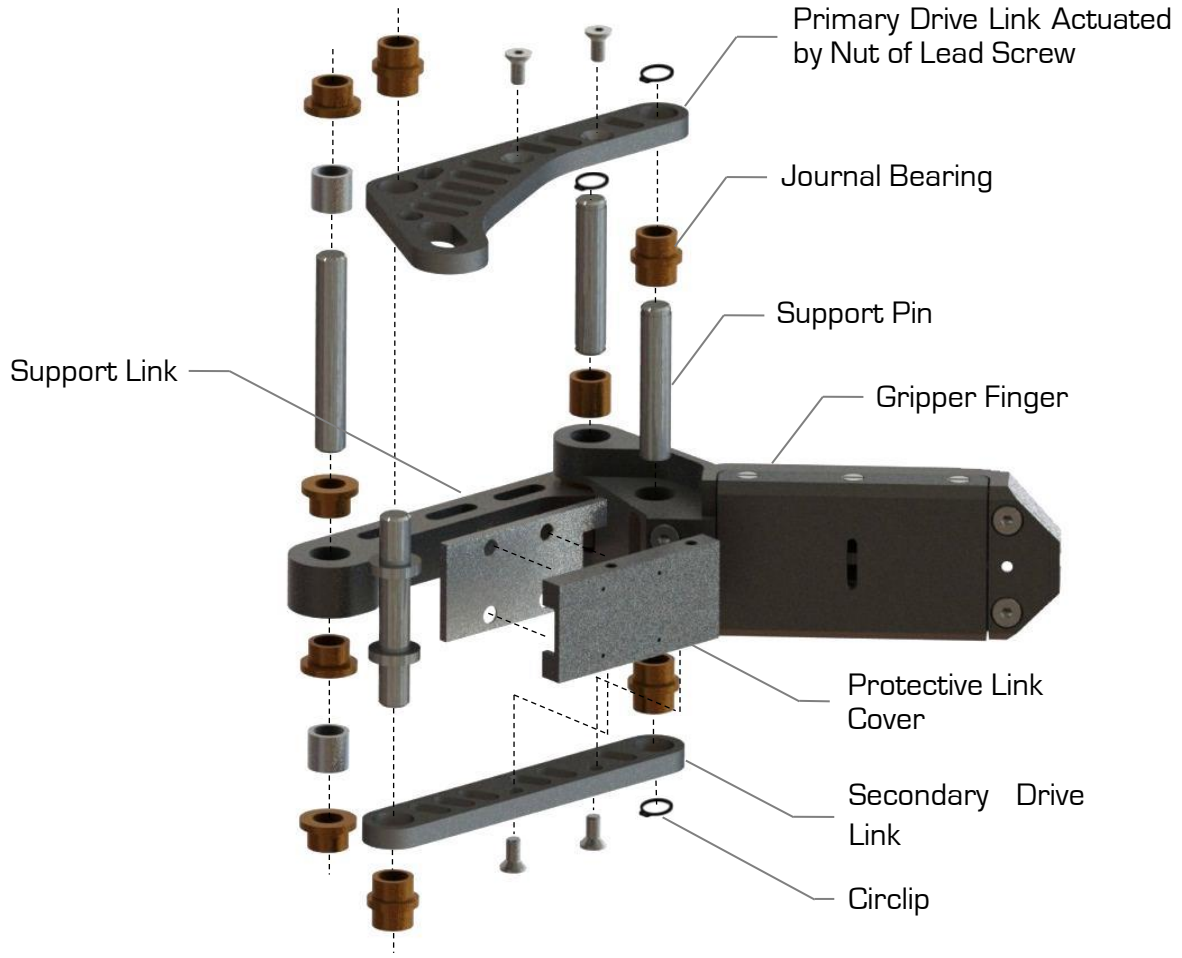

Figure 5-17: Exploded View of the Four-Bar Parallel Mechanism

Figure 5-17, above, presents an exploded view of the four-bar linkage mechanism that was used to actuate the gripper fingers. As can be seen from the figure, the parallel mechanism consists of three driving links, namely two laser cut stainless steel levers and one aluminium support link. Torque is applied to the gripper fingers through the 'primary drive links' which slide on the brass nut of the lead-screw as can be seen in Figure 5-14.

The 'protective link covers' are there to add rigidity to the two steel drive levers and to create a channel for the wiring to the gripper fingers. Four silver steel support pins were used to locate the mechanism at the base section and at the gripper fingers.

Four different kinds of phosphor bronze bearings were designed in various configurations and used extensively in the linkage mechanism and the base housing. Three of the bearing types are shown in Figure 5-17, above, with the thrust bearings illustrated in Figure 5-14. Circlips and M3x6mm countersunk hex socket screws were selected to secure the various components together.

Four-Bar Parallel Linkage Mechanism Calculations

The following section will briefly outline the supporting theory and some calculations describing the selected four-bar linkage design.

Due to the requirement that the gripping fingers always stay parallel to each other, a four-bar planar parallel linkage mechanism was a clear choice. According to *Kutzbach-Grübler's* equation [50] for planar mechanisms, the **DOF** for such a system may be derived by:

$$F = 3(n-1) - 2f$$

Where F = DOF, n = Total number of (binary) links, f = Total number of (revolute) joints

This would imply that the position B (below) can be defined by a single independent variable. Before designing the individual gripper parts, the dimensions of the four-bar linkage mechanisms needed to be established. This involved scaling the lengths of the links to deliver as high a force at the gripper fingers as possible, whilst conforming to the gripper stroke specifications in Table 5-1. Weight considerations also needed to be taken into account.

Figure 5-18 shows the various dimensions that needed to be considered in the optimisation process. Although lengths *d* and *e* would be superfluous when used to optimise the four-bar linkage mechanism alone, these variables were also used to position points A and D relative to the gripper housing to ensure a suitable grip stroke. For this reason the variables have been presented separately rather than combined.

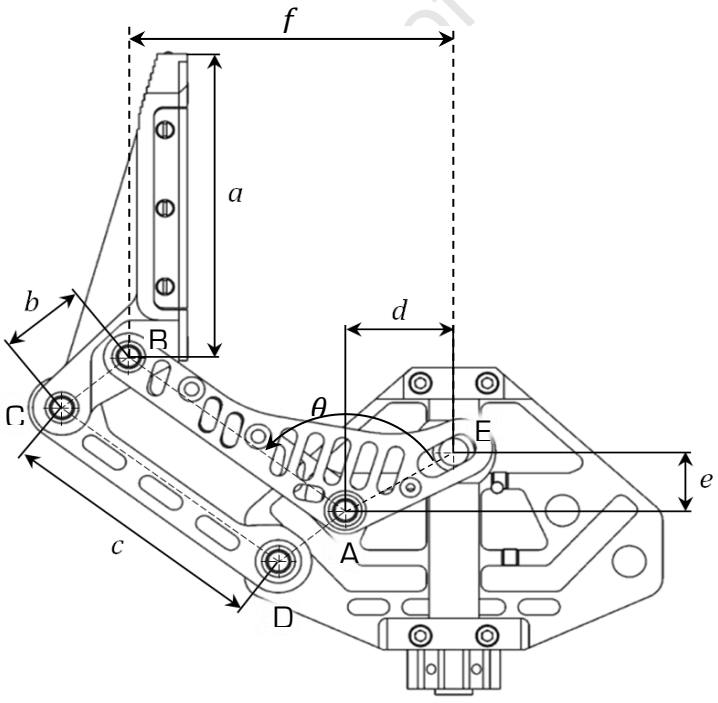

Figure 5-18: Gripper Link Lengths

After multiple design iterations, the following suitable dimensions were established:

$$\theta = 113°, a = 77.3mm, b = 20.6mm, c = 65mm, d = 26mm, e = 18.5mm, f = 81.5mm$$

With these dimensions, the following force and position equations demonstrate some performance characteristics of the gripper at stall conditions for a closing operation:

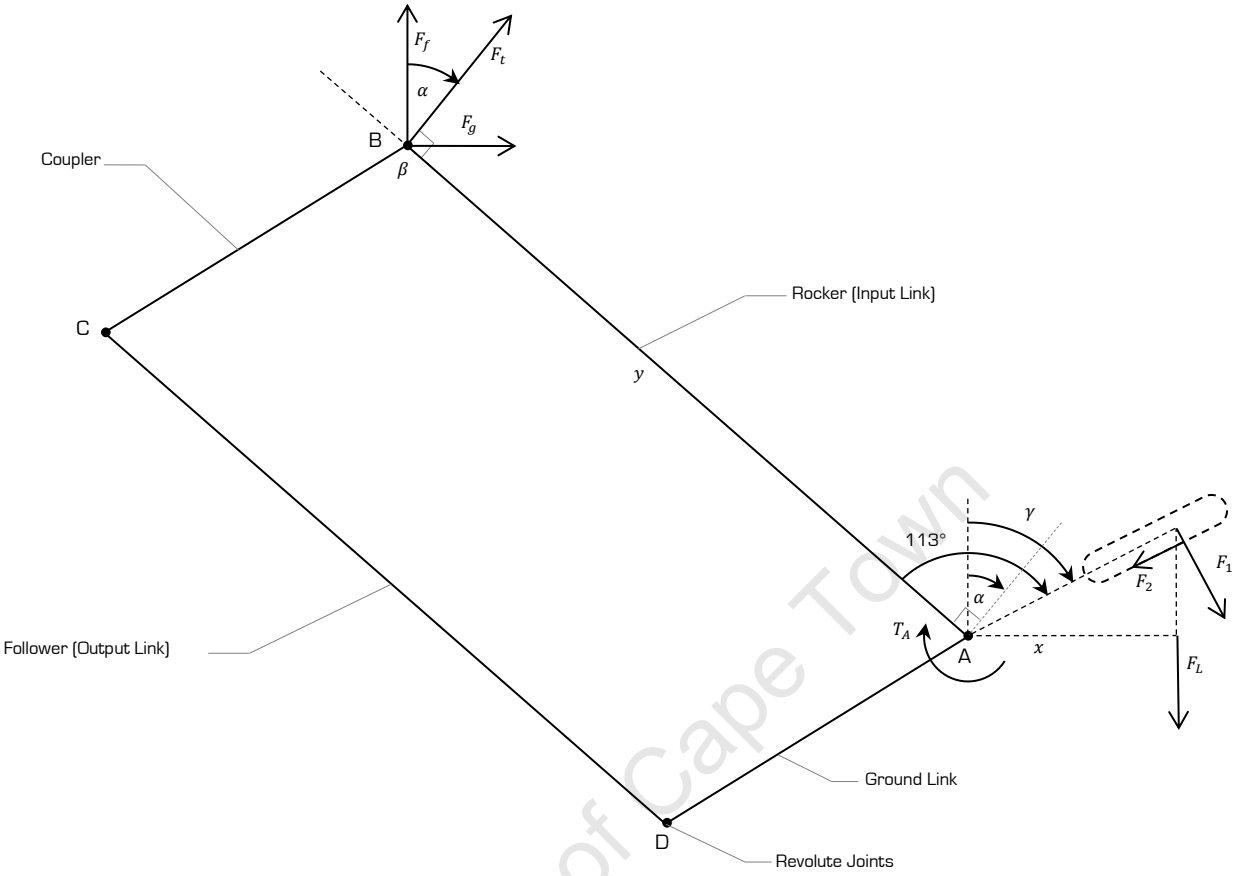

Figure 5-19: Force Derivation using the Parallel Four-Bar Linkage Mechanism

$F_1 = Reaction\ force\ on\ lever\ by\ lead\ screw\ nut\ with\ lead\ screw\ force\ F_L = 1320N$

$F_2 = Friction\ force\ on\ lever\ by\ lead\ screw\ nut\ with\ \ F_L = 1320N$

$T_A = Torque\ applied\ to\ the\ 'Input\ Link'\ by\ lead\ screw$

$F_t = Perpendicular\ force\ applied\ by\ 'InputLink'\ to\ the\ gripper\ finger$

$F_g = Gripper\ prehension\ force\ i.e.normal\ force\ exerted\ on\ items\ being\ gripped$

$F_f = The\ force\ that\ tries\ to\ 'push'\ items\ out\ of\ the\ gripper\ until\ the\ friction\ force\ generated\ as\ a\ result\ of\ the\ normal\ prehension\ force\ becomes\ sufficiently\ large$

From Figure 5-19, the following deductions were made about the forces being exerted by the gripper fingers:

$$F_g = F_t sin\alpha = F_t \sin(\gamma - 23°)$$
$$F_f = F_t cos\alpha = F_t \cos(\gamma - 23°)$$

With

$$54.6° \leq \gamma \leq 123.6°\ (Fully\ open\ to\ fully\ closed)\ and\ F_t = \frac{F_L \cos\gamma * 3.5 * 10^{-3} + F_L sin\gamma * \frac{0.026}{sin\gamma}}{0.065}$$

The following graph illustrates these formulae graphically:

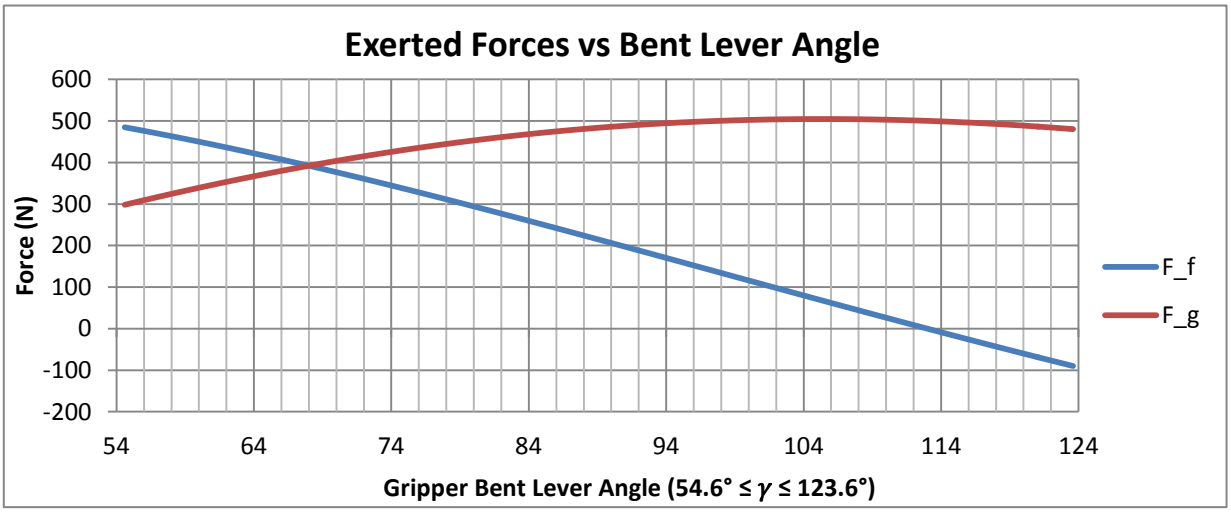

Figure 5-20: Graph Showing Potential Gripper Force (N) vs Bent Lever Angle γ (°)

As the gripper will be operated remotely, it will be important for an operator to know the current gripper position. The following graph demonstrates the relationship between the grip stroke (mm) and the lead screw travel (mm). It should be noted that the lead screw travel zero position was measured at a fully closed position i.e. $e = -17.3\text{mm}$ in Figure 5-18 above.

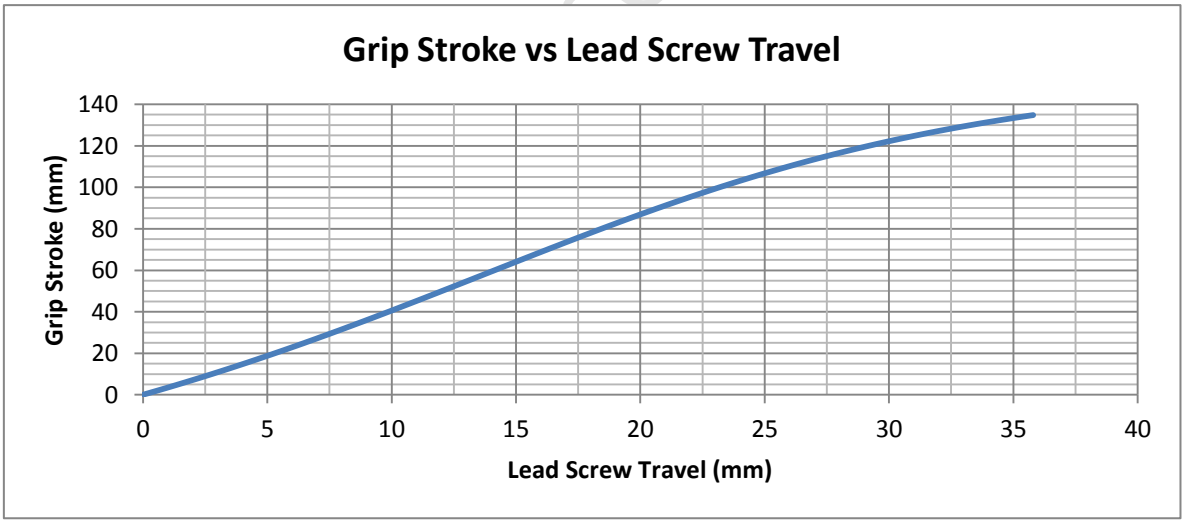

Figure 5-21: Graph Showing Grip Stroke (mm) versus Lead Screw Travel (mm)

The following equation describes the relationship (shown in Figure 5-21) between the grip stroke and the lead stroke travel '**e**'. It was derived trigonemtrically using Figure 5-18 and includes the established links lengths as stated previously:

$$Grip\ Stroke = 2 * \left(65 * \cos\left[67° - arctan\left(\frac{e - 17.3}{26}\right)\right] + 12\right)$$

Although the strength characteristics of many components were checked by hand, basic **FEA** (**F**inite **E**lement **A**nalysis) analysis was also performed in SolidWorks on critical system elements as shown below. As the gripper drive links are mirrored over the middle of the gripper housing, only one side was analysed.

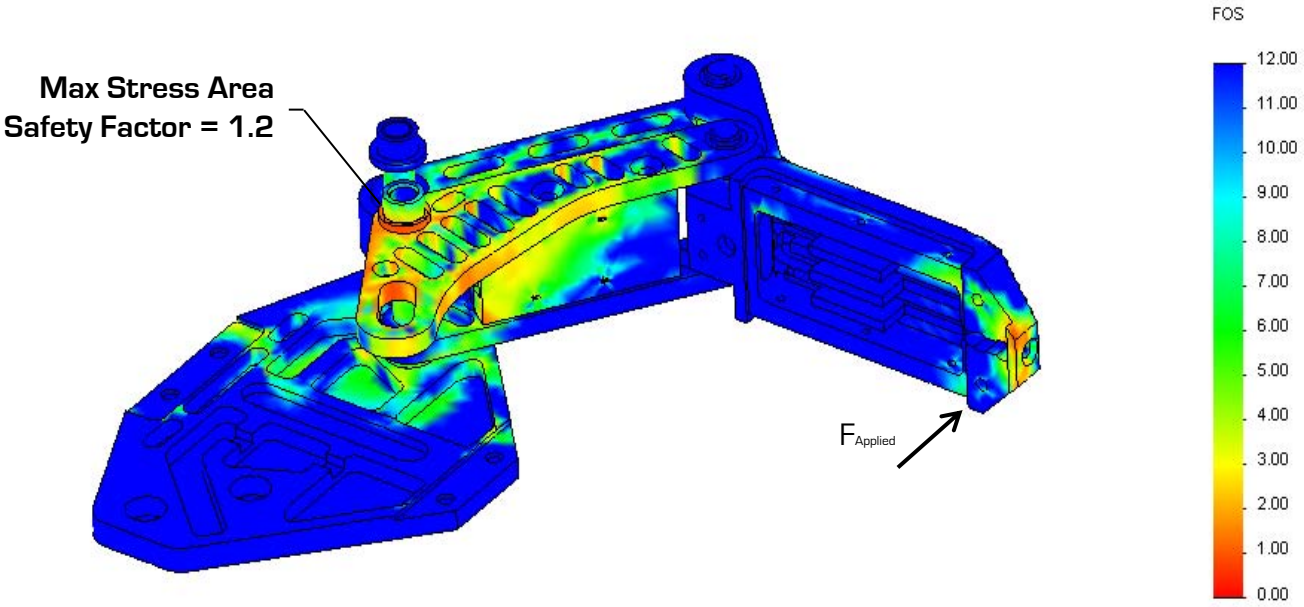

Figure 5-22: Basic FEA on the Gripper System

This type of simulation was particularly useful for performing weight savings on intricate link components that would not be able to be analysed by hand easily. The minimum **FOS** (**F**actor **o**f **S**afety) that was established at maximum load conditions was 1.2.

Lead Screw and Nut

The first step in attempting to decide on a suitable power screw solution was to determine if any size and weight constraints were applicable to the gripper. It was determined that the maximum diameter of the power screw should not exceed 14mm and that the weight be limited to a maximum of 50g (based on deductions from the previous parallel gripper).

After discussions with the author's supervisor, Stephen Marais, and the Mechanical Engineering workshop staff, it was concluded that a double start M12x1.75 60°V ISO thread would provide a good size and weight compromise. Having fixed the diameter, the weight could then be minimised by hollowing out the shaft, while maintaining sufficient strength. It should be noted that although a V-thread was not the ideal choice for a power screw setup (lowered efficiency) compared with a square or ACME thread, it was the only thread type available for manufacture in the workshop. Figure 5-23 and Figure 5-24, below, illustrate the interaction between the drive motor and the lead screw as well as the interface between the force transmission levers and the brass nut.

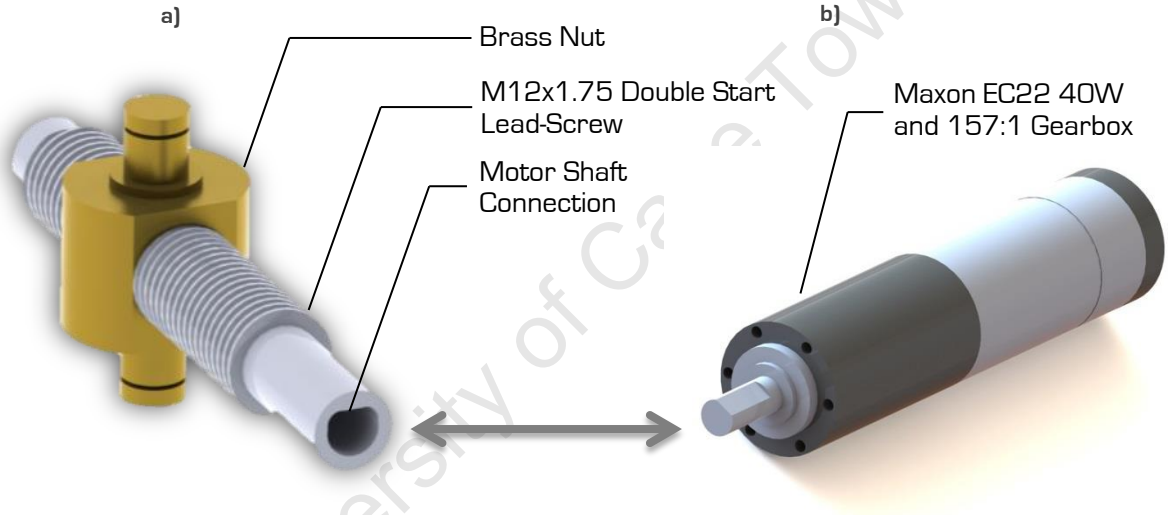

Figure 5-23: Render of a) Lead Screw and Nut, b) Maxon Motor and Gearbox

Figure 5-24: a) Interface between the Nut and Bent Levers b) Manufactured Lead Screw and Nut

As described in the **Material Selections** section, the lead-screw was manufactured out of Silver Steel with a Brass nut. Due to the high axial forces that the lead would exert on the gripper, Phosphor Bronze journal thrust bearings were used to transfer the axial forces exerted during opening and closing into the gripper housing.

The original lead-screw design stipulated that a shoulder should be left on the front of the lead-screw in order to have a flat-on-flat interface with the thrust bearing during closing operations (which should be more common than opening where the axial force will be reversed). However, because of time constraints in the workshop, this was not realised in the manufactured version.

A feature that was added to the lead screw was its unique connection to the motor shaft. Where a set screw or a key may have normally been used, it was decided to rather machine an extruded cut into the lead-screw shaft so that it could slide over the motor shaft. This was done to reduce backlash and to ensure the robustness of the connection.

The subsequent section presents a summary of the calculations that were performed during the lead-screw design process. The following book was used as the primary reference source for the calculations: "Fundamentals of Machine Component Design" by R. Juvinall and K. Marshek [51].

The Maxon motor and gearbox combination that was pre-selected for this project was critical to the lead screw calculations and is summarised below.

Table 5-3: Maxon Motor and Gearbox Characteristics

Motor Property	*Value*
Motor Type	Maxon EC22 40W (386658)
Attached Gearbox	Maxon 157:1 Planetary (30786)
Intermittent Max Torque at Gearbox Output	3.5Nm

The following table presents all of the symbols for the following calculations:

Table 5-4: Lead Screw Calculations Symbols and Descriptions

Symbol	*Description*
SF	Safety Factor (= 1.5)
M_T	Applied Torque (= 3.5Nm)
W	Load
d_m	Mean Pitch Diameter of Power Screw
f_l	Lead Screw Coefficient of Friction (= 0.19 Steel on Brass Lubricated)
α_n	Thread angle (= 30° for ISO Thread)
L	Lead of Power Screw
f_c	Thrust Bearing Coefficient of Friction (= 0.35 Steel on Phosphor Bronze)
d_c	Thrust Bearing Mean Diameter

The following equation provides a method to calculate the total axial load W that can be exerted by a power screw when a torque M_T is applied. This equation includes the added torque required to overcome the thrust bearing friction and a safety factor of 1.5. With the load acting against the direction of motion of the nut:

$$SF * M_T = \frac{W d_m}{2} \frac{f_l \pi d_m + L\cos(\alpha_n)}{\pi d_m \cos(\alpha_n) - f_l L} + \frac{W f_c d_c}{2} \quad (1)$$

Assumptions:

$$d_m = \frac{d_{major} + d_{minor}}{2} = \frac{12 + 9.85}{2} \approx 10.9mm$$

$$d_c = \frac{d_{outer} + d_{inner}}{2} = \frac{16mm + 9mm}{2} = 12.5mm$$

From (1) above, the estimated maximum intermittent axial load that can be exerted by the lead screw is $\boldsymbol{W \approx 1320N}$ with a safety factor of 1.5.

An important additional factor to consider was if the lead screw is self-locking (i.e. can it be reverse driven?). Self-locking behaviour would be favourable for a parallel gripper as current would only need to be drawn during actual movement of the gripper fingers, thus improving power consumption as well as controllability of the system. Neglecting thrust bearing friction, the following equation demonstrates if the power screw exhibits self-locking behaviour:

$$f \geq \frac{L\cos(\alpha_n)}{\pi d_m} = \frac{0.0035 * \cos(30)}{\pi * 0.0109} = 0.089 \quad (2)$$

As the limiting friction is 0.089 compared with a lead screw friction of $f_l = 0.19$, the power screw is self-locking.

Checking the power screw efficiency with lead angle $= \arctan\left(\frac{L}{\pi d_m}\right) = 5.84°$:

$$\eta = \frac{\cos(\alpha_n) - f\tan(\lambda)}{\cos(\alpha_n) + f\cot(\lambda)} = \frac{\cos(30) - 0.19\tan(5.84°)}{\cos(30) + 0.19\cot(5.84°)} \approx 31\% \quad (3)$$

This relatively low efficiency could be improved by using a lower friction thread type such as an ACME or square thread.

As previously mentioned, weight savings were to be achieved by hollowing out the lead screw. Using the distortion energy theory, the minimum internal diameter could be calculated:

$$\tau = \frac{16T}{\pi({d_r}^3 - {d_i}^3)} = \frac{16 * 3.5}{\pi(9.85 * 10^{-3^3} - {d_i}^3)} \qquad \sigma = \frac{F}{A_t} = \frac{F}{\pi\left(\frac{d_r}{2}\right)^2 - \pi\left(\frac{d_i}{2}\right)^2} = \frac{880}{\pi\left(\frac{9.85 * 10^{-3}}{2}\right)^2 - \pi\left(\frac{d_i}{2}\right)^2}$$

Distortion Energy Theory: $\sigma_e = SF * \sqrt{\sigma^2 + 3\tau^2}$ $S_y(Silver\ Steel) = 440MPa$

Based on these calculations, an internal diameter of 6mm was selected for the lead screw resulting in a 24% weight saving when compared with the original solid lead screw shaft.

Gripper/Wrist Interface

In the field, the requirement to change or remove the gripper from the wrist system 'on the go' is an important consideration. This may be due to the fact that another type of end-effector (like a drill) may be required to perform a particular job or to improve the performance of the manipulator arm by reducing the weight when the gripper is not in use. Figure 5-25 shows the wrist/gripper interface that was designed for the end-effector.

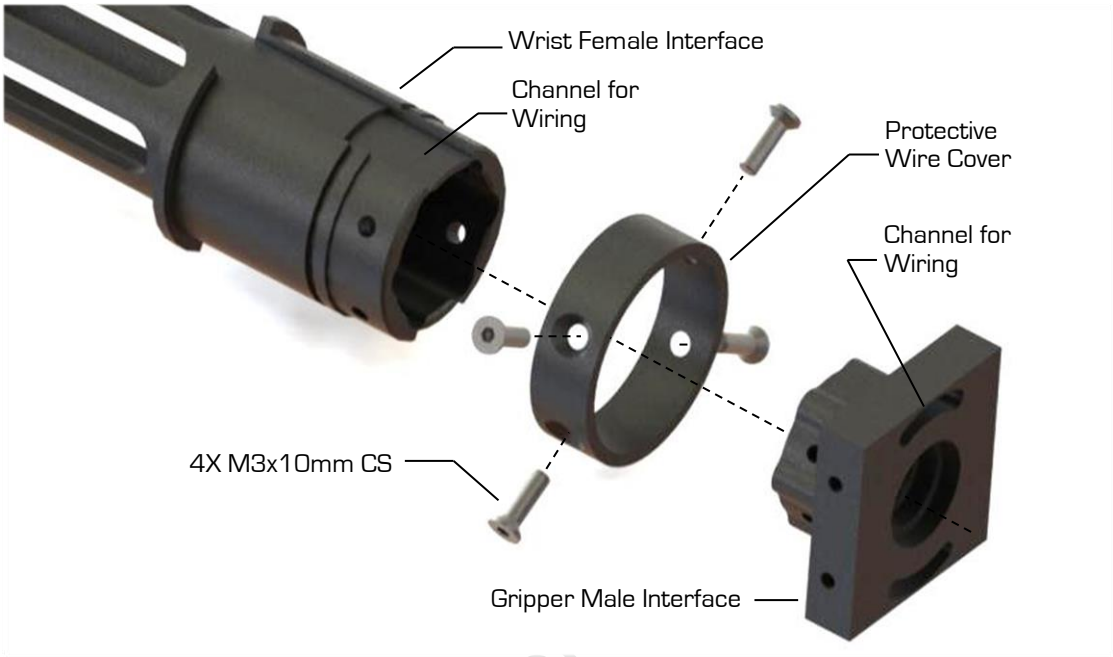

Figure 5-25: Wrist/Gripper 'Spline' Type Interface

It was envisaged that some type of spline interface should be implemented to simplify and speed up the removal or exchange of the gripper. After speaking to the workshop staff, it was realised that the workshop did not have the capability to manufacture a traditional spline. For this reason, a rounded six tooth spline was designed that could be easily manufactured on the CNC mill. The interface was secured using four M3x0.5 10mm hex socket countersunk screws that should allow the gripper to be removed within approximately 30 seconds.

As seen in Figure 5-25, internal wiring was included in the interface which runs along set channels on the wrist and into the gripper. A protective wire cover on the outer side of the wrist interface was secured using the screws as shown above. Although an attempt was made to find a good quality electrical connector to link the systems, no suitable version was found. Therefore, Molex PicoClasp connectors were selected as a substitute.

Gripper Fingers

The gripper fingers are an important subsystem of the gripper as they are the only point of contact to an object being manipulated. As described in the detailed module specifications, they would need to house a large subset of the sensors and functional capabilities of the gripper system. Furthermore, they would need to be robust, compact as well as aesthetically pleasing and in compliance with the rest of the manipulator arm and **MRP**.

Figure 5-26: Final Design of a Gripper Finger

The following exploded view shows the individual components that make up a finger.

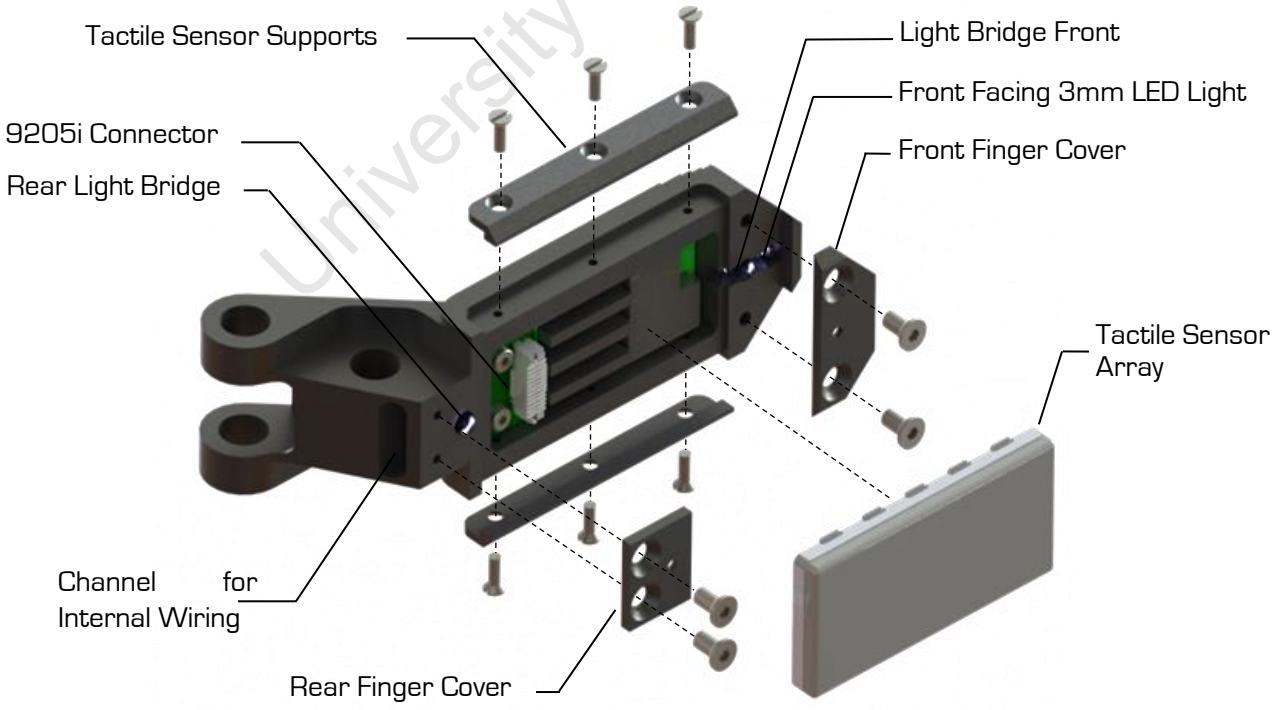

Figure 5-27: Exploded View of a Gripper Finger with a 9205i Tactile Sensor Array

As can be seen in Figure 5-27, the fingers became more complex than initially anticipated. Functions that have been integrated include recessed 3mm high-bright LEDs, two infrared light bridges, recesses for internal wiring and physical mounts for both FSR sensor and 9205i tactile sensor configurations. Depending on the application, these sensors can easily be exchanged 'on the go'. Figure 5-28 shows a gripper finger in a a) 9205i tactile sensors configuration and b) FSR sensor configuration.

a) b)

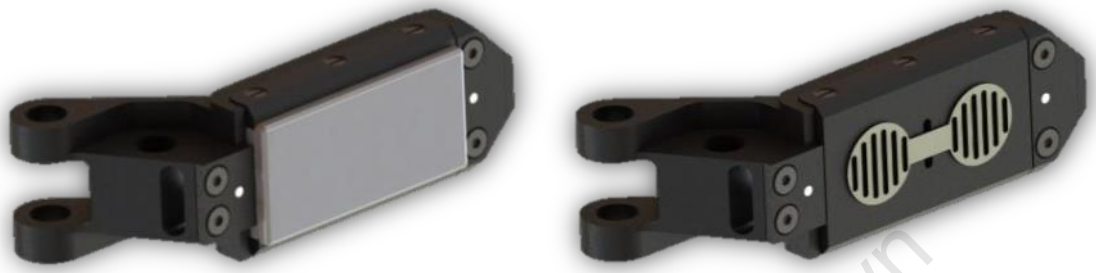

Figure 5-28: Gripper Finger a) Tactile Sensor Array Configuration, b) FSR Configuration

The FSR configuration shown above was covered using 2mm neoprene rubber that was manufactured on UCT's laser cutter and etched with a 'Zig Zag' pattern. The intention was to protect the FSR sensors and distribute the load more evenly between them. The neoprene rubber was also used to make covers for the front and rear sections of the fingers as well as the mid link sections located between the drive links. Figure 5-29 and Figure 5-30, below, show the neoprene rubber covers and two manufactured fingers.

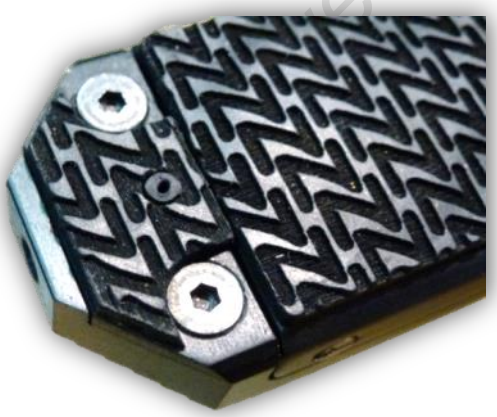

Figure 5-29: Neoprene Cover with an etched 'Zig Zag' Pattern

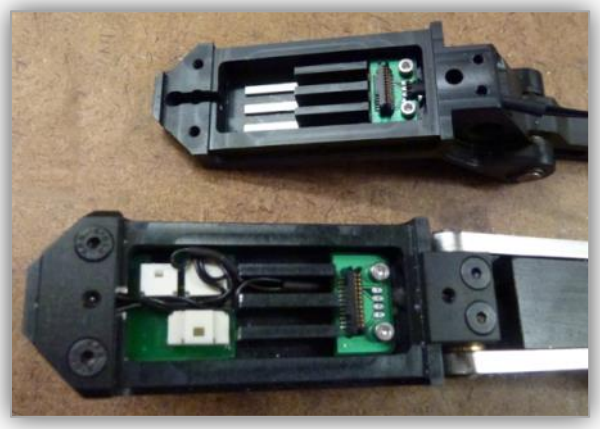

Figure 5-30: Two Manufactured Fingers with Mounted Electronics Boards

Gripper Electronics Housing

The gripper electronics housing went through multiple iterations before the following design was realised. The intention was to generate a housing that was compact and functional, yet attractive to look at and easy to maintain. The housing needed to accommodate the custom gripper embedded microcontroller board, proposed KX-1 camera, LED lighting and all the gripper internal wiring which would be fed through slots cut into the gripper top base plate.

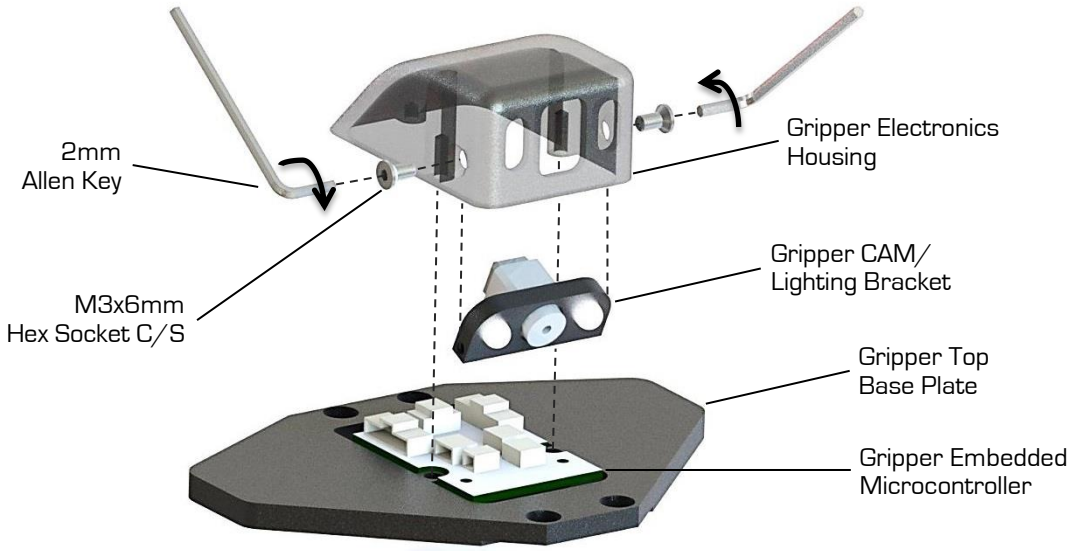

Figure 5-31: Render of Electronics Housing Showing the Adjustment of the Camera/Lighting Module

Figure 5-31, above, presents the housing that was designed. As can be seen from the figure, a gripper camera and lighting bracket was created that was fastened to the housing using two M3 6mm hex socket countersunk screws. The idea behind this bracket was that the viewing angle of the camera could be modified easily using two Allen Keys. This was ideal for the initial setup of the system, as well as future adjustments before operations.

5.4 Gripper Electronics Design

It should be noted that the gripper electronics module refers only to the electronic components within the physical gripper and does not include the electrical actuation of the module from the primary controller. Based on the module specific specifications presented in Table 5-1, design targets and desired functionality were set for the gripper electronics module. This chapter will detail the design and development of the following key modules:

- **Background Debug Mode Interface for Programming**
- **Circuitry to Power the KX-1 Camera (Manual Switching)**
- **Circuitry for two Infrared Light Bridges**
- **Hall Effect Sensors**
- **Force Sensing Resistors Sensors**
- **Interface to connect two 9205i Sensors**
- **Driver circuit for high bright LED lighting**
- **Gripper Finger Connector Distribution Board**

Gripper Embedded Controller

It was initially envisaged to use an ARM Cortex-M3 processor running the LabView ARM Embedded Module to control all of the end-effector electronic and electrical systems. However as features and functionality were added, it soon became evident that this would not be a practical solution, both in terms of available IO ports on the microprocessor as well as wiring throughout the system.

For this reason a dedicated custom Freescale MC9S08GT16A embedded microprocessor board was designed that would be housed in the gripper itself. This specific processor is popular in the **RARL**, due to familiarity with its operation, its reliability and cost-effectiveness. Figure 5-32 presents the connection diagram of the gripper that was created prior to designing the embedded controller.

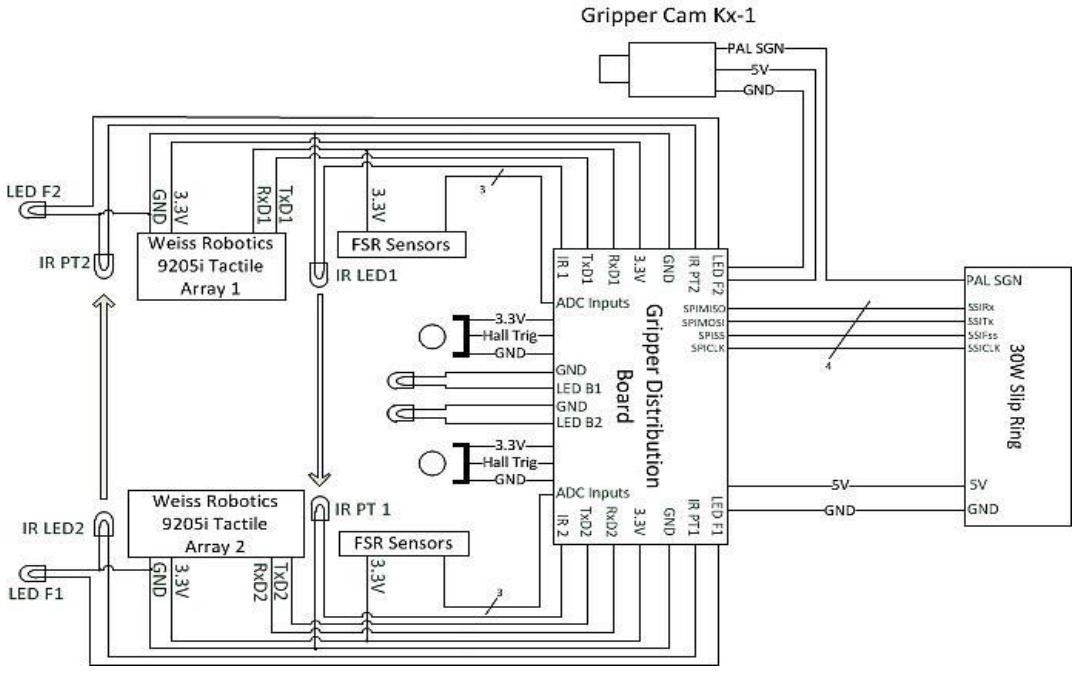

Figure 5-32: Gripper Module Electrical Connections

The board was designed from the ground up considering core design criteria including compactness, flexibility, reliability and customisability. As such, the gripper electronics module and sensors are essentially a complete system unto themselves, needing only communication and power to function. The completed board is presented below.

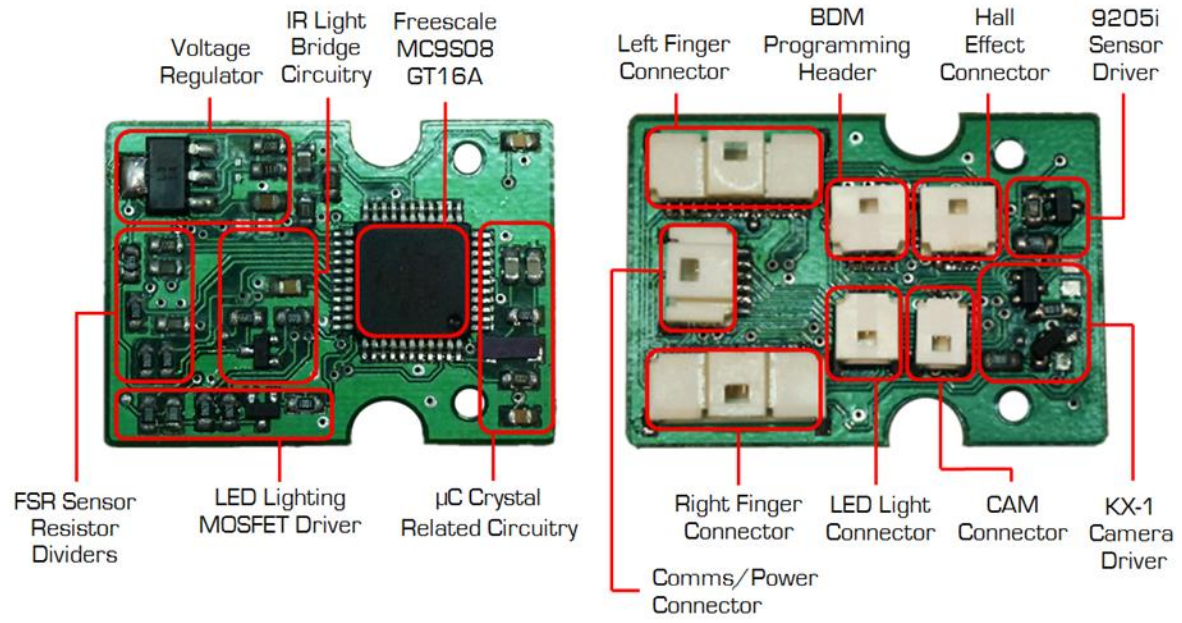

Figure 5-33: Gripper Embedded Microcontroller Board Highlighting Various Operational Modules

The following figure presents a pinout diagram and specifications for the embedded gripper board. Note the Molex PicoClasp surface mount connectors that have been used due to their small size and positive locking ability.

Specification	Value
Communications	SPI
Processor Type	18.87MHz MC9S08GT16A
Flash Memory	16KB
SRAM	2KB
General Purpose Timers	2
UART	2
SPI	1
10-Bit ADC	8
PWM	4
General Purpose I/O	22
Supply Voltage	5V
Power	0.6W (Idle)

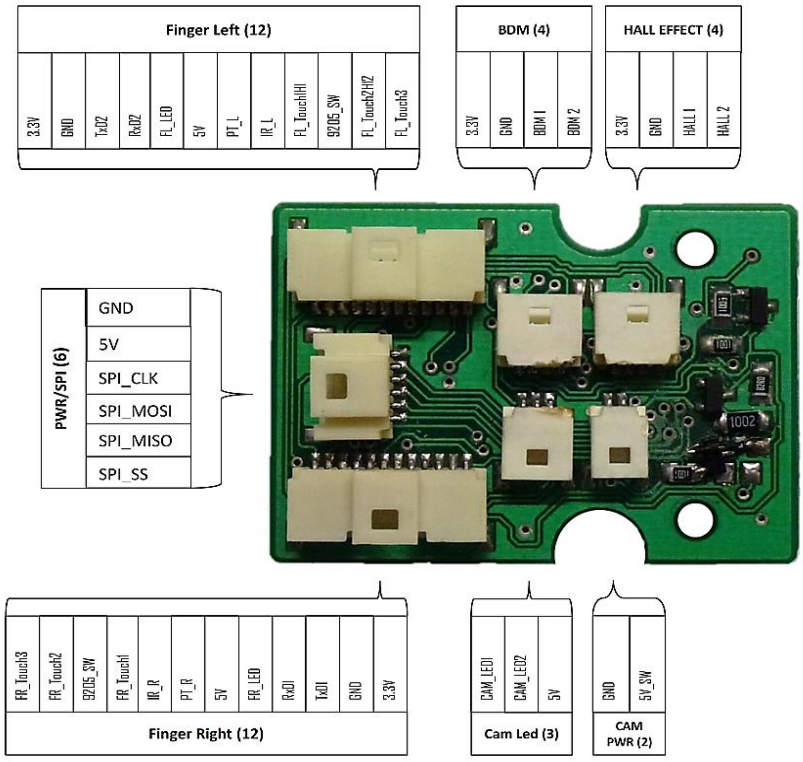

Figure 5-34: Specifications and Pinout Diagram of the Embedded Gripper Controller

SPI was chosen as the communication protocol to the primary controller because of its high speed and ability to be easily implemented. In this configuration the GT16A would act as a slave device. Although the **UART** (**U**niversal **A**synchronous **R**eceiver/**T**ransmitter) protocol would have been a more appropriate choice, both **UART** ports were reserved for the option to install tactile sensing arrays. As the wrist was envisioned to rotate continuously through 360°, the communication and power wires had to be fed through a slip-ring located at the rear of the wrist module.

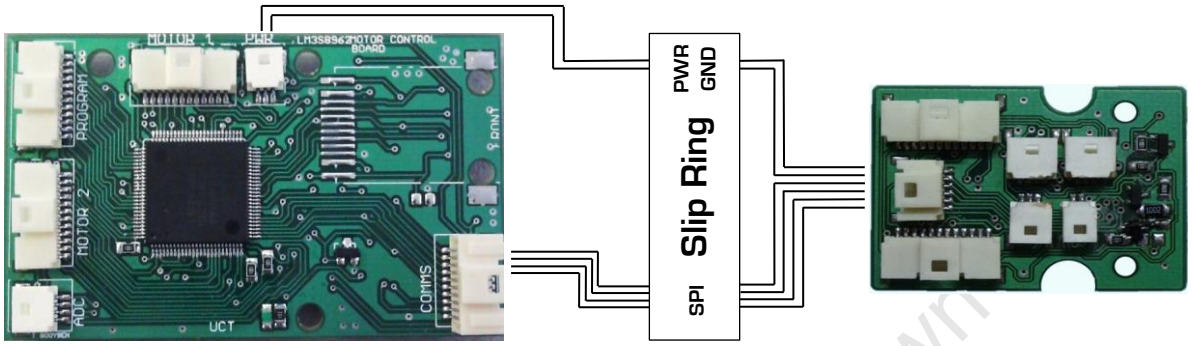

Figure 5-35: Microcontroller Interconnections

KX-1 Camera

When the decision was made to incorporate a camera in the gripper module, it was realised that a compromise would need to be made between size and video quality. After investigating various cameras, the $50 KX-1 micro colour CMOS PAL camera was selected due to its small form factor, low power consumption (+- 80mA @5V), excellent low light performance and VGA quality video feed (Figure 5-36).

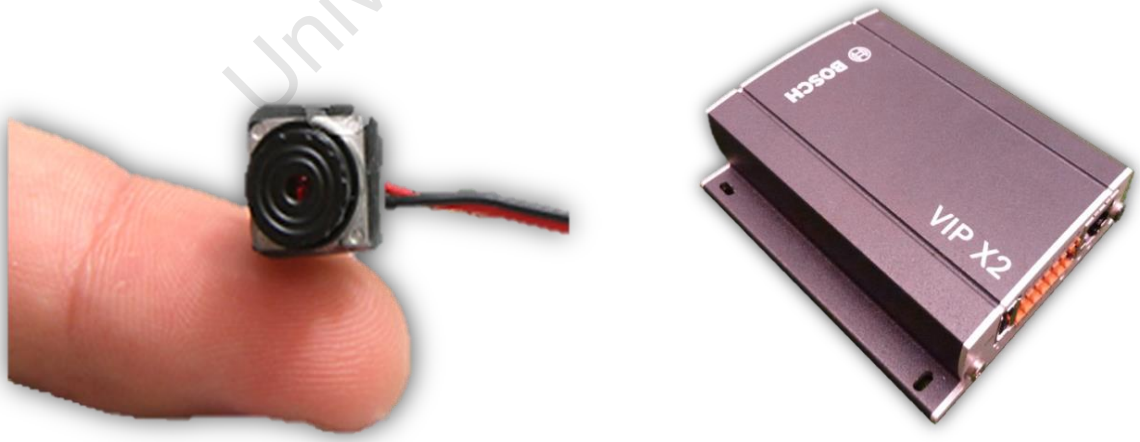

Figure 5-36: RangeVideo KX-1 Colour PAL Camera [52] (Left) and Bosch VIPX2 IP Video Encoder (Right)

The PAL signal from the camera was fed through the top section of the manipulator arm using coaxial video cable to a BOSCH VIPX2 Dual Channel Video Encoder (Figure 5-36) located in the sensor payload. From there the feed was compressed to an **RTSP** (**R**eal **T**ime **S**treaming **P**rotocol) video stream and displayed on a LabView user interface for viewing and post-processing.

The circuit below was designed to give an operator the ability to switch the camera off when not in use and to perform power cycles if required. The circuit uses a p-channel and an n-channel MOSFET to perform the switching of the 5V voltage rail using the GT16A microprocessor.

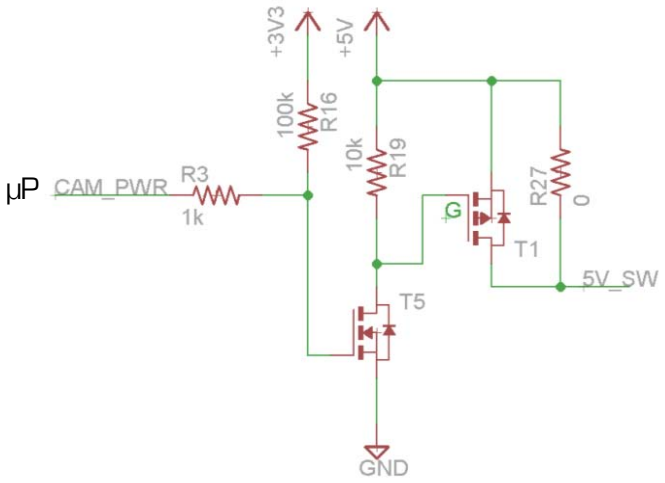

Figure 5-37: Gripper Camera Power Circuit

Infrared Light Bridge Circuitry

The ability for an operator to detect when an object has entered the gripper fingers is of importance if a successful manipulation operation is to be completed. Two 3mm 940nm (±30° Viewing Angle) infrared LEDs and matched phototransistors were selected to perform this function (See schematics below). It should be noted that these are functional schematics. The actual diodes and phototransistors are connected to the microcontroller board through the gripper fingers and are not board mounted.

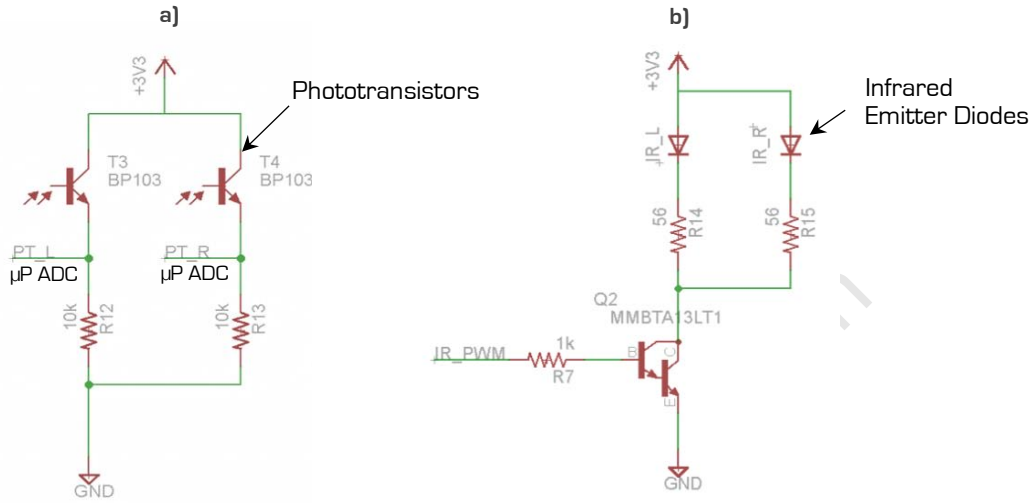

Figure 5-38: Functional Schematics of a) Phototransistor Receivers, b) Infrared Emitters

As seen above, the phototransistor emitters were connected to **ADC** (**A**nalog-to-**D**igital **C**onverter) inputs on the **µP,** essentially forming voltage dividers. The infrared emitter diodes were driven by a Darlington PNP transistor off a **PWM** (**P**ulse **W**idth **M**odulation) pin (PTD3) at a frequency of 1 kHz. By pulsing the emitter diodes and reading the corresponding light reflections from the phototransistors, ambient light can be neglected and a deduction can be made on whether the bridges are obscured by an object or not. Figure 5-39, below, illustrates the operation of the light bridges and shows a render of a bottle blocking the rear sensor.

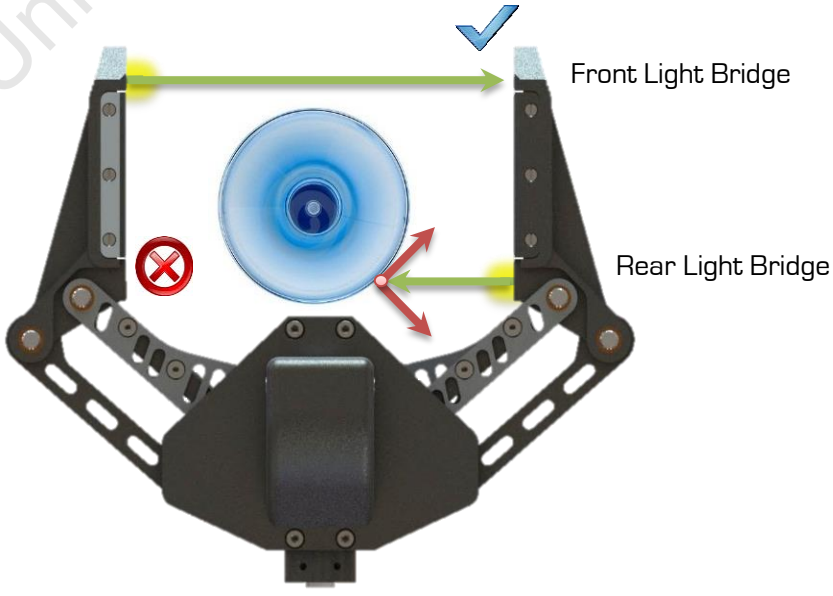

Figure 5-39: Gripper Render Illustrating a Bottle Blocking the Rear Light Bridge [54]

For a detailed explanation on how the emitter diodes are pulsed to eliminate ambient light, see Figure 5-52 in the **Gripper Software Development** section of this chapter.

End Stop Hall Effect Sensors

Due to the fact that the Maxon Quadrature Encoder MR module is a relative shaft encoder, some form of initial calibration was needed to zero the gripper upon start-up. To accomplish this, two SIP3 Hall Effect sensors powered off 3.3V were installed into the gripper base plate together with a Ø5x3mm round Neodymium magnet recessed into one of the gripper links. The sensors were mounted with epoxy so that they would trigger when the gripper was at its end-stops (with a slight margin to avoid hitting the mechanical stops). The setup is shown below.

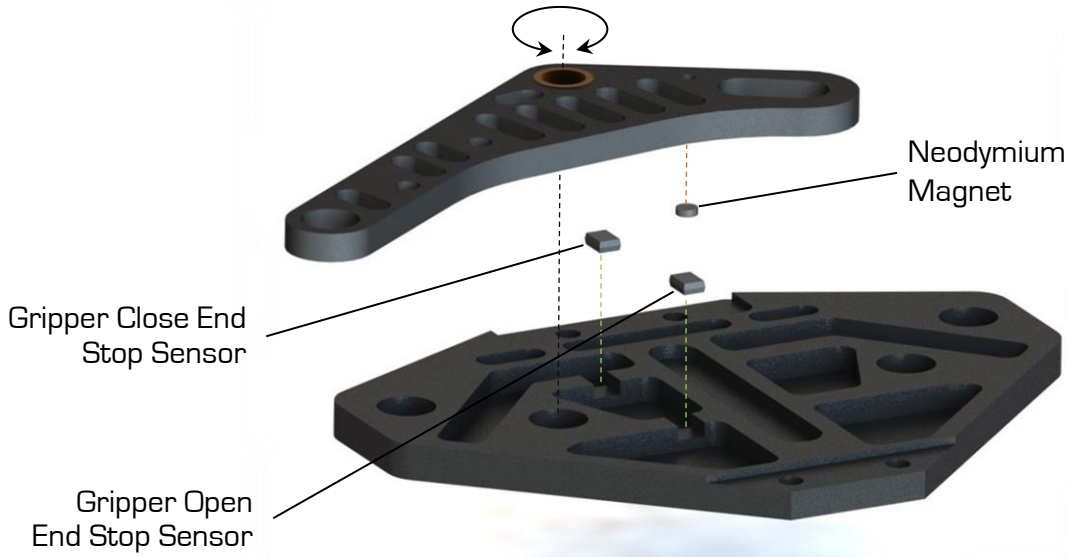

Figure 5-40: Hall Effect Sensors and Neodymium Magnet as Virtual End-stops

Force Sensing Resistor Sensors

As an alternative solution to tactile sensing arrays, standard force sensing resistor pads were also implemented as an optional configuration. As seen in Figure 5-41, an Aluminium cover was designed with a slot for the **FSR** wiring in the centre. The pads were glued onto the cover, after which they were covered with a Neoprene rubber (Figure 5-29) to distribute the force more evenly.

This alternative configuration was implemented due to its simplicity, robustness over tactile arrays and usability for everyday operation of the gripper. For more information on the operational performance of these sensors, see **Chapter 9. Testing and Results**, section **9.2.3 Gripper Prehension Test**.

As seen in Figure 5-42, the option for six **FSR** sensors was integrated onto the embedded controller board. As the sensors are essentially just variable resistors, a simple voltage divider circuit fed into the GT16A ADC port was sufficient to obtain the forces for each individual sensor. A 2.2k resistor, obtained by practical investigation, was selected for the voltage divider to obtain an acceptable sensitivity. It should be noted that due to their size, only four sensors were actually installed.

Figure 5-41: Gripper Finger with Two FSR Sensor Pads

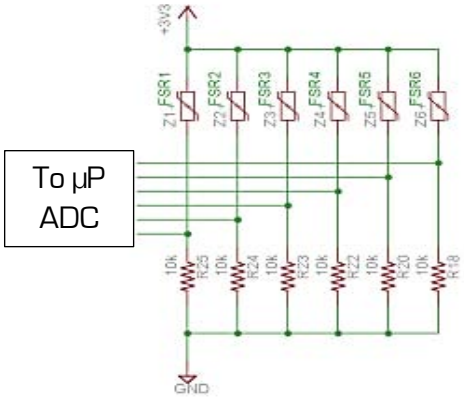

Figure 5-42: Functional Schematic of FSR Sensor Connections

Weiss Robotics 9205i Tactile Sensing Arrays

The sensors chosen for tactile sensing were Weiss Robotics 9205i tactile sensing arrays. These sensors are made up of 84 tactile cells, with each individual cell outputting a 10bit value between 0 and 1023. Communication to the gripper embedded controller was facilitated using serial **UART** at 3.3V LVTTL voltage levels. These sensors were selected due to their superior spatial resolutions of 3.4mm, their ease of use and their simple installation. The sensors were powered off a 3.3V supply controlled by a LM317 linear voltage regulator and drew approximately 65mA during operation. Due to this relatively high current draw (when compared to the rest of the gripper electronics), a power switching circuit (See Figure 5-44) was designed to allow power savings when the sensors are not in use.

A custom **PCB** (**P**rinted **C**ircuit **B**oard) was created to mount the sensors into the gripper fingers using the provided ERNI MicroStac 12 pin universal connectors. As seen in Figure 5-43 [55] below, the connector boards were recessed into the fingers so that either a 9205i sensor or a **FSR** sensor configuration was possible. The wiring was fully integrated, running along designated channels to the gripper embedded controller.

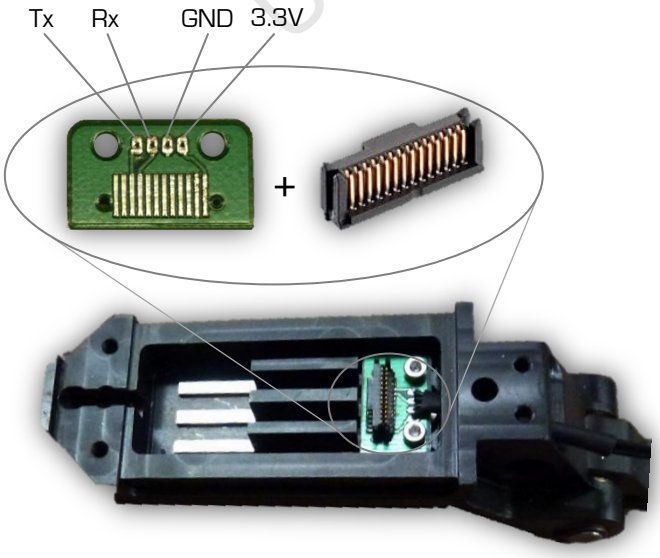

Figure 5-43: 9205i Sensor Mount in the Gripper Finger [55]

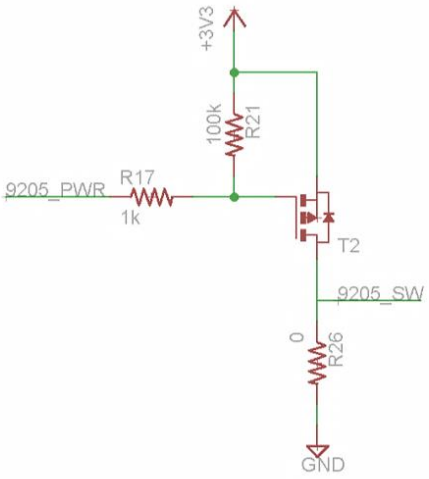

Figure 5-44: Tactile Sensor Power Switching Circuit

Figure 5-45, below, shows a Weiss Robotics 9205i sensor pad mounted onto a gripper finger. Note the retaining support brackets above and below the sensor.

Figure 5-45: Weiss Robotics 9205i Sensor Installed in a Gripper Finger

It should be noted that the sensors were not interfaced with the gripper embedded controller directly during testing, but were rather connected to a PC using an isolated custom etched controller board (Figure 5-46) via RS232. Utilising this external board, the sensors were monitored using the Weiss Robotics DSA-Explorer software (included with the sensors).

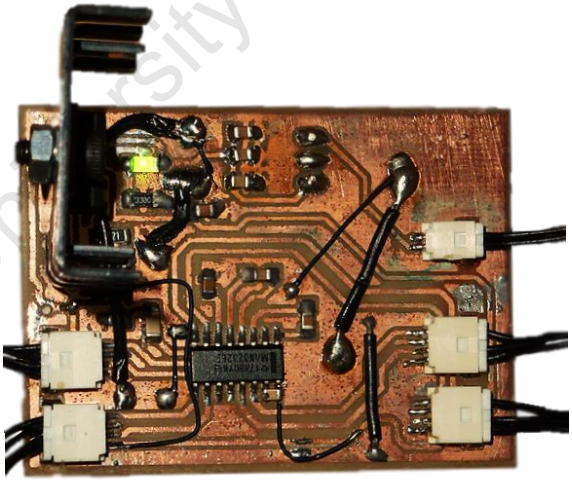

Figure 5-46: External Tactile Sensor Driver Board for Testing

This method was used due to time constraints in overcoming the programming intricacies of the RS485 communications protocol with the manipulator arm. When connected to the gripper embedded controller, sensor data transmission would only be possible at 0.65Hz over RS485 (excluding status information from the end-effector). As such, some type of alternating packet algorithm would need to be implemented to retain sufficient control of the end-effector.

In addition to obtaining data from the Weiss Robotics DSA Explorer software, basic data acquisition was also implemented using LabView. Figure 5-47, below, presents the data that was captured through LabView at 50Hz. The X and Y axes represent the 6 x 14 tactile cell arrays for each sensor with the Z axis indicating the magnitude of the force reading (/1023).

Sensor 1, below, demonstrates a single human fingertip exerting pressure on the centre of the sensor cell, while Sensor 2 shows two fingertips exerting a low force on the cell. As seen from the figure, the sensor resolution is excellent and should prove to be an ideal aid for a remote operator performing gripping operations. For more information on how the data was retrieved from the sensors, see the code that has been included on the attached DVD. The DVD also includes recorded videos of the tests performed below.

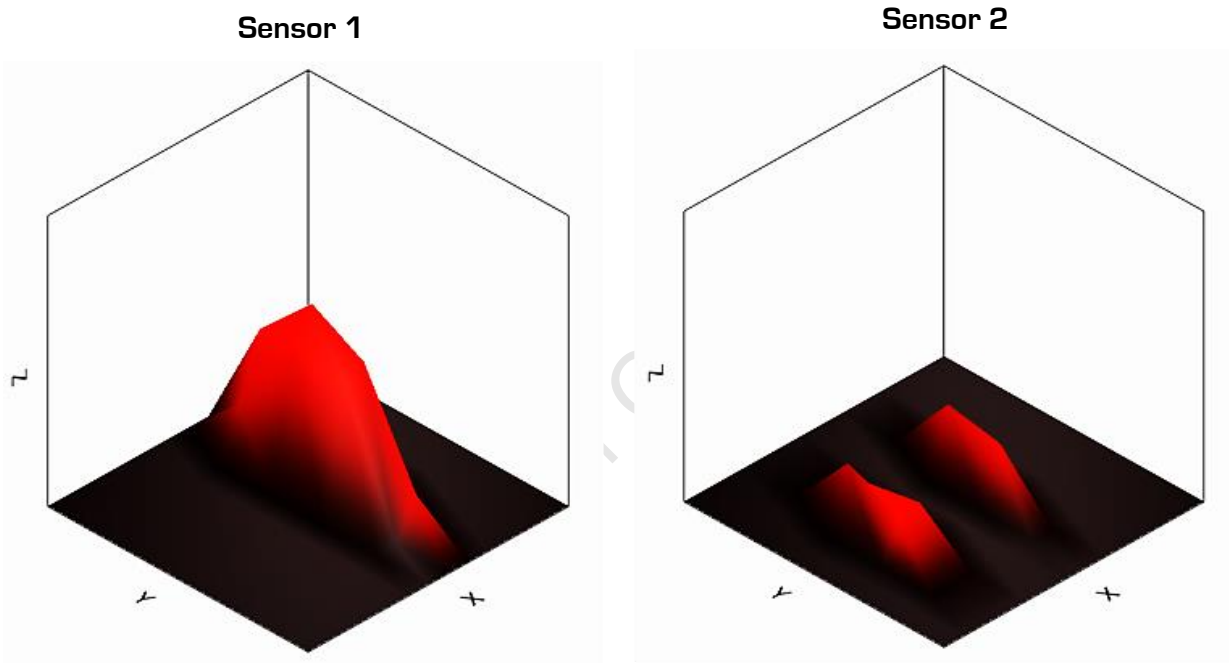

Figure 5-47: Weiss Robotics Sensor Data Acquired in LabView

LED Lighting

Lighting is an important feature of an end-effector and even more so if the application is rescue robotics related. The lighting should be sufficient to allow the operator to see adequately in complete darkness up to 0.5m. It should be noted that the gripper lighting should be considered to be secondary lighting, as the sensor payload and robot base already have powerful lighting solutions.

The lighting system that was selected consists of two 3mm and two 5mm white high bright LEDs located in the gripper fingers and the electronics housing respectively (Figure 5-48). The two LEDs in the housing were intended to illuminate any objects within the gripper fingers with the front LEDs to be used for general camera lighting.

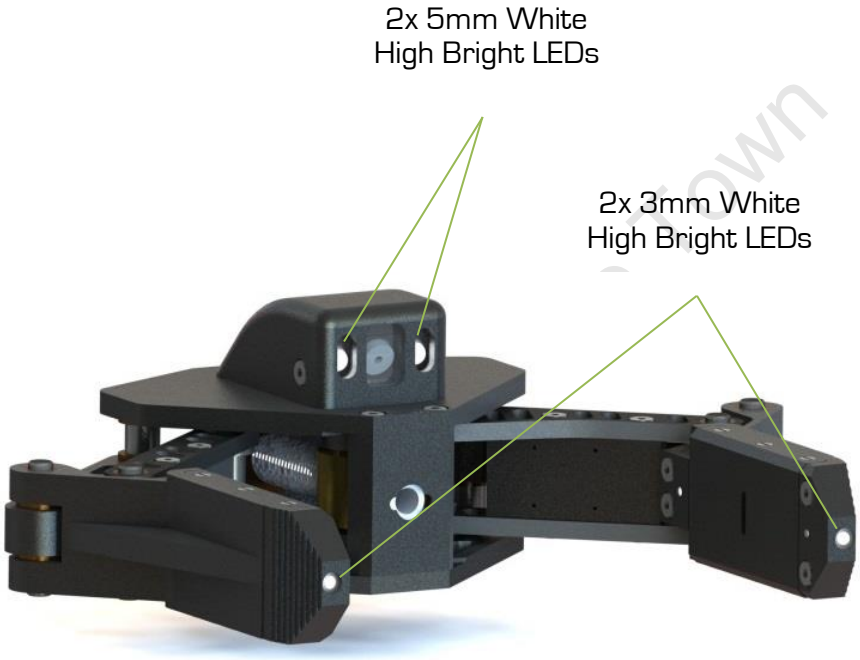

Figure 5-48: Lighting Solution in the Gripper Module

The lighting circuit that was designed is shown on the right. A PNP Darlington transistor was used to drive the four LEDs at 1 kHz from PTD0 using the **µP PWM** module. This meant that all LEDs were driven off the same duty cycle and could not be controlled individually. At full brightness the current draw was approximately 50mA at 3.3V. See **Chapter 9. Testing and Results**, section **9.2.6**, for a detailed analysis on how the lighting system performed in various environments.

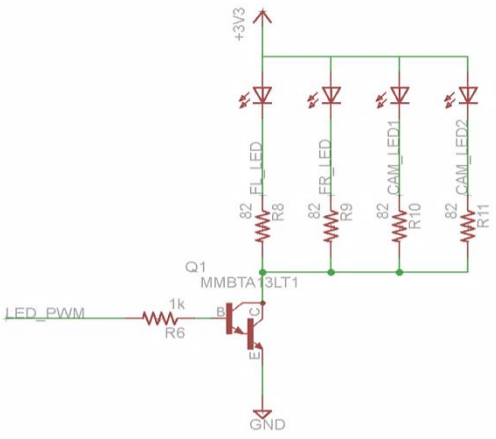

Figure 5-49: Gripper lighting Functional Schematic

Gripper Finger Connector Distribution Board

Due to the additional functionality that was added to the gripping fingers including swappable sensors, LED lighting, Hall Effect switches and object presence sensors, wiring proved to be quite challenging. One of the initial design requirements of the end-effector was to create a system that was robust and easy to maintain.

For this reason, a connection distribution board was designed and manufactured to make wiring the gripper finger module more manageable. Figure 5-30 shows the location of the board while Figure 5-50, below, shows the pinout diagram of a completed board.

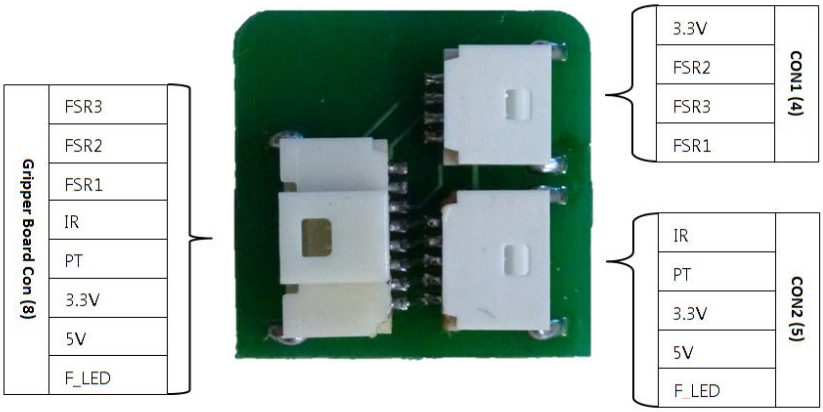

Figure 5-50: Gripper Connection Distribution Board

5.5 Gripper Software Development

In order to operate the gripper subsystem, various electronic and software modules are needed. This section will only examine the control and software of the embedded gripper controller. For a more detailed review of the top-level primary gripper controller software, see **Chapter 8. Programming and System Control**.

The following flow diagram illustrates the general operation of the code running on the MC9S08GT16A. The fully commented C-Code can be found on the accompanying DVD.

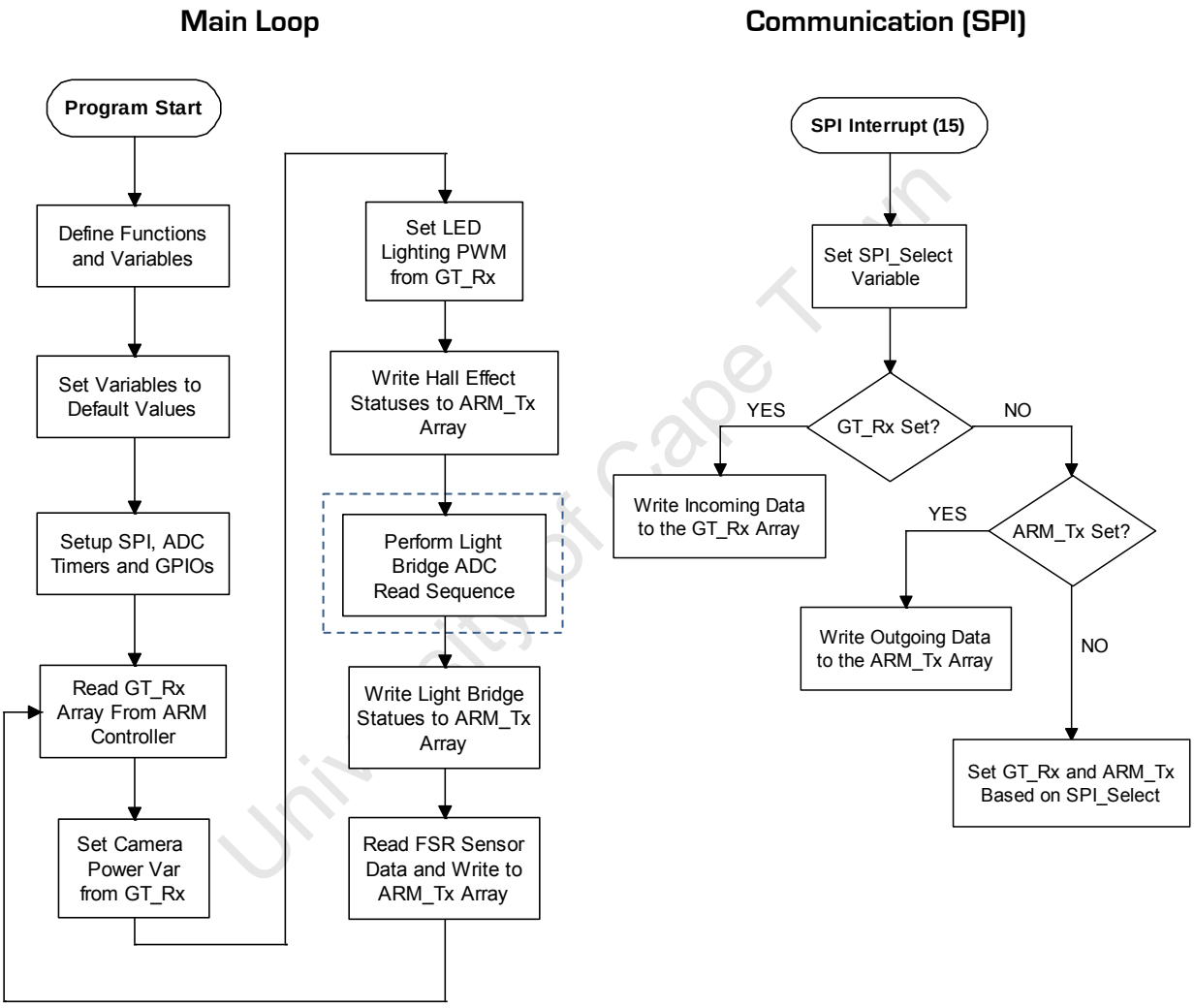

Figure 5-51: Gripper Embedded Microcontroller C-Code Flow Diagram

As seen above, the gripper software is made up of two parts, namely the main loop and an **SPI** interrupt. Primary communications are handled in the **SPI** interrupt which updates the GT_Rx input array and writes the ARM_Tx array back to the primary controller. The main loop is tasked with handling the camera power, LED lighting, Hall Effect sensors, **FSR** sensors, reading the light bridge statuses and writing information back to the global ARM_Tx array.

The highlighted flow block "Perform Light Bridge ADC Read Sequence" will now be examined in further detail as it serves an important function. The sensors operate by modulating the emitter diodes at 1 kHz, 50% duty cycle and calculating the difference between the minimum and maximum ADC values returned from the phototransistor.

Figure 5-52, below, illustrates this concept.

As the emitter pulses (upper plot), the phototransistor reacts (lower plot) and rises to a voltage V_{High} after a certain rise time. In the middle of the phototransistor pulse (indicated by the yellow marker) an ADC reading is taken. When the emitter switches off, another ADC reading is taken, this time at V_{Low} which is the ambient light DC shift. The difference between the minimum and maximum received pulses can then be calculated ($V_{Diff} = V_{High} - V_{Low}$) and compared to a set 'sensitivity' value which is determined by the user through the GT_Rx global array mentioned above.

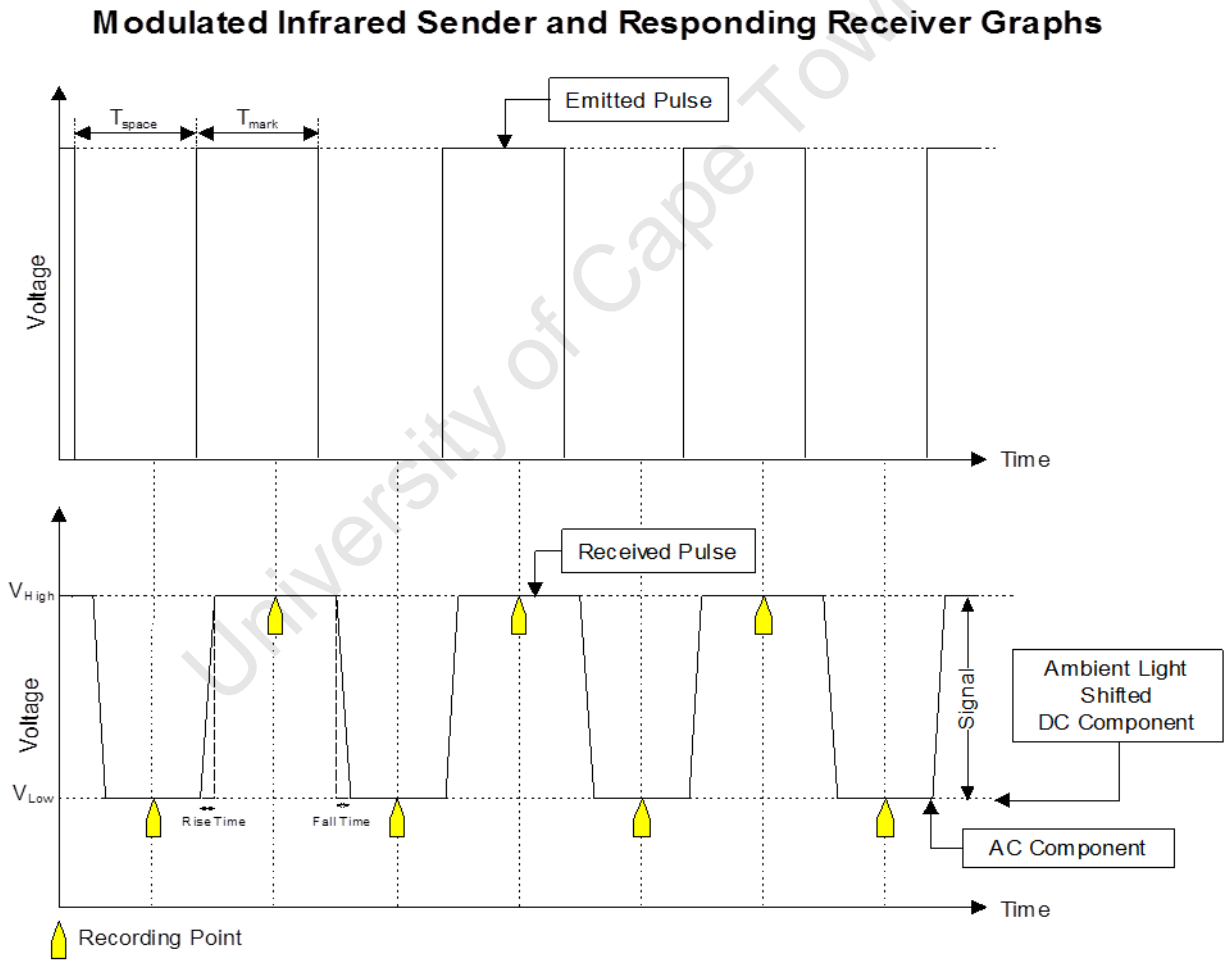

Figure 5-52: Simulated Signal Plot of the Infrared Transmitter and Receivers [53]

For full detailed testing of the system discussed above please see **Chapter 9. Testing and Results,** section **9.2.9 Gripper Light Bridge Performance Test**.

5.6 Summary

The gripper system was designed to meet all of the desired specifications listed at the beginning of this subsystem chapter. The intention was to create a stand-alone system that would include a high level of sensory functionality coupled with a robust and effective mechanical structure.

For detailed testing and verification of the specifications outlined in this chapter, see **Chapter 9. Testing and Results**.

Chapter 6. Wrist Subsystem, that follows, examines the design process and final solution that was developed for the wrist subsection of the end-effector.

Chapter 6. Wrist Subsystem

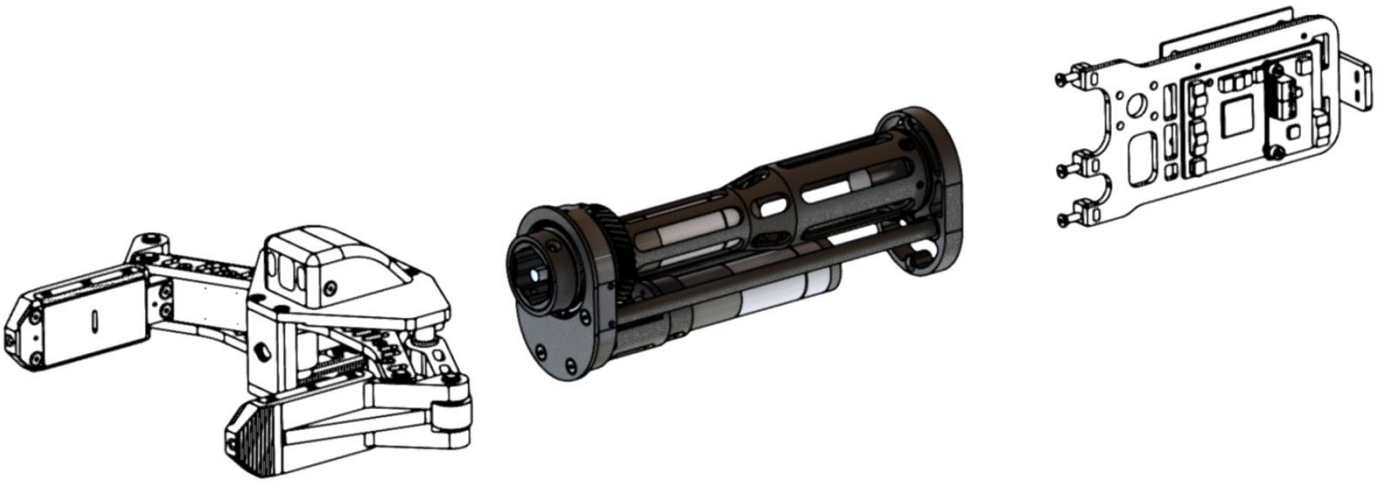

Figure 6-1: Highlighted Gripper Subsystem as Part of the Overall End-Effector

Figure 6-1, above, illustrates the wrist subsystem as part of the overall end-effector. The wrist houses two Maxon EC22 40W 157:1 drive motors and is fitted with Hall Effect sensing for quadrature position control and calibration, temperature monitoring as well as a 30-way slip ring to facilitate continuous wrist rotation. Figure 6-2, below, presents an image of the completed wrist subsystem.

Figure 6-2: Manufactured End-Effector Wrist Subsystem

This chapter will detail the complete design process and development of this module as well as describe its interaction with the rest of the end-effector system. Focus will be placed on the following key areas:

- **Conceptual Design Process**
- **Overall Assembly of the Wrist Subsystem**
- **Achieved Weight Saving**
- **Gear Calculations**
- **Internal Wiring and Connection Diagrams**
- **Hall Effect and Temperature Sensors**

The chapter starts by presenting module specific detailed specifications of the wrist subsystem including design justifications.

6.1 Module Specific Specifications

The following detailed wrist specifications are rooted in the primary specifications presented in Chapter 3. They present critical and non-critical design requirements that will be validated against when full module testing is performed. After presenting the detailed module specifications below, justifications are provided to clarify the design choices that were made.

Table 6-1: Wrist Specific Module Specifications

Location	Design Requirement	Desired Value
Physical Specifications		
6.1.1	Wrist Length (Excluding Electronics)	200mm
6.1.2	Wrist Cross-Sectional Dimensions	68mmx48mm
6.1.3	Wrist Mass (Excluding Motor and Electronics)	300g
Functional and Performance Specification		
6.1.4	Wrist Motor and Gearbox	Maxon EC22 40W 157:1 GP22HP
6.1.5	Continuous Rotation of the Wrist	Yes
6.1.5	Minimum Achievable Wrist Rotational Speed	60 rpm
6.1.5	Minimum Achievable Wrist Torque	5Nm
6.1.6	Wrist Gear Ratio	2:1
Electrical and Electronic Specifications		
6.1.7	Wrist Position Feedback	512 CPT Maxon Quad Encoder
6.1.8	Wrist Positional Accuracy Required	1°
6.1.9	Wrist Limit Sensors	Digital Hall Effect
6.1.4	Wrist Motor Controller	Maxon DEC24/3
6.1.10	Current Sensor Feedback	25mA Resolution
6.1.11	Temperature Monitoring Ability	Yes

6.1.1 The overall length of the wrist system that protrudes into the manipulator arm was defined to be 300mm by Peter Henson. Of this 300mm, 200mm was assigned to the wrist subsection with the remaining 100mm available to the electronics module.

6.1.2 The cross-section of the upper manipulator arm section is a revised version (far right) of the original specification (right) that was significantly larger. With the new size, severe space constraints were imposed on the wrist subsystem.

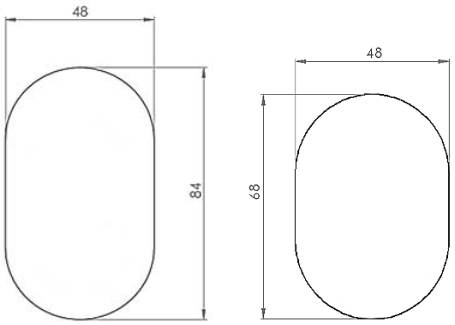

Figure 6-3: Original and Revised Upper Arm Cross-Sections Designed by Peter Henson

6.1.3 A maximum mass of 800g was specified for the overall end-effector excluding electronics systems. Of this overall mass, 300g has been assigned to the wrist section.

6.1.4 Maxon 24V 40W EC22 (Nr: 386658) motors were pre-selected for this project due to their high quality and reliability, as well as their good weight (85g) to power (19.7mNm @ 31900rpm) output. This motor was matched to a Maxon 157:1 GP22HP (Nr: 370786) planetary gearbox and a Maxon DEC24/3 speed controller to provide a potential 3Nm torque @ 200rpm of the output shaft.

6.1.5 Please see **Chapter 3. Primary Specifications** for detailed justifications on these main system specifications.

6.1.6 A 2:1 reduction ratio was selected to increase the output torque of the wrist and reduce the speed from 200rpm to 100rpm (closer to the target specification of 60rpm). Additionally, the gear set would need to conform to the size restrictions discussed in 6.1.2.

6.1.7 Position feedback of the wrist motor will be provided by a factory fitted 512 **CPT** Maxon MR Quadrature Encoder (Order Nr: 201940). Together with the integrated quadrature encoder interface on the primary controller, high resolution position feedback will be available.

6.1.8 A rotational accuracy of 1° was chosen for the wrist with the above quadrature encoder. This should be more than accurate enough for most applications where position control may be required in the field.

6.1.9 The Maxon MR quadrature encoders are relative shaft encoders and need to be recalibrated upon power up of the system. During this calibration process, a digital Hall Effect switch could act as an ideal non-contact end stop.

6.1.10 Due to the fact that the Maxon DEC 24/3 speed controllers do not offer integrated motor current sensing, an external board should be developed to provide high resolution current measurements. The current sense resolution has been matched to that required by the gripper module to standardise on the external current sensor.

6.1.11 As the **MRP** may be exposed to extreme environmental conditions, which may fall outside its operating range, the ability to monitor the internal temperature of the end-effector system within the arm section may be advantageous to a remote operator.

6.2 Initial Design Development Process

From the background research that was performed and based on the detailed wrist specifications, the following investigation into the conceptual phase of the wrist subsystem was undertaken.

As briefly outlined in the gripper conceptual design section, of the three undergraduate projects that were run only the angular [34] and parallel [35] end-effectors included the added requirement to design a wrist section. These two designs are outlined below.

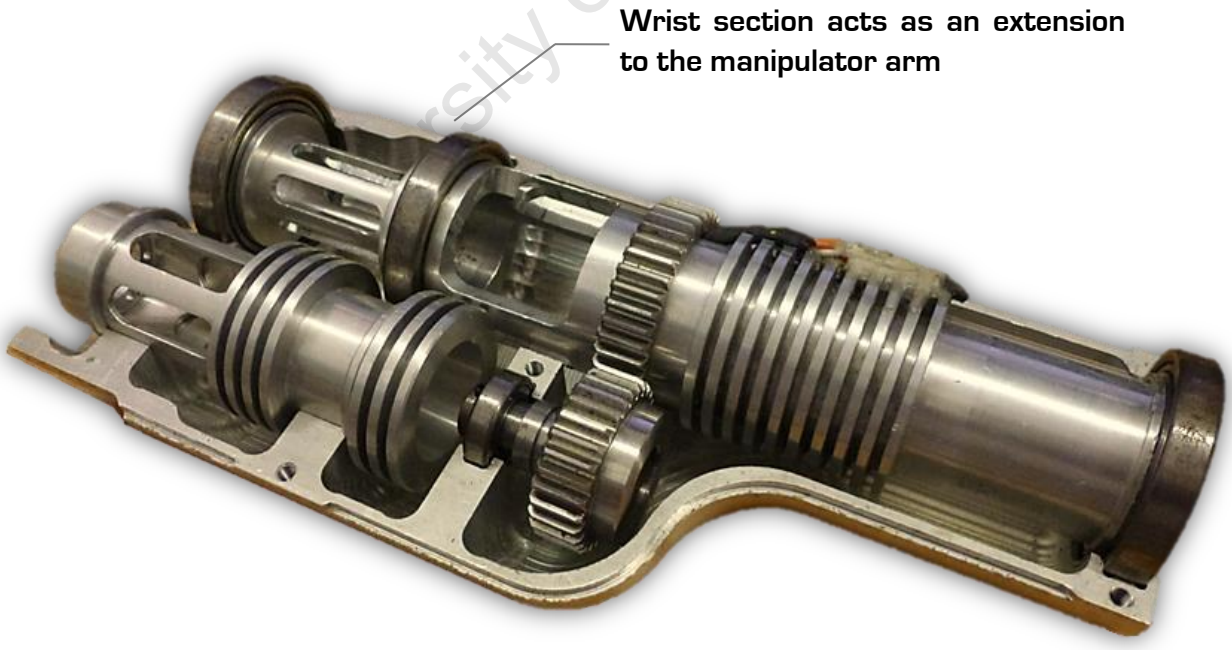

Figure 6-4: Render of the Angular Gripper and Wrist Section [34]

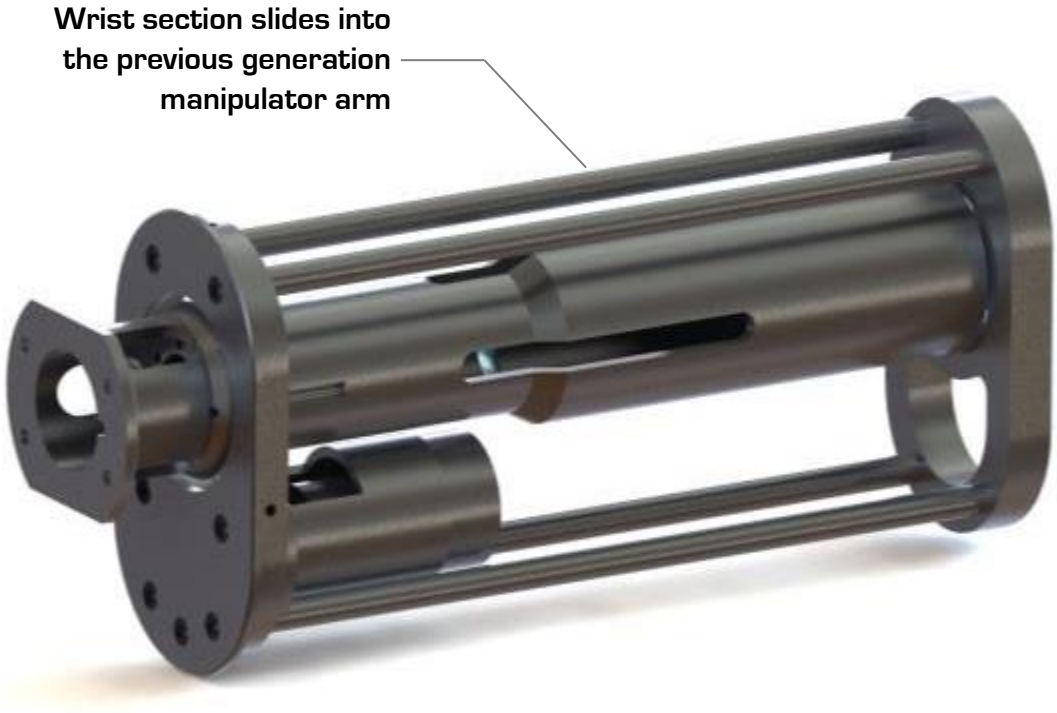

Figure 6-5: Solidworks Render of T. Scott's Parallel End-Effector Wrist

The following table provides an overview of some key performance characteristics that were extracted from the project reports of both wrist systems.

Table 6-2: Summary of Key Performance Indicators for Past Wrist Systems

Desired Specification	M. Cross	T. Scott
Mass	Approx. 800g	493g
Torque	8 Nm	7 Nm
Rotation Speed	65rpm	47rpm
Rotation	360° Continuous	360° Continuous
Actuation Method	Spur Gear Set	Spur Gear Set
Length (Excluding Electronics)	254mm	190mm
Position Control	No	No
Limit Sensors	Yes	No
Current Monitoring	No	No
Ease of Assembly and Maintenance	Moderate	Simple

Based on the characteristics above, the following conclusions were drawn:

- The mass of M. Cross's wrist is excessive at approximately 800g (the actual target for the overall end-effector). The weight of T. Scott's wrist is acceptable, but it would need to be lightened substantially to bring it in line with the specified target.
- Scott's wrist is compact and relatively simple to assemble and install with few parts
- The rotational speed for both configurations is acceptable, although 47rpm for Scott's wrist is marginal.
- The lack of wrist position control, current monitoring and digital limit switches on both systems are drawbacks that will need to be addressed.

Based on these system characteristics, Scott's wrist was selected for further development. An improved prototype version was designed and manufactured for the new arm cross section Figure 6-6. This prototype was designed to be used with various gripper types in order to perform the tests and investigations that aided in the development of the final end-effector system.

Figure 6-6: Redesigned Wrist Prototype Based on T. Scott's Existing Design

Although a number of components were redesigned (including the front and back plates), an attempt was made to reuse as many existing parts as possible.

Modifications included reducing the number of supporting rods while retaining overall stiffness, compacting the overall design (and thus reducing the mass by over 10% to 430g), changing the front design to ease assembly as well as remounting the gears more securely.

6.3 Detailed Mechanical Design

The conceptual design process that was presented above was critical to the detailed design that is presented in this chapter. The manufacture of a physical prototype aided in testing the functional performance of the wrist system before starting a detailed final design. Utilising the knowledge gained from these tests and the conclusions drawn from Chapter 2, the following full detailed design was developed.

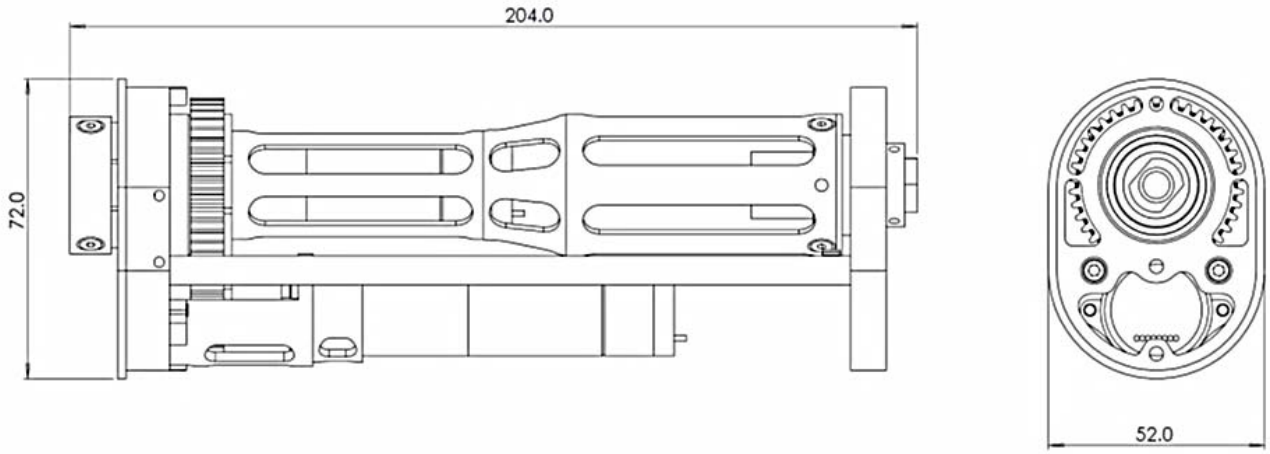

Figure 6-7: Physical Dimensions of the End-Effector Wrist Subsystem

Figure 6-7 presents the overall physical dimensions of the wrist subsystem with both the gripper and wrist motors installed. The figure below presents the manufactured and assembled wrist subsystem without motors prior to hard black anodising.

Figure 6-8: Assembled Wrist Subsystem Excluding Motors/Electronics Prior to Anodising

The following sections of the design process will be examined in this chapter:

- **Design of the Wrist Components**
- **Manufacturing**
- **Weight Saving Methods**
- **Gear Calculations**

Design of the Wrist Components

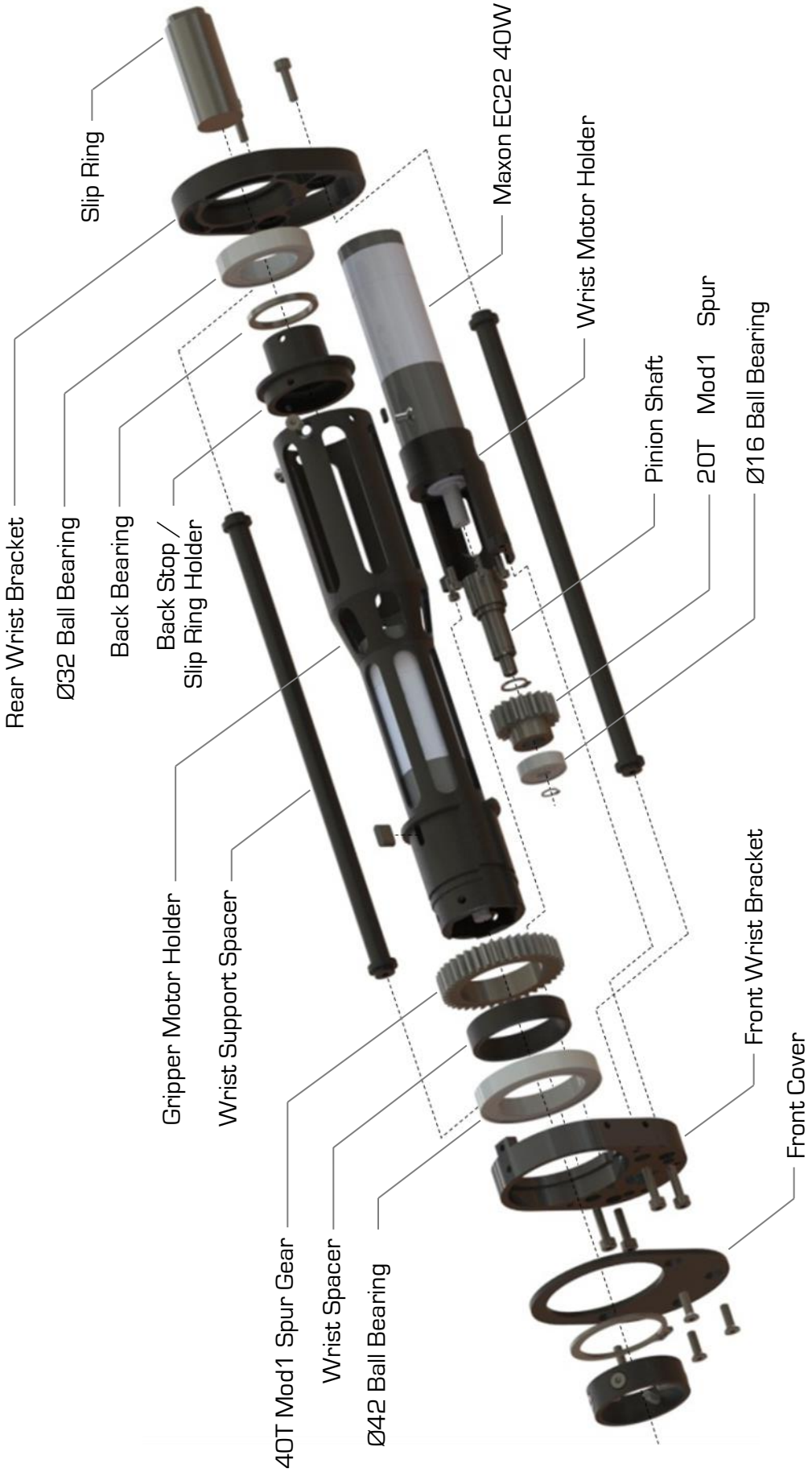

Figure 6-9: Exploded View of the Wrist Subsystem

Figure 6-9 presents an exploded view of the entire wrist system including both drive motors. It is evident that the basic structure of T. Scott's wrist has influenced the design of the new system; however fundamental differences are evident upon closer inspection.

Similarly to the design of the gripper subsystem, **DFMA** principles influenced many design decisions throughout the development process as the maintainability and simplicity of the system was of key importance. An example of this is demonstrated in Figure 6-10, below.

Figure 6-10: Examples of DFMA on the Front Wrist Bracket

As seen in the exploded view, the overall assembly is made up of two support brackets (front and back) held together by two *Support Spacers* with the *Gripper Motor Holder* section rotating freely on ball bearings along the length.

The motor that actuates the wrist is attached to the front wrist bracket by the *Wrist Motor Holder*. The *Front Cover* and the *Retaining Circlip* secure the entire front assembly including the motor holder and the ball bearing.

A 20T Mod1 spur gear is mounted onto a connecting shaft which drives the 40T Mod1 gear attached to the *Gripper Motor Holder* via a key. A 2:1 ratio was selected in addition to the Maxon 157:1 gearbox to reduce the wrist speed to approximately 100rpm and increase the torque to approximately 6Nm. With the use of a 30-way slip ring at the rear of the section, continuous rotation of the wrist and gripper was achieved.

Figure 6-11, below, presents a sectional view of the front wrist module to visually demonstrate how the components are arranged.

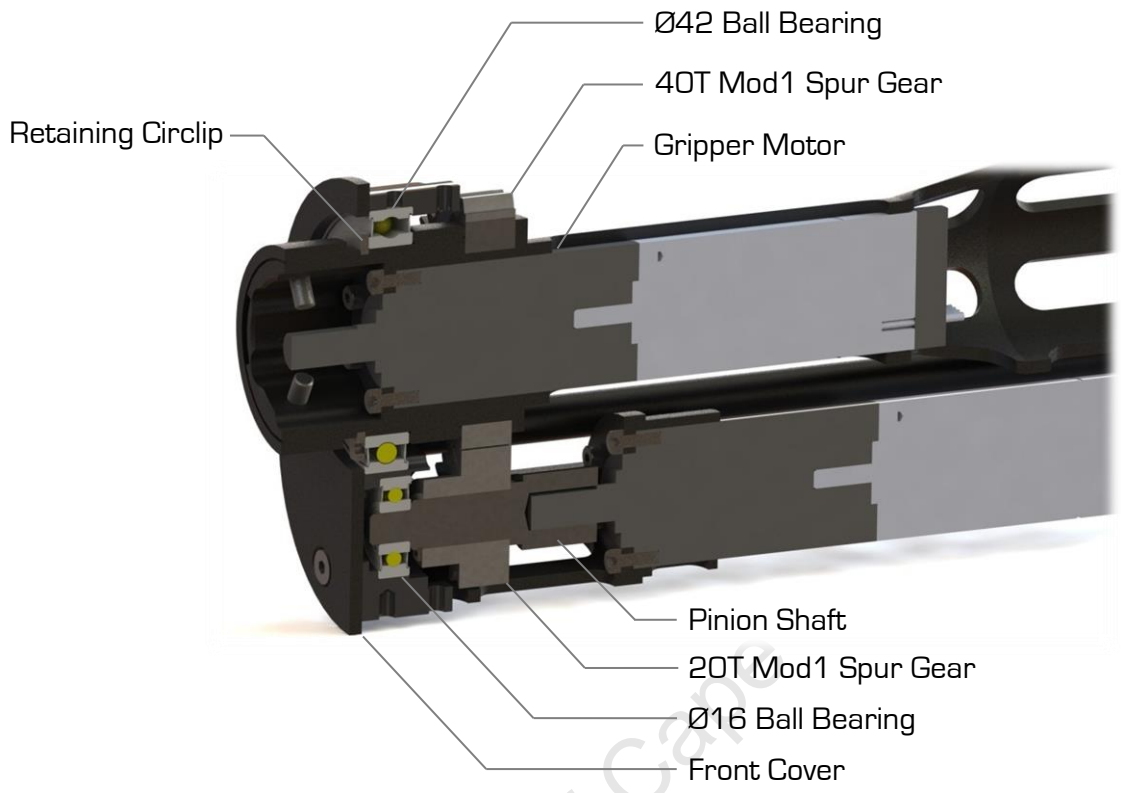

Figure 6-11: Wrist Section View Showing Motor Arrangment

The render below illustrates how the wrist section slides into the manipulator arm. Eight M3x6mm hex socket countersunk screws secure the system in place.

Figure 6-12: Render of the Wrist Being Slid into the Manipulator Arm

Manufacturing

Similarly to the gripper subsystem, the decision was made to manufacture almost all wrist components from *Aluminium 6061*. Again, its high strength to weight characteristics, machinability, corrosion resistance and its wide availability in the UCT Mechanical Engineering Workshop made it ideal as the principal material.

For components that were not manufactured out of *Aluminium* (such as the pinion gear shaft), *Silver Steel* was selected. Overall, an attempt was made to use corrosion resistant materials where possible, while retaining sufficient strength with minimal weight gain.

All components, except for the gear set and the **Front Cover**, were manufactured in UCT's Mechanical Engineering Workshop using either a CNC mill, CNC lathe or by hand. The gear set was ordered through Technisales [56] and was then modified in the workshop. The **Front Cover** was sent to Vulcan Steel for laser cutting.

Figure 6-13 shows various wrist components during manufacturing stages.

Figure 6-13: Wrist Components in Various Stages of Machining

a) Wrist Motor Holder on the CNC mill, b) Gripper Motor Holder Being Hollowed out on the CNC Lathe. c) Weight Saving Slots to be cut on the CNC Mill, d) Gripper Motor Holder Interface Being Milled

Weight Saving Methods

The overall mass of the end-effector system was a critical design requirement as it directly affects the performance of the manipulator arm. At 1.6m outstretch, every additional gram will negatively affect the moment of inertia of the system, as well as increase the required torque exerted on the base link.

The overall allowable mass for the wrist section was specified to be 300g, with 500g assigned to the gripper module. This was considerably less than the prototypes that were tested (Angular: 800g, Parallel: 493g, Modified Parallel: 429g) and was an ambitious target. The final mass of the wrist excluding electronics and motors was 317g (648g including both drive motors), 17g more than the specified target. Although some further weight reductions were possible, this would have required re-machining of critical parts which was not possible due to heavy workshop load.

The following figures illustrate some of the weight saving methods that were employed on selected wrist components.

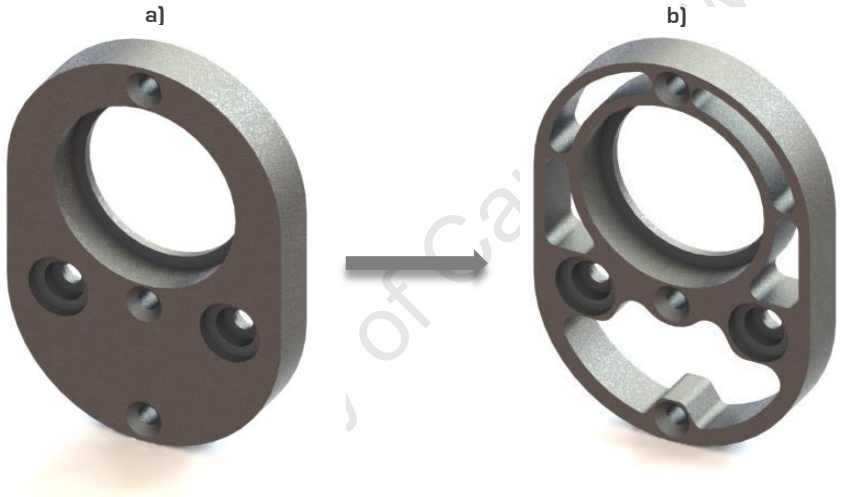

Figure 6-14: Render of the Wrist Back Bracket a) Initial (43g) b) Final (23g)

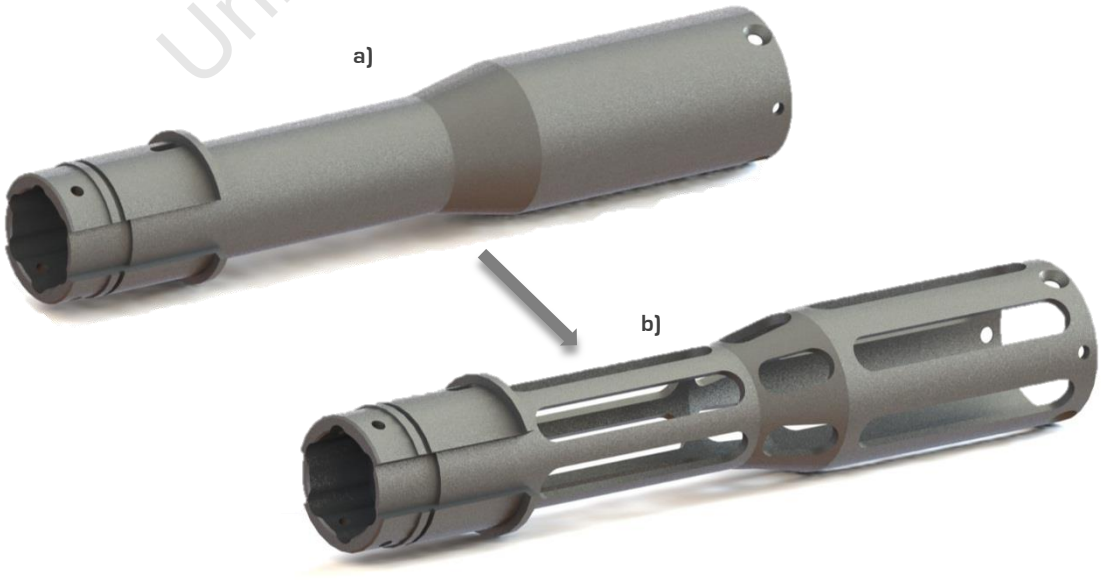

Figure 6-15: Gripper Motor Holder a) Initial (98g), b) Final (65g)

Gear Calculations

Spur gears were selected as the power transmission medium because of their local availability and relative cost when compared with other gear types. Due to the fact that a 2:1 reduction gear ratio was pre-selected and severe space constraints were applicable, the decision was made to select a 20T and 40T Module 1 EN8 gear set from Technisales [56] and to post-machine them in the UCT workshop. Machining involved hollowing the gears and reducing the face width as far as possible to lighten them. The render below illustrates how the gear set was to be mounted.

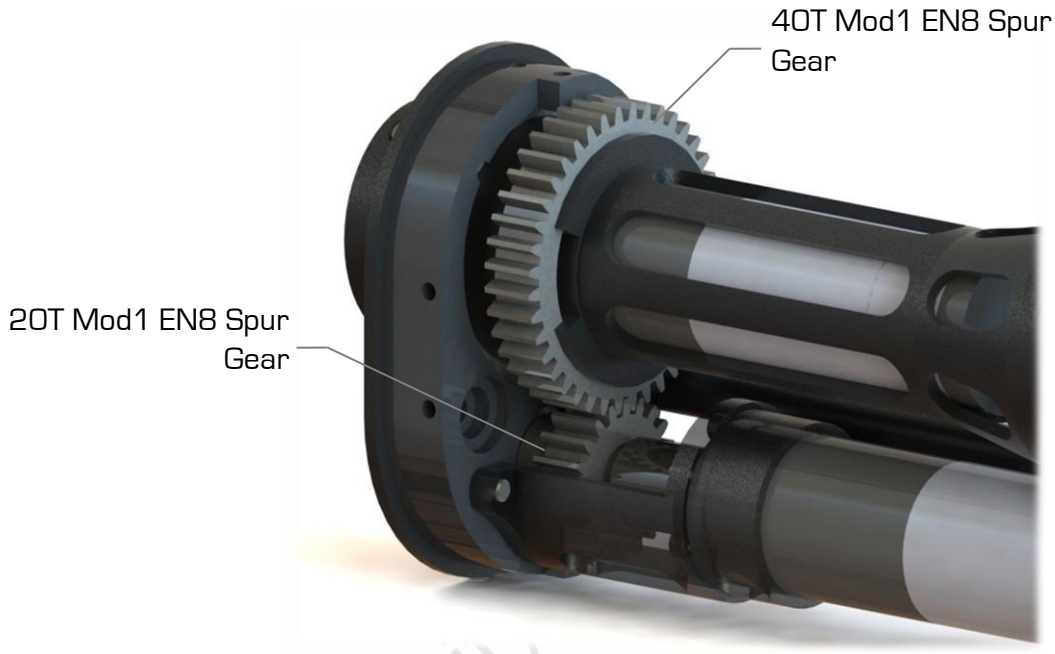

Figure 6-16: Gear Arrangement to Rotate the Gripper Continuously

In order to optimise both gear widths for strength and weight, the following stress calculations were performed based on the *Lewis Equation* for gear-tooth-bending. The calculations that follow were based on principles presented in "Fundamentals of Machine Component Design" by R. Juvinall and K. Marshek [51].

Table 6-3: Maxon Motor and Gearbox Characteristics

Motor Property	***Value***
Motor Type	Maxon EC22 40W (386658)
Attached Gearbox	Maxon 157:1 Planetary (30786)
Maximum Torque at Gearbox Output	3Nm
Maximum Speed at Gearbox Output	203rpm

Table 6-4: Wrist Gear Calculation Symbols and Descriptions

Symbol	*Description*
SF	Safety Factor (= 1.2 as operating conditions are well defined and mass reduction is critical)
M_T	Applied Torque (= 3Nm)
F_T	Tangential Force (N)
S_u	Ultimate Tensile Strength (EN8 = 550Mpa [57])
S_e	Equivalent Stress Estimated at $1/3\ S_u$
S_d	Strength Including Safety Factor
σ_b	Gear Tooth Bending Stress
J	Spur Gear Geometry Factor
K_v	Dynamic Factor (Indicates severity of impacting gear teeth)
K_o	Overload Factor (Degree of Non-uniformity of Driving and Load Torques)
K_m	Mounting Factor (Accuracy of Mating Gear Alignment)
m	Gear Module
b	Gear Width

First, the weaker of the two gears needed to be found. This was done by comparing the $\boldsymbol{S_d * J}$ values of both gears as seen in the table below. For both gears, the geometry factor $\boldsymbol{J}$ was read off *Figure 15.23* in [51].

Table 6-5: Table Summarising Material and Strength Properties of the Proposed Gear Set

	Material	S_u (MPa)	S_e (MPa)	S_d (MPa)	J	$S_d * J$
Gear	EN8	550	183.3	152.8	0.38	58.05
Pinion	EN8	550	183.3	152.8	0.34	51.95

Having established that the pinion would fail first, analysis was performed on this gear.

With $F_t = \frac{2*M_T}{d_p} = 300N$ and $v = \omega r = 0.21\frac{m}{s}$

$K_v = \frac{3.05+v}{3.05} = 1.07\ \left(With\ v < 10\frac{m}{s}\right)$

$K_o = 1.0\ (Uniform\ power, Uniform\ driven)$

$K_m = 1.3\ (Accurate\ mountings\ with\ small\ bearing\ clearances, b < 50mm)$

Therefore using:

$Lewis\ Equation$: $\sigma_b = \frac{F_t K_v K_o K_m}{mbJ}$ gives a gear width $\boldsymbol{b = 8.03mm}$

Therefore a gear width of 8mm (with a safety factor of 1.2) was selected for both gears.

6.4 Electrical Distribution and Sensor Design

The wrist system facilitates the interface between the gripper subsystem and the primary system controller, as well as the distribution of the signals required to drive the two Maxon EC22 motors. Additionally, it incorporates a temperature sensor as well as a digital Hall Effect limit switch for calibration of the wrist upon system start-up.

6.4.1 Slip Ring Connections

A 30-way slip ring (shown below) mounted at the rear of the wrist in the *Gripper Motor Holder* was used, together with a *Gripper Finger Connector Distribution Board* presented in the previous chapter, to distribute the various power, control and communications signals throughout the end-effector. The distribution board was added to simplify the assembly and serviceability of the system.

Figure 6-17: 30-Way Slip Ring

The following table illustrates the various connections that were passed through the slip ring. Note that power connections, such as the motor windings, were distributed over multiple wires due to the high current that may be drawn from the gripper motor. It should be noted that **SPI** speed tests were run through the slip ring up to 1MHz to verify the communications stability at maximum wrist rotational speed.

Table 6-6: Slip Ring Connection Table

Connection	Function	Connection	Function
1	**QE V_{cc}**	12 - 14	**Motor Winding 2**
2	**QE GND**	15 - 17	**Motor Winding 3**
3	**QE $Ph\ A$**	18	**Motor V_{cc} Hall**
4	**QE $Ph\ \overline{A}$**	19	**Motor GND**
5	**QE $Ph\ B$**	20	**Motor Hall Sensor 1**
6	**QE $Ph\ \overline{B}$**	21	**Motor Hall Sensor 2**
7	**QE $Ph\ I$**	22	**Motor Hall Sensor 3**
8	**QE $Ph\ \overline{I}$**	23 - 30	**Gripper Controller Power and Communications**
9 - 11	**Motor Winding 1**		

6.4.2 Temperature and Digital Hall Effect Sensing

As described in the detailed specifications at the beginning of this chapter, the ability for an operator to remotely monitor the temperature in the arm section may be quite useful. Figure 6-18 shows the location of an LM35 temperature sensor which is connected to an ADC input on the primary controller mounted on the rear of the wrist subsection.

A digital Hall Effect sensor was also installed with a Ø3.2x1.4mm round Neodymium magnet recessed into the *Gripper Motor Holder*. This limit switch will be used to recalibrate the wrist using the motor quadrature encoder module.

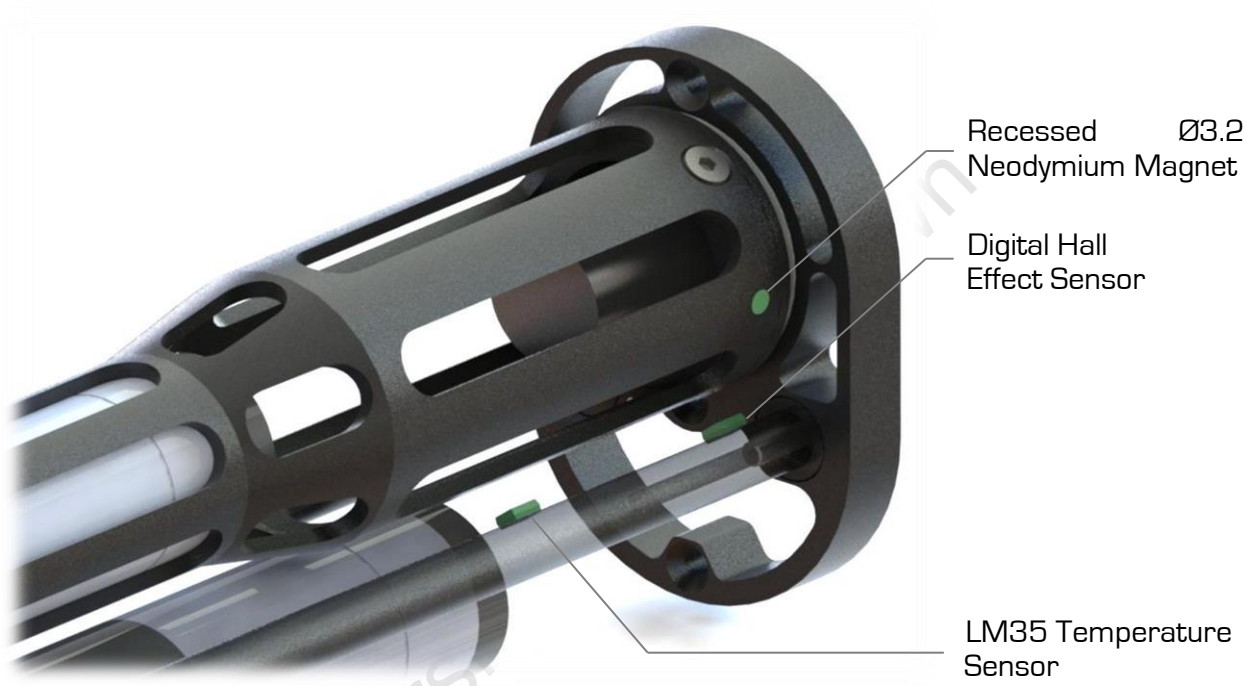

Figure 6-18: Temperature and Digital Hall Effect Sensors Mounted at the Rear of the Wrist

6.5 Summary

The wrist system was designed to comply with all desired specifications detailed at the beginning of this chapter. A significant goal was to reduce the weight as far as possible while retaining overall rigidity and robustness. Additionally, the system was designed with ease of manufacture and assembly in mind to simplify future maintenance and serviceability of the subsystem.

Chapter 7. Electrical and Electronics Subsystem, which follows, describes the development and design of electronics module located at the rear of the wrist subsystem and its integration with the end-effector as a whole.

Chapter 7. Electrical and Electronics Subsystem

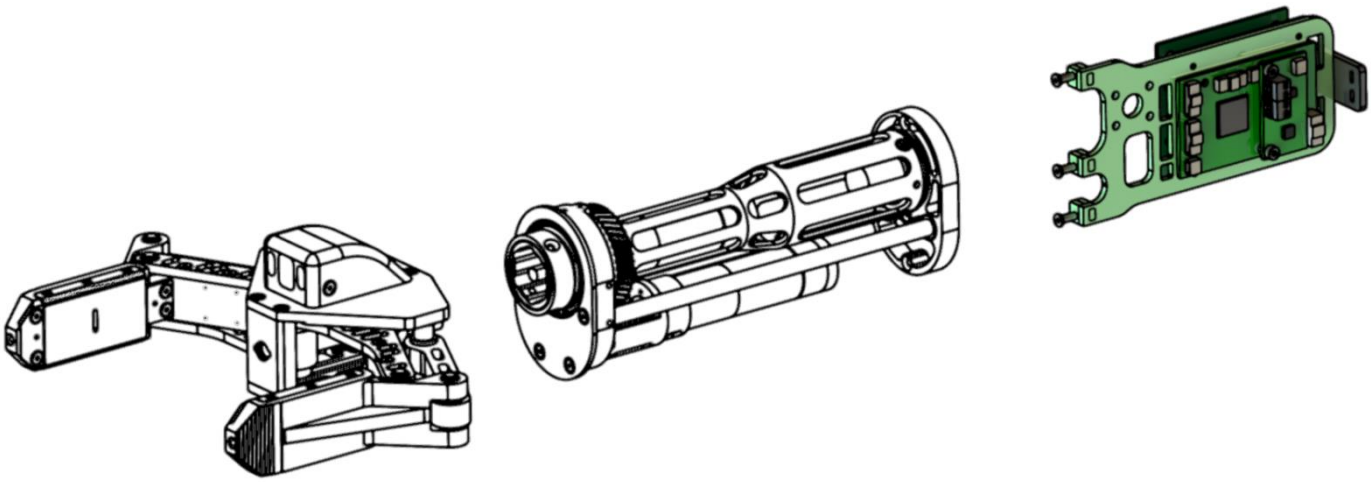

Figure 7-1: Highlighted Electronics Subsystem as Part of the Overall End-Effector

The electrical and electronics subsystem located at the rear of the end-effector is made up of a combination of modules providing functionality including power regulation, communications, system control and system performance monitoring. Figure 7-1, above, illustrates the module as part of the end-effector system. The module is made up of two Maxon DEC24/3 speed controllers, a custom designed ARM Cortex-M3 LM3S8962 embedded controller, a custom dual current sensor as well as a connection distribution board.

Figure 7-2, below, presents the complete system mounted on the wrist.

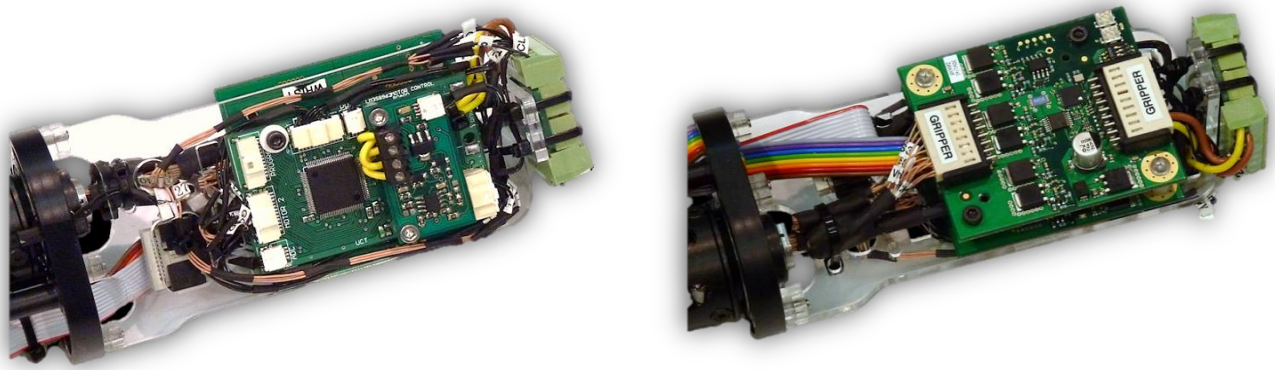

Figure 7-2: Images of the Electronics System Mounted at the Rear of the End-Effector

This chapter will detail the complete design process and development of this module and will illustrate the functionality and feature set of each electronic subsystem. The chapter will begin by presenting a set of overall module specific specifications. Thereafter, the overall system will be presented, detailing the interaction between modules. The custom LM3S8962 embedded microcontroller board and the custom current sensor will then be examined individually.

7.1 Module Specific Specifications

The following detailed system specifications draw from the primary specifications presented in Chapter 3. They present critical and non-critical design requirements that will be validated when full module testing is performed. After presenting the detailed module specifications below, justifications are provided to clarify the design choices that were made.

Table 7-1: Gripper Specific Module Specifications

Location	Design Requirement	Desired Value
LM3S8962 Embedded Controller		
7.1.1	LM3S8962 Embedded Controller Dimensions	70mmx42mmx15mm
7.1.2	LabView ARM Embedded Capability	Yes
7.1.3	Ethernet Capability	Yes
7.1.4	Quadrature Encoding Modules	2
7.1.5	ADC Inputs	4
7.1.6	8-Bit DAC Output	4
7.1.7	Communication Protocol (Gripper Controller)	SPI
7.1.7	Communication Protocol (Master Controller)	I2C
7.1.8	Supply Voltage	5V,12V
7.1.9	Maximum Controller Current Draw	300mA
Dual ACS712 Current Sensor		
7.1.1	Dual ACS712 Current Sensor Dimensions	22mmx42mmx12mm
7.1.10	Current Sensor Resolution (5A Configuration)	25mA
7.1.10	Current Sensor Resolution (20A Configuration)	100mA
7.1.8	Supply Voltage	5V
7.1.11	Adjustable Gain	Yes
7.1.11	Adjustable Current Offset Capability	Yes

7.1.1 The overall dimensions of the embedded controller were restricted by the manipulator arm cross-section. Together with Bradley Springer, maximum target dimensions of 70mmx42mmx15mm were set to allow enough space for additional wiring and airflow.

7.1.2 One of the features, as requested by the head of the RARL, was that the chosen microprocessor should be able to be programmed using the LabView ARM Embedded Development module. This was done in an attempt to keep the software solution standard across all platforms in line with other projects running in the RARL.

7.1.3 The ability for the microprocessor to have Ethernet capability would be a great advantage as modules could simply be added to the network running within the robot platform. This would make the system easier to implement as well as fast to deploy.

7.1.4 Due to the fact that Maxon speed controllers were pre-selected for this and other projects, position control would have to be implemented using the quadrature encoder modules attached to the Maxon motors. Therefore, a microprocessor with this decoding capability should be selected.

7.1.5 A minimum of four **ADC** inputs should be available on the microprocessor to ensure that measuring devices like temperature sensors or current sensors could be used.

7.1.6 Although Maxon DEC 24/3 speed controllers were selected for this project, other robot systems require the use of larger controllers that have inputs for both current limiting and speed input. For this reason at least four **DAC** (**D**igital-to-**A**nalog **C**onverter) 8-bit outputs should be available to control these inputs.

7.1.7 **I2C** was selected as the primary communication protocol by MSc student Peter Henson, although Bradley Springer was required to review this selection. **SPI** was selected as the communication protocol to the embedded gripper controller due to its speed and ease of use.

7.1.8 Peter Henson designed the manipulator arm with 5V, 12V and 18V rails available.

7.1.9 As the primary controller will be used throughout the robot platform, the current draw should be minimised as far as possible. A target of 300mA was set to keep the overall power usage (at 5V) to a reasonable level.

7.1.10 It was mentioned in the gripper detailed specifications that an attempt was going to be made to relate the current draw of the gripper motor to the prehension force being exerted by the gripper fingers. This would require high resolution current sensing. A resolution target of 20mA resolution was therefore set for the 5A current sensors, with a 100mA resolution for the general purpose 20A version.

7.1.11 To increase the customisability of the current sensor so that it can be used by multiple persons in the RARL, the ability to have an adjustable gain and current offset could be highly advantageous.

7.2 Electronics System Overview

The exploded view below presents the rear electronics modules. The modules were mounted onto a laser cut Perspex bracket that was fitted to the rear wrist support with M3 screws. Cut-outs in the Perspex allowed for wiring to be passed from one side to another. Another bracket at the rear allowed for the mounting of a signal distribution board (designed by B. Springer) for easy connection to the rest of the manipulator arm. The overall mass of this module and the gripper electronics was established at 207g.

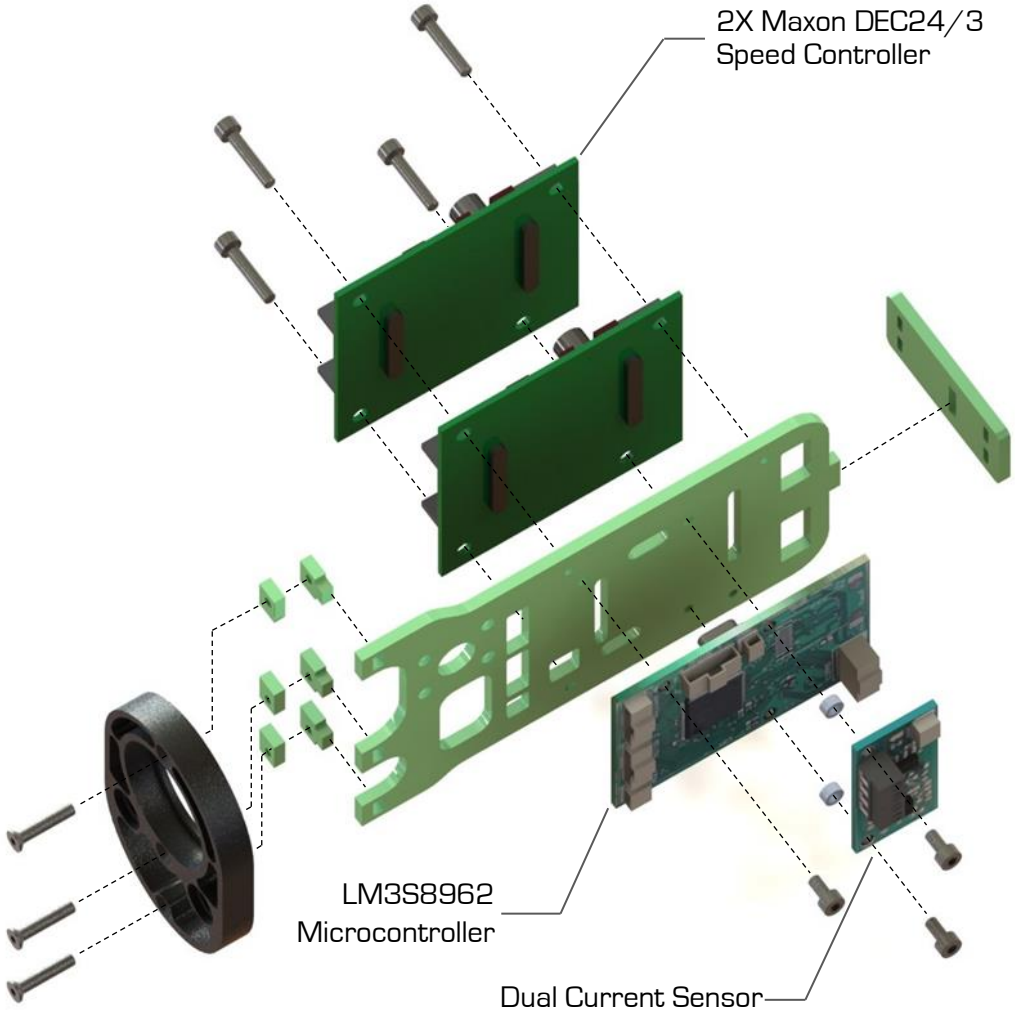

Figure 7-3: Exploded View of Electronics System

Connections (as per Figure 7-4) were made using PicoClasp connectors due their compactness and their positive locking ability. All wires were shortened to reduce overall clutter and have been labelled for efficient disassembly and servicing.

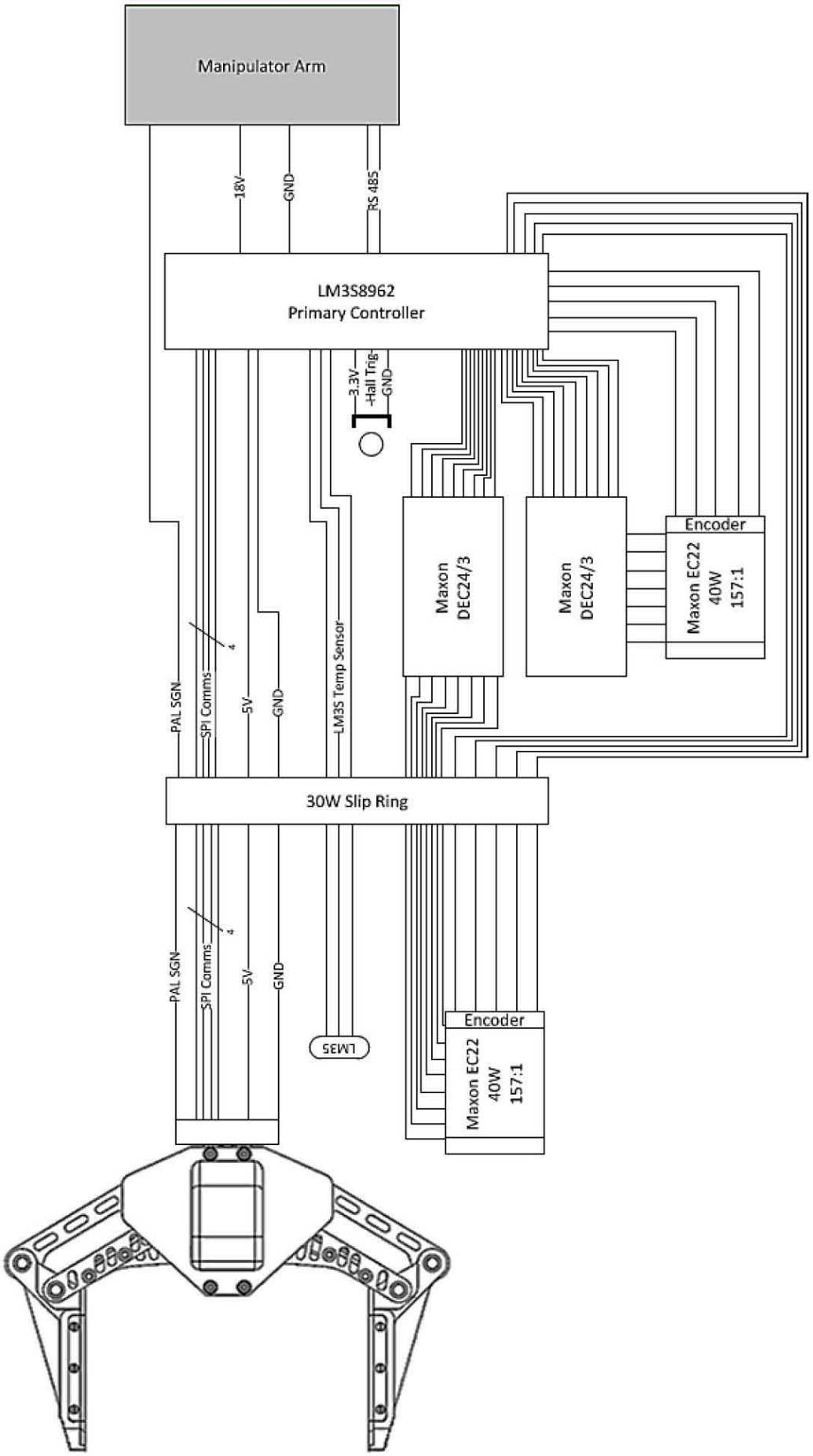

Figure 7-4: Overview of Electronics Module Wiring Diagram

When the design for the electronics module was started, the operation and performance of some modules such as the current sensors or the quadrature encoders was unknown. The test circuit below illustrates a prototype board that was designed and manufactured on **UCT**'s **CNC PCB** mill to test these modules. The board was fitted with two ACS712 current sensors connected to differential amplifiers, quadrature encoding filtering circuitry, voltage divides for speed monitoring and protection circuitry for ADC inputs of a µP.

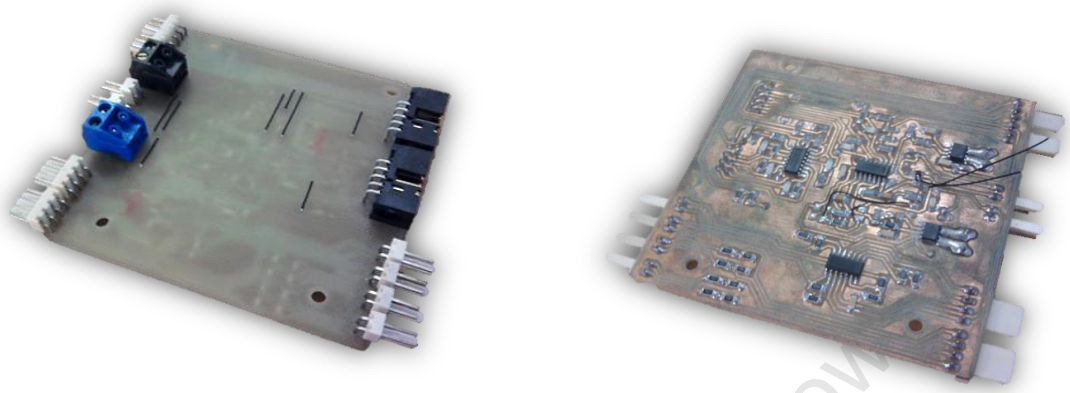

Figure 7-5: Prototype PCB Used to Test Subsystem Functionality

It was realised that for development and testing, the end-effector would most likely not be installed in the manipulator arm and would be operated in isolation. For this reason a control box was designed which could house all the circuits needed to mimic those found in the arm. These would include independently switchable power inputs, an Ethernet connection, RS232/RS485 DB-9 plug and an end-effector connector. A Bosch VIPX2 Dual-Channel Video Encoder was also included to operate the KX-1 CMOS camera.

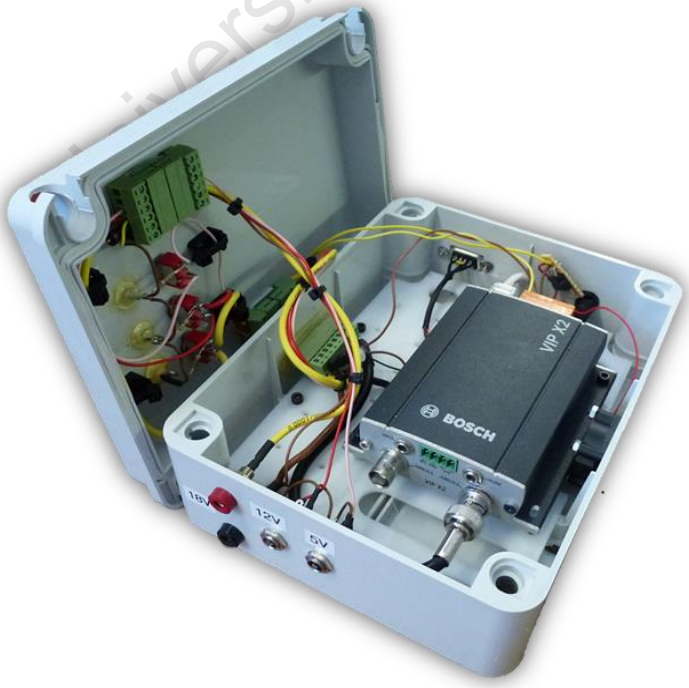

Figure 7-6: End-Effector Testing Control Box

7.3 Maxon DEC24/3 Speed Controller

Maxon DEC 24/3 digital closed loop 1-Quadrant speed controllers [58] were pre-selected for this project by MSc student Peter Henson. The choice was made to select a speed controller rather than a Maxon Epos position controller due to the substantially lower cost and size implications. The intention was to use the quadrature encoder module of the motor, together with a control algorithm, to execute position control.

The DEC 24/3 has a nominal input voltage of 24V and with a 3A maximum continuous output. The controller takes in four signals to control the motor: *Enable*, *Direction*, *Brake* and *Set Speed Value*. The figures below present the controller and the connections required for operation.

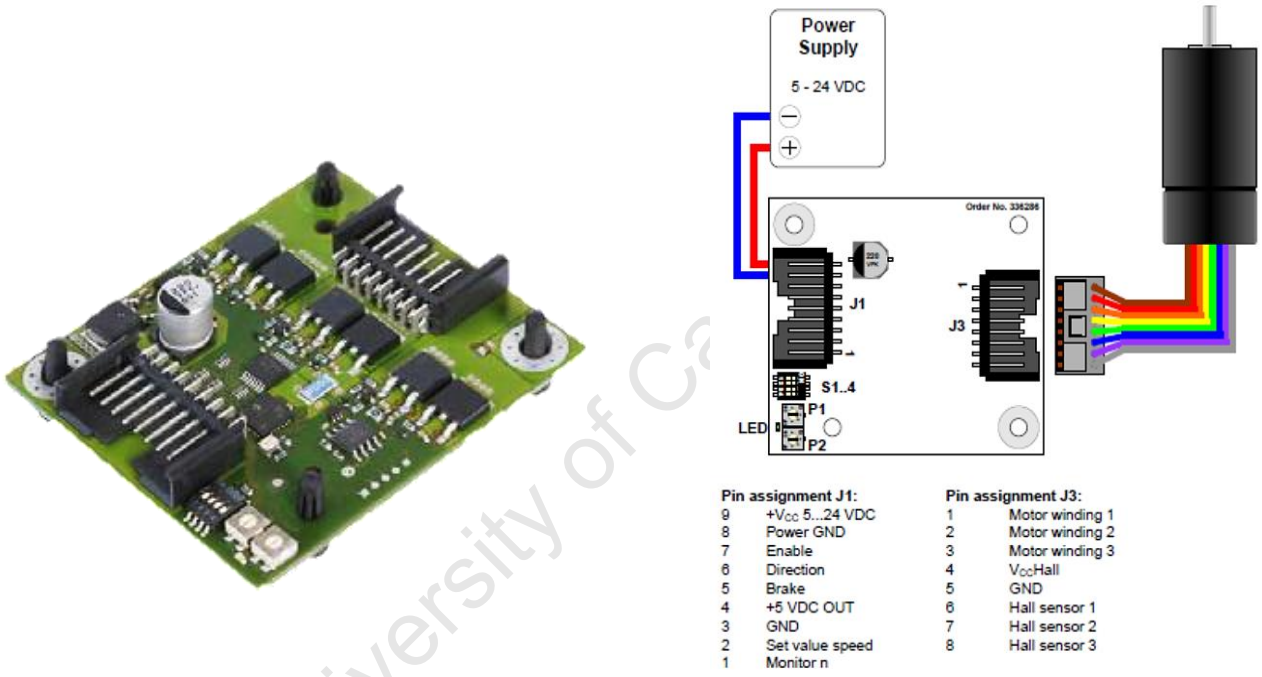

Figure 7-7: Maxon DEC 24/3 Speed Controllers Illustrating Connections Required for Operation [58]

During operation of the end-effector, it was realised that the DEC 24/3 controller has the protective function of restricting current if the motor shaft is blocked for longer than 1.5s. This behaviour, and its negative effect on the controllability of the end-effector system, is discussed in further detail in **Chapter 9. Testing and Results**.

7.4 LM3S8962 Embedded Controller

In order to control, process and monitor system performance, some type of central control unit was required. The specifications of such a microcontroller have already been presented in the detailed subsystem specifications at the beginning of this chapter.

One of the desired requirements was that the microprocessor should be compatible with the National Instruments (NI) LabView ARM Embedded Development Module. Figure 7-8 presents the developed primary controller; a Texas Instruments LM3S8962 Tier-1 LabView ARM compatible microprocessor on a custom designed 3rd Generation RARL PCB.

Specification	Value
Communications	RS-485
Processor Type	50MHz 32-Bit
Flash Memory	256KB
SRAM	64KB
General Purpose Timers	4
I2C	1
UART	2
Ethernet	1
SSI	1
CAN	1
10-Bit ADC	4
PWM	6
Quadrature Decoding	2
12-Bit DAC Output	4
General Purpose IO	34
Supply Voltage	11V – 30V
Power	1.5W Idle

Figure 7-8: Generation III ARM Cortex-M3 LM3S8962 Custom Embedded Controller

The design of this embedded controller was undertaken in collaboration with Tracy Booysen of the **RARL** and fellow MSc students Bradley Springer and David Lwabona. In total, four different versions of the **PCB** were designed and manufactured, with each version iteratively improving on the previous design. It should be noted that the author was mainly involved in the development and testing of the first three versions, with B. Springer assisting T. Booysen on the fourth generation.

This chapter will provide a brief outline of the design process that was followed in the development of these controllers, highlighting the various board generations and their respective feature sets. Additionally, a pinout diagram and a system interconnection chart of a Generation IV board will be provided to illustrate the interface between the various subsystems currently installed in the end-effector.

7.4.1 Initial Design Development

The Luminary Micro ARM Cortex-M3 LM3S8962 50MHz, 32-bit processor was selected for the design of the primary controller due to its compatibility with the LabView Arm Embedded development suite. Four controller versions were developed, each featuring additional capabilities and functionality.

Figure 7-9 presents the four controller generations.

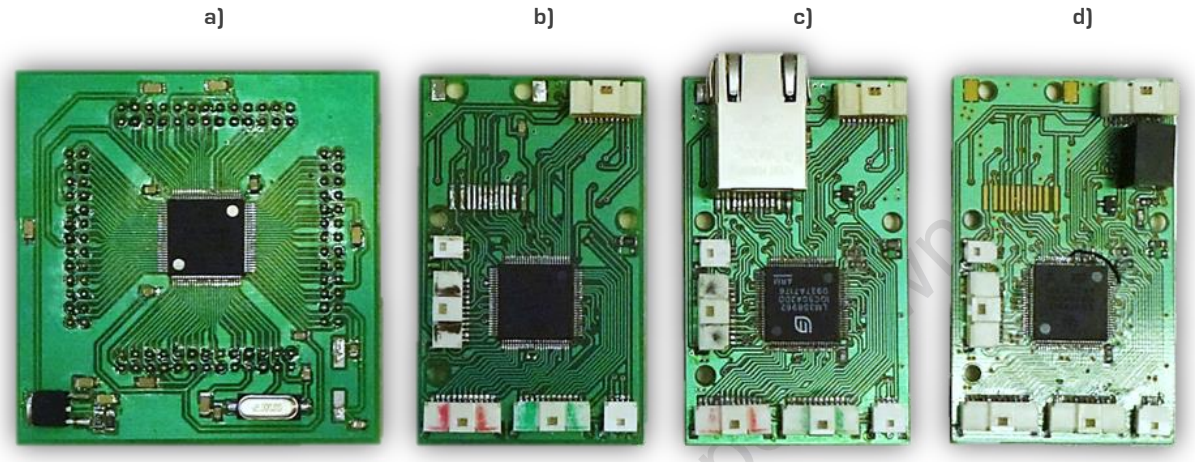

Figure 7-9: ARM Cortex-M3 LM3S8962 Board Generations a) Gen I, b) Gen II, c) Gen III, d) Gen IV

Generation I: The first generation board was used as a 'proof of concept' design to test functionality including quadrature encoding, **SPI** and **I2C**. Additionally, the performance of the processor was gauged to verify if it would be suitable to perform the various control and processing operations required for the end-effector.

Generation II: This was the first design intended for deployment throughout the **MRP**. As discussed in the detailed specifications, the dimensions of the **PCB** were dictated by the cross-section of the manipulator arm. Features that were added to this board included PicoClasp connectors, an RJ45 jack for Ethernet, two MAX3232 ICs for RS232 communications, a quad 12-bit TI DAC7565 and compatibility with the current sensor board being designed alongside.

Generation III: The third generation board featured added quadrature encoder protection circuitry in the form of Schottky diodes and resistors due to a maximum of 5V on the input to the **µP**. The values of these protection components were calculated and then verified using a quadrature encoder test rig. Additionally, the previous DAC was replaced with a simpler and cheaper DAC7554.

Generation IV:

This final version of the **PCB** included two significant changes. The first was the switch from RS232 to RS485 to improve communications stability and future expansion. The second improvement was the addition of a switch-mode DC-DC regulator powered off 18V to allow the board to be powered off a wide range of input voltages.

The three previous versions were powered off 5V and 12V only. Due to the length of the wires and the relatively high current draw, brownouts were detected under heavy arm loading conditions.

Figure 7-10, below, illustrates the conditions that lead to these brownouts. The yellow plot shows the 5V line during heavy motor operation with the green graph showing the 3.3V rail powering the **µP**. As seen from the graph, the supply rail dips down to 1.04V initiating a brownout condition. With the use of the DC-DC regulator, this issue was rectified.

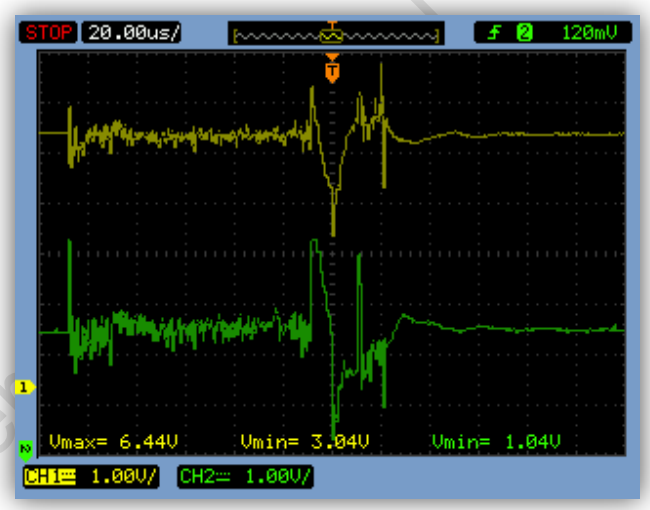

Figure 7-10: Voltage Spikes on the 5V and 3.3V Lines

7.4.2 Final Detailed Design

The following figure provides a detailed pinout diagram of the 4th generation controller. For more detailed information on the previous generation boards, see the accompanying DVD.

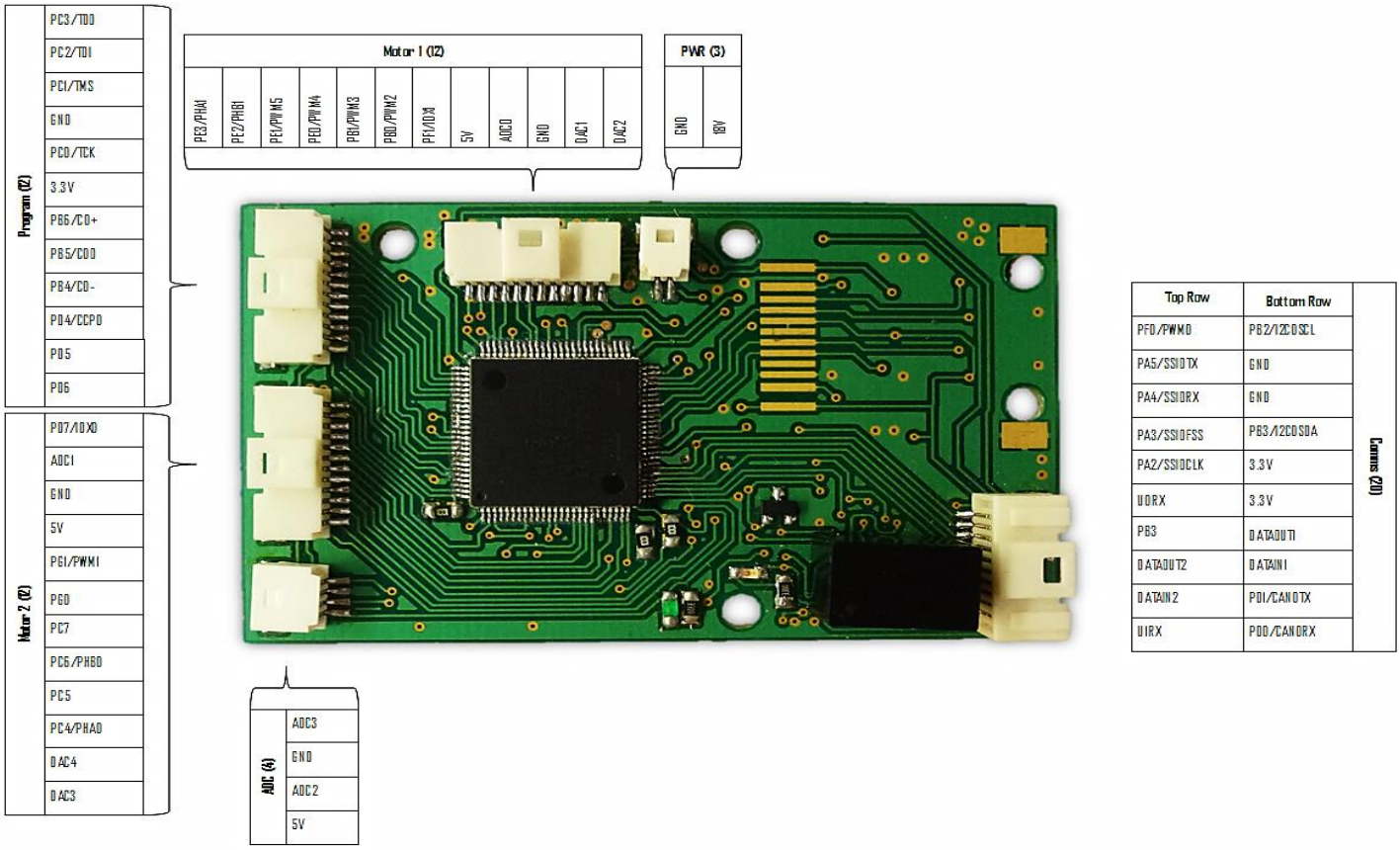

Figure 7-11: LM3S8962 Generation IV Embedded Controller

Utilising the board above, the following table lists the current connections as found in the end-effector.

Table 7-2: Wiring Connections as Currently Installed on the End-Effector

Motor 1 (12)		Motor 2 (12)		Comms (20)	
PE3	Wrist Quad Enc. Phase A	PD7	Gripper Quad Enc. Phase I	PF0	RS485 Loopback
PE2	Wrist Quad Enc. Phase B	GND	Gripper Quad Encoder GND	PA5	SSI0TX
PE1	Wrist Enable	5V	Gripper Quad Encoder PWR	PA4	SSI0RX
PE0	Wrist Direction	PG1	Gripper Speed Monitor	PA3	SSI0FSS
PB1	Wrist Brake	PG0	Gripper Brake	PA2	SSI0CLK
PB0	Wrist Speed Monitor	PC7	Gripper Direction	DO2	RS485
PF1	Wrist Quad Enc. Phase I	PC6	Gripper Quad Enc. Phase B	DI2	RS485
5V	Wrist Quad Encoder PWR	PC5	Gripper Enable	U1RX	RS485 Loopback
ADC0	LM35 Temp. Sensor	PC4	Gripper Quad Enc. Phase A	3.3V	LM35 Temp PWR
GND	Wrist Quad Encoder GND	DAC3	Gripper Speed Set	3.3V	Hall Effect PWR
DAC1	Wrist Speed Set			PD1	Wrist Hall Effect
ADC (4)					
ADC3	Wrist Current Mon.				
ADC2	Gripper Current Mon.				

In order to facilitate easy programming of the primary controller (even once installed), a programming header was included in the **PCB** design. Utilising a Texas Instruments Stellarisware ICDI JTAG (as shown below) and the Keil µVision development suite, the board can be programmed from within LabView. For a detailed description on the programming process, see the guide included on the accompanying DVD.

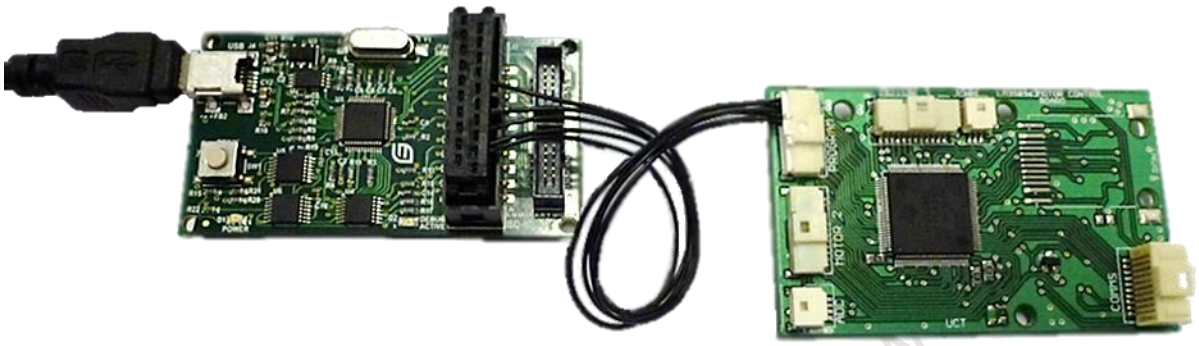

Figure 7-12: Stellarisware ICDI JTAG Programmer Connected to the LM3S8962 Board

7.4.3 Concluding Remarks

The LM3S8962 embedded controller was designed as the standard high-performance controller for the **RARL** and has been deployed extensively throughout the MRP controlling and monitoring various systems. By choosing a processor that could run code generated by LabView's ARM Embedded Development module, standardisation across all **RARL** projects was achieved.

For relevant performance information of this controller, see **Chapter 9. Testing and Results**.

7.5 Custom Current Sensor Board

The ability to monitor the status of components in a complex system like a rescue robot is of vital importance to verify correct and optimal operation of the platform. Of the various sensors that may be employed, current sensing is one of the most important. For the end-effector system current sensing was particularly important, as one of the requirements was to establish whether the current draw could be used to give accurate force estimates for the gripper.

As no cost-effective, off-the shelf current sensing solution was available at the time, custom sensor boards were to be designed for the end-effector. To standardise the robot platform, it was decided that these boards should also be used throughout the robot to monitor various motors and electronic systems. The dual sensor boards that were designed and manufactured are shown below.

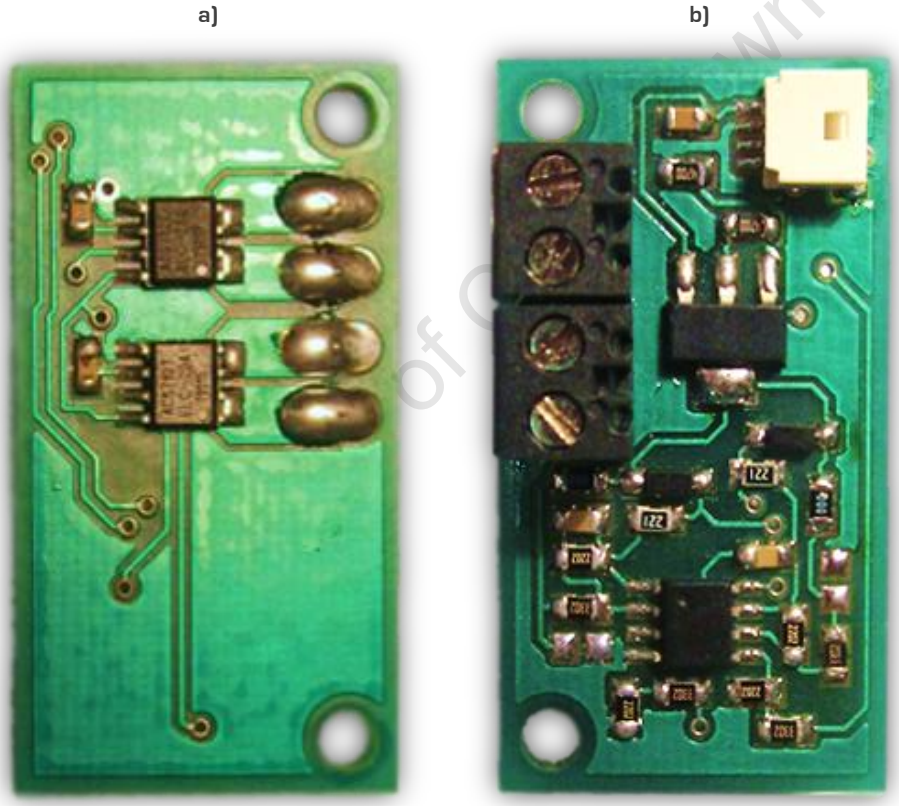

Figure 7-13: Current Sensors Boards for use Throughout the MRP a) Back b) Front

This section will examine the development process that was followed in creating these custom current sensor boards and will present the features and functionality that were included in their design.

7.5.1 Initial Design Development

Before the design of the board was started, some background research into effective current sensing solutions was performed. Two types of sensors were found to be widely used for DC current measurements, namely Shunt Resistors and Hall Effect Sensors.

Shunt Resistor:

In simple terms, a shunt resistor type sensor utilises Ohm's Law to measure the voltage drop over a known resistance, thereby allowing the current to be calculated. Small resistors (often in the mΩ region) are used to reduce the power losses caused by high currents at the expense of reducing sensing resolution. This is partly due to the reduced voltage drop over the shunt resistor and is dependent on the measurement resolution of the microprocessor ADC acquiring the signal. As only a resistor and some post-processing circuits are needed for this circuit, it is quite cost effective. As illustrated below, two shunt resistor configurations can be used.

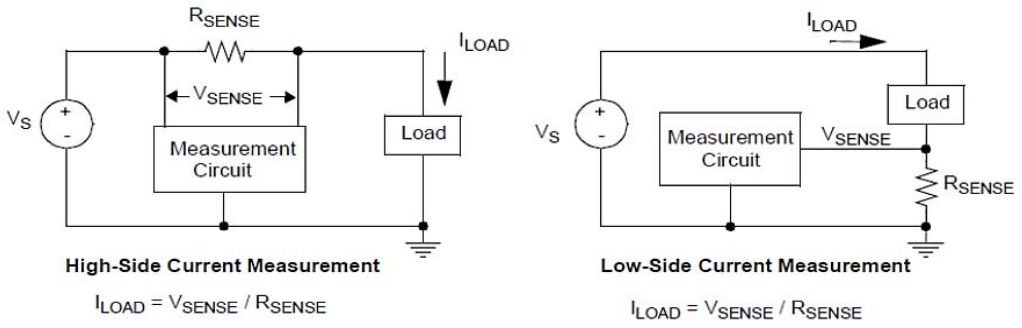

Figure 7-14: High-Side and Low-Side Current Sensing Using a Shunt Resistor [59]

The high-side configuration has the advantage that it is less intrusive on the circuit than the low-side option as it does not alter the ground level of the load. However, the high-side has the disadvantage that the voltage being sensed is approximately equal to the supply voltage, possibly complicating any post-processing circuitry that would need to accept these high signals. A prototype high-side shunt resistor circuit built on Veroboard provided promising performance results with the end-effector system, although high power losses were prevalent in the system which made it unsuitable for use on the **MRP**.

Hall Effect Sensing:

Hall Effect sensors operate using the principle that a voltage is induced in an electrical current carrying conductor in a magnetic field. A typical sensor setup is shown in Figure 7-15.

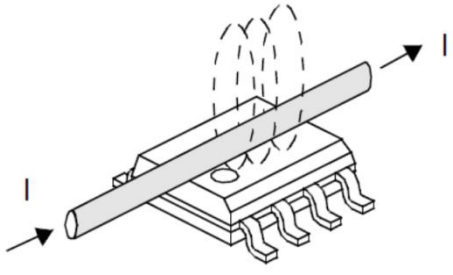

Figure 7-15: Hall Effect Sensor Measuring the Flux Created by Current Flowing in the Wire [59]

These types of sensors offer an advantage in that they are non-intrusive and are isolated from the system being measured. The sensors are usually found as packaged ICs and the output can usually be fed straight into a microprocessor ADC. Furthermore, they provide a high-current measuring capability whilst retaining good accuracy with minimal power losses. A downside is that they are often more expensive when compared to other sensing solutions. An example of a Hall Effect sensor is the Allegro ACS712 [60] available in various current measuring capacities including ±5, ±20A and ±30A.

Based on the brief summary of the sensor that was presented on the previous page, it was decided that Hall Effect sensing should be selected for inclusion in a custom current sensor board. This was mainly due to their simplicity, compactness and potential higher current capability over shunt resistor types.

7.5.2 Final Detailed Design

The board was designed from the ground up to be as customisable as possible so that it could be used throughout the robot platform. Two standard configurations were created, one with a set of ACS712 ±5A sensors and the other with two ACS712 ±20A. Figure 7-16, below, presents a pinout diagram of a manufactured current sensor board.

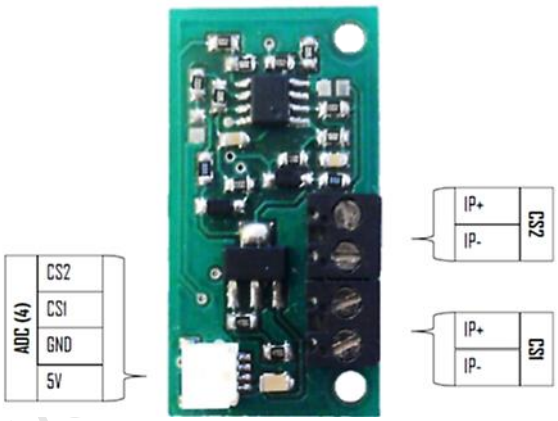

Figure 7-16: Current Sensor Pinout Diagram

The output of the ACS712 current sensors is in the range of 0V-5V, with 2.5V indicating 0A current draw. In order to potentially increase the sensor resolution and to keep the output voltage within the limits of the LM3S8962 ADC input voltage of 3V, a differential amplifier was designed with a selectable inverting input V_1. A short circuit resistor provided the option to either reference 0V or 2.5V (provided by a LM317 linear voltage regulator).

With the ability to ignore all negative currents by soldering a short circuit resistor to provide a 2.5V reference to the differential amplifier, the sensor resolution could be optimised by choosing a suitable gain value. The following equation describes the differential amplifier circuit presented in the full board schematic below (Figure 7-17).

$$V_{Out} = (V_2 - V_1) * \frac{R_2}{R_1} \qquad with\ V_1 = 0V\ or\ 2.5V\ in\ the\ current\ configuration$$

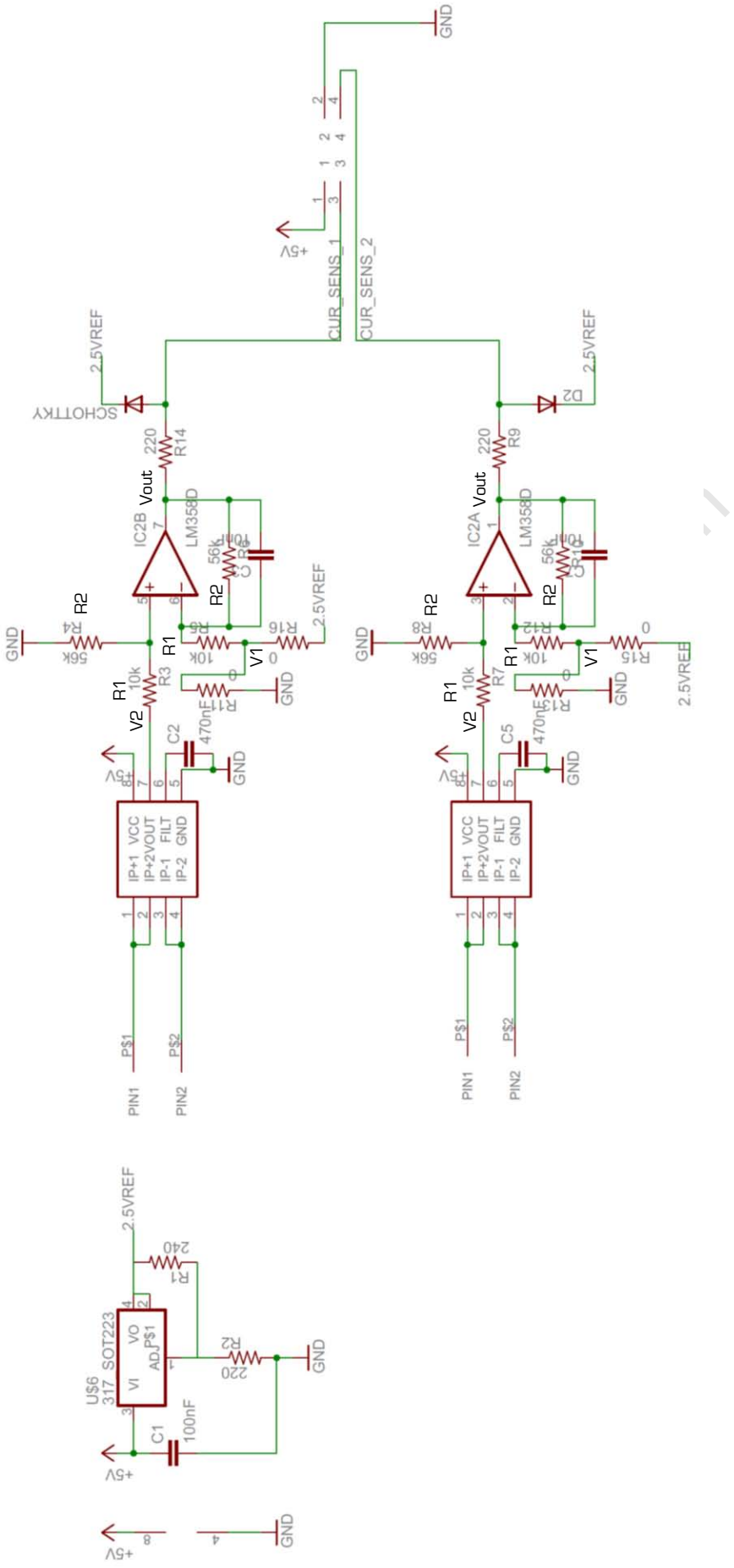

Figure 7-17: Circuit Diagram of a Dual Current Sensor Board

7.5.3 Concluding Remarks

The dual current sensor boards were distributed throughout the **MRP** monitoring systems including batteries, front drive motors, flipper motors, manipulator motors and the end-effector. Each board could be customised to perform optimally based on the system being monitored. Due to their small size, high current capability and their ability to be mounted onto LM3S8962 controllers, the sensors proved to fulfil the requirements set out in the detailed specifications.

7.6 Summary

As both the LM3S8962 embedded controller and the dual current sensor were custom designed for the **RARL,** many different specifications needed to be met. For the primary controller, a significant goal was to create a standardised electronics module that could be programmed using the LabView ARM Embedded Development module thereby substantially decreasing development time for projects.

Chapter 8. Programming and System Control, that follows, examines the software and control systems that were implemented using the LM3S8962 embedded controller.

Chapter 8. Programming and System Control

8.1 Software System Overview

The software system that controls the end-effector can be broken down into two main sections, namely the code running on the end-effector embedded controller and the software that runs on the remote operator's control station. Both of these systems were developed in collaboration with Bradley Springer as the end-effector was a fully integrated subsystem of the manipulator arm. The custom designed operator control station is shown in Figure 8-2. Additionally, test code was created for autonomous QR code discovery and 'Signs of Life' detection using the Bosch VIPX2 gripper camera feed. This test code is detailed in the **Testing and Results** chapter below.

As previously discussed, National Instruments' LabView Suite was used throughout the **RARL** as the standard programming platform. This includes the ARM Embedded Development module for programming the ARM Cortex-M3 processors.

Figure 8-1, below, illustrates the communications system layout of the manipulator arm [3] with the end-effector system highlighted in green. As seen from the diagram, the control station communicates with the Master LM3S8962 controller over a wireless TCP/IP link. From there, the master controller relays the sent data to the relevant slave arm controllers via RS-485.

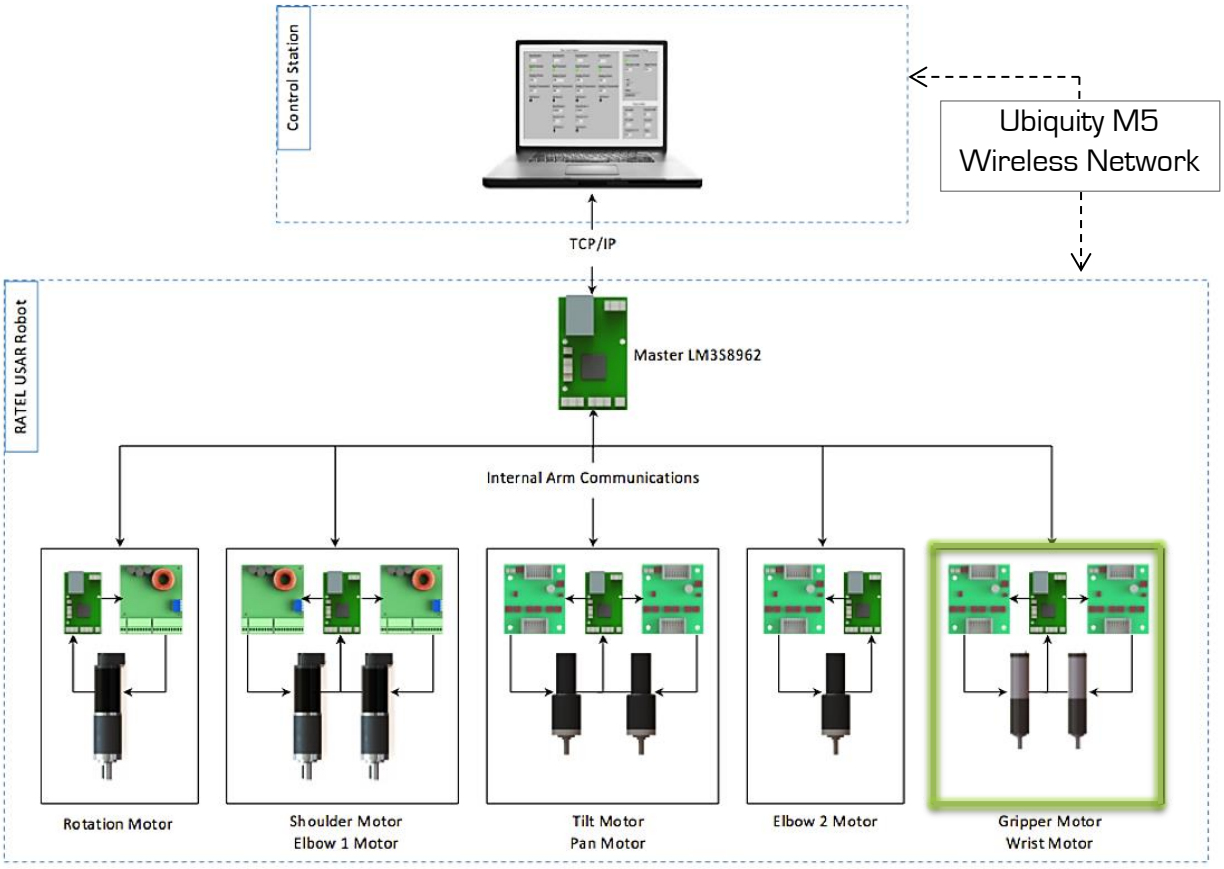

Figure 8-1: Layout of the Communications System in the Manipulator Arm [3]

Originally, **I2C** was specified as the primary communications protocol. As demonstrated by Bradley Springer [3], **I2C** proved to lack the robustness to facilitate communications up the arm due to the low voltage nature of the protocol and respective length of the communications wires.

Hereafter, the RS-232 (point-to-point) protocol was implemented. This protocol proved to be a lot more stable but due to lack of native serial interrupts in the LabView ARM Embedded module, proved challenging to implement in a daisy-chain fashion.

Finally, the RS-485 (point-to-multipoint) protocol was implemented with the Generation IV controllers. As seen in Figure 8-1, a master controller converts TCP/IP data to RS-485 data packets with each board being sequentially addressed. A full write/read operation executed in a continuous rolling fashion provides communications at approximately 13Hz per board.

The following sections will focus on the embedded controller and operator station software solutions that were developed for the end-effector system. For more detailed information on the actual code that was implemented, see the documented LabView files on the attached DVD. For more information on the arm communications refer to Bradley Springer's dissertation [3].

Figure 8-2: Operator Control Station with Lenovo Y570 Laptops and Recessed AOC USB Monitors

8.2 Operator Control Station Software

In user-interactive robotics, the interaction between an end-user and the electro-mechanical system is critical. A good system can be unusable if the user-interface is not effective. In **USAR** robotics this is may be even more essential as the overall system will be used in challenging environments by various personnel and the overall effectiveness of the interface will determine how quickly and easily rescue operations can be performed. A good user-interface should also reduce the training time for a new operator as far as possible.

A good **G**raphical **U**ser **I**nterface (**GUI**) is characterised by how clear, responsive, natural, attractive and efficient the interface is at allowing the user to perform designated tasks. Figure 8-3, below, illustrates the LabView Front Panel of the manipulator control interface with the end-effector elements highlighted in green. This **GUI** was jointly developed with Bradley Springer. The following elements were included in the end-effector interface:

1. Gripper camera feed with lighting controls overlaid on the right side
2. Gripper force sensor and current draw outputs in the form of horizontal bar graphs
3. Gripper and wrist dynamic status images illustrating the current physical orientation of the end-effector
4. Hall Effect and light bridge LED indicators superimposed on the gripper status image
5. Temperature indicators and gripper/wrist calibration buttons
6. Indicator light showing if the communications link has been established

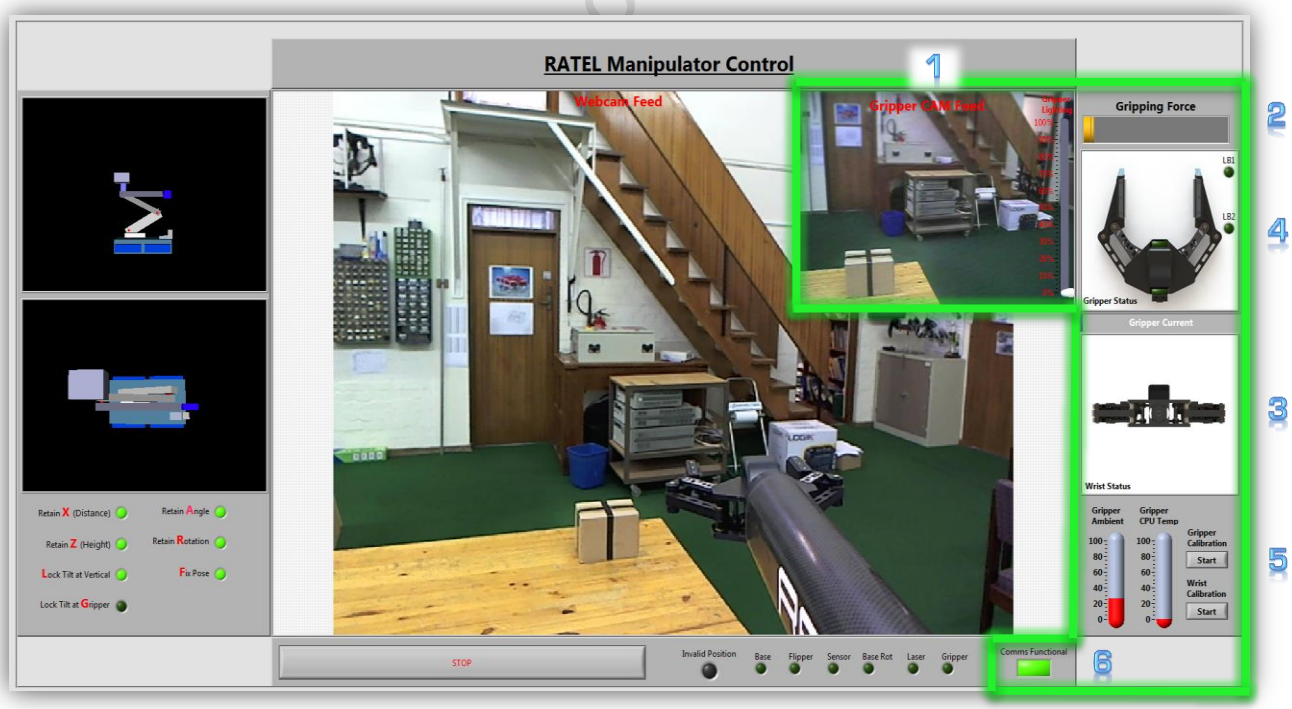

Figure 8-3: Manipulator Arm Control GUI with Relevant End-Effector Section Highlighted in Green [3]

Inputs to the end-effector were provided using keyboard arrows (Up/Down to Open/Close the gripper, Left/Right to rotate the wrist) with lighting being controlled with '**<**' and '**>**'.

The data that was captured from the Front Panel was saved in a global variable and flattened using the function presented in Figure 8-4, below. Due to the nature of the RS-485 protocol developed by Bradley Springer, 20 byte data packets had to be transmitted and received. This required the data to be compressed as much as possible. Similarly to the compression function, a decompression function was utilised on the received data on the end-effector controller.

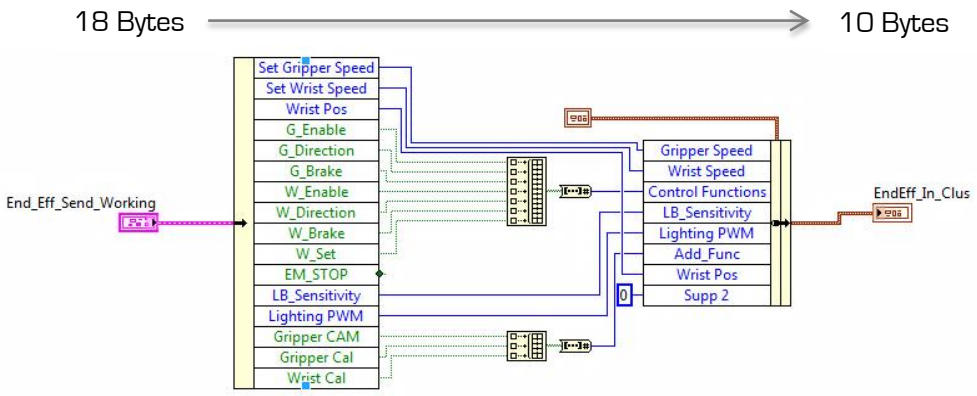

Figure 8-4: PC_Cluster_to_Send.vi Data Compression Function

The following table shows the 20 byte data packet that was to be sent to the master control over the wireless TCP/IP link. The specific board address assigned to the end-effector for the RS-485 protocol was *0xE5E5*.

Table 8-1: 20 Byte Data Packet to be Sent from the Control Station to the Master Controller

Byte Nr	**1 - 2**	**3 - 4**	**5 - 6**	**7**	**8**	**9**
Data	*Board Address*	*Gripper Speed*	*Wrist Speed*	*Wrist Pos*	*Control Functions*	*Light Bridge Sensitivity*
Byte Nr	**10**	**11**	**12**	**13-18**	**19 - 20**	
Data	*Light PWM*	*Add_Func*	*Supp_2*	*Empty*	*CRC-16 Checksum*	

After receiving the data detailed above, the end-effector would respond to the master controller with the following 20 byte packet:

Table 8-2: 20 Byte Data Packet to be Received by the Control Station from the Master Controller

Byte Nr	**1**	**2**	**3**	**4**	**5**	**6 - 7**	**8**
Data	*Sensors*	*FSR1*	*FSR2*	*FSR3*	*FSR4*	*Gripper Current*	*Gripper Pos*
Byte Nr	**9**	**10**	**11**	**12**	**13 - 18**	**19 – 20**	
Data	*Wrist Pos*	*Temp Amb*	*Temp CPU*	*Error*	*Empty*	*CRC-16 Checksum*	

For full detailed descriptions of these variables and their possible values, see the commented code on the attached DVD.

8.3 Embedded Controller Software

The software on the embedded controller is responsible for the control of the end-effector as well as monitoring system functions and communicating with the RS-485 master board.

Figure 8-5 graphically illustrates how the code is generated for deployment on the LM3S8962 processor. In simple terms, a LabView C-Code generator is used to convert the LabView VI to C-Code. The Keil µVision IDE is then used to compile the required files (and libraries) and deploys them to the Keil RTX Real-Time Operating System running on the ARM Cortex-M3 device. The code can then be seen to run as an 'application' on the processor.

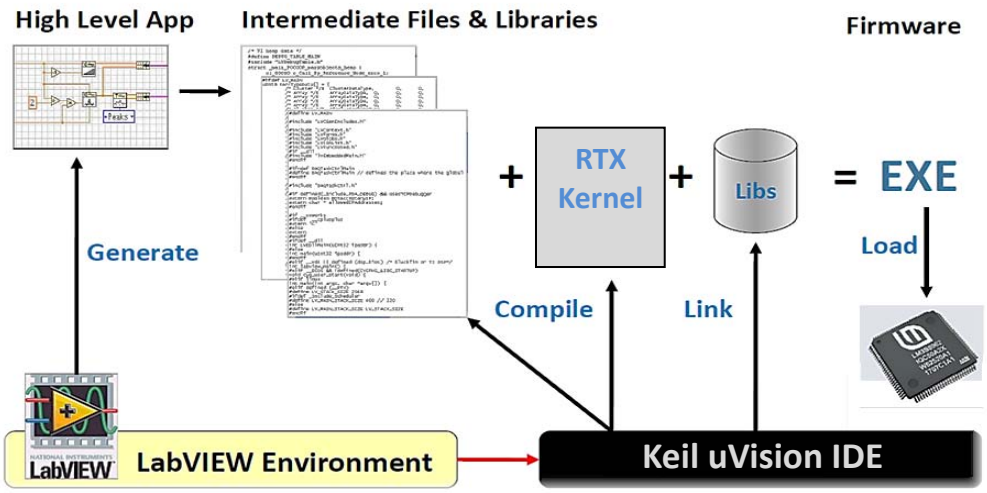

Figure 8-5: Graphical Illustration of the LabView ARM Embedded Development Environment [61]

Due to the potential complexity of the software for the embedded controller, it was decided to utilise the state machine design method to 'modularise' the code. Figure 8-6, below, presents the basis for state machine programming in LabView.

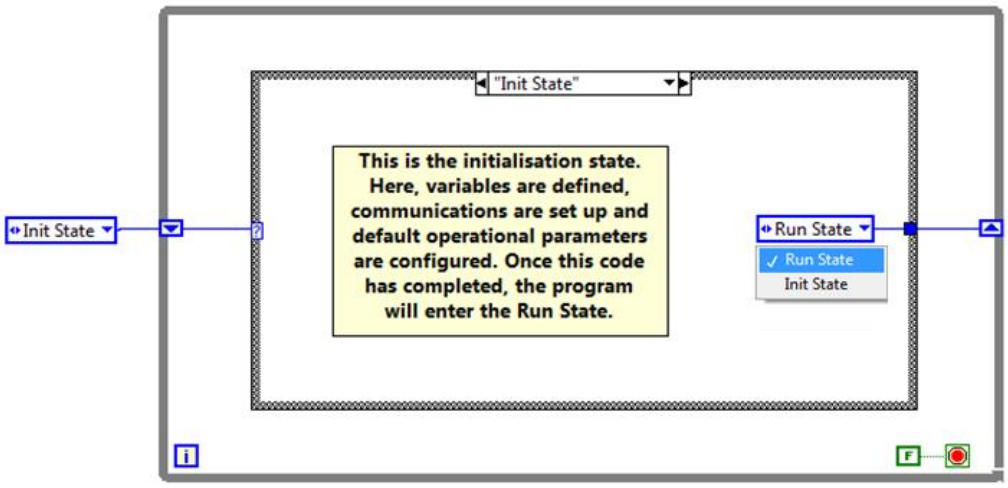

Figure 8-6: A Basic State Machine in LabView as used on the Embedded Controller

The following flow chart illustrates the various possible states of the embedded controller program and briefly outlines their operation. Three interrupts run independently of the main states. Both the **SPI** Communications interrupt and the **CPU** (**C**entral **P**rocessing **U**nit) Temperature interrupt are generated using the timer module of the processor. The RS-485 interrupt is generated by the loopback of the U1RX pin to pin PF0 with interrupt generation on PF0.

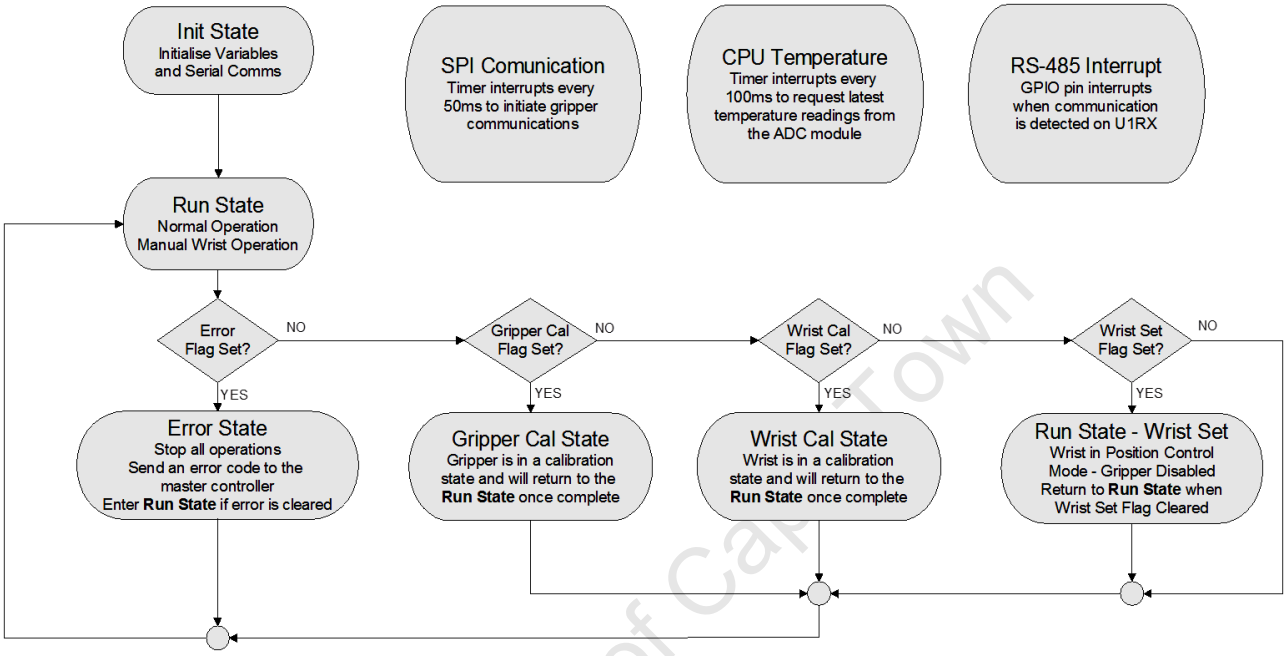

Figure 8-7: Brief Outline of the End-Effector Software with the use of a State Diagram

The following table presents the data packets that were used for **SPI** communications between the primary controller and the gripper controller. The Hall Effect and the Light Bridge Trigger bytes are bitwise representations of the current sensor statuses. The **FSR** sensor readings were sent back as unsigned 16-bit variables to maintain accuracy as the values were recorded using the GT16A ADC in 10-bit mode.

Table 8-3: 3 Byte Data Packet to be Received by Gripper Controller from the Primary Controller

Byte Nr	**1**	**2**	**3**
Data	*Gripper CAM Enable*	*Light Bridge Sensitivity*	*Lighting PWM*

Table 8-4: 11 Byte Data Packet to be Received by Primary Controller from the Gripper Controller

Byte Nr	**1**	**2**	**3**	**4 - 5**	**6 - 7**	**8 - 9**	**10 - 11**
Data	*Ping*	*Hall Effect Triggers*	*Light Bridge Triggers*	*FSR1*	*FSR2*	*FSR3*	*FSR4*

The control of the gripper was implemented by modifying the Enable, Brake and Direction pins based on the inputs provided by the user operating the control station. Originally position control was to be implemented on the gripper, but after substantial use it was found that this type of basic control proved more than capable.

For wrist control, two options were implemented (As seen in Figure 8-7). The first method was the same as that used to control the gripper and was soon found to be acceptable, but rather more difficult to utilise. For this reason proportional position control was also implemented as an additional option.

For more information on the performance of these control methods see the **Testing and Results** chapter.

8.4 Summary

The information provided above was a brief overview of the software and control system implemented on the operator control station and the end-effector system. For more detailed information on the code that was implemented (including previous code revisions) please see the fully commented LabView and C-Code programs on the attached DVD.

Chapter 9. Testing and Results, that follows, details the various tests that were performed on subsystem components to verify compliance with the desired specifications.

Chapter 9. Testing and Results

The specifications that were set in Chapters 3, 5, 6 and 7 defined the required features and functionality that were envisaged for the end-effector system. By testing the actual performance of the various modules in a structured environment, these specifications can be verified and the operational capability of the system can be ascertained. Once these factors are known, operating procedures and guidelines can be established for individual subsystems and the system as a whole.

The following chapter will present a summarised version of the testing procedures and relevant findings of the tests that were conducted. The full detailed testing section can be found on the accompanying DVD and includes expanded test methods, descriptions of the equipment used, full test results and detailed conclusions.

9.1 Overall System Testing

The following tests involved investigations that would affect the overall performance of the end-effector system and validate how well the various subsystems could operate together.

9.1.1 Mass Measurement Tests

9.1.1.1 Testing Overview

One of the primary specifications for the end-effector was related to its weight. The aim of this test was to determine individual component masses, subsystem masses and the largest mass contributors. This test was significant as the end-user performance could rely heavily on the mass of the end-effector and future designs could be optimised based on the test results.

9.1.1.2 Testing Procedure

The tests that were conducted focussed on three specific mass areas:

1. Individual Component Masses
2. Subsystem Masses
3. Overall System Mass

The first step in conducting the test was to set up a Mettler PM30-K scale on a flat and even surface. Parts and subsystems were placed on the scale and the masses were recorded. The SolidWorks mass analysis feature, which proved to have high accuracy, was also used on some parts that were already assembled and that could not be weighed. The final test involved establishing overall system mass. From the recorded readings, Pie charts were created to graphically illustrate the highest mass contributors for each subsystem as well as the overall system.

9.1.1.3 Test Results

Figure 9-1 shows the mass breakdown of the gripper subsystem. As can be seen from the chart, the greatest mass contributors were the *Force Transmission Levers* at 23% and the *Gripper Fingers* at 16%. The various pins holding together the linkages made up about 10% of the total with each subsequent component group contributing 5% - 9%.

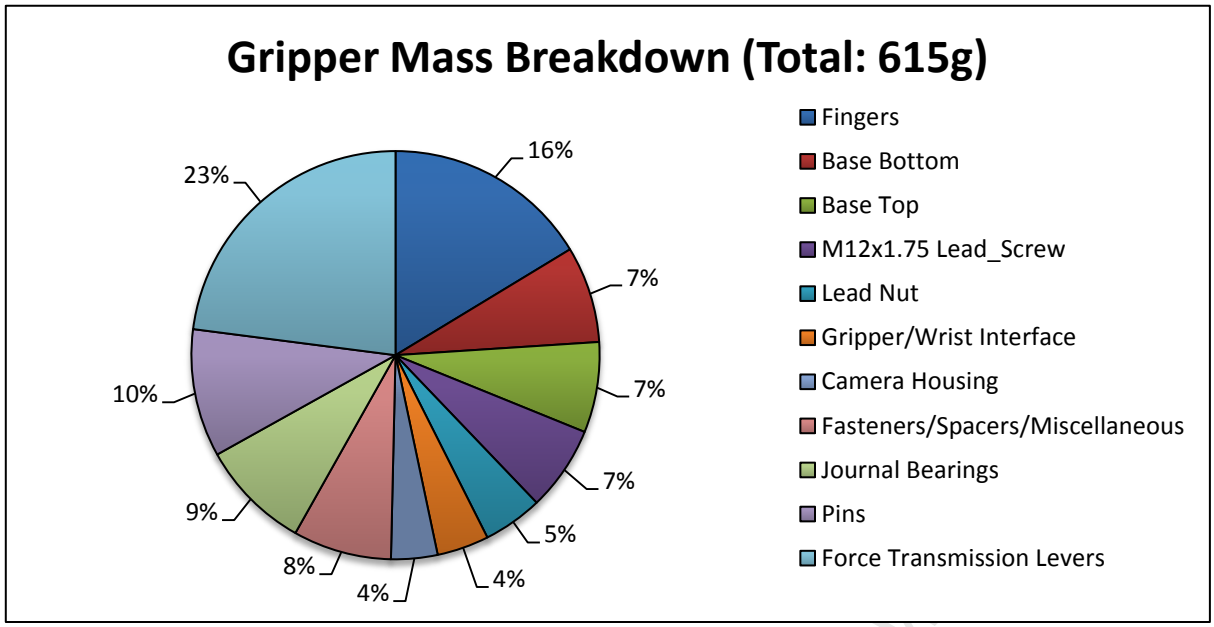

Figure 9-1: Gripper Primary Mass Contributors

The wrist mass breakdown is shown in the figure below. Of the 317g total, the *Gripper Motor Holder* was the largest mass contributor at 21%, followed by the *Gears* at 17% and the various *Bearings* at 15%.

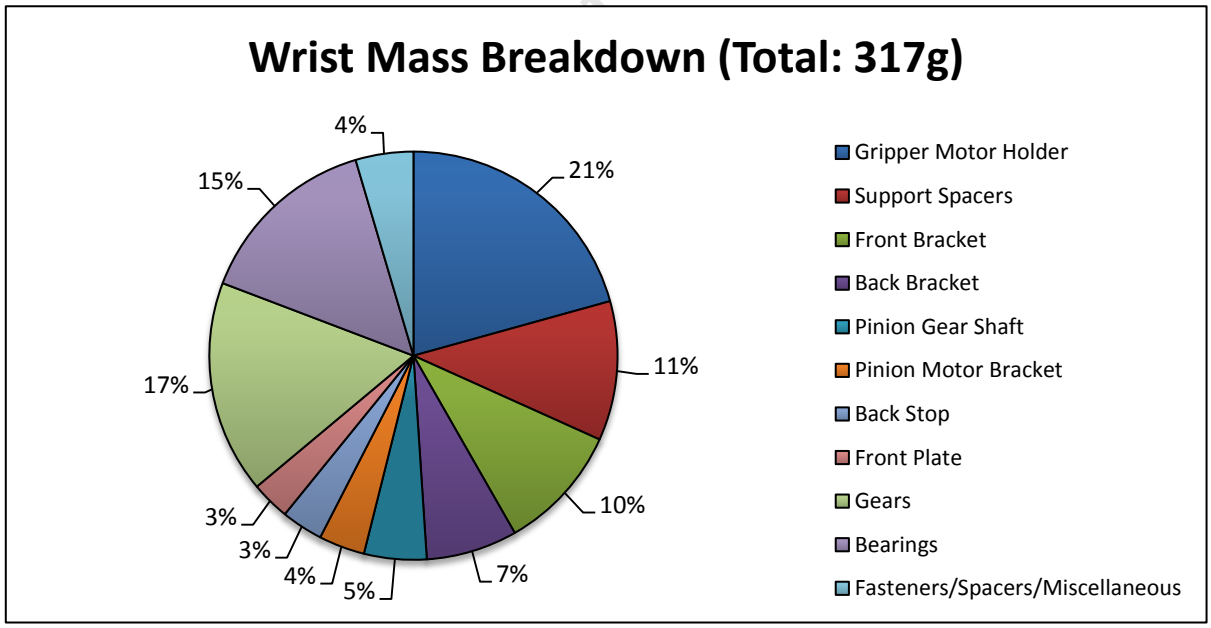

Figure 9-2: Wrist Primary Mass Contributors

A mass breakdown was not performed for the electronics module due to the large variety of components that were involved, including wires, connectors and sensors. The final mass was determined to be approximately 200g, including two Maxon DEC 24/3 speed controllers, an LM3S8962 embedded controller, one dual current sensor board, a 30-way slip-ring as well as temperature and Hall Effect sensors.

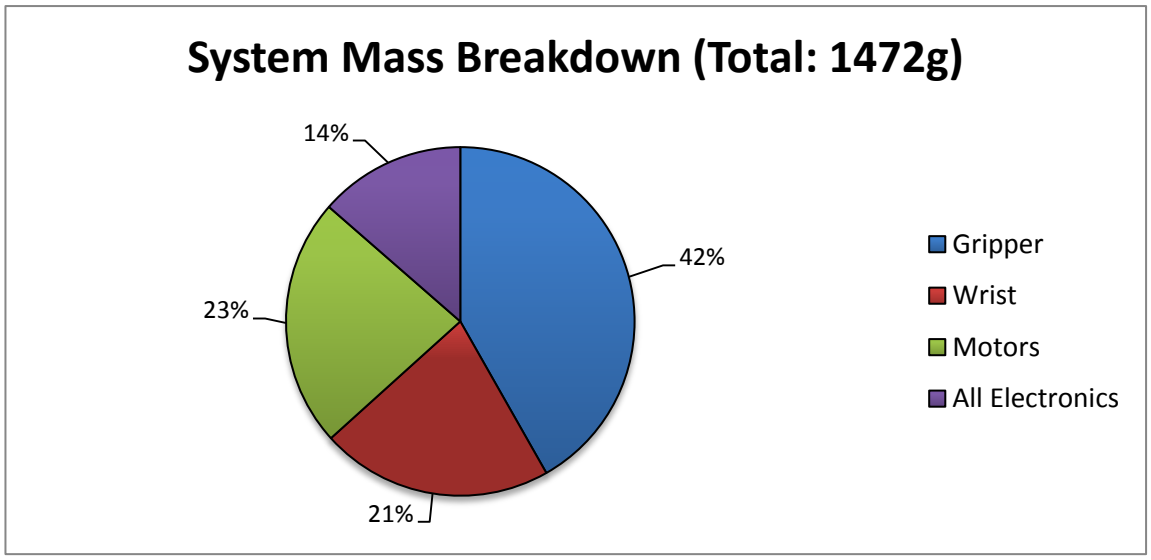

Figure 9-3: Overall End-Effector Subsystem Mass Contributors

The total mass of the end-effector was determined to be 1472g. As was expected, the gripper module was the largest mass contributor at 615g, followed by the two Maxon motors at 23% and the wrist section at 21%. Surprisingly, the electronics subsystem also made a significant contribution at 14%.

The original target mass set by Peter Henson was 800g for the gripper and the wrist sections excluding the motors and electronics systems. Together, the final mass for these two systems was 932g, 17% more than was originally specified. Significant weight reductions were implemented throughout the mechanical design of the system, but further reductions may be possible with a more aggressive strength-to-weight analysis. With lower power motors, the total weight could also be reduced further.

9.1.2 Overall System Power Consumption Test

9.1.2.1 Test Overview

The rescue **MRP** is powered off six Makita 18V 3Ah batteries. Therefore, the power consumption of every subsystem is important to the overall efficiency of the system. The following tests involved isolating each subsystem and measuring the current drawn at certain voltages. Figure 9-4 illustrates the test setup.

Figure 9-4: Power Measurement Test Setup [62] [63]

9.1.2.2 Test Procedure

The tests were performed by isolating every subsystem in turn and measuring the current on the 18V line. These systems included the gripper and wrist motor controllers, the LM3S8962 embedded controller, the dual current sensor and the gripper integrated controller.

9.1.2.3 Test Results

In an idle state, the tests indicated that the end-effector drew approximately 3.5W, peaking at 5.3W with the gripper camera and lighting activated. The individual power consumers at this 5.3W state are shown below. From the chart it may be concluded that the LM3S8962 embedded controller was the largest power consumer at 29% with the gripper camera next at 23%. The LED lighting and integrated gripper controller each made up 12% of the total usage

The power consumption of the entire system under full load could not be simulated due to the complexity of simultaneously loading the gripper and wrist modules, but the peak power draw was estimated to be approximately 85W including both Maxon 40W motors. Although additional power savings could have been implemented by switching all electronic systems off, this would only save 3.5W and could have a significant negative impact on the stability of the RS485 communication chain.

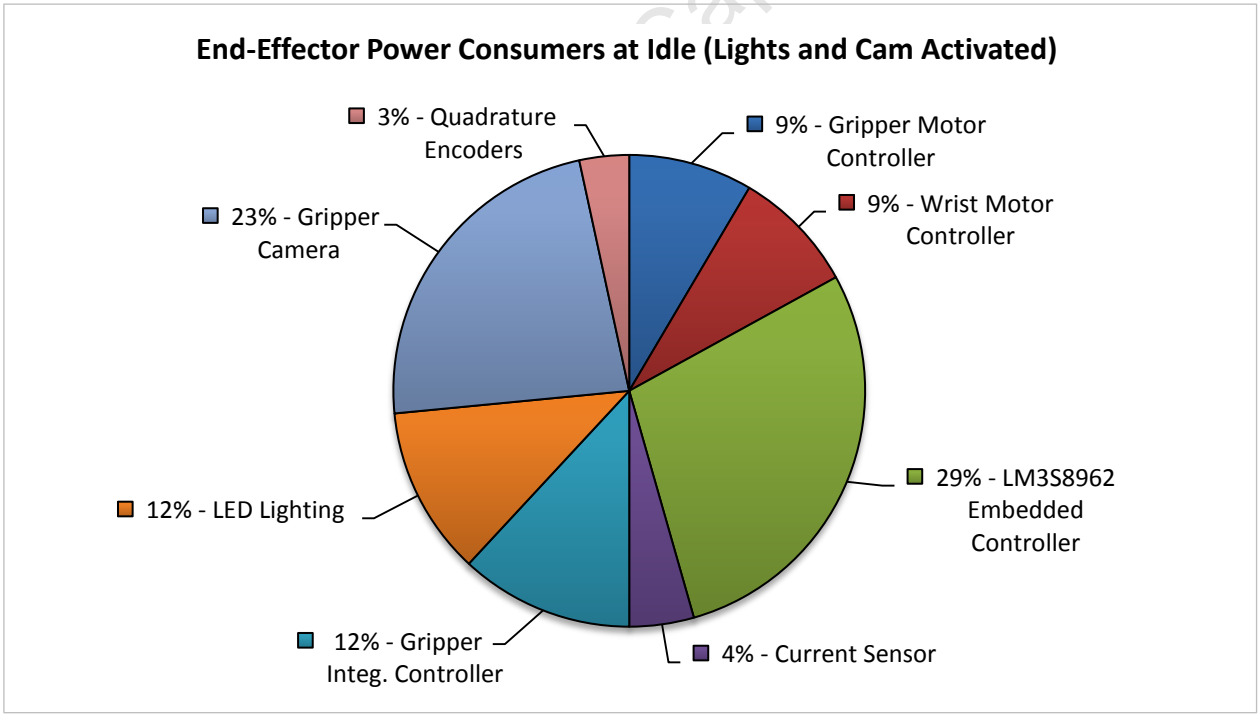

Figure 9-5: Individual Power Consumers

9.1.3 System Usability Testing

9.1.3.1 Test Overview

The usability and intuitiveness of an electro-mechanical system is of vital importance to a remote operator, both in terms of optimising movements and making the system simple to operate. In order to test for these criteria, nine people were selected to each perform the task of gripping a bottle and placing it on a specified target. It should be noted that the test candidates had no prior experience in operating the manipulator arm.

After fulfilling the task, a candidate would then be asked to fill out a short questionnaire. These tests were performed in collaboration with Bradley Springer, who was working on the inverse kinematic control of the manipulator arm.

9.1.3.2 Test Procedure

After initial power-up and calibration of the arm and end-effector systems, the manipulator was set to its home position. The user was then informed about the basic functionality of the manipulator arm and the features of the GUI.

Two assisted runs were performed where the operator had to relocate a bottle from one position to another. A final unassisted run was performed for each user after which a short questionnaire was given out for feedback on the operator's experience. This final test run was timed and the precision of the placement measured with a ruler.

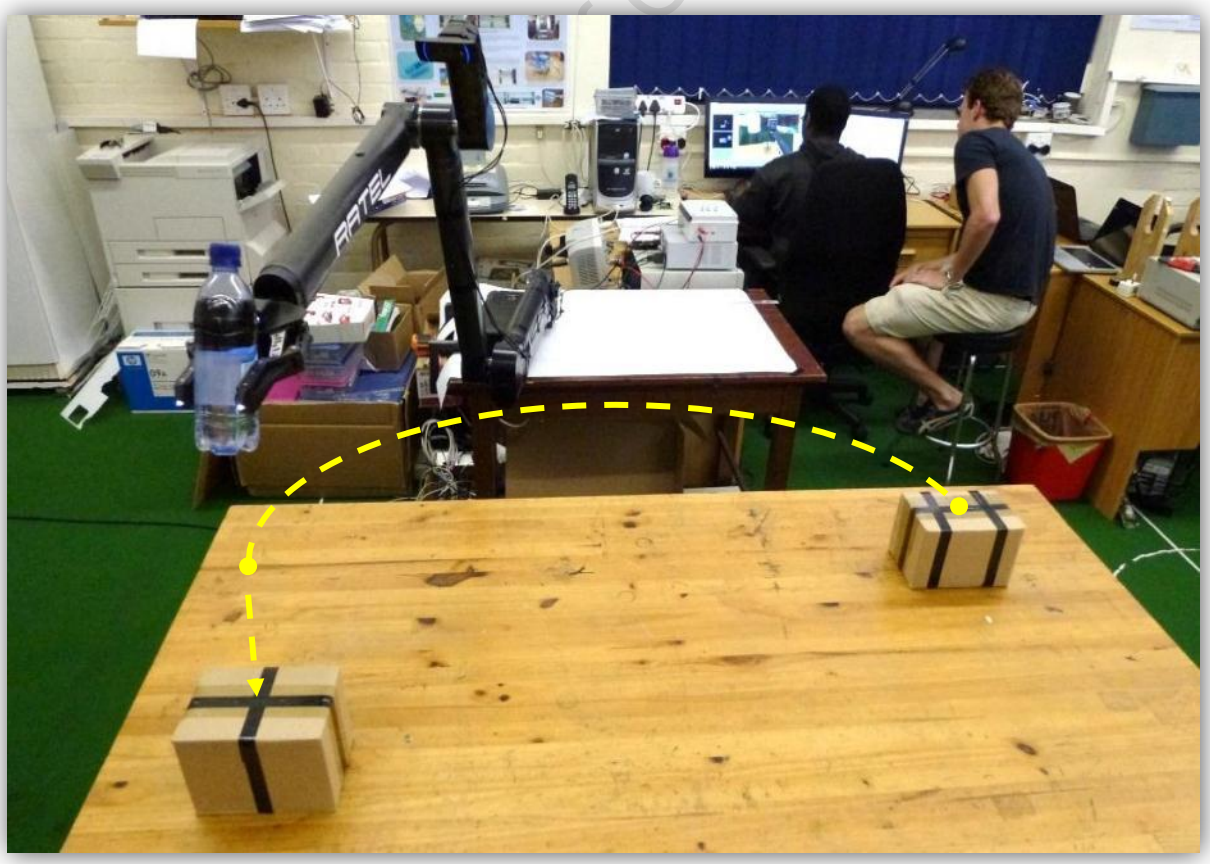

Figure 9-6: An Inexperienced User on a Test Run

9.1.3.3 Test Results

Figure 9-7 illustrates the average responses for each relevant sub-function of the end-effector system and GUI.

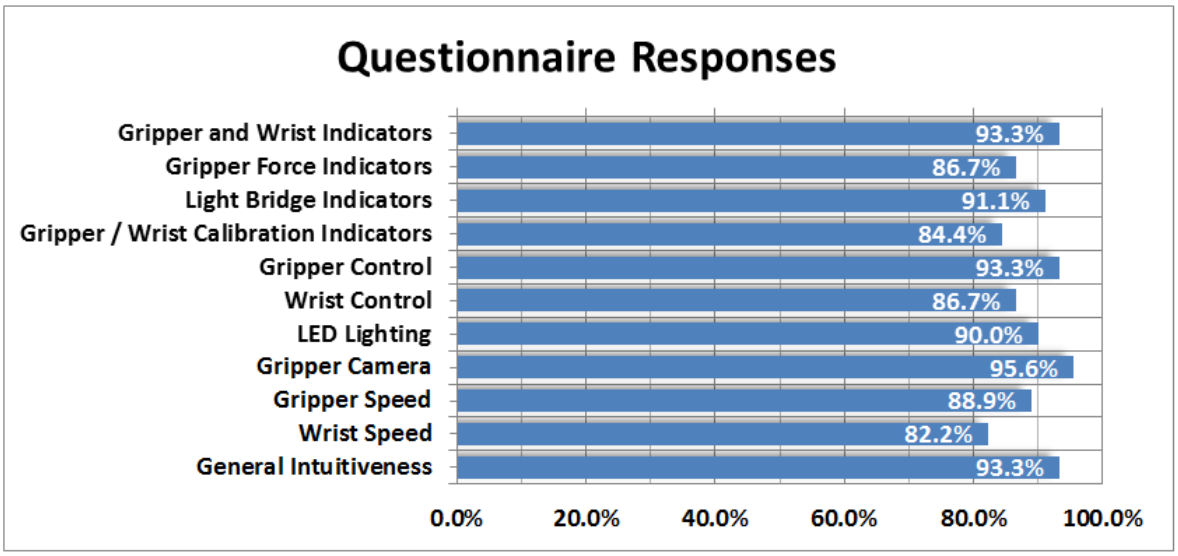

Figure 9-7: Summary of the Responses of the Usability Testing

As explained above, the time to complete the final task and the placement accuracy was recorded for each user. The following graph presents these results.

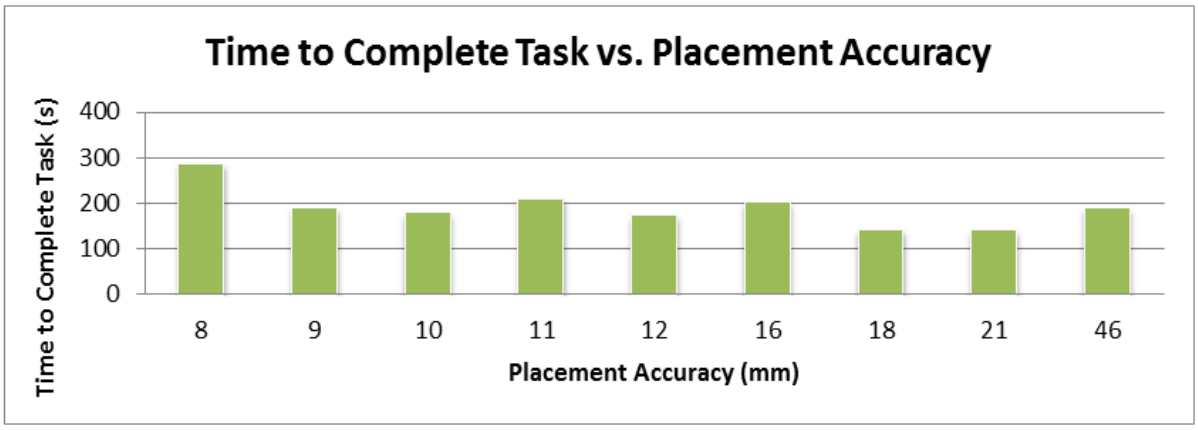

Figure 9-8: Time to Complete Task vs. Placement Accuracy

A user required an average of 3 minutes to complete the final task with an average accuracy of 15mm. For an inexperienced user this was remarkably good and these figures may certainly be improved upon with additional practice and training.

Although definitive conclusions may not be drawn from data above due to the relatively small sampling size (nine users), it would appear that users were satisfied with the intuitiveness and functionality of the GUI providing overall positive feedback and comments.

For a full list of comments by users, see the Detailed Testing Appendix on the accompanying DVD.

9.1.4 Dual Current Sensor Board

9.1.4.1 Test Overview

The ability to sense the current draw of various systems within the robot (not just the end-effector) was an important factor during the design of the **MRP** as it could directly relate to the force or torque being exerted by the system being measured. The current sensors that were developed were available in 5A and 20A configurations. The 5A version was to be used on low-current (e.g. end-effector) systems, whereas the 20A versions would be used on general robot systems such as the drive motors, flipper motors etc.

9.1.4.2 Test Procedure

5A Current Sensor Board: This version of the current sensor was configured using an Allegro ACS712 5A chip with a differential amplifier referenced to 2.5V and a gain of 5.6. The end-effector was fitted with this sensor configuration.

20A Current Sensor Board: This version of the current sensor was configured using an Allegro ACS712 20A chip with a differential amplifier referenced to ground and a gain of 0.67. General MRP and manipulator arm systems were fitted with this configuration.

The tests were conducted by shorting a Manson power supply through one of the modules on the current sensor board. The built-in current limit of the power supply was used to restrict the amount of current to the board but was not used to actually measure this current. This was done using an Agilent multi-meter in series with the sensor. The output voltage was recorded for each current reading using an Agilent DSO1002A oscilloscope. For the 20A sensor, the current range was limited to+-15A by the power supply. The 5A sensor was tested along its full current range of +-5A.

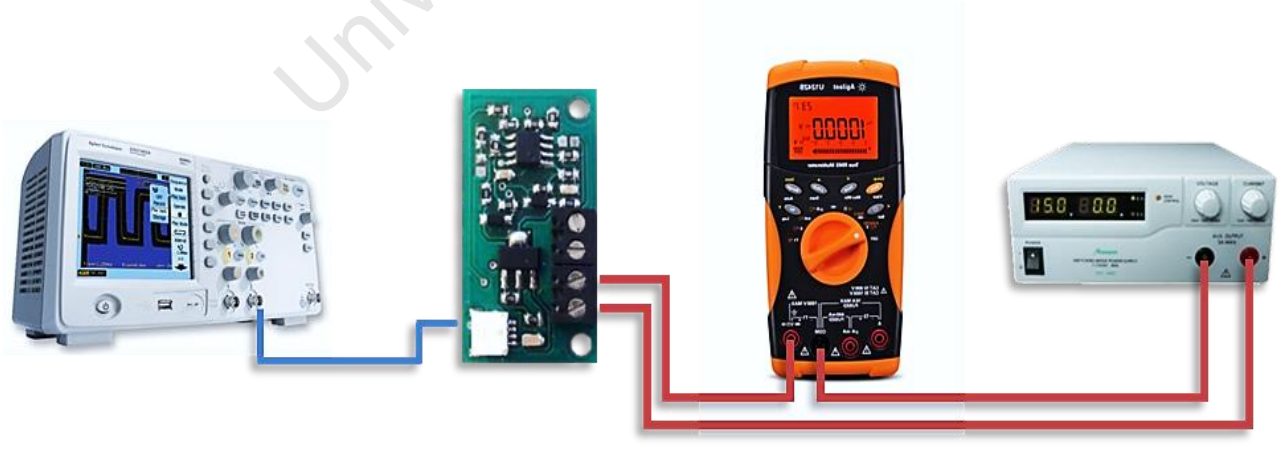

Figure 9-9: Current Sensor Test Setup and Connections [63] [62] [64]

9.1.4.2 Test Results

The graph below shows a plot of the 5A current sensor board with a 2.5V reference on the inverting input of the differential amplifier. The gain and voltage reference were selected to give an improved output resolution in the range 0 - 3A to aid in the force derivation from the motor current draw.

As can be seen in the plot below, negative currents up to -5A gave an output of 0V as expected. On the positive current side, the linear relationship of voltage vs. current is visible up to approximately 2.7A. After this, the installed Schottky protection diode starts to conduct (protection for the µP ADC) and the voltage linearly tapers off.

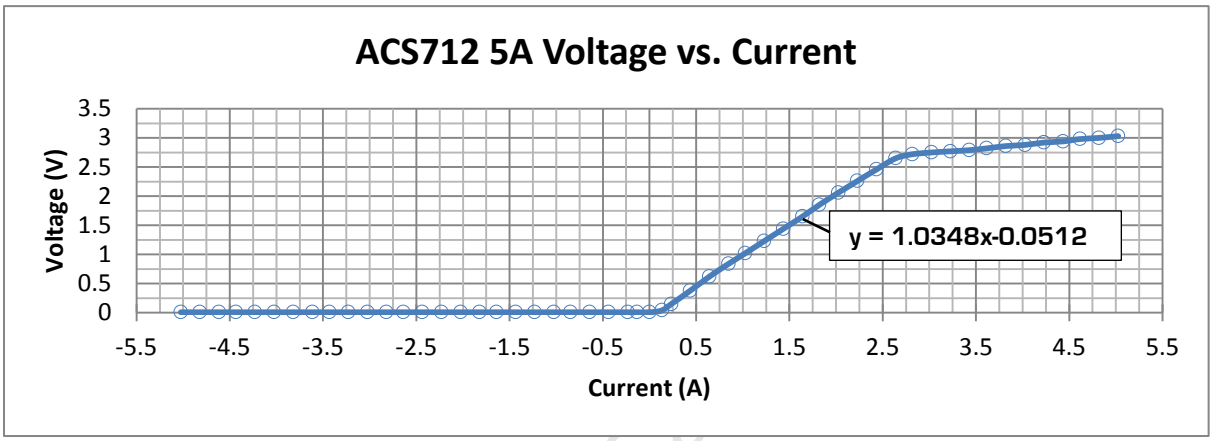

Figure 9-10: Graph Showing Output Voltage of 5A Current Sensor vs. Measured Current

The second current sensor that was tested was configured for 20A operation with a ground reference inverting input of the differential amplifier. As can be seen from the plot below, a linear relationship is clearly visible when operating within a +-15A range.

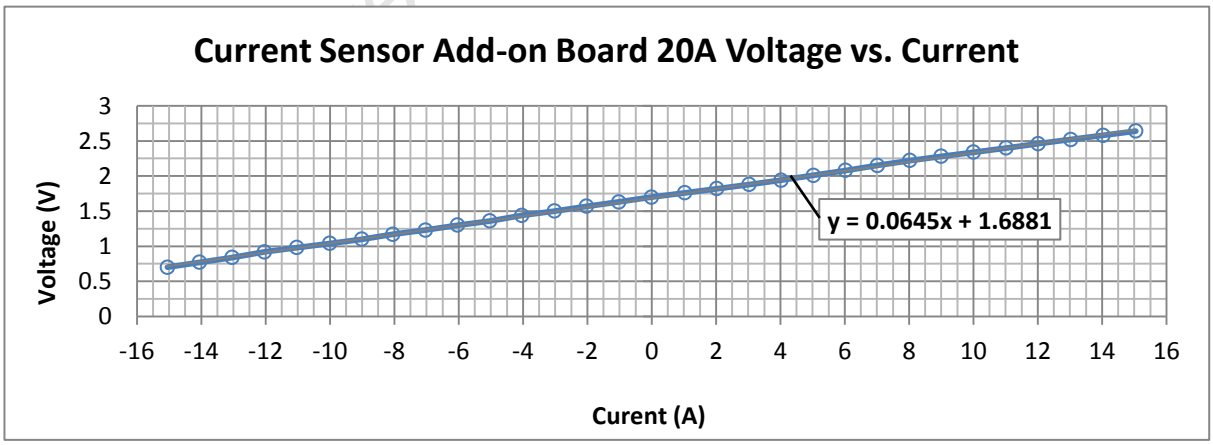

Figure 9-11: Graph Showing Output Voltage of 20A Current Sensor vs. Measured Current

In summary, the derived equations for the two sensor configurations were established as:

$$\boldsymbol{5A\ Current\ Sensor\ Output\ (V) = 1.0348 * Current\ (A) - 0.0512}$$
$$\boldsymbol{20A\ Current\ Sensor\ Output\ (V) = 0.0645 * Current\ (A) + 1.6881}$$

Based on the 10-bit resolution of the LM3S8962 ADC, this would result in a 3mA resolution/bit for the 5A sensor (with 0V equal to 0A) and a 46mA resolution/bit for the 20A version (with 1.5V equal to 0A).

9.1.5 Temperature Monitoring During Operation

9.1.5.1 Test Overview

In rescue robot operations, temperatures may often be extreme and the ability for the overall system to continue operating in harsh environments is vital. For the end-effector system two temperature sensors were available for monitoring, an LM35 to monitor the ambient temperature in the arm section and the internal sensor of the LM3S8962 to monitor the processor.

9.1.5.2 Test Procedure

As the temperatures were acquired through the ADC of the LM3S8962, conversions needed to be performed as per the required datasheets [65] [66]. Two sets of tests were conducted, each monitoring a different temperature sensor. The ambient actuator temperature test was run over approximately 18 minutes and the LM3S8962 over 30 minutes. The tests were performed by running the systems under loaded operating conditions and automatically logging temperature readings at 1s intervals. The ambient temperature for the tests was 24°C.

9.1.5.3 Test Results

As seen in the plots below, the actuator temperature increased to a maximum of 32°C with the processor reaching a peak of 65°C. During subsequent outdoor tests in direct sunlight, these values increased dramatically to 45°C and 75°C respectively.

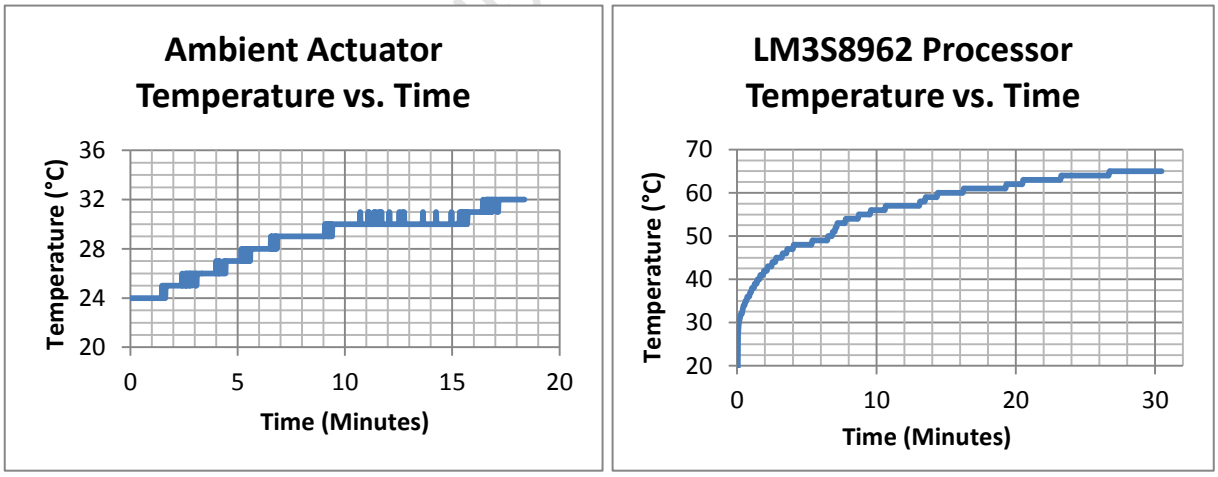

Figure 9-12: Graphs Showing Temperature Increases over Time

Both of the tests showed that the maximum temperatures were still well within the operating ranges of the system components (Maxon EC22s: -20°C -> 100°C, LM3S8962: -40°C to 85°C) although the processor temperature rise did not leave much headroom. A heat-sink may need to be installed in the future to lower this temperature to more acceptable levels.

9.2 Gripper System Testing

9.2.1 Gripper Open/Close Times

9.2.1.1 Test Overview

One of the specifications of the gripper subsystem was a minimum open/close time of 5s. This was an important performance characteristic to test as it directly influences the usability of the end-effector system.

9.2.1.2 Test Procedure

LabView test code was created to measure the time to open and close the gripper using the Hall Effect limit switch. This was done at incrementally increased speed settings. The results of every open and close run were plotted on chart to graphically illustrate the responsiveness of the gripper at these speeds.

9.2.1.3 Test Results

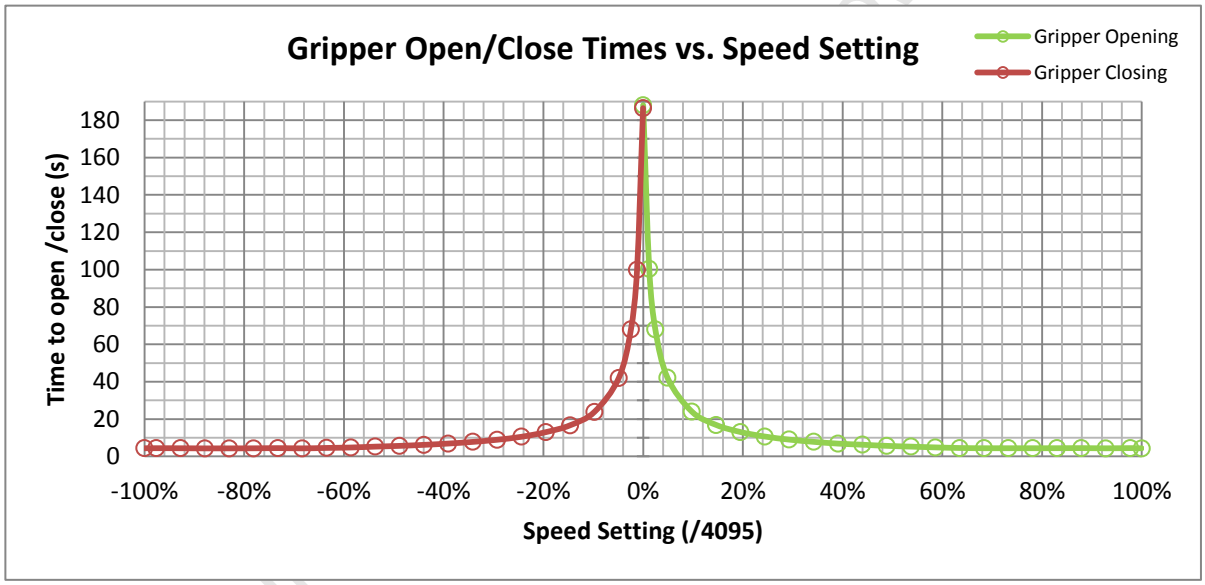

Figure 9-13: Plot Showing Open/Close Times Versus Speed Settings

At the slower speed settings the open and close times were established to be approximately 185s. At the maximum operating speed the times were about 4.4s. It should be noted that the optimal opening and closing speeds where reached at about 65% speed setting. The results that were attained were well within the boundaries of the specification that was set and should provide an operator with a responsive and intuitive system.

9.2.2 Gripper Backlash Test

9.2.2.1 Test Overview

Backlash is an undesirable physical characteristic of a system and should be minimised as far as possible. The parallel arrangement of the gripper fingers reduced the amount of backlash compared with other types of grippers, but could not be eliminated entirely. The following test was conducted to establish the amount of backlash at various gripper positions and to determine if some type of relationship could be identified.

9.2.2.2 Test Procedure

The tests were conducted by setting the gripper to various standard positions and measuring the backlash at these points using a Vernier calliper. The backlash was measured by manually extending and contracting the gripping fingers by hand and measuring the maximum and minimum parallel distances between the gripper fingers.

9.2.2.3 Test Results

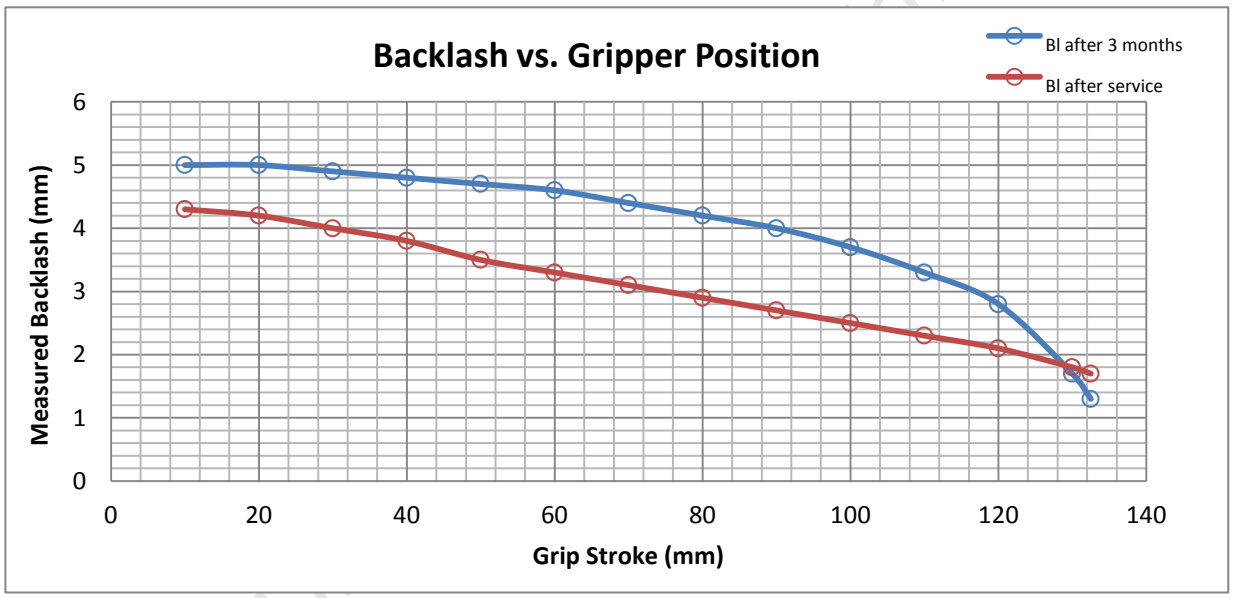

Figure 9-14: Gripper Backlash at Various Grip Strokes

The maximum backlash for the first test (3 months run-in) was approximately 5mm, whereas the maximum after a short system overhaul was approximately 4mm. These values occurred at the minimum grip stroke. As the grip stroke increased the backlash decreased (as could be expected), indicating that there was a significant relationship between the grip stroke and the backlash of the system. The maximum backlash of the system was significantly higher than expected and should be reduced further where possible by identifying high backlash components and either modifying or replacing them.

9.2.3 Gripper Prehension Test

9.2.3.1 Test Overview

Gripper operations in rescue scenarios may be wide ranging with various objects being gripped. During such operations, a user may find it useful to know the prehension force that is being exerted on an object by the gripper. For example, a glass bottle would be handled with a lot more care than a plastic bottle. The following tests will quantify the actual force being exerted on a gripped object by monitoring the current and force sensing resistor readings of the gripper. Conclusions on whether the gripping force can be accurately deduced will be drawn based on the results of these tests.

9.2.3.2 Test Procedure

The setup for the test is shown in Figure 9-15, below, and consisted of two parallel plates separated by compression springs mounted in the gripper. Two linear potentiometers, located on either side of the plates, were used to verify the distance between the plates during testing. The distance was calculated using the quadrature encoder position of the motor derived in Chapter 5. By knowing the distance between the plates and the equivalent spring constant (See below), the actual prehension force could be determined.

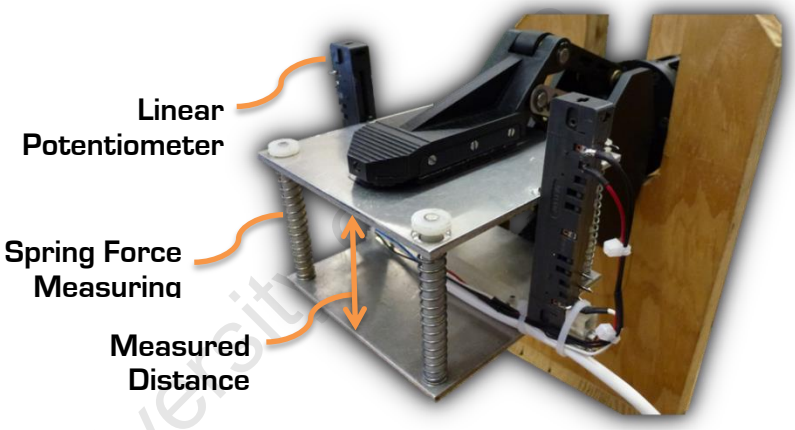

Figure 9-15: Prehension Force Test Apparatus with Linear Potentiometers Installed

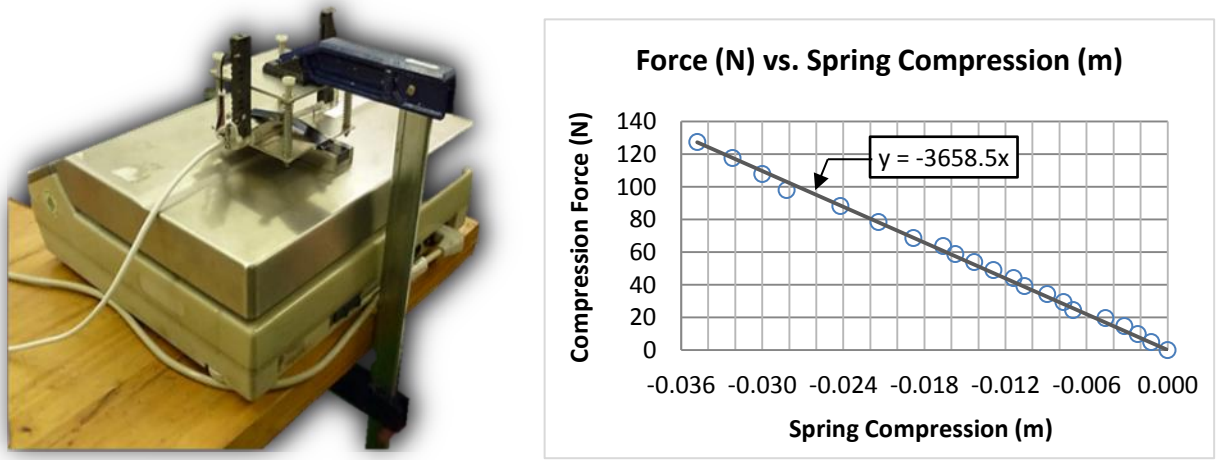

Figure 9-16: Test to Ascertain the Equivalent Spring Constant for the Device

Figure 9-16 shows the spring compression device on a Mettler PM30-K scale being compressed by a large G-clamp. The graph on the right illustrates the compression force (i.e. weight indicated on the scale) plotted against the compression distance measured with a Vernier Calliper. The equivalent spring constant could then be read off the graph (gradient) and was determined as $3658.5 N/m$.

The tests were run by compressing the spring device at incrementally higher speeds and recording the gripper motor current and the FSR sensor readings. This data was graphed and analysed in order to determine if the current or the FSR sensors could be used to accurately predict the gripper prehension force.

9.2.3.3 Test Results

The following graphs present the data that was captured for the various speed settings.

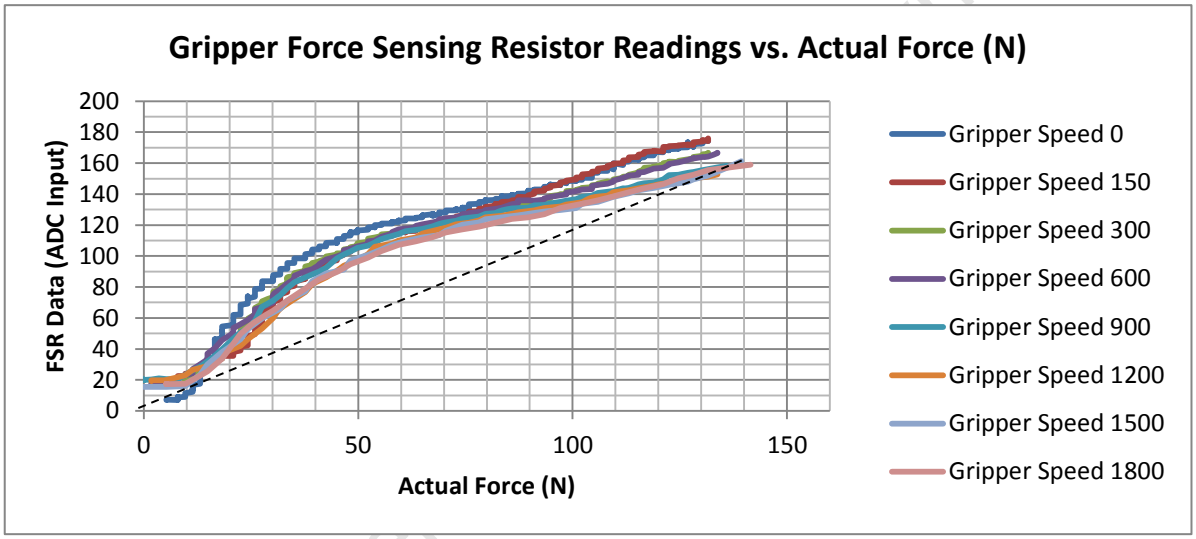

Figure 9-17: Graph Showing the Gripper FSR Readings vs. Actual Force (N)

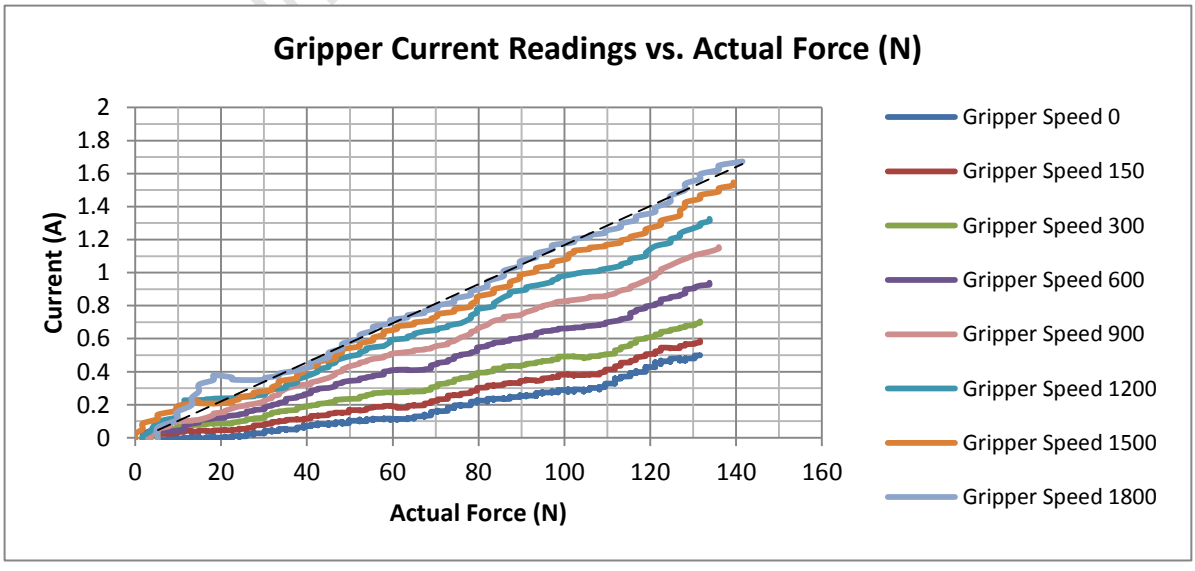

Figure 9-18: Graph Showing the Gripper Current vs. Actual Force (N)

Figure 9-17 presents the FSR data that was collected over the various test runs. As can be seen from the graph, the relationship appears non-linear, but fairly consistent between the various test runs. The superimposed trend-line indicates the plot that may have been expected from such a sensor. Potentially a lookup table could be used, in combination with the gripper speed setting, to deduce the actual force from the FSR reading.

Figure 9-18 shows a plot of the current readings and the respective forces for various speeds. The graph suggests that a linear realtionship may exist between the force and the current for the specific speeds being tested. It may be possible that this is only the somewhat linear region of the sinusoidal relationship between the gripper force and the lead screw travel that was deduced in Chapter 5. Nonetheless, it was assumed to be linear for this region.

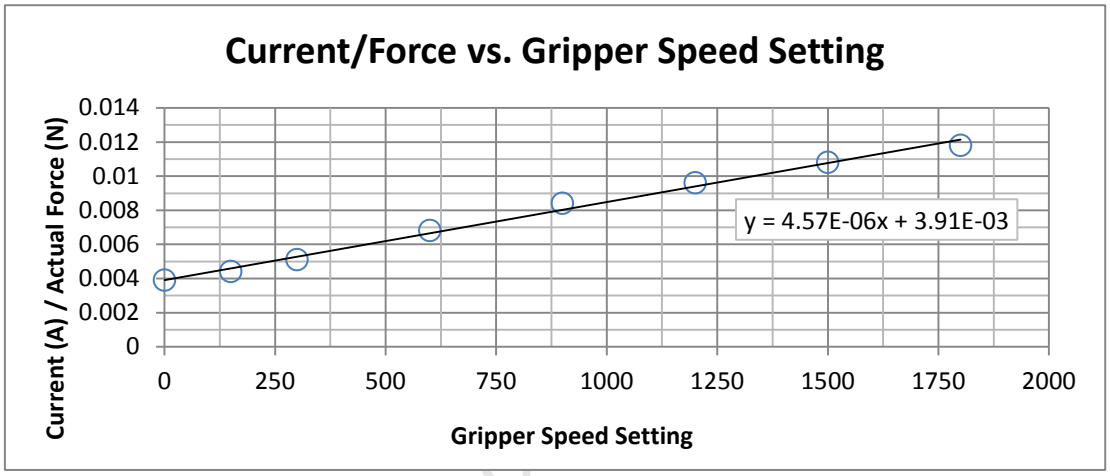

Figure 9-19: Graph Showing the Current/Force Relationship Dependant on Gripper Speed

The figure above provides a potential method of deducing the actual force using the gripper speed and the instantaneous current draw. The following formula was established from the plot:

$$Force(N) = \frac{Current(A)}{4.57 * 10^{-6} * Speed\ (/4095) + 3.91 * 10^{-3}}$$

Based on the data of the various tests, the following conclusions were drawn.

Using the equation established above, the current may prove to be a useful method to determine the force currently being exerted on an object. However, the tests were all performed using the spring force device and further testing may need to be performed using a variety of objects at different grip strokes to verify this equation.

The recorded FSR readings appeared to indicate a non-linear relationship between the measured force and the sensors. However, the relationship appeared to remain the same under various speed settings. By setting up a lookup table or estimating a function based on the data that was recorded, a rough reading for the force may certainly be established.

In summary, utilising a combination of current sensing and FSR sensors should provide a good estimate of the actual force being exerted on an object.

9.2.4 Tactile Sensor Array Object Identification Test

9.2.4.1 Test Overview

As mentioned in the prehension force tests conducted previously, it could be of great advantage to an operator to know the force with which an object is being handled. However, of even more benefit would be to not only know the force, but the actual pressure distribution across the face of the gripped area. This could provide information on the actual geometry of an object being manipulated as well as if an object is moving (or slipping) in the gripper. The following test will demonstrate the outputs of two Weiss Robotics 9205i 84 cell tactile sensing arrays gripping a variety of objects.

9.2.4.2 Test Procedure

The objective of these tests was to verify if any type of geometry identification could be performed using the Weiss Robotics 9205i tactile sensor arrays. For this test, the sensors were not interfaced with the gripper embedded controller directly (as described in the **Gripper Subsystem** chapter), but were rather powered by an isolated custom etched driver board. This method was used due to time constraints of interfacing the sensors with the rest of the end-effector systems and particularly due to the intricacies of programming the extended communications protocol for RS485 communication with the manipulator arm.

The tests were conducted by gripping a variety of objects (Figure 9-20) and recording the tactile sensor profile for each item. The prehension force was increased over three stages to illustrate pressure distributions during soft, medium and hard grips on both sensor pads. Based on the acquired images, conclusions were then drawn as to whether object geometries could potentially be identified and if the sensors could aid an operator during manipulation operations. Some videos of the gripper operations have been included on the accompanying DVD.

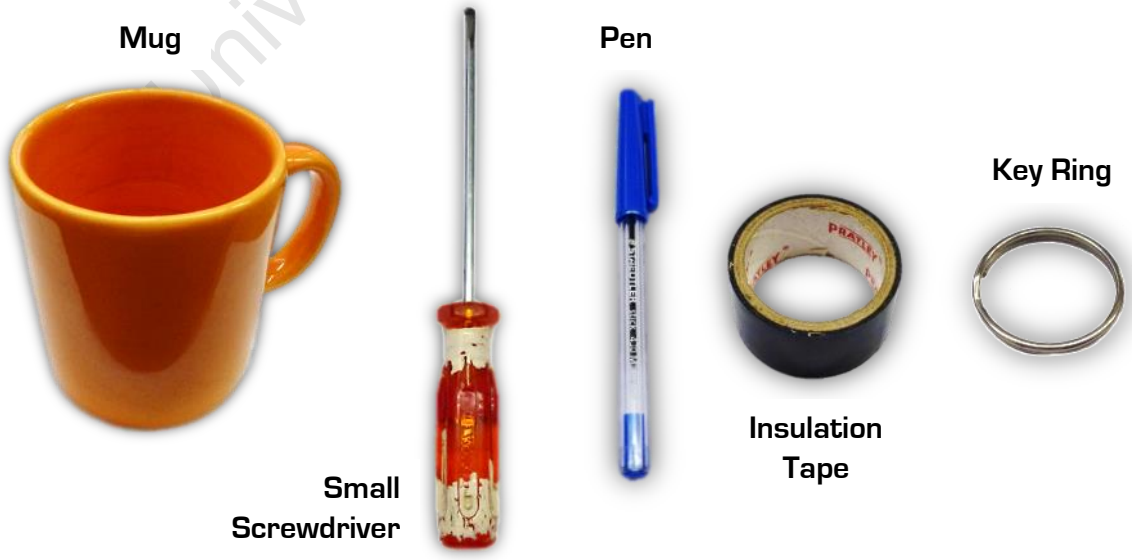

Figure 9-20: Various Items for Testing Object Verification with the Tactile Sensor Arrays

9.2.4.3 Test Results

The first item that was selected for testing was a standard coffee mug. The objective was to determine if some type of curved distribution would present itself, as would be expected when gripping such an object. As seen in Figure 9-21, over the three frames a definite arc shape became visible, particularly as the pressure increased towards the right.

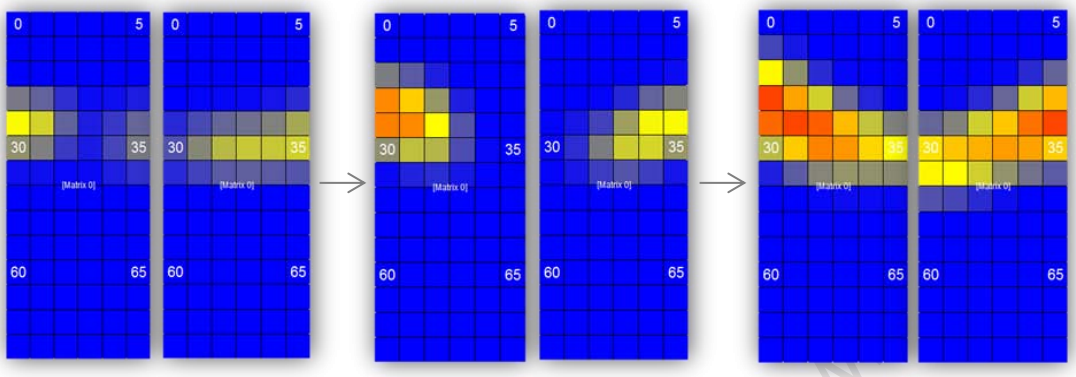

Figure 9-21: Tactile Sensor Pressure Distribution When Gripping a Mug Handle

Figure 9-22 and Figure 9-23 present the pressure distributions for a small screwdriver (approximately 17mm in diameter) and a vertical pen respectively. For both items the first frames did not provide much information relating to the geometry of the objects, but as the pressure increased, longitudinal force distributions became apparent.

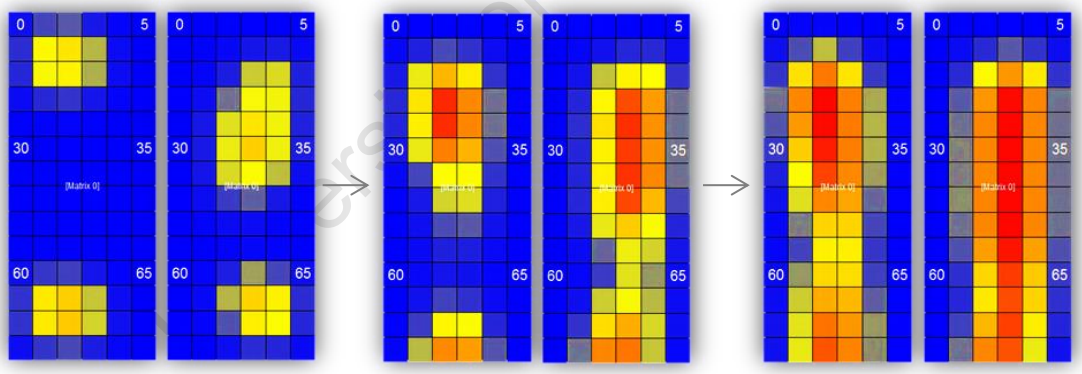

Figure 9-22: Tactile Sensor Pressure Distribution When Gripping a Screwdriver Lengthwise

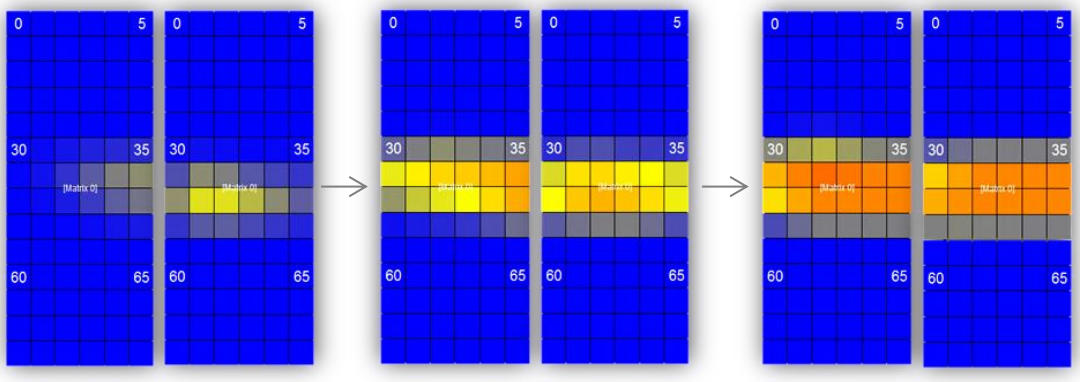

Figure 9-23: Tactile Sensor Pressure Distribution When Gripping a Vertical Pen

To test if the sensor pads could identify objects with circular geometries, a roll of insulation tape (Figure 9-24) and a key ring (Figure 9-25) were tested.

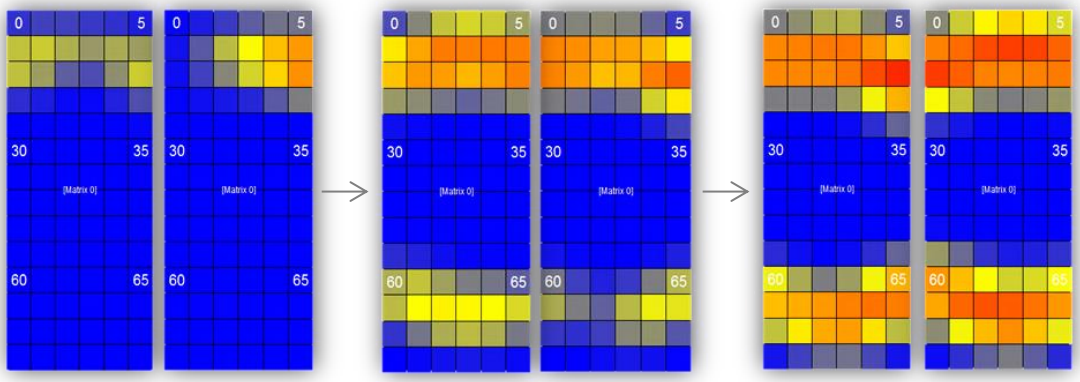

Figure 9-24: Tactile Sensor Pressure Distribution When Gripping a Roll of Insulation Tape

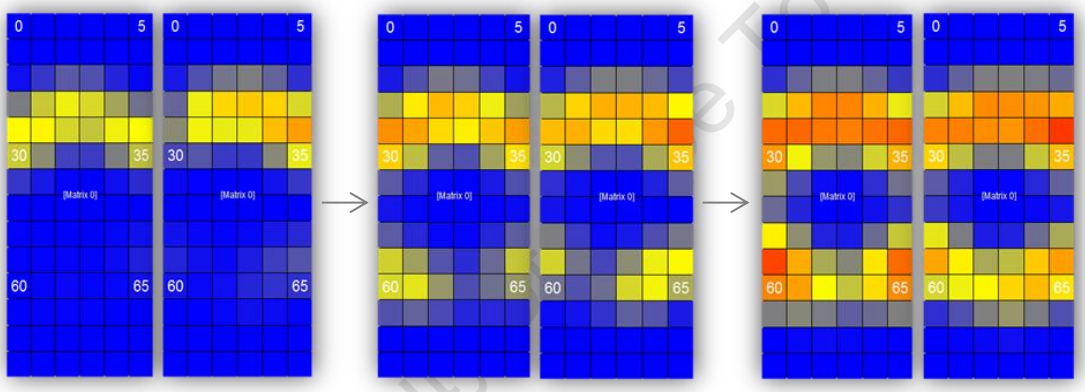

Figure 9-25: Tactile Sensor Pressure Distribution When Gripping a Key Ring

As seen in the figures, distinct circular patterns emerged for both the roll of tape and the key ring, with the key ring features being slightly more distinct due to the smaller diameter.

From the results above, the conclusion may be drawn that object geometries can definitely be identified using the Weiss Robotics 9205i tactile sensor arrays. Compared with standard FSR sensors, the high resolution pressure distributions can provide insight into what type of objects are being gripped, how much pressure is being exerted and if there is any movement of the item within the fingers (possible due to slippage). Once these sensors are fully interfaced with the control station, a remote operator will have far more control and an excellent overview when performing gripping operations.

9.2.5 Gripper CAM Range and Visual Acuity Performance

9.2.5.1 Test Overview

In **USAR** robotics, the ability to visually inspect an environment with a camera is of primary importance to responders. The quality of the acquired images is directly related to the performance of the camera system including the image sensor, lens, electronic circuitry, lighting and the communications medium.

The following tests will be performed based, in part, on the **USAR** robot standards report prepared by J.M. Evans for **NIST** on the recommended tests for visual acuity [67]. These tests include a Snellen chart, an EIA Resolution Chart 1956 and a grid distortion matrix test chart.

9.2.5.2 Test Procedure

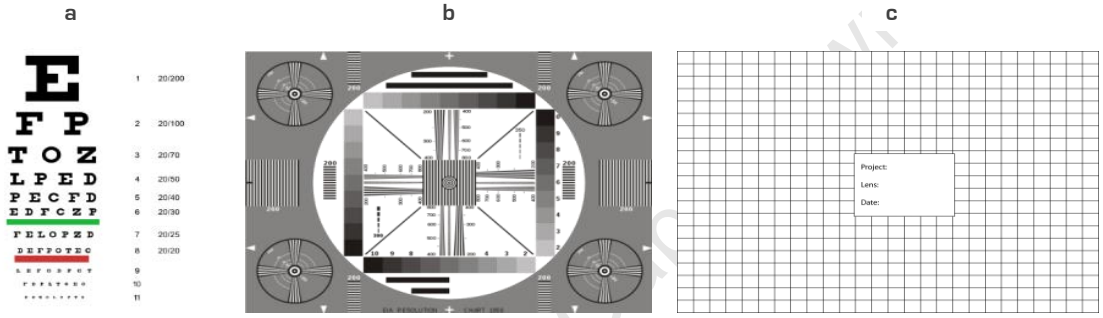

Figure 9-26: a) Snellen Chart [69], **b) EIA Resolution Chart 1956** [67], **c) Distortion Grid Matrix** [68]

Snellen Chart:

To keep in line with standard Snellen chart testing of having the ratio of the chart distance to the height of the top letter equal to 68.2, the chart was printed on an A4 page and placed at 3.27m from the camera. However at this distance the camera quality proved too poor to attain a reasonable image for analysis. As a result, the chart was placed at 1.5m where the letters were more readable.

EIA Resolution Chart:
The Electronic Industries Association 1956 Resolution chart was primarily designed to determine the limiting horizontal resolution of a camera feed. In order to establish this, the four linear sets of wedge patterns around the centre need to be visually inspected. Once individual lines start to blur into one, the scanned resolution can be read off the wedge legend. The test was performed at 385mm distance to fully fill the camera image.

Distortion Grid Chart:
The distortion grid matrix chart was designed to ascertain if a camera distorts an image. Distortion may occur for a variety of reasons including a low-quality imaging sensor or due to physical characteristics of the camera lens. By accurately measuring the vertical and horizontal distances of the image, the horizontal and vertical FOVs could be calculated as well as the aspect ratio. For the test, the chart was placed at 385mm from the camera.

9.2.5.3 Test Results

The following still images were recorded during the Snellen chart test with the gripper lighting at maximum.

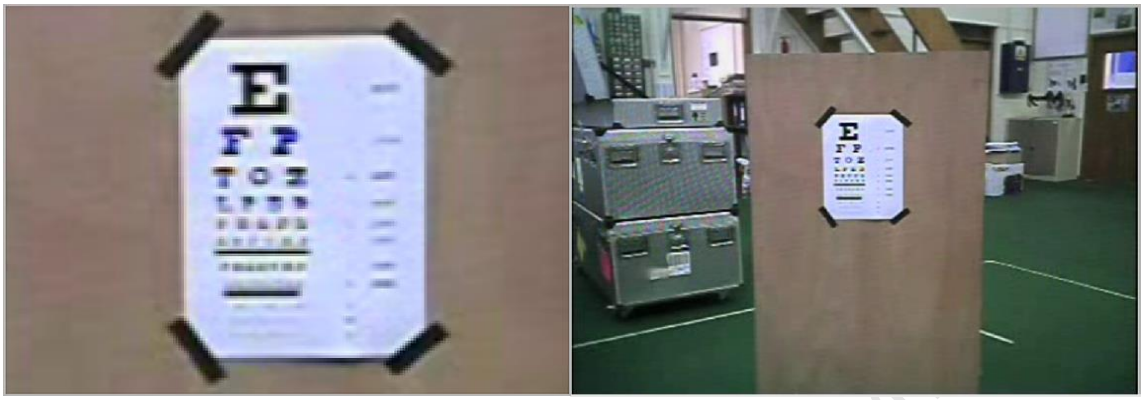

Figure 9-27: Snellen Chart Still Images at 1.5m (Left: Digital Zoom, Right: No Zoom)

As seen in the image, the first three lines could be read relatively easily (**E** | **F P** | **T O Z**). The fourth line (**L P E D**) was a lot more difficult to recognize. As the chart was not placed at the required 3.27m distance, a difinitive value for visual acuity was not established, although it can be said that the camera quality appears good enough to perform basic visual inspections.

Figure 9-28, below, presents the two images that were captured for the EIA Resolution Chart 1956 and the Distortion Grid Matrix Chart.

a) b)

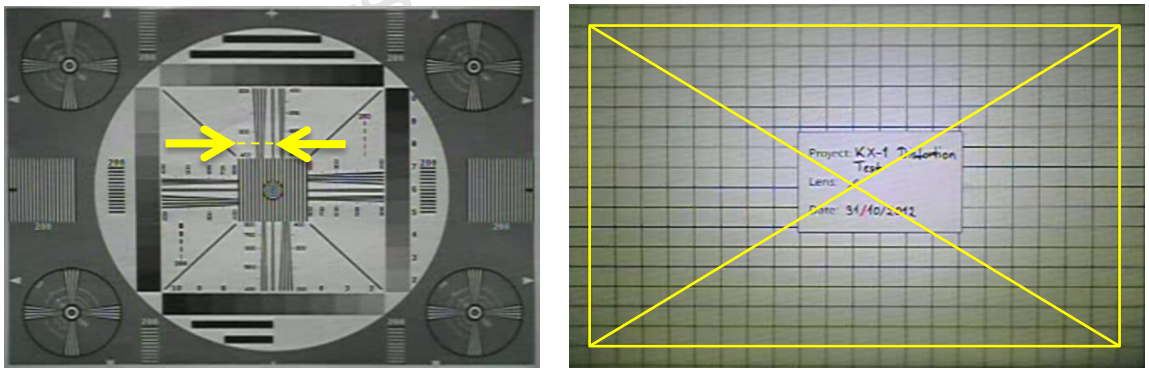

Figure 9-28: Still Images of a) EIA Resolution Chart 1956, b) Distortion Grid Chart

By visual inspection, the limiting horizontal resolution of the camera was approximated at 350 lines (indicated by the yellow arrows) as the converging wedge lines became indistinguishable at this value. For the distortion test, a rectangle (yellow) was superimposed on the image to determine if there was any indication of image distortion (primarily barrel or pincushion). As can be seen in the acquired image, there was almost no visible distortion and the matrix grid matched up well with the superimposed rectangle.

The KX-1 CMOS camera was chosen for its compact size, low cost and low power consumption. Based on the image quality assessments that were conducted, the camera performance was on par with what one would expect from such a device. As such, it would be well suited as an end-effector camera for basic visual inspection with the option to implement basic image and motion detection functionalities.

9.2.6 Gripper CAM Lighting

9.2.6.1 Test Overview

In **USAR** disaster environments response robots will often be deployed to areas that are dark and isolated. Without artificial lighting cameras would not be able to operate effectively in such conditions. Although **UCT**s **MRP** has powerful LED lighting solution installed in the sensor payload, additional lighting has been implemented in the gripper body and fingers to aid the operator when performing close up operations using the gripper camera.

The following tests will evaluate the various lighting settings and will attempt to define the relationship between distance and brightness. This is expected to present itself in the form of an inverse square law.

9.2.6.2 Test Procedure

Figure 9-29 presents the setup that was used to test the lighting capability of the end-effector system. As can be seen from the image, the setup consisted of a LM-8000 light meter mounted onto a section of plywood placed at set distances from the gripper.

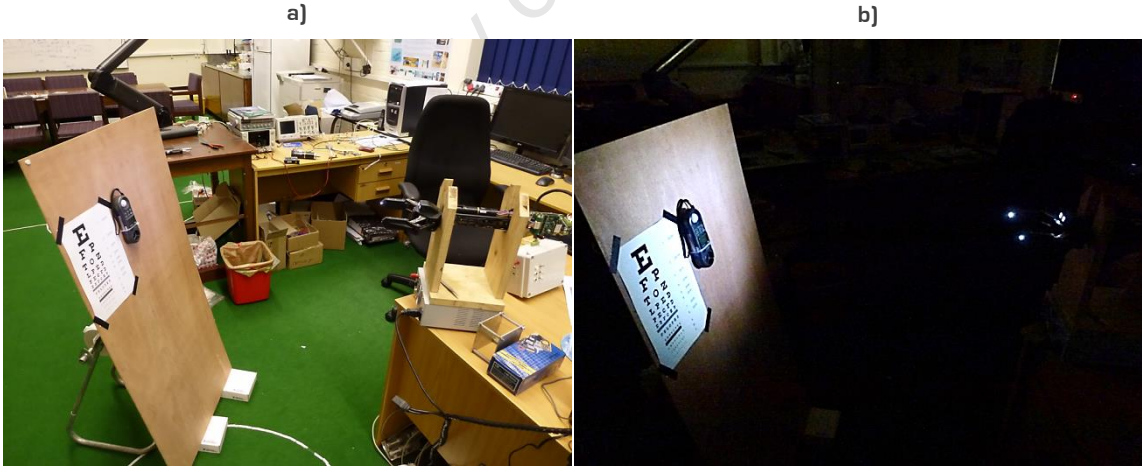

Figure 9-29: Gripper Lighting Testing a) Test Setup, b) Test in Full Darkness

The tests were performed in complete darkness which was verified by the lux meter to be 0 Lux. At every distance interval the brightness level of the gripper lights was increased incrementally and the lux reading on the light meter recorded.

9.2.6.3 Test Results

As was to be expected, the measured luminance was linearly related to the brightness setting of the gripper lights (Figure 9-30). The larger the distance to the end-effector, the smaller the increased lux per unit distance.

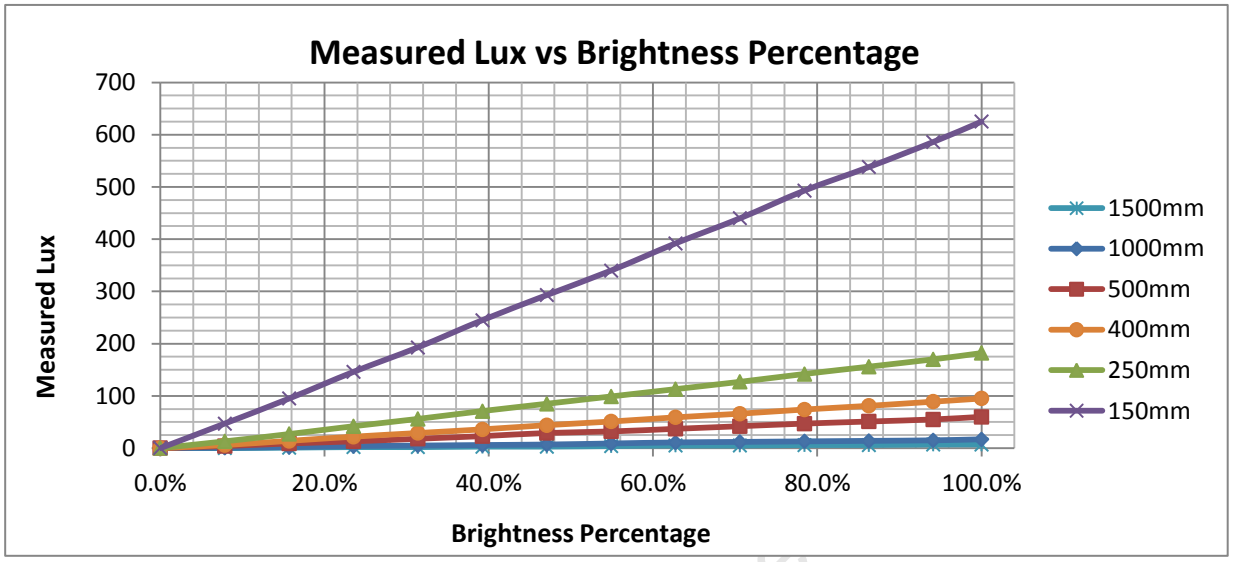

Figure 9-30: Measured Lux vs. Brightness Percentage

In theory the luminance in a given area is inversely proportional to the square of the distance of the area. Figure 9-31 presents a plot of the maximum luminance per measurement against the distance at which the reading was taken. A trendline, superimposed on the plot, provided the equation of the graph.

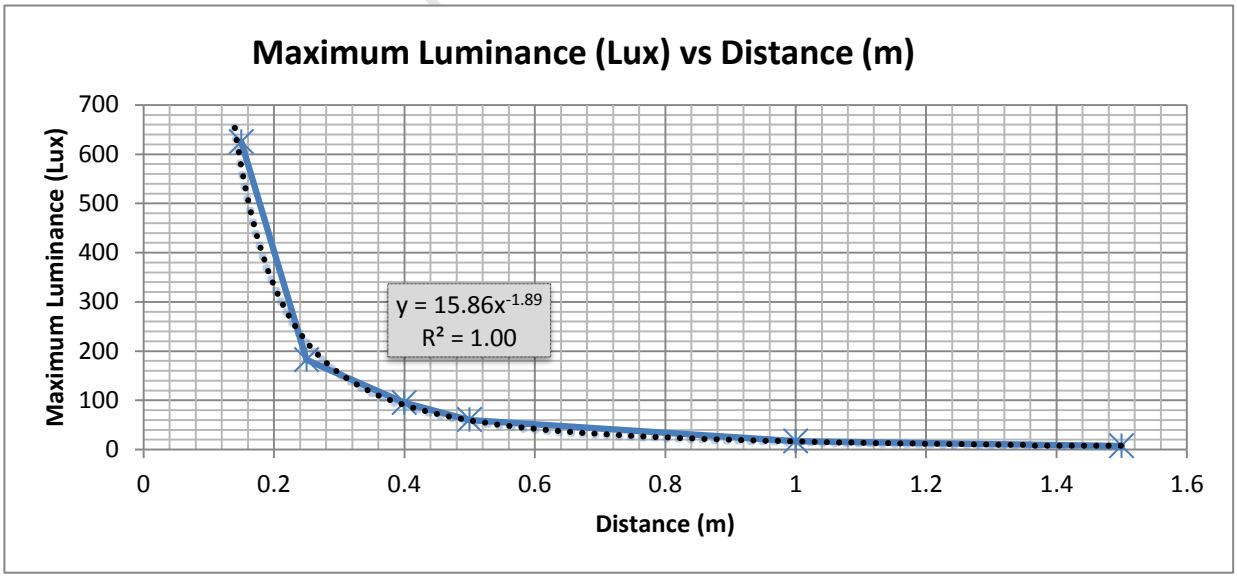

Figure 9-31: Maximum Luminance vs. Distance

Based on the trendline, the following equation was determined:

$$Luminance\ (Lux) = 15.86 * Distance(m)^{-1.89}$$

This equation suggests an inverse square relationship (as expected) with an R-squared coefficient of 1.00 indicating a very good trendline fit. The performance observed in Figure 9-31 indicates that the gripper lighting is very effective at distances below 0.5m. This is ideal as the gripper lighting was primarily included to assist with manipulation operations.

9.2.7 Gripper CAM Data Throughput

9.2.7.1 Test Overview

USAR MRPs are often operated wirelessly and the bandwidth available for video transmissions may therefore be severely limited, particularly during long range missions. The aim of the following test was to determine the bandwidth that is consumed by the gripper camera during no motion and high motion scenes.

9.2.7.2 Test Procedure

The gripper camera is connected to a Bosch VIP X2 that converts the analogue PAL signal to IP packets which get transmitted over a wireless link to the operator control station. In order to determine the bandwidth required to perform this operation, a Bosch VIP X2 was connected to a laptop over wired Ethernet. Then the bandwidth was measured during no motion and high motion scenes and plotted on a Windows generated graph.

9.2.7.3 Test Results

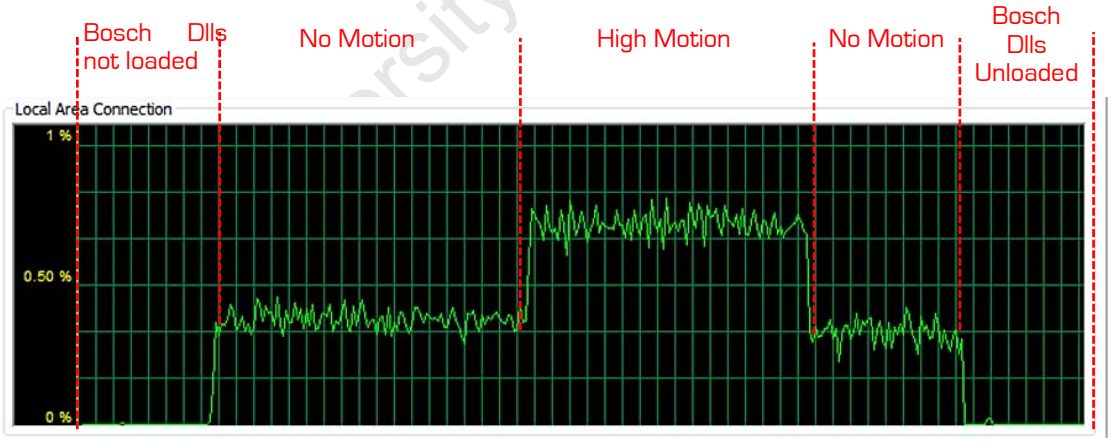

Figure 9-32: Plot of Bandwidth Usage vs. Time Throughout Variable Motion Scenes (100Mbit)

As seen in the figure above, the video stream required varying amounts of bandwidth dependant on the scenes being recorded. During 'No Motion' scenes the network usage idled at around 0.35% (i.e.350kbps) with an increase to 0.75% (750kbps) during 'High Motion'. Even during high motion scenes a data rate of 750kbps should be sustainable at close to medium ranges (<50m).

9.2.8 Gripper CAM QR Code and Signs of Life Detection

9.2.8.1 Test Overview

In real-world rescue scenarios, the ability of a vision system to detect victims autonomously is of great advantage. One method of achieving this is to perform motion detection analysis on a live video stream. Another feature that is helpful (and which was newly implemented at RoboCupRescue 2012) is the automatic detection of QR Codes. The following tests demonstrate the capabilities of the end-effector to perform both of these functions autonomously.

9.2.8.2 Test Procedure

As seen in Figure 9-33 and Figure 9-34, a custom LabView VI was created to test for autonomous *QR Code* and *Signs of Life* detection capabilities. As seen in the figures, the left side of the program presents the video stream from the Bosch VIPX2 with QR Code recognition (green square) superimposed on the image. The right side of the VI illustrates any motion that was detected (based on set parameters) in red. The green circle indicates the centre of motion.

QR Code detection was performed by holding various Version 4 codes (45x45mm) in front of the end-effector camera at increasing distances and brightness levels. The ability to detect the *QR Code* at these distances was then recorded.

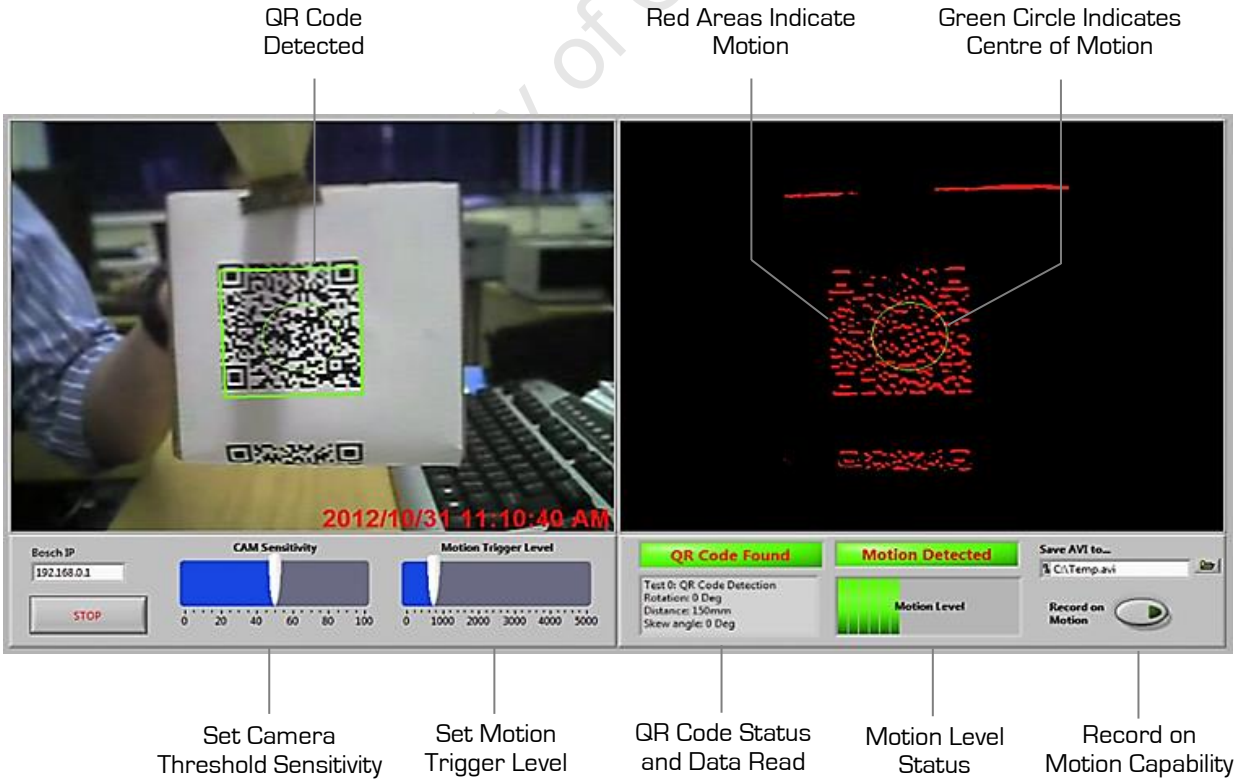

Figure 9-33: QR Code Autonomous Detection Test Program

Signs of Life detection was performed to verify if the end-effector could detect motion autonomously. The test consisted of a small DC motor (Figure 9-34, Left) with an attached rotating flag operating at various speeds and distances (0.5m, 1.5m, 3m and 5m) from the setup. When motion was detected, the video stream was saved to an AVI file with an overlay indicating when the motion occurred and where in the image the motion was located. The figure below presents the test VI detecting the motion of the flag.

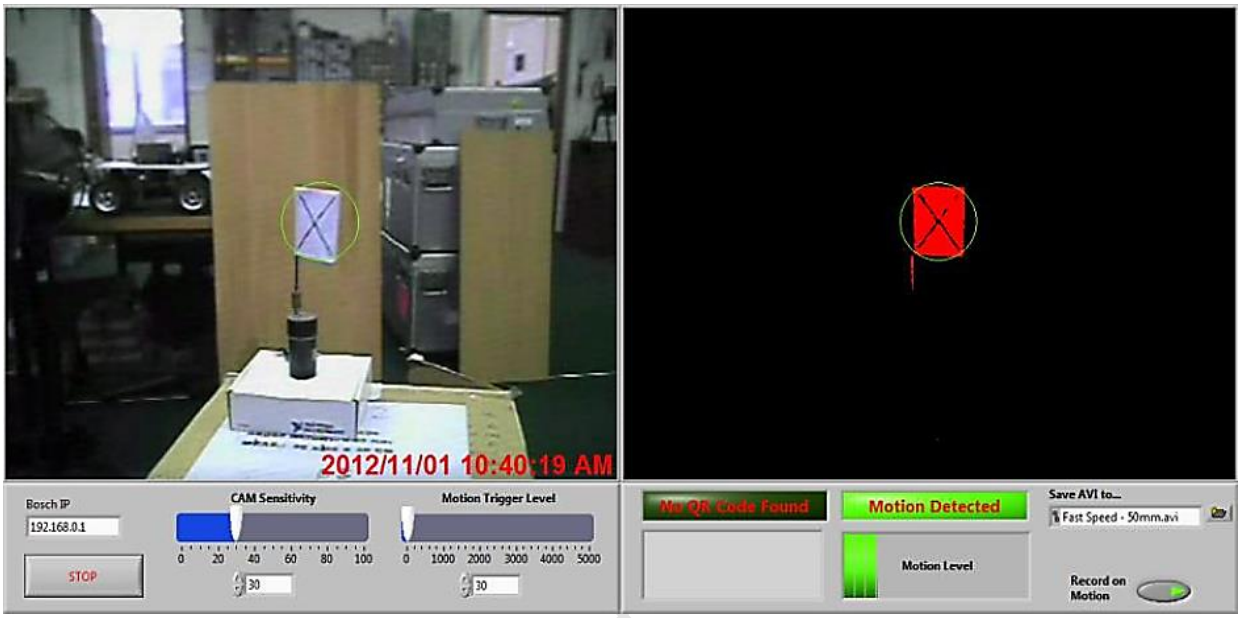

Figure 9-34: Original Image (Left) with Motion Detected Image (Right) at 0.5m

9.2.8.3 Test Results

For all motion detection tests at distances up to 5m, the end-effector consistently identified motion correctly and captured video to an AVI file. Almost no false triggering was detected during any of the tests. Further detailed testing information, including motion detection videos, can be found on the accompanied DVD.

QR Codes were successfully detected from 80 to 300mm with an extra 40mm gained with activated lighting. For use in RoboCupRescue and real-life rescue scenarios, this should prove to be more than adequate. With an auto-focus camera in the gripper, this distance could be extended to a meter or more.

9.2.9 Gripper Light Bridge Performance Test

9.2.9.1 Test Overview

When performing gripping operations remotely it may be very difficult to judge the depth of objects based solely on the video feed. For this reason the end-effector was fitted with two light bridges to inform the operator where an object is currently located relative to the gripper. The following tests will demonstrate the performance of the light bridges in various lighting conditions and environments.

9.2.9.2 Test Procedure

The first test to be performed was a base performance test to determine if any false triggering would occur during various lighting conditions. These results are presented in Table 9-1 below.

The next set of tests involved measuring the performance of the light bridges by placing various objects between the gripper fingers and recording if the sensors could detect items of different transparencies. These results are shown in Table 9-2.

9.2.9.3 Test Results

Table 9-1: Light Bridge Performance in Various Lighting Environments

Lighting Condition	Observations
No ambient light (0 Lux Vertical)	No false triggering
Fluorescent lighting (400 Lux Vertical)	No false triggering
Outside (Sunny Conditions)	Some false triggering when light shone directly into the phototransistor opening
Outside (No Direct Sunlight)	No false triggering
Incandescent light (Close Range)	Some false triggering at small angles with light falling directly into the phototransistor opening

Table 9-2: Light Bridge Test for Various Objects

Object to be manipulated	Gripper Half Closed	Gripper Full Open
Clear Plastic Bottle 500ml (Empty)	Intermittent triggering	Consistent Triggering
Clear Plastic Bottle 500ml (Full)	Intermittent triggering – better than with an empty bottle	Consistent Triggering
Clear Glass Bottle 500ml	Some false triggering	Consistent Triggering
Opaque Green Plastic Bottle (750ml)	Consistent Triggering	Consistent Triggering
Wood Block 100mm Cube	n/a	Consistent Triggering
Portable Phone	Consistent Triggering	Consistent Triggering

The tests demonstrated that objects could be effectively detected between the gripper fingers but with some false triggering occurring during specific lighting conditions and with transparent objects. In an attempt to remedy these issues, the openings of the phototransistors were reduced to allow less ambient light to fall onto the sensing area. This greatly reduced the amount of false triggering, whilst still allowing the sensor to still trigger successfully. This modification is illustrated in Figure 9-35 below.

It is the opinion of the author that the sensors were invaluable during remote gripping operations and assisted greatly in performing successful manipulations. Without them and relying only on a camera feed alone, the operator would have to be significantly more cautious and make small corrections far more frequently.

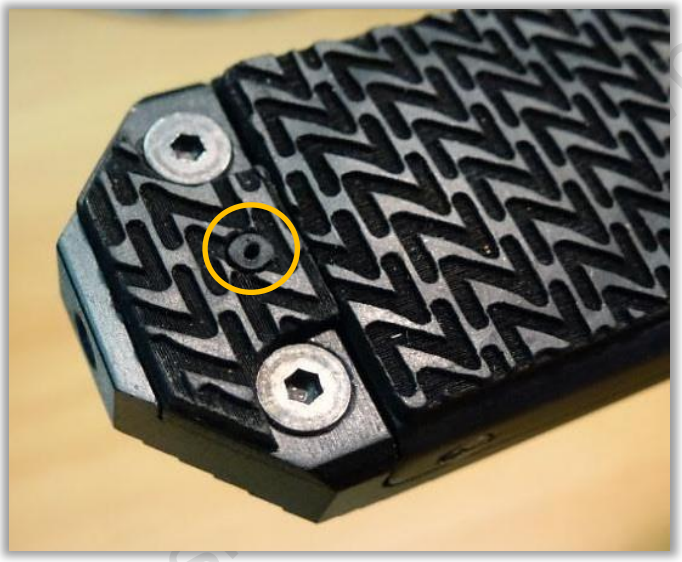

Figure 9-35: Light Bridge Phototransistor Opening Modifications

9.3 Wrist System Testing

9.3.1 Wrist Rotational Speed Test

9.3.1.1 Test Overview

The rotational speed of the wrist affects the performance and responsiveness of the overall system, particularly when performing manipulation tasks such as drilling, opening doors or undoing screws. The following tests demonstrate the various speeds of the wrist for different DAC outputs.

9.3.1.2 Test Procedure

A LabView test program was created to automatically increase the speed setting of the wrist whilst continuously logging the latest speed reading from the velocity register of the quadrature encoder. The speed setting was increased by 2 units (/4095) at 75ms intervals. The average of the speed readings over this period was calculated and recorded and is presented on the graph below.

9.3.1.3 Test Results

Figure 9-36, below, illustrates the speed ramp that was applied to the wrist system. As can be seen from the plot, a maximum speed of approximately 84rpm was reached at a speed setting of 2650 (/4095). Subsequent speed settings had no effect on the maximum speed of the motor due to the speed range that was selected on the Maxon DEC 24/3 speed controllers.

The minimum achievable wrist rotation was initially specified at 60rpm. As demonstrated below, the achieved rotational speed was approximately 84rpm. It should be noted that some vibrations were identified in the system, particularly between 30rpm and 80rpm. This was most likely due to the misalignment of the spur gear set driving the wrist section and should be corrected in a future revision.

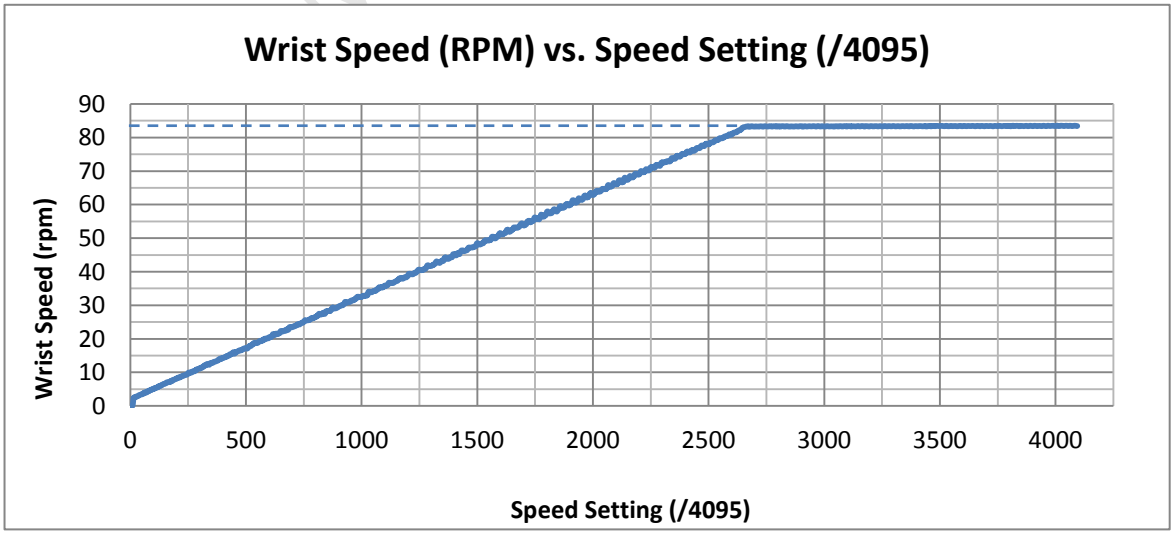

Figure 9-36: Wrist Rotational Speed Test

9.3.2 Wrist Torque and Current Draw Tests

9.3.2.1 Test Overview

Wrist operations in disaster areas are wide-ranging and may include activities such as using tools like screwdrivers or moving objects such as bottles or rubble. The amount of torque and the torque characteristics of the end-effector are important factors to consider for a remote operator undertaking such tasks. The following tests will present torque and current draw characteristics for various speed settings of the wrist and will attempt to validate if they meet the minimum requirements presented in the detailed specifications listed in Chapter 6.

9.3.2.2 Test Procedure

Figure 9-37, below, presents the test rig setup. The tests were conducted by securing a piece of wood in the gripper at 220mm*cos(20°) from the scale. Using this fixed distance, the torque could be determined by measuring the weight indicated on the scale. This lead to the following equation:

$$Wrist\ Torque\ (Nm) = 0.22 * \cos(20°) * 9.81 * Mass\ (kg)$$

As the scale had no simple way to provide a data stream of the current mass being applied, a program was written in LabView utilising the Machine Vision Module with Optical Character Recognition algorithms and a Logitech HD webcam pointed at the digital display. The program was trained with approximately 20 sample images which required manual highlighting of the position and value of characters on the sampled image. Once this training had been completed, the required data could be read off the scale in real-time at sufficient speeds to perform the tests.

Each test was performed at a different wrist speed with the current and mass values being recorded at regular intervals. The torque was applied for approximately 2s with the piece of wood touching the scale (i.e. the wrist was stationary during the tests).

Figure 9-37: Apparatus for Measuring the Wrist Torque

Figure 9-38, below, illustrates the webcam setup (left and centre) and the LabView VI (right) that was generated.

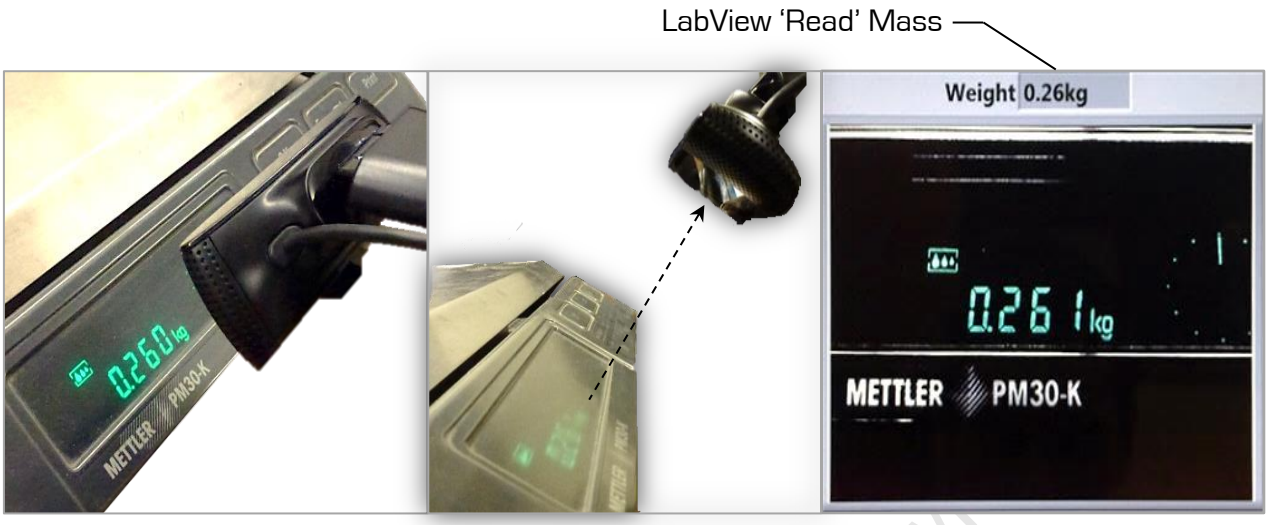

Figure 9-38: LabView Machine Vision Using OCR with a Logitech Webcam to 'Read' the Current Mass

9.3.2.3 Test Results

The following figures present data that was captured over the various tests. The first figure shows the torque characteristics of the wrist during different speed runs.

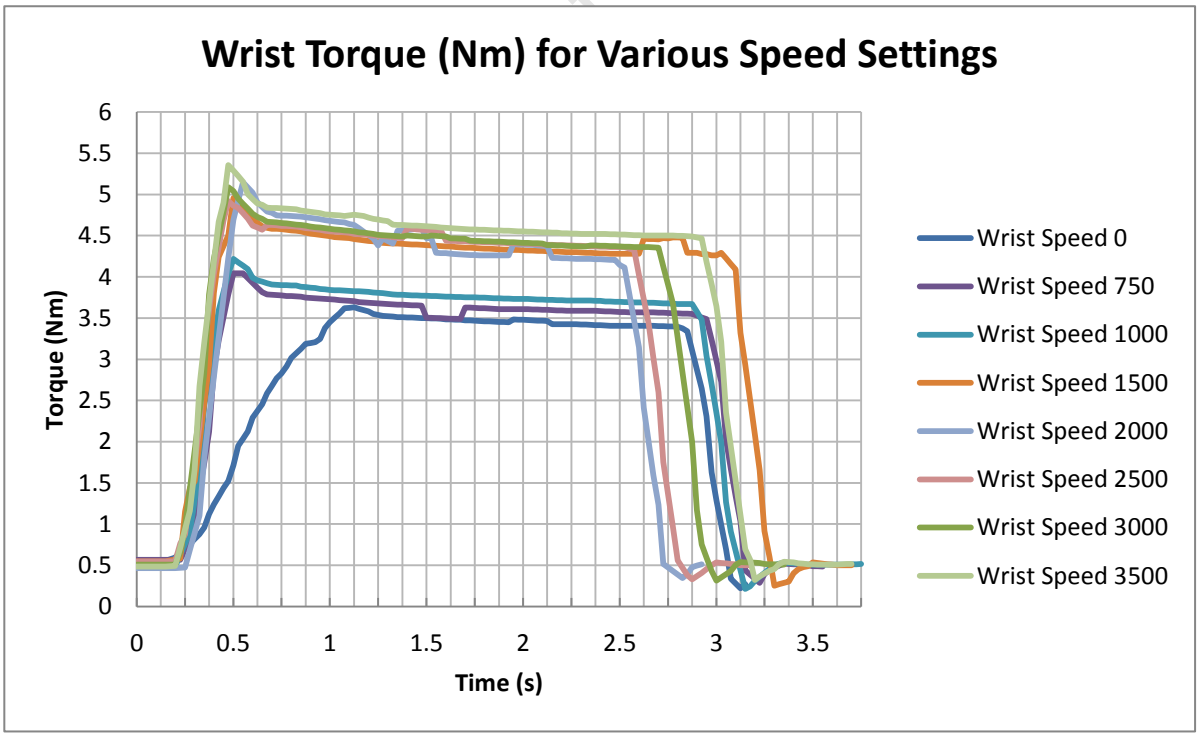

Figure 9-39: Wrist Torque (Nm) Plotted Against Time (s) for Various Speed Settings

Figure 9-40 shows the current that was simultaneously captured over the same test runs.

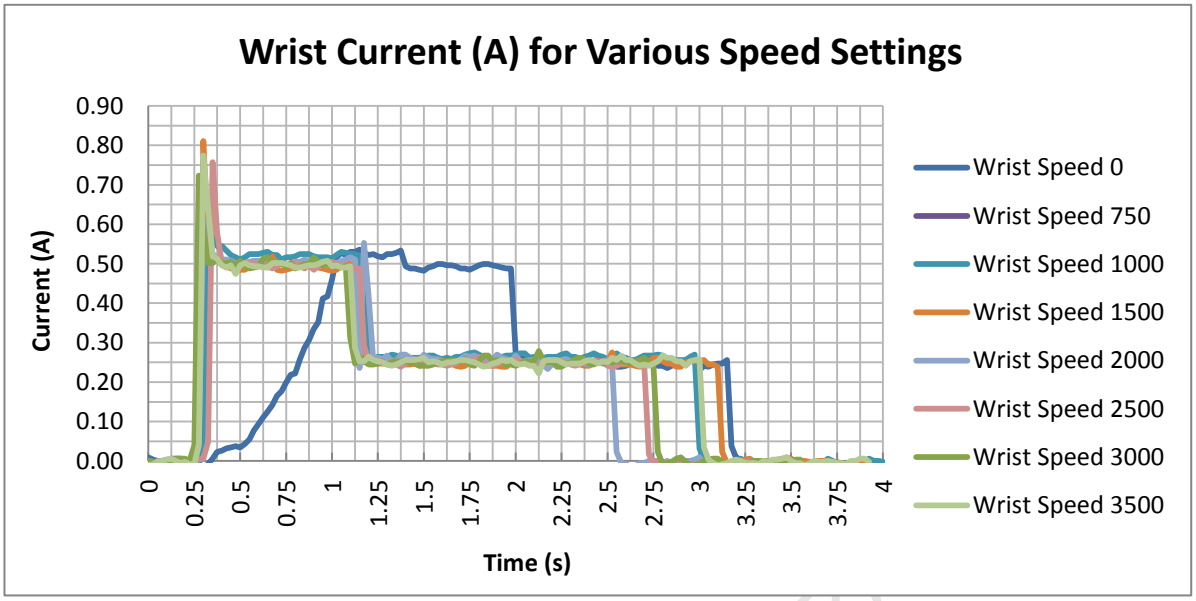

Figure 9-40: Wrist Current (A) Plotted Against Time (s) for Various Speed Settings

From the data that were captured, it was concluded that the maximum torque that the wrist could constantly generate was approximately 4.6Nm @ 0.5A with a peak of 5.2Nm @ 0.8A. For comparative purposes, a Metabo 400Watt DRILLBE4006 has a rated torque of 6Nm [70]. The original specification detailed in Chapter 4 required a maximum achievable torque of 5Nm.

As can be seen from Figure 9-39, the speed setting of the wrist appeared to have little effect on the amount of torque that the wrist motor could produce although two distinct torque 'bands' at 3.5Nm (below a speed of 1000) and 4.5Nm (above 1000) could be identified.

From Figure 9-40 it was also concluded that the current draw would not prove to be an effective way to measure the wrist torque unless only peak current draws were to be monitored. This was due to the nature of the Maxon DEC 24/3 speed controller and the step-wise current drop-off under stall conditions (i.e. Motor shaft blocked error). A torque indicator based on the current draw would therefore be difficult to implement, but not impossible.

9.3.3 Wrist Position Accuracy

9.3.3.1 Test Overview

Based on user feedback from the usability tests, it became apparent that some form of wrist position control should be implemented. Due to its simplicity, straight proportional control was applied to wrist system. The following tests will illustrate the positional accuracy of using such a control method and will evaluate if the positional accuracy achieved is acceptable. It should be noted that the tests were run under no load conditions due to the nature of the Maxon speed controllers not being able to provide a holding torque and entering a 'Shaft Blocked' protection state.

9.3.3.2 Test Procedure

In this test a laser pointer was used to determine the positional accuracy of the proportional control algorithm that was implemented. The laser was mounted onto the gripper at a distance of 3400mm from a white board and the wrist was re-calibrated to a zero position using an auto calibration routine. Marks were then made on the white board at 0°, 5°, 10° and 15° projected angles (Figure 9-41).

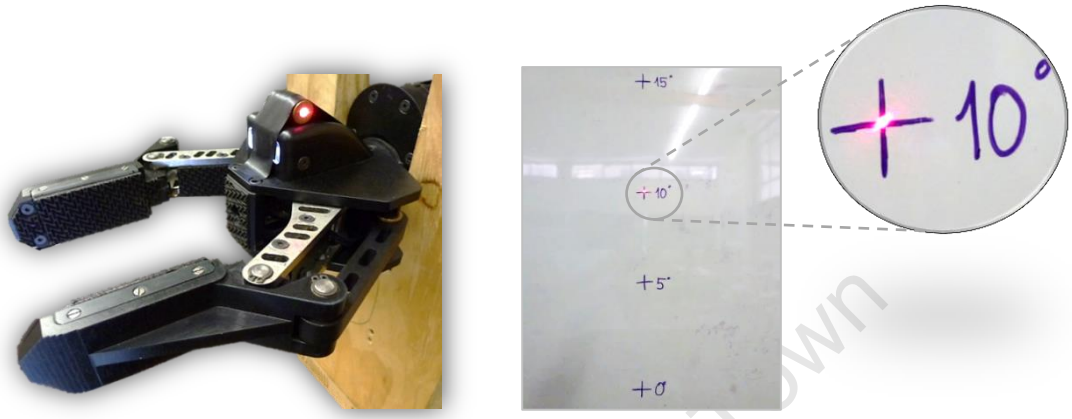

Figure 9-41: Laser Pointer Mounted Onto the Wrist (Left) and Laser Measurements (Right)

The test was run by setting the wrist to these angles sequentially over eight runs. For every position change, the vertical error from the accurate position was recorded using a ruler. A positive value indicated an error above the desired position with a negative value indicating an error below. Although this was by no means an extensive position accuracy test, it should at least provide an indication of the maximum error that could be expected during operational conditions.

Figure 9-42, below, illustrates the method used to determine the positional error angle based on the laser error on the white board.

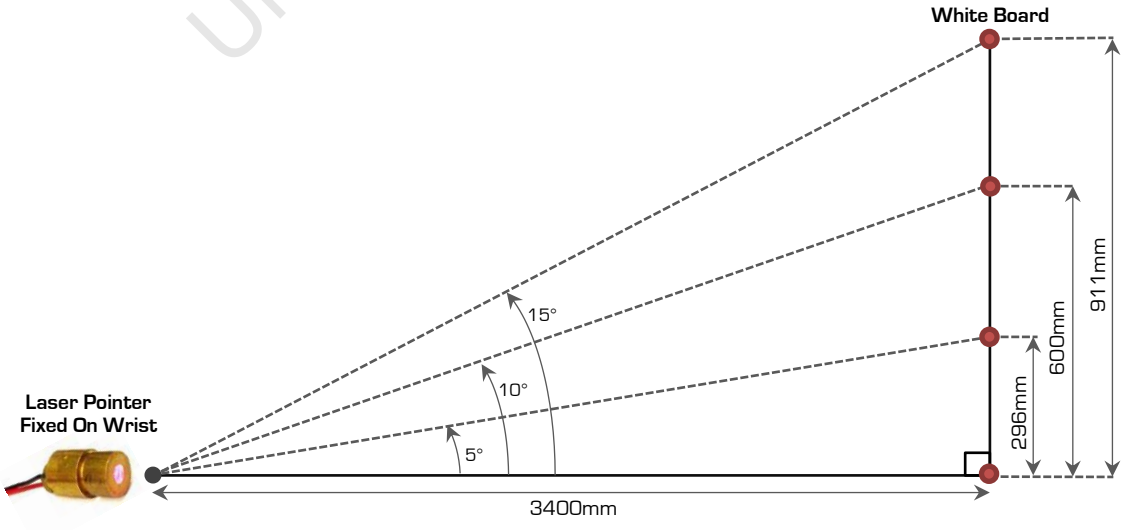

Figure 9-42: Test Rig Setup with Laser Focussed on a White Board

9.3.3.3 Test Results

The maximum error that was recorded over the various test runs was approximately 14mm, with a calculated average over all readings of 7mm. The following deductions were made based on these values:

$$PosError_{max} = \arctan\left({}^{14mm}/_{3400mm}\right) = 0.24°$$

$$PosError_{avg} = \arctan\left({}^{7mm}/_{3400mm}\right) = 0.12°$$

The positional accuracy of the wrist was specified as 1° in the wrist detailed specifications in Chapter 6. From the tests above, it may be concluded that the maximum error over all the runs was 0.24° with an average error of 0.12°. This should prove more than sufficient to position the wrist under no load conditions. It should be noted that there were some oscillations on some test runs which would indicate that the proportional control may require some further optimisation.

9.4 Summary

The tests that were presented in this chapter were performed to verify certain system specifications and to demonstrate system functionality and features. Overall, most of the desired specifications were met, with some exceptions including the subsystem masses and the resultant overall system mass.

This chapter was a summary of a **Detailed Testing** supplement that contains more comprehensive and detailed testing information and results. The supplement can be found on the accompanying DVD.

Chapter 10. Conclusions and Recommendations, that follows, draws conclusions based on the various tests that were presented in this chapter and presents recommendations on how to improve the overall system for future development.

Chapter 10. Conclusions and Recommendations

The research, design and development of the end-effector system, based on the specifications that were set, resulted in a system that was easy to operate and effective to use yet that could be improved and expanded in the future. This chapter will present the conclusions that were drawn from **Chapter 9. Testing and Results** and will detail recommendations based on the conclusions. Possible future developments and extensions to the project will also be discussed.

10.1 Conclusions

10.1.1 Gripper System

10.1.1.1 Mechanical Design

One of the greatest design challenges for the gripper system was the 500g target weight that was set. For this reason *Aluminium* was chosen for most components with *Stainless Steel* and *Silver Steel* only used for critical parts. As was illustrated in the mass breakdown, the overall weight of the gripper was 615g excluding all electronics, 23% more than specified. Of the overall total system weight of 1472g, the gripper made up 42%. However, based on the performance of the manipulator arm during testing, this proved acceptable.

The dimensional specifications were all achieved including finger lengths of approximately 80mm, a gripper length of 177mm (mounted in the wrist) and a grip stroke of 135mm (25mm more than the previous parallel gripper design). This large grip stroke meant that various objects could be gripped effectively, which should prove ideal for unstructured disaster environments.

The M12x1.75 power-screw actuation method proved to work very effectively allowing precision control of the gripper with the capability of being non-back driveable. Due to the manufacturing process, the backlash of the system at 4mm was acceptable, but higher than what was originally hoped for. The modular gripper fingers also proved to work very effectively, with application dependant sensors being easily swappable. The internal wiring of the fingers also made the system look neat and compact.

The performance of the gripper system during testing provided verification of many specifications. The maximum prehension force achieved during testing was approximately 140N. This prehension force was, in part, restricted by the Maxon speed controller. Therefore, the actual practical maximum prehension force may be far higher. The minimum gripper open and close times were determined to be 4.4s.

The decision was made not to include a native tool handling capability in the design of the gripper and to rather focus on the sensory capabilities of the system. However, various tools could potentially still be used as will be shown in the recommendations section to follow.

10.1.1.2 Electrical Design

Overall, the electronic and electrical system complied with the specification and design requirements that were established.

The gripper electronics system consisted of an embedded controller with a Freescale MC9S08GT16A processor programmed in C-Code that was specifically designed to fit into the camera housing. This board provided capabilities including adjustable LED lighting, camera power switching, light bridge and Hall Effect sensing as well as reading both the FSR sensors and Weiss Robotics 9205i tactile sensing arrays. Some important features of the controller included the capability to shut down systems like the tactile sensors and the camera to conserve power when not in use.

The KX-1 CMOS camera that was selected proved to function very well for its cost and size, providing good quality images, particularly in low lit areas. No distortion of the image was found during testing. Additionally, the ability to adjust the camera and lighting angle in the housing with Allen keys, without having to disassemble the system, proved very helpful.

From the testing section it was found that the LED lighting solution was effectively usable to 0.5m, which should be more than enough for close up manipulation operations. In total, the system power consumption was 3.5W at idle, increasing to a potential maximum of approximately 85W under full system load.

In the system usability tests it was shown that the light bridges performed well, although false triggering on transparent items like plastic bottles was evident. For opaque and solid objects, the sensors were completely reliable.

One of the more important tests attempted to clarify if the current could be used to measure the gripper force as this could improve the reliability of force readings using sensor fusion. It was found that the current could potentially be used to provide force feedback, but that the gripper speed would need to be known as well. Additionally, due to the non-back driveable nature of the lead-screw, the measurements would need to be read during motion operations as this would be the only time that current is drawn from the motor. The following equation describes these results:

$$Force(N) = \frac{Current(A)}{4.57 * 10^{-6} * Speed\ (/4095) + 3.91 * 10^{-3}}$$

During testing of the Weiss Robotics 9205i tactile sensor arrays, it was found that object geometries could be identified with a high level of reliability and that the high resolution pressure distributions could provide an operator with additional information that would be very useful during manipulation operations.

Lastly, the position of the gripper fingers was determined by using the Maxon quadrature encoder together with a LM3S8962 quadrature decoding module. This was done natively in LabView ARM Embedded and was used to dynamically update the end-effector position indicators on the operator control station GUI. This worked well as the resolution of the quadrature encoder provided $1 * 10^{-3}$ degrees resolution on the output shaft, substantially more than was required to implement proper control algorithms.

10.1.2 Wrist System

10.1.2.1 Mechanical Design

As with the gripper system, the weight specification was one of the primary design requirements for the wrist. A goal of 300g was set in order to achieve the set total of 800g for the overall system. As shown in the mass breakdown test, 317g was achieved, 6% above the desired specification. Of the overall total system weight of 1472g, the wrist made up 21%.

The assembly of the wrist showed that the extra time taken to consider DFMA principles was well worth it. Although the system was tightly packed due to the dimensions of the arm cross-section, assembly was straightforward and servicing parts simple and fast. The continued use of support rods between the rear and front brackets provided a robust and rigid framework, whilst keeping overall weight down.

The selected 2:1 gearbox ratio provided an ideal balance between torque and speed with a maximum continuous torque of 5.2Nm achieved at 0.8A. The maximum recorded speed was 84rpm, 24rpm faster than the 60rpm specified. As the torque test essentially examined the stall torque only (worst case conditions for the DEC 24/3 speed controller), it may be assumed that the actual continuous torque available for operations such as drilling is far higher.

This is due to the nature of the Maxon DEC 24/3 speed controller and the fact that it gives a 'Shaft Blocked' error message under stall conditions, ignoring all inputs and limiting current to 300mA. Only when the load has been removed does it return to normal operation. This undesirable behaviour was also prevalent in tests where the wrist had to hold a load at a certain angle and is illustrated in the current draw graphs in the **Testing and Results** chapter. A positional accuracy of 1° was originally specified for wrist position control. Based on the tests that were performed, a maximum error of 0.24° and an average error of 0.12° were established.

10.1.2.2 Electrical Design

Both the Hall Effect switch and the LM35 temperature that were installed functioned well and complied with the design requirements. The maximum temperature that was recorded in the arm was 45°C during a full sunlight outdoor test.

The continuous rotation of the wrist through the use of a 30-way slip-ring worked well, with full communications and power being available through the entire speed range.

10.1.3 Electronics Systems

10.1.3.1 Current Sensor

The custom current sensors that were developed were able to monitor two separate current circuits. Two configurations were produced, a ±5A version that was used in the end-effector and a ±20A version used throughout the robot platform.

As seen from the tests that were conducted, the sensors performed very well providing linear results that could be read into a **µP ADC**. Both of the outputs included over-voltage protection as well as the ability to customise the gain and inverting input reference of the differential amplifier circuit to suit the application.

10.1.3.2 ARM Cortex-M3 Embedded Controller

The ARM Cortex-M3 controller boards that were developed were used throughout the robot platform to control motors and monitor system performance. For most functions, the ability to program in LabView was an advantage in that the software development process was sped up and simplified substantially.

However, a big drawback, and a limiting factor for some applications, was the lack of native serial interrupts in the LabView module. This meant that alternatives like manually generating interrupts or running communications in a parallel loop (slowing down the processor substantially) needed to be devised. For more information on the communication issues that were encountered, see Bradley Springer's dissertation [3].

Of the four generation boards that were developed, the third and fourth generations may be considered fully operational and deployable.

10.1.4 Software and System Control

Although the LabView ARM Embedded module had various shortcomings, the native LabView environment running on the operator control station was ideal for creating an effective and intuitive GUI. Camera feeds and indicators were relatively simple to implement with TCP/IP communications operating well over the wireless link to the robot platform. Positive feedback was provided through user testing whereby inexperienced operators had to accomplish a manipulation task. Each user provided criticisms and comments on a questionnaire.

Although autonomous QR Code discovery and Signs of Life detection were implemented in the testing stages, they were not included in the final interface as they would have potentially overcomplicated the jointly developed manipulator arm GUI. Nevertheless, testing showed that QR code detection worked effectively with codes being detectable from 80mm-300mm using the VGA quality gripper camera. Similarly, the algorithm designed to identify motion in the video feed worked well up to approximately 5m with minimal false readings.

10.2 Recommendations

Although the overall end-effector system achieved most of the design requirements and specifications that were set, all the subsystems have the potential for further improvements to add features and functionality and to correct issues that arose during testing.

10.2.1 Gripper System

As the gripper is currently 23% over the specified weight requirement, further weight reduction should be undertaken. Currently the steel force transmission levers make up 23% of the total weight with the gripper fingers contributing 16%. These should be the first components to be investigated for weight reductions. Furthermore, if a less powerful gripper motor were to be used, substantial mass savings may be possible due to reduced component stresses.

Due to what is assumed to be a manufacturing flaw, the lead-screw currently rotates off centre. This is demonstrated in a video located on the attached DVD. This was first seen in the rhythmic fluctuating current draw during opening and closing operations of the gripper. This influence negatively affects the ability to gauge the prehension force from the current draw. To address this problem, a replacement lead-screw should be manufactured.

The **MRP** will most probably be used in dusty and damp disaster environments. For this reason it is recommended that the system be reworked to an IP54 standard in order to prevent major dust particles and water spray from affecting the operation of the system. This would not necessarily involve enclosing open areas of the gripper but rather ensuring that the gripper would still be able to operate when exposed to such environments.

Although an attempt was made to make the gripper as easy as possible to remove from the wrist, the PicoClasp connectors were not ideal and required some patience to plug in. Good quality connectors should be investigated to replace the connectors currently installed. Furthermore, the mechanical mounting using four screws should be re-evaluated and a system that is faster to remove (perhaps with tool-less screws) should be investigated.

In order to make the operation of the gripper easier for the operator, some type of auto-close function should be implemented in code on the primary end-effector controller. A potential drop-down menu could be used on the front panel GUI to select a prehension strength based on known objects (glass bottle, wooden block, cell phone). This might be more intuitive than inputting a force in Newton.

One upgrade that would be more complex to implement would be to design a tilt mechanism for the gripper camera. This would allow an operator to observe an environment with the added flexibility that the camera could look up and down. This could potentially be achieved with an RC servo or DC motor. An upgrade to the camera (possibly including a microphone) would also be a useful performance enhancement.

During user testing, operators often found it difficult to judge the distance of the end-effector to an object using only the camera feed. Possible solutions to this problem would be the inclusion of some type of laser pointer (simple) or distance range finder (more

complex) mounted onto the gripper. In the same light, the inclusion of more object presence sensors in the gripper fingers would also help an operator to better judge if an object is currently in a graspable position or not. Figure 10-1 presents examples of the solutions provided above.

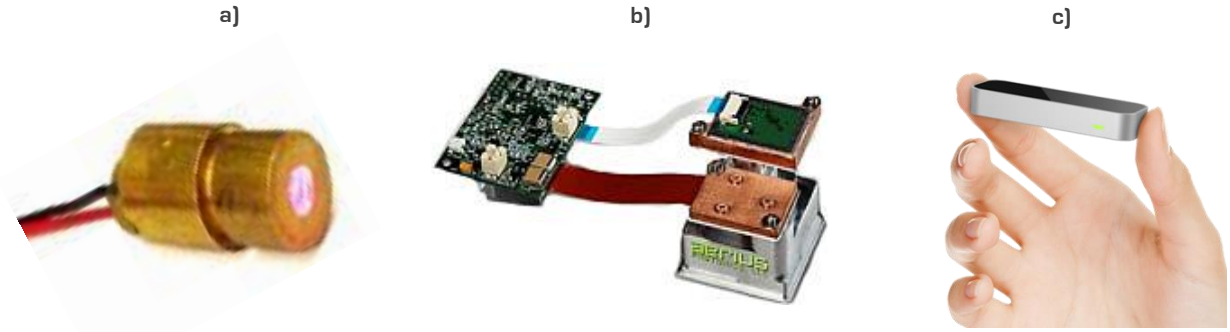

Figure 10-1: a) Small, low-cost laser pointer, b) FLIR MLR-100 Mini Laser Rangefinder [71], **c) Leap** [72]

Another possible solution to this problem would be to install a device like the 'Leap' seen in Figure 10-1 c) underneath the gripper. The 'Leap' is a type of 3D mapping device (similar to the Microsoft Kinect) that will be released in 2013 and could provide a 3D representation of objects within the manipulators grasp. Such a device could prove invaluable to an operator during manipulation operations and would render other object presence detectors obsolete.

As mentioned in the conclusions section, a tool handling ability was not specifically developed for the gripper. However, the gripper should be able to grip custom designed tools (such as the multi-purpose socket holder below) to perform these types of operations.

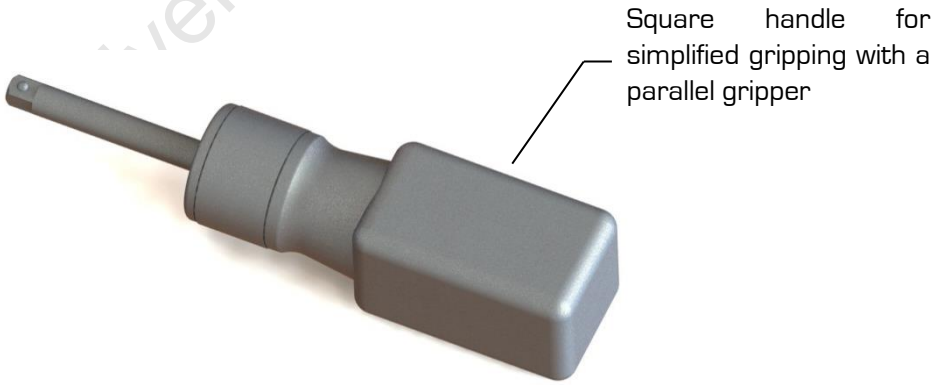

Figure 10-2: Potential Grippable Socket Tool (Modified from [73]**)**

Although testing data was recorded using the 9205i tactile sensor arrays, the sensors were not directly interfaced with the gripper controller. This was partially due to the intricacies involved in transferring the sensor data back over the RS485 communications protocol. Once these sensors are fully interfaced with the control station, a remote operator will have far more control and an excellent overview when performing gripping operations.

One final function that should be investigated is the ability to detect slip using the Weiss Robotics tactile sensing arrays. Based on the journal papers that were examined, this is no trivial task as it relies on many factors including the ability to measure certain frequencies in the sensor that may predict slippage. Nevertheless, an attempt should be made to implement such a system as it would greatly enhance the capability of the gripper to perform successful manipulation operations.

10.2.2 Wrist System

The wrist subsystem was only 6% over the 300g target specification but even so, additional weight savings should be investigated. As the *Gripper Motor Holder* makes up 21% of the overall mass and is not exerted to large stresses, this should be one of the first components to be modified. By simply reducing the wall thickness by 0,5mm to 1.5mm, an estimated 10g can be removed providing a 3% weight saving.

Although the wiring is relatively neat already, it could be cleaned up even more by cutting a small channel into the Gripper Motor Holder and adding mounting points for the LM35 temperature sensor and the Hall Effect switch. This would allow the wires to be neatly recessed while providing additional weight savings.

One significant improvement that could also be made is to reinforce the front cover plate of the wrist that holds the large wrist rotation bearing in place. It was not foreseen how much stress could potentially be exerted on this part, particularly during pulling operations with the **MRP,** where the axial load could exceed 800N.

The most important component of the wrist system that should be replaced is the Maxon DEC 24/3 speed controller. As mentioned in the **Testing and Results** section as well as in the conclusions above, the speed controller could not provide a holding torque at zero speed. When attempting such an operation (like holding a bottle at 90°), the controller would simply indicate a shaft blocked error message after 1.5s and ignore all inputs until the load was removed. This made the controller unsuitable for wrist control. A Maxon EPOS2 24/2 position controller could be used as a replacement. This controller is smaller than the DEC 24/3 but only has a continuous output current of 2A with an intermittent output of 4A. Nevertheless, this should provide enough torque for general wrist operations.

10.2.3 Software and Electronics Systems

The dual current sensors worked well with the LM3S8962 controllers and provided good performance characteristics during testing. However, some improvements can certainly be made to the board. These include replacing the current LM317 linear voltage regulator with a precision voltage reference and substituting the gain resistors for lockable potentiometers. As a result, if a new application requires a different differential amplifier gain, the potentiometer could simply be adjusted as required rather than having to remove and solder on new resistors.

As recommended by operators during user testing, additions to the LabView **GUI** should be made including adding speed controls for the wrist and gripper motors as well as implementing wrist position control. Although the wrist position control has already been employed on the end-effector, it has not yet been deployed to the front panel **GUI**.

In general the LM3S8962 embedded controller performed well, although certain factors, such as the lack of serial interrupts in the LabView ARM Embedded module, proved to make some software components challenging to implement. It is recommended that an investigation be made into programming the processor directly in C-Code through the Keil µVision IDE. Not only will this provide the user with the full access to the processor and its functions, but it will reduce power consumption as well (during testing it was shown that loading the RTX Real-Time Operating System would increase the power draw of the processor by 100%).

As an addition to using C-code to program the LM3S8962 controllers the use of **ROS** (**R**obot **O**perating **S**ystem) should be investigated as it is used internationally as a standard robot software development framework. **ROS** could be used in combination with LabView (as the GUI frontend) and would simplify many operations including communications between systems.

10.3 Summary

The recommendations that were made in this chapter are by no means an exhaustive list and are only those improvements that were critical or straightforward to implement. Of the recommendations that were made the key ones are:

- Reduce the overall system weight further focussing on key components
- Remanufacture and replace the lead-screw
- Investigate new electrical connectors to interface the gripper with the wrist
- Reinforce the front cover panel of the wrist to allow higher axial loads to be achieved
- Replace the Maxon DEC 24/3 speed controller with an EPOS2 24/2 position controller
- Complete recommended additions to the LabView front panel GUI
- Attempt to program the LM3S8962 board in C-Code with the possible implementation of the **ROS** operating system as an overall robot framework

Chapter 11. List of References

[1] R. Whittemore (Photographer). "UCT USAR Robot Platform (Photograph)," 2012. .

[2] E. Dreyer. "Development of the RATEL UGV Platform," University of Cape Town, 2012.

[3] B. Springer. "Development of the Control for an Urban Search and Rescue Robot Manipulator Arm," University of Cape Town, 2013.

[4] K. Mathia. *Robotics for Electronics Manufacturing: Principles and Applications in Cleanroom Automation*, Cambridge University Press, 2010.

[5] Leonardo-Da-Vinci-Biography. "Leonardo Da Vinci Robotic Expertise! And his Robots!," 2009. Online: http://www.leonardo-da-vinci-biography.com/da-vinci-robotic.html [Accessed: February 4, 2013].

[6] Tesla Memorial Society of New York. "Remote control boat built by Tesla," Online: http://www.teslasociety.com/teslamuseum.htm [Accessed: October 16, 2012].

[7] L. Kahney. "Robots Scour WTC Wreckage," *Wired*, 2001. Online: http://www.wired.com/science/discoveries/news/2001/09/46930?currentPage=all [Accessed: October 16, 2012].

[8] A. Boyle. "How high-tech is coming to the rescue," *MSNBC*, 2005. Online: http://www.msnbc.msn.com/id/9131498/#.UH0-g8XMg84 [Accessed: October 16, 2012].

[9] A. Knapp. "Robots Sent In To Monitor Fukushima Power Plant (Update)," *Forbes*, 2011. Online: http://www.forbes.com/sites/alexknapp/2011/04/18/robots-sent-in-to-monitor-fukushima-power-plant/ [Accessed: October 16, 2012].

[10] FEMA - Responder Knowledge Base. "iRobot 710 Warrior," 2012. Online: https://www.rkb.us/pictureviewer.cfm?content_id=285438 [Accessed: October 18, 2012].

[11] G. Galitzine. "iRobot in Deal to Provide 125 PackBots," *TMCnet*, 2010. Online: http://blog.tmcnet.com/robotics/2010/08/irobot-in-deal-to-provide-125-packbots.html [Accessed: October 18, 2012].

[12] RoboCup. "RoboCup Rescue," 2011. Online: http://www.robocuprescue.org/ [Accessed: May 4, 2011].

[13] A. Jacoff, E. Messina, H.-M. Huang, A. Virts, A. Downs, and R. Norcross. "Standard Test Methods For Response Robots," National Institute of Standards and Technology - U.S. Department of Commerce, 2011.

[14] RoboCupRescue Robot League. "RoboCupRescueLeagueRules(v2009.1D)," 2010. Online: http://robotarenas.nist.gov/2010/RoboCupRescueRobotLeagueRules(v2009.1D)pdf.pdf.

[15] R. Whittemore. "Robocup 2012 Team Photographer," 2012. .

[16] R. Sheh and H. Komsuoglu. "Manipulation for SSRR Test Methods and Solutions," Alanya, Turkey: 2012.

[17] G.J. Monkman, S. Hesse, R. Steinmann, and H. Schunk. *Robot Grippers*, Weinheim: Wiley-VCH, 2007.

[18] L. Birglen, C. Gosselin, and T. Laliberté. *Underactuated Robotic Hands*, Springer, 2008.

[19] H. Bin, L.W. Zhen, and L.H. Feng. "A survey on underactuated mechanisms," *Advanced Computer Control (ICACC), 2010 2nd International Conference on*, IEEE, 2010, pp. 551–555.

[20] Applied Robotics. "Gripper tutorials," 2012. Online: http://www.arobotics.com/technical/tutorials.aspx [Accessed: May 15, 2011].

[21] Schmalz GmbH. "Tailored to Any Application: Vacuum Suction Pads Ensure Secure Handling Every Time," 2011. Online: http://us.schmalz.com/aktuelles/presse/vakuumkomponenten/01842/ [Accessed: July 18, 2012].

[22] iRobot. "Packbot 510," 2011. Online: http://blog.tmcnet.com/robotics/iRobot PackBot 510 with FasTac Kit 3.jpg [Accessed: May 26, 2011].

[23] iRobot. "Photos," *Image Directory*, 2011. Online: https://irobot.mt-ap.net/ims/mainview.do;jsessionid=A594BF8B04C6E35558127869B158BF39 [Accessed: May 26, 2011].

[24] iRobot. "310 SUGV Specifications," *Online Brochure*, 2010. .

[25] iRobot. "510 PackBot," *Online Brochure*, 2011. p. 8 Online: http://www.irobot.com/gi/filelibrary/pdfs/robots/iRobot_510_PackBot.pdf.

[26] Kraft Telerobotics. "Predator Force Feedback Manipulator," *Online Brochure*, 2011. pp. 2–8 Online: http://krafttelerobotics.com/products/predator.htm.

[27] Kraft Telerobotics. "Viper Force Feedback Manipulator," *Online Brochure*, 2011. Online: http://krafttelerobotics.com/products/viper.htm [Accessed: May 19, 2011].

[28] Kraft Telerobotics. "Kraft Telerobotics - Intermeshing Jaws," *Online Brochure*, 2011. Online: http://krafttelerobotics.com/catalog.asp?gpcid=5&cid=31&scid=116&ItemID=119 [Accessed: May 25, 2011].

[29] Northrop Grumman Systems Corporation. "Robotic Platform and Sub-Systems Applications," *Product Description*, 2012. Online: http://www.is.northropgrumman.com/by_solution/remote_platforms/applications/index.html [Accessed: September 30, 2012].

[30] Sandia National Laboratories. "Sandia National Laboratories," *News Article*, 2001. Online: http://www.sandia.gov/media/NewsRel/NR2001/bombbot.htm [Accessed: May 26, 2011].

[31] A.M. Dollar and R.D. Howe. "Simple, reliable robotic grasping for human environments," *Technologies for Practical Robot Applications, 2008. TePRA 2008. IEEE International Conference on*, IEEE, 2008, pp. 156–161.

[32] A.M. Dollar and R.D. Howe. "The Harvard Hand - An Adaptive gripper for Simple, Robust Grasping," 2007. .

[33] M. Guarnieri, I. Takao, E.F. Fukushima, and S. Hirose. "HELIOS VIII search and rescue robot: Design of an adaptive gripper and system improvements," *2007 IEEE/RSJ International Conference on Intelligent Robots and Systems*, Oct2007. pp. 1775–1780 Online: http://ieeexplore.ieee.org/lpdocs/epic03/wrapper.htm?arnumber=4399372.

[34] M. Cross. "Development of a Angular Gripper/Multi-Tool and Wrist for the UCT RARL Rescue Robot," University of Cape Town, 2010.

[35] T. Scott. "Development of a Parallel Jaw Gripper/Multi-Tool and Wrist for the UCT RARL Rescue Robot," University of Cape Town, 2010.

[36] S. Walker. "Development of an Adaptive Gripper for the UCT RARL US&R Robot," University of Cape Town, 2011.

[37] R.D. Howe. "Tactile sensing and Control of Robotic Manipulation," *Journal of Advanced Robotics*, vol. 8, 1994. pp. 245–261 Online: http://www.ingentaconnect.com/content/vsp/arb/1993/00000008/00000003/art00002 [Accessed: July 20, 2011].

[38] R.. Crowder. "Tactile Sensors," *Course Notes*, 1998. Online: http://www.soton.ac.uk/~rmc1/robotics/artactile.htm [Accessed: July 21, 2011].

[39] "Interlink Electronics," Online: http://www.interlinkelectronics.com/ [Accessed: July 23, 2011].

[40] FSR. "Force Sensing Resistor Integration Guide and Evaluation Parts Catalog," *Catalog*, Online: http://www.media.mit.edu/resenv/classes/MAS836/Readings/fsrguide.pdf [Accessed: July 20, 2011].

[41] Interlink Electronics. "Force Sensing Resistors Integration Guide," *Online Catalogue*, 2010. Online: http://www.interlinkelectronics.com/sites/default/files/94-00004A_FSR_Integration_Guide_0.pdf [Accessed: July 23, 2011].

[42] Weiss Robotics GmbH & Co. KG. "Intelligent Sensor Module DSA 9205i," 2012. Online: http://www.weiss-robotics.de/tactile-sensing/intelligent-sensor-modules/intelligent-sensor-module-dsa-9205i.html [Accessed: October 25, 2012].

[43] Weiss Robotics. "DSACON32-H Sensor Controller," 2011. Online: http://www.weiss-robotics.de/en/products/tactile-sensing/sensor-controllers/90-dsacon32-h.html [Accessed: July 24, 2011].

[44] B. Siciliano and O. Khatib. *Springer handbook of robotics*, Springer-Verlag New York Inc, 2008.

[45] Pressure Profile Systems Inc. "Capacitive Tactile Sensing," 2010. Online: http://www.pressureprofile.com/technology-capacitive.php [Accessed: July 28, 2011].

[46] C.W. de Silva. *Sensors and Actuators: Control System Instrumentation*, CRC Press, 2007.

[47] S. Pirozzi. "Development of angular, force and tactile sensors for tendon - driven robotic hands," Seconda Università degli studi di Napoli.

[48] Robotiq. "Robotiq Adaptive Gripper," *Brochure*, .

[49] VulcanDesigns. "Vulcan Steel," 2012. Online: http://www.vulcansteel.co.za/ [Accessed: January 4, 2013].

[50] H.G. Phakatkar. *Theory of Machines and Mechanisms I*, Nirali Prakashan, 1999.

[51] R.C. Juvinall and K.M. Marshek. *Fundamentals of machine component design*, John Wiley & Sons, 2006.

[52] RangeVideo. "KX-1 Micro color CMOS camera," 2013. Online: http://www.rangevideo.com/index.php?main_page=product_info&products_id=212 [Accessed: January 6, 2013].

[53] M. Rieger. *Simple Swarm Robotic Platform*, 2010.

[54] Dreamstime. "Water bottle top view," 2013. Online: http://www.dreamstime.com/royalty-free-stock-photo-water-bottle-top-view-image6356685 [Accessed: January 7, 2013].

[55] SAGER Electronics. "ERNI's MicroStac® Mezzanine Connector Delivers," 2013. Online: http://www.sager.com/new-products/ernis-microstac-mezzanine-connector-delivers/ [Accessed: January 7, 2013].

[56] "Technisales (PTY.) LTD.," 2005. Online: http://www.gearboxes.co.za/ [Accessed: January 14, 2013].

[57] Macsteel. "Special Steels Catalogue," 1983. Online: http://www.macsteel.co.za/system/files/080m40_en8_black.pdf?download=1.

[58] Maxon Motors. *Maxon Motor Control - 1-Q-EC Amplifier DEC 24/3 Operating Instructions*.

[59] J. Lepkowski. "Motor Control Sensor Feedback Circuits," 2003. pp. 1–18.

[60] Allegro Microsystems Inc. *ACS712 Datasheet*, 2011.

[61] M. Schmid and S. Ahrends. *Rapid Prototyping with LabVIEW on Microprocessors*, 2013.

[62] Atlantec. "Manson HCS-3300," 2012. Online: http://www.atlantec.pl/zasilacz-laboratoryjny-15v-60a-manson-hcs3300-p-323.html [Accessed: December 12, 2012].

[63] Hensley Technologies. "Agilent U1242B Handheld Digital Multimeter," 2009. Online: http://www.hensleytech.com/agilent-u1242b-handheld-digital-multimeter-4-digit [Accessed: December 12, 2012].

[64] Farnell Element 14. "Agilent Technologies - DSO1002A Oscilloscope," 2010. Online: http://uk.farnell.com/agilent-technologies/dso1002a/oscilloscope-2-ch-60-mhz/dp/1704738 [Accessed: December 12, 2012].

[65] Texas Instruments. *LM35 Precision Centigrade Temperature Sensors*, 2000.

[66] Texas Instruments. *Stellaris LM3S8962 Microcontroller Datasheet*, 2011.

[67] J.M. Evans. *Standards for Visual Acuity*, Newtown: 2006.

[68] The RealVision KnowledgeBase. "Stereoscopic QC and the corner pin," 2012. Online: http://realvision.ae/blog/2011/10/stereoscopic-qc-and-the-corner-pin/ [Accessed: November 5, 2012].

[69] J. Dahl. "Snellen chart," 2008. Online: http://en.wikipedia.org/wiki/File:Snellen_chart.svg [Accessed: November 5, 2012].

[70] Metabo. "Product Catalogue - DrillBE4006," 2012. Online: http://www.metabo.co.za/Product-catalogue-handheld-powertools.23996+M52e83dffa59.0.html [Accessed: December 21, 2012].

[71] FLIR Systems. "MLR100 - Mini Laser Rangefinder," 2012. Online: http://www.flir.com/cvs/cores/view/?id=56598 [Accessed: January 23, 2013].

[72] Leap Motion Inc. "Leap," 2012. Online: https://www.leapmotion.com/ [Accessed: February 7, 2013].

[73] Torqueleader. "TLS Standard Torque Slipping Screwdriver SD 0/W," *3D ContentCentral*, 2013. Online: http://www.3dcontentcentral.com/Download-Model.aspx?catalogid=8622&id=380331 [Accessed: January 27, 2013].

[74] J. Hannah. "Bomb-sniffing robots put to test in Iraq," *MSNBC*, 2007. Online: http://www.msnbc.msn.com/id/17874529/ns/technology_and_science-innovation/t/bomb-sniffing-robots-put-test-iraq/#.UIRkTcXMg84 [Accessed: October 21, 2012].

Appendix A
Assessment of Ethics in Research Projects

Appendix B
Technical Drawings

Introduction

This appendix presents a selection of the technical drawings that were created for manufacture in the Department of Mechanical Engineering Workshop at the University of Cape Town.

For a full set of drawings of all the end-effector components, see the accompanying DVD.

Table of Contents

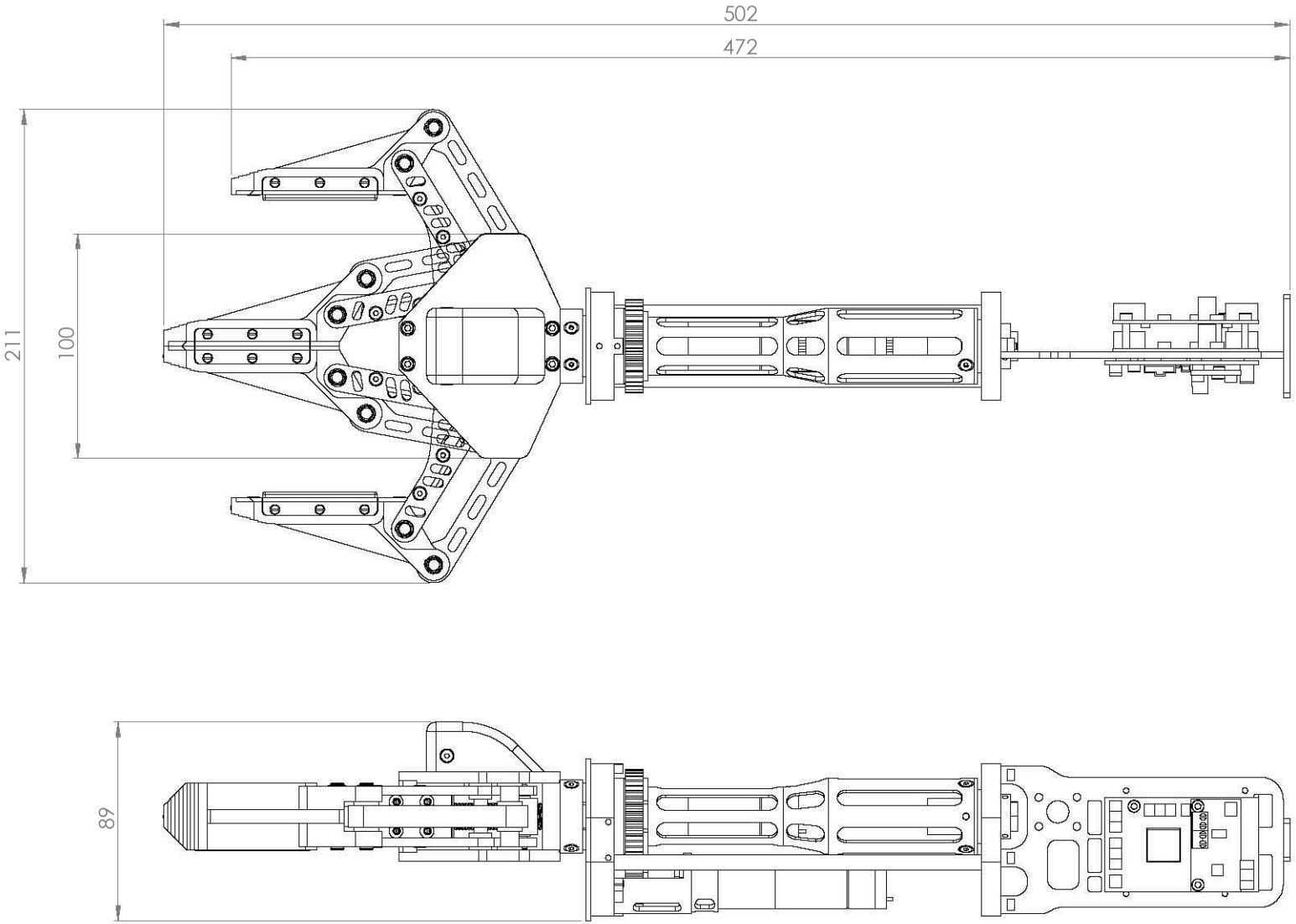

A3 Landscape	University of Cape Town Department of Mechanical Engineering			
	Title: X_Overall_Assembly			
Assembly Drawing	Scale: 1:2	Date: 2013/02/06	Sheet1	of 1
	Drawn By: Michael Rieger		Drawing Number O_X1	

SolidWorks Student Edition.
For Academic Use Only.

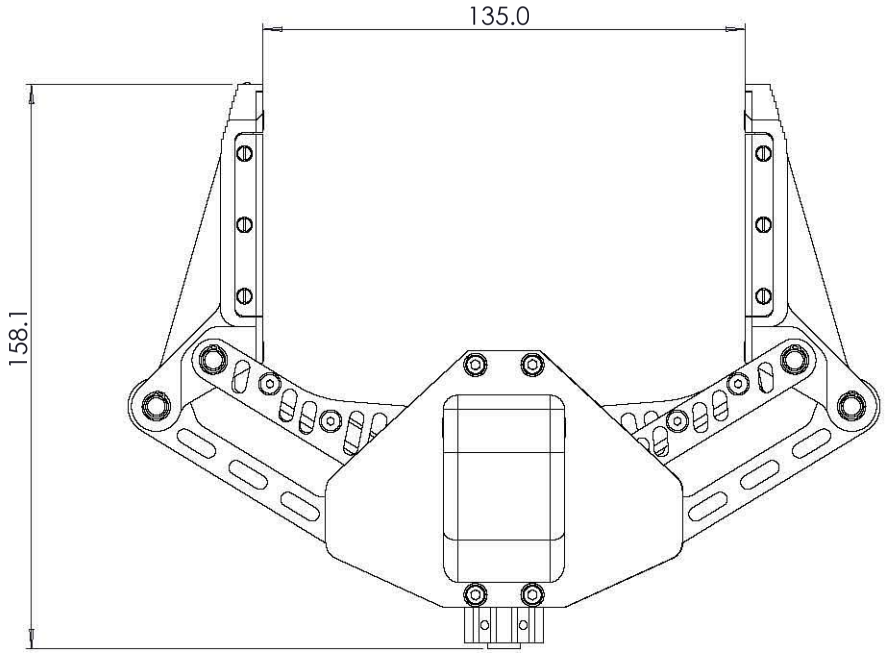

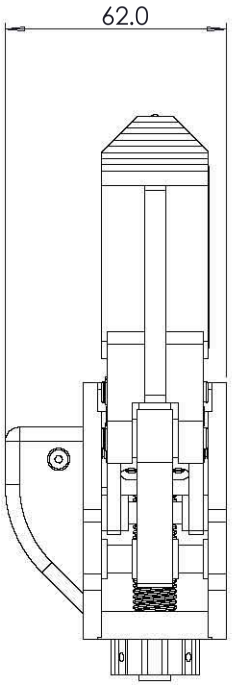

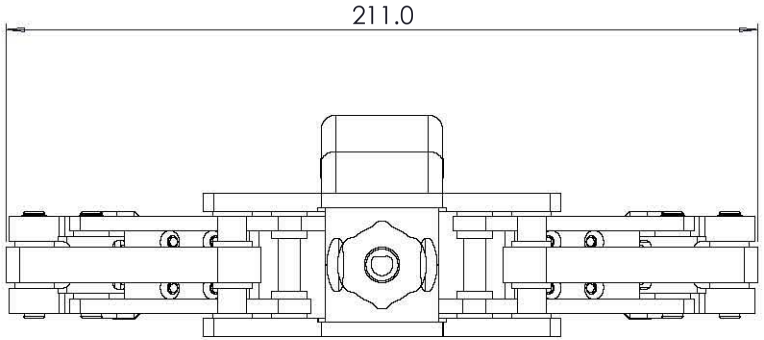

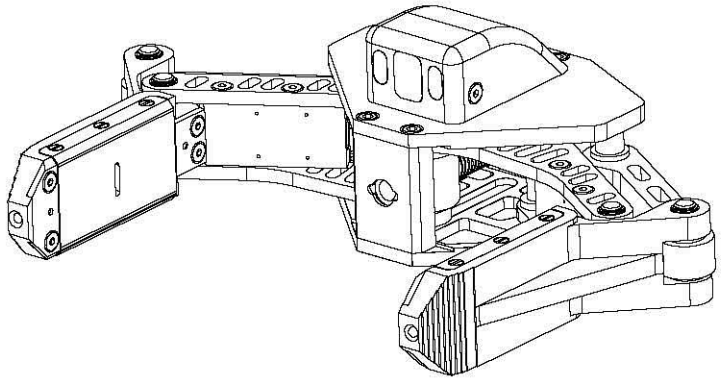

SolidWorks Student Edition.
For Academic Use Only.

Gripper Open Position

A3 Landscape	University of Cape Town Department of Mechanical Engineering			
	Title: X_Gripper_Assembly			
Assembly Drawing	Scale: 1:1.5	Date: 2013/02/06	Sheet1	of 1
	Drawn By: Michael Rieger RGRMIC005 - Robotics Lab		Drawing Number G-X	

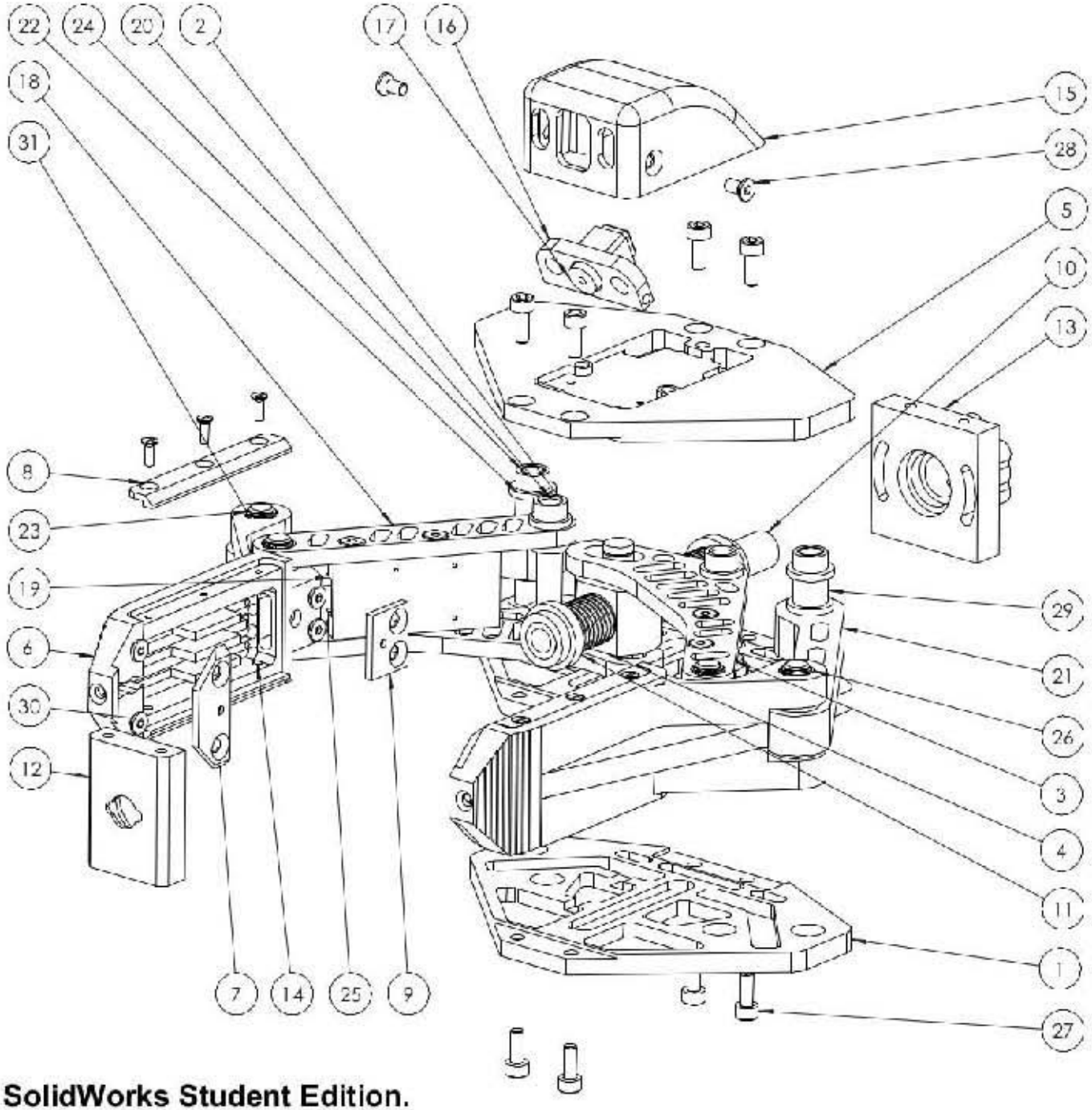

ITEM NO.	PART NUMBER	QTY
1	Gripper_Base_Bottom	2
2	Gripper_Bent_Lever_Bush	8
3	Gripper_Bent_Lever_Steel	2
4	Gripper_Lead_Nut	1
5	Gripper_Base_Top	1
6	Gripper_Finger	2
7	Gripper_Finger_Cover_Front	2
8	Gripper_Finger_Sensor_Mount	4
9	Gripper_Finger_Cover_Back	2
10	Gripper_M12x2_Lead_Screw	1
11	Gripper_Thrust_Bearing	2
12	Gripper_Bearing_Mount_Front	1
13	Gripper_Wrist_Interface	1
14	B18.6.7M - M2 x 0.4 x 6 Slotted FHMS – 6C	12
15	Gripper_Camera_Housing	1
16	Gripper_Camera_Mount	1
17	Gripper_KX-1_CMOS	1
18	Gripper_Mid_Link_Steel	2
19	Gripper_Mid_Link_Pad	2
20	Gripper_Base_Pin	2
21	Gripper_Mid_Out_Link	2
22	Gripper_Finger_Bearing	12
23	Gripper_Finger_Pin	4
24	Gripper_Base_Pin_Outer	2
25	Gripper_Mid_Link_Pad_Cover	2
26	Gripper_Mid_Out_Link_Bearing	4
27	B18.3.1M - 3 x 0.5 x 8 Hex SHCS - - 8NHX	8
28	B18.3.5M - 3 x 0.5 x 6 Socket FCHS – 6N	2
29	Gripper_Outer_Link_Spacer	4
30	B18.3.5M - 3 x 0.5 x 6 Socket FCHS – 6C	16
31	B27.7M - 3AM1-6	4

A3 Landscape

University of Cape Town
Department of Mechanical Engineering

Title: K_Gripper_Exploded

Assembly Drawing | Scale: 1:1 | Date: 2013/10/10 | Sheet 1 of 1

Drawn By: Michael Rieger
RGRMIC005 - Robotics Lab

Drawing Number: G-XE

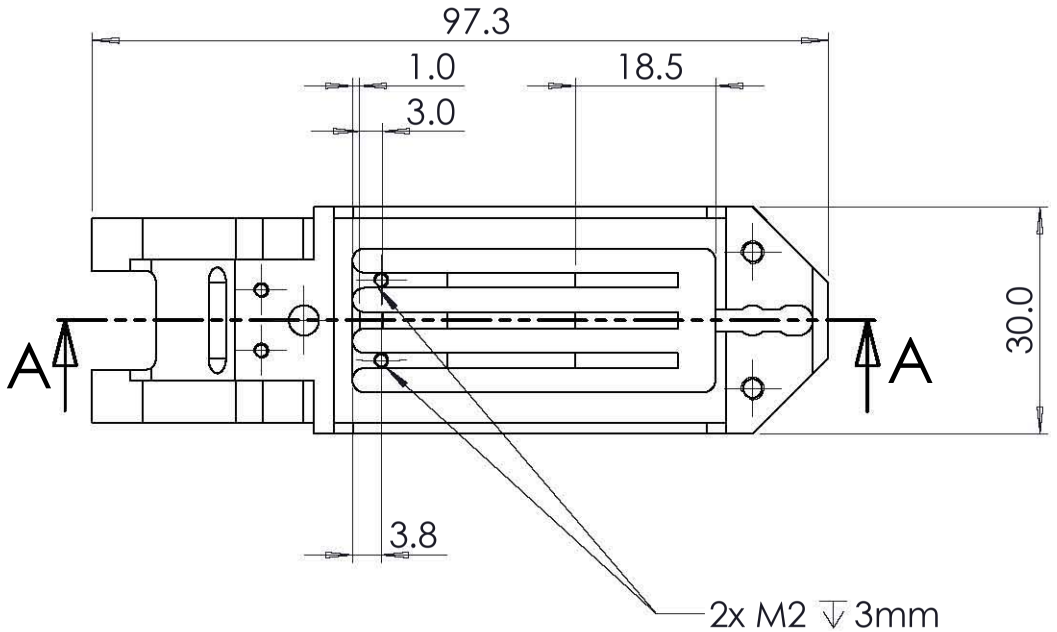

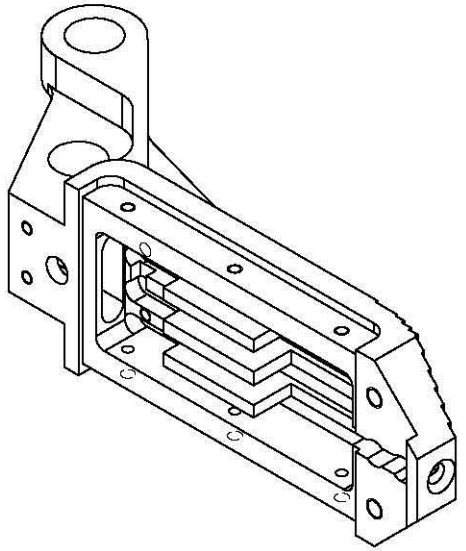

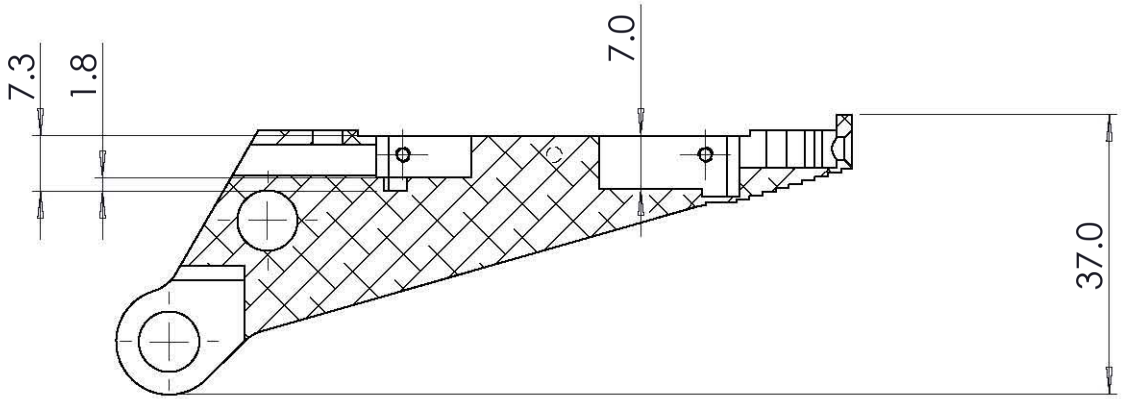

SECTION A-A

SolidWorks Student Edition.
For Academic Use Only.

A4 Landscape	University of Cape Town Department of Mechanical Engineering			
	Title: Gripper_Finger			
Part Finish	Scale: 1:1	Date: 2013/02/07	Sheet1	of 1
Material: 6061 Alloy	Drawn By: Michael Rieger		Drawing Number G-1 Mod	

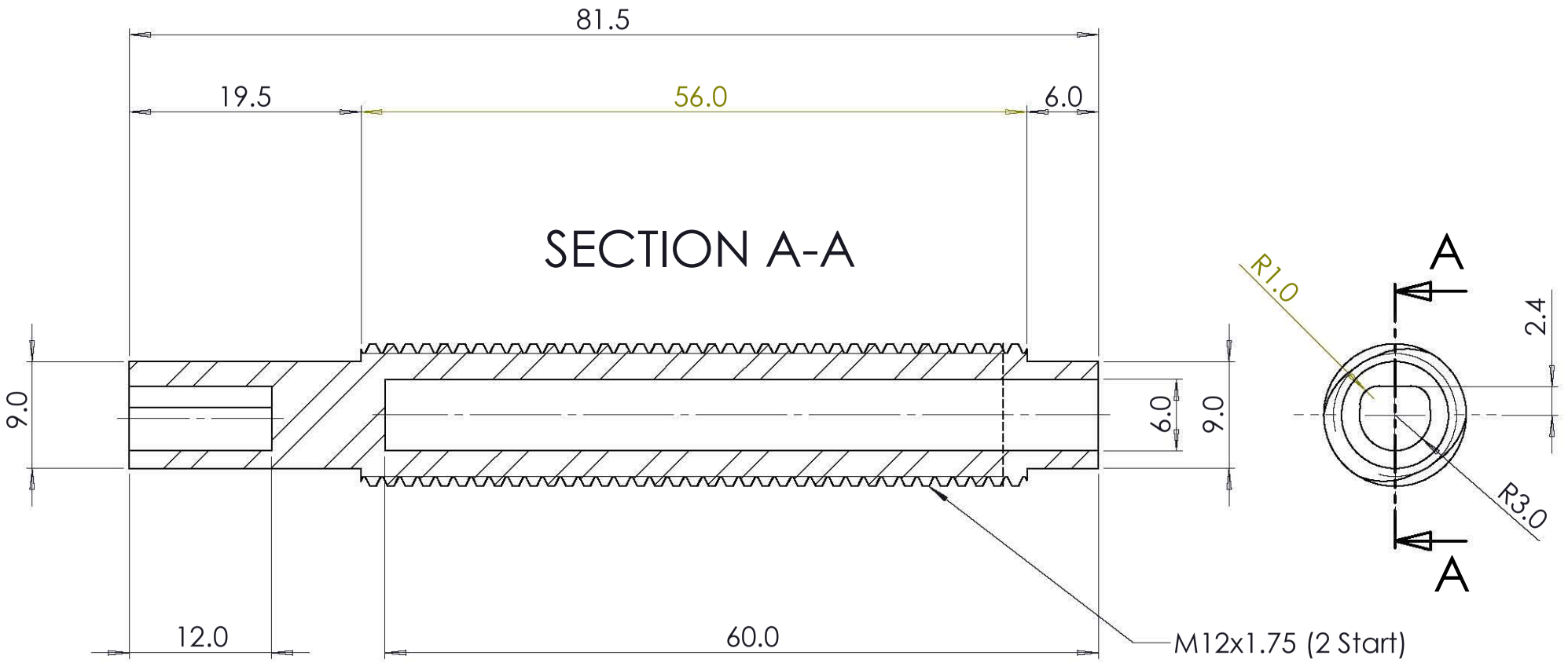

SolidWorks Student Edition.
For Academic Use Only.

A4 Landscape	University of Cape Town Department of Mechanical Engineering				
	Title: Gripper_M12x2_Lead_Screw				
Quantity: 1	Part Finish	Date: 2013/02/06	Scale: 2:1	Sheet1	of 1
Material: Plain Carbon Steel	Drawn By: Michael Rieger RGRMIC005 - Robotics Lab			Drawing Number G-12	

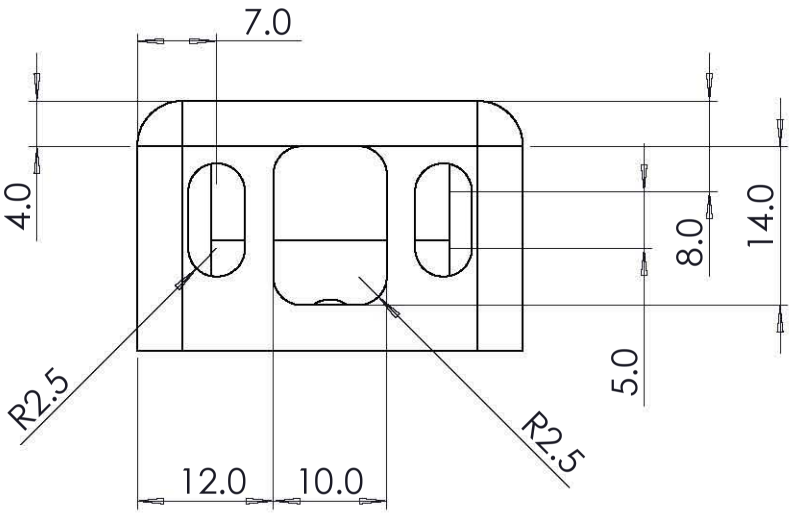

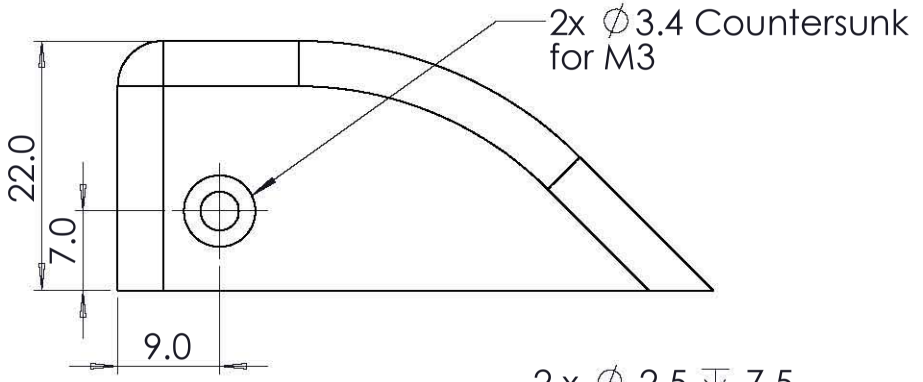

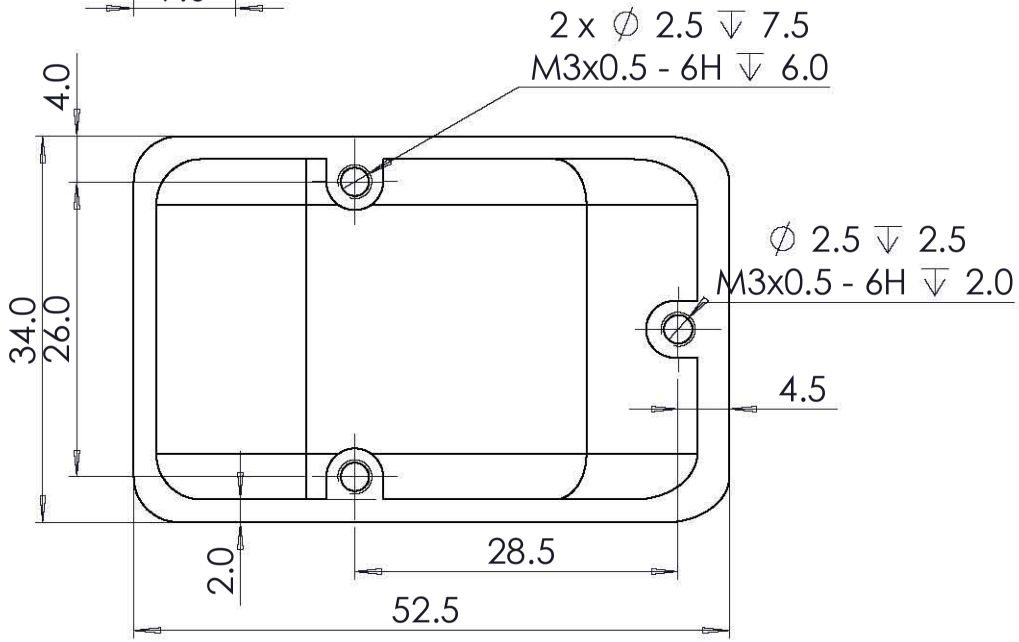

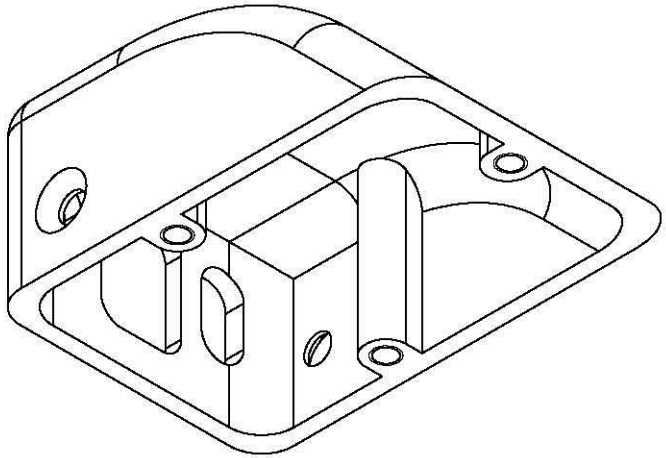

SolidWorks Student Edition.
For Academic Use Only.

A4 Landscape	University of Cape Town Department of Mechanical Engineering				
	Title: Gripper_Camera_Housing				
Quantity: 1	Part Finish	Date: 2013/02/06	Scale: 1.5:1	Sheet1	of 1
Material: 6061 Alloy	Drawn By: Michael Rieger RGRMIC005 - Robotics Lab			Drawing Number G-22	

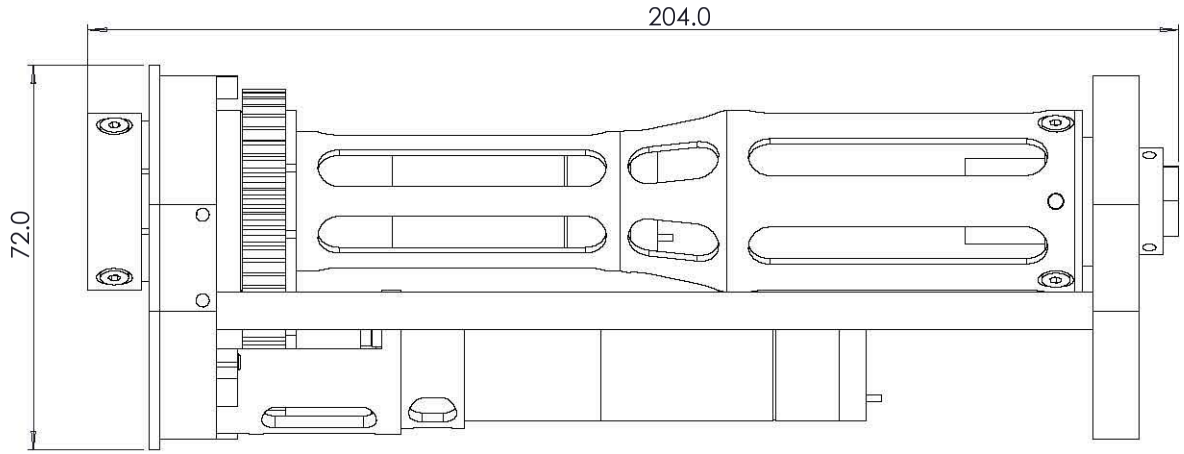

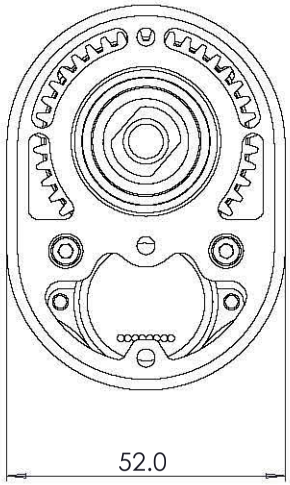

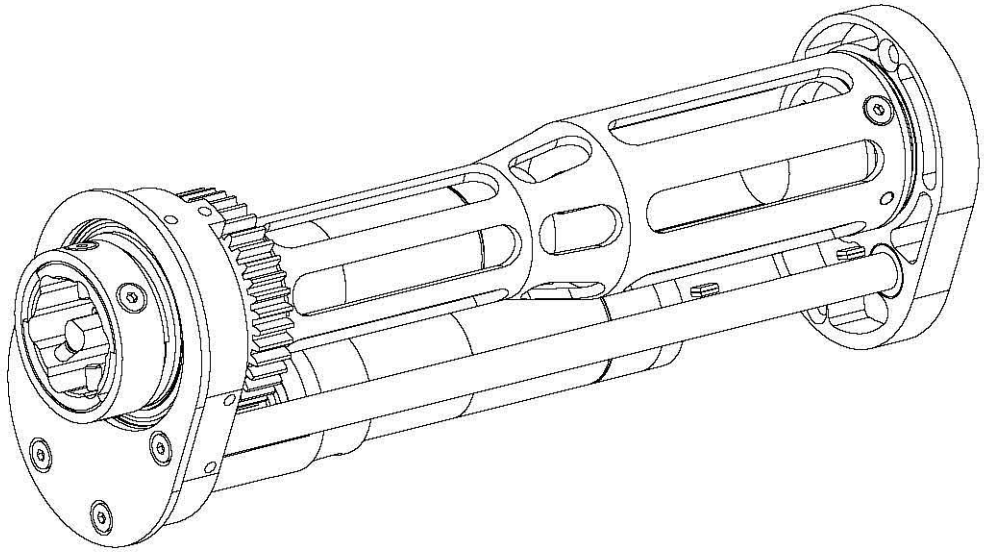

SolidWorks Student Edition.
For Academic Use Only.

A3 Landscape	University of Cape Town Department of Mechanical Engineering			
	Title: X_Wrist_Assembly			
Assembly Drawing	Scale: 1:1	Date: 2013/02/06	Sheet1	of 1
	Drawn By: Michael Rieger Robotics Lab		Drawing Number W-X	

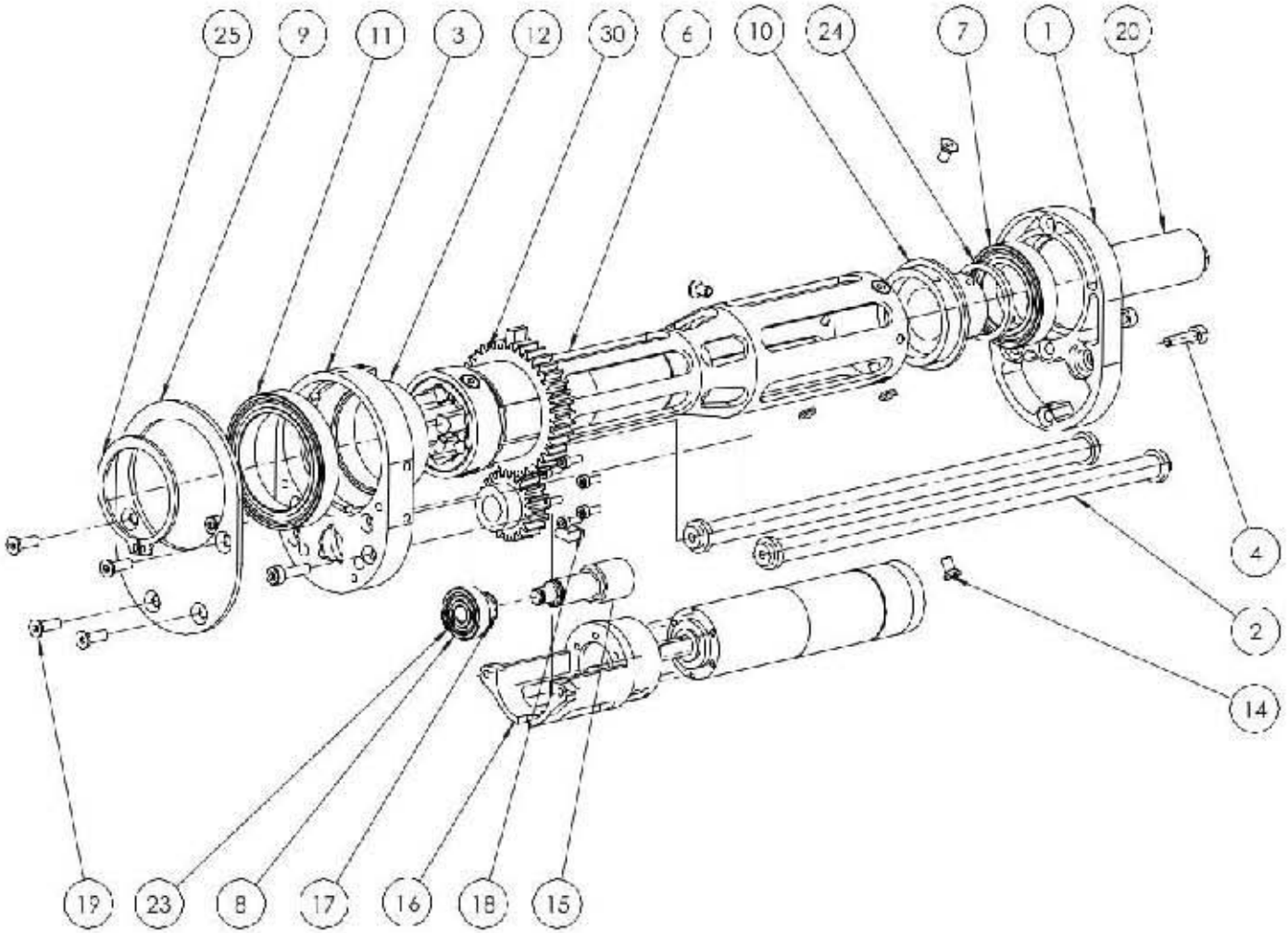

ITEM NO.	PART NUMBER	Default/QTY
1	Wrist_Back_Bracket	1
2	Wrist_Long_Spacer	2
3	Wrist_Front_Bracket	1
4	B18.3.1M - 3 x 0.5 x 12 Hex SHCS -- 12NHX	6
5	FC22_GP22_Sens_Motor_Assembly	2
6	Wrist_Gripper_Motor_Holder	1
7	61804_2R7	1
8	625_2Z	1
9	Wrist_Front_Bracket_Plate	1
10	Wrist_Back_Stop	1
11	61806_2R7	1
12	Wrist_Gear_Bearing_Spacer	1
13	B18.3.1M - 2 x 0.4 x 6 Hex SHCS -- 6NHX	12
14	B18.3.5M - 3 x 0.5 x 6 Socket FCHS -- 6N	5
15	Wrist_Pinion_Gear_Shaft	1
16	Wrist_Pinion_Motor_Bracket	1
17	627.7M - 3AM1-8	1
18	Wrist_Gear_Key	2
19	B18.3.5M - 3 x 0.5 x 10 Socket FCHS -- 10N	4
20	Wrist Slip Ring BTC016 30	1
21	Wrist_Pos_Magnet_3x1	1
22	Wrist Hall Effect	2
23	627.7M - 3AM1 5	1
24	Wrist_Rear_Spacer	1
25	627.7M - 3AM1 30	1
26	Top Section Composite Tube	1
27	Arm_Interface	1
28	Wrist_Front_Wire_Cover	1
29	B18.3.5M - 3 x 0.5 x 10 Socket FCHS -- 10C	4
30	ISO - Spur gear 1M 40T 14.5PA 8FW -- S40A75H50 30.0N	1
31	ISO - Spur gear 1M 20T 14.5PA 8FW -- S20B14H14L8.0N	1

A3 Landscape

University of Cape Town
Department of Mechanical Engineering

Title: X_Wrist_Exploded

Assembly Drawing | Scale: 1:1.0 | Date: 2013/10/10 | Sheet 1 of 1

Drawn By: Michael Rieger, Robotics Lab

Drawing Number: WRXE

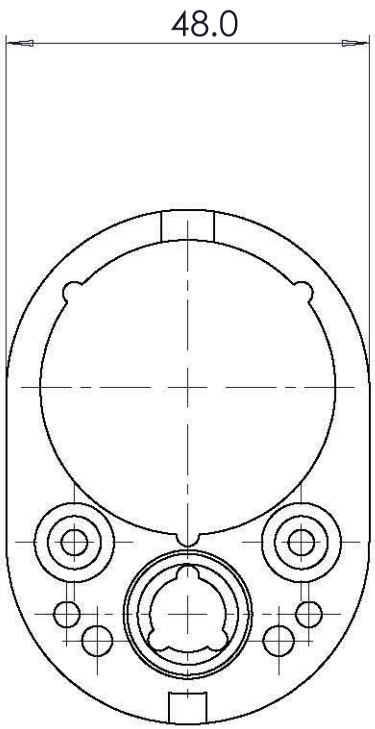

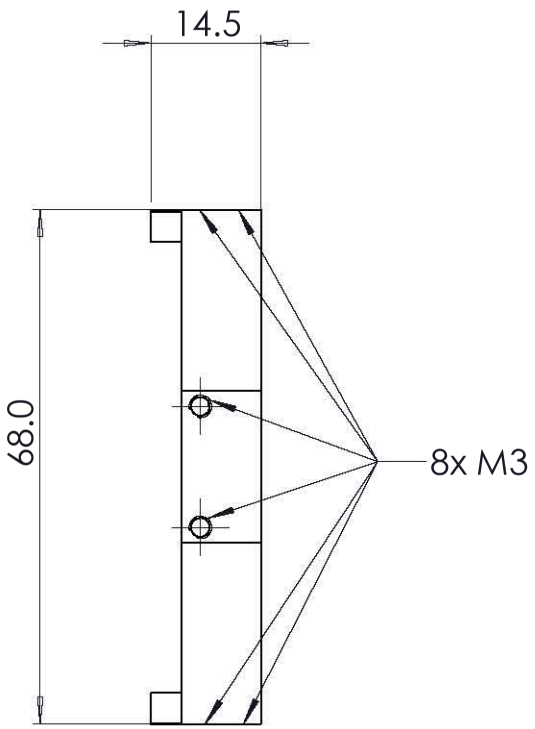

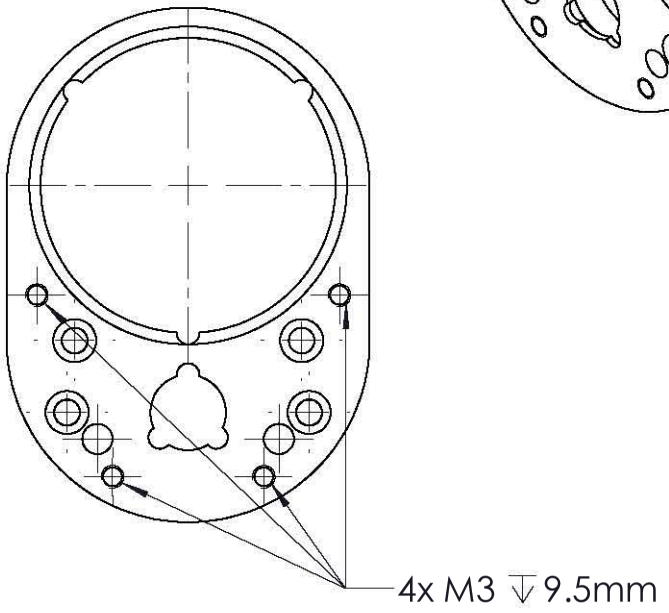

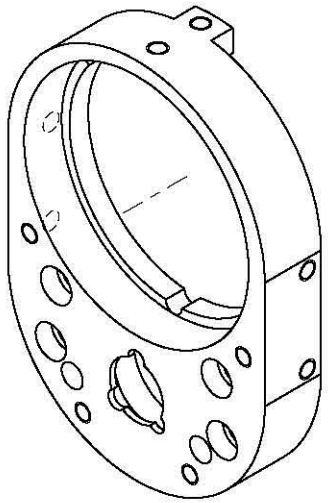

SolidWorks Student Edition.
For Academic Use Only.

A4 Landscape	University of Cape Town Department of Mechanical Engineering				
	Title: Wrist_Front_Bracket				
Quantity: 1	Part Finish	Date: 2013/02/06	Scale: 1:1	Sheet1	of 1
Material: 6061 Alloy	Drawn By: Michael Rieger Robotics Lab			Drawing Number W-9	

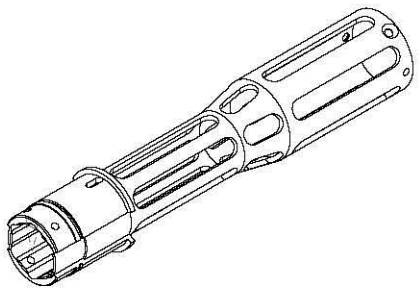

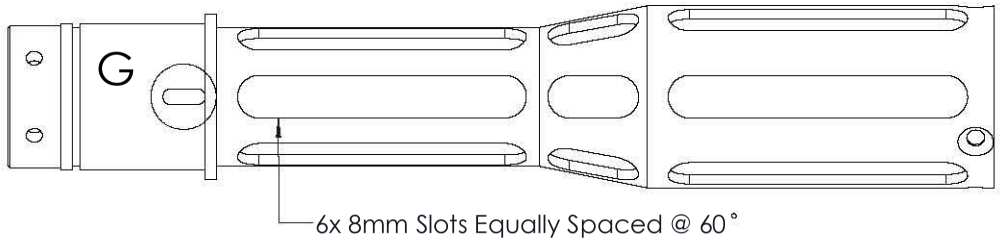

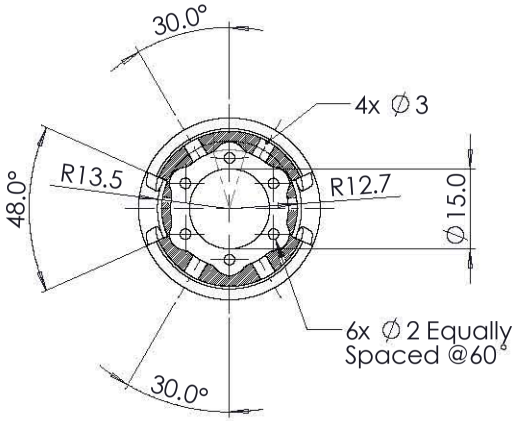

SECTION B-B
SCALE 1 : 1

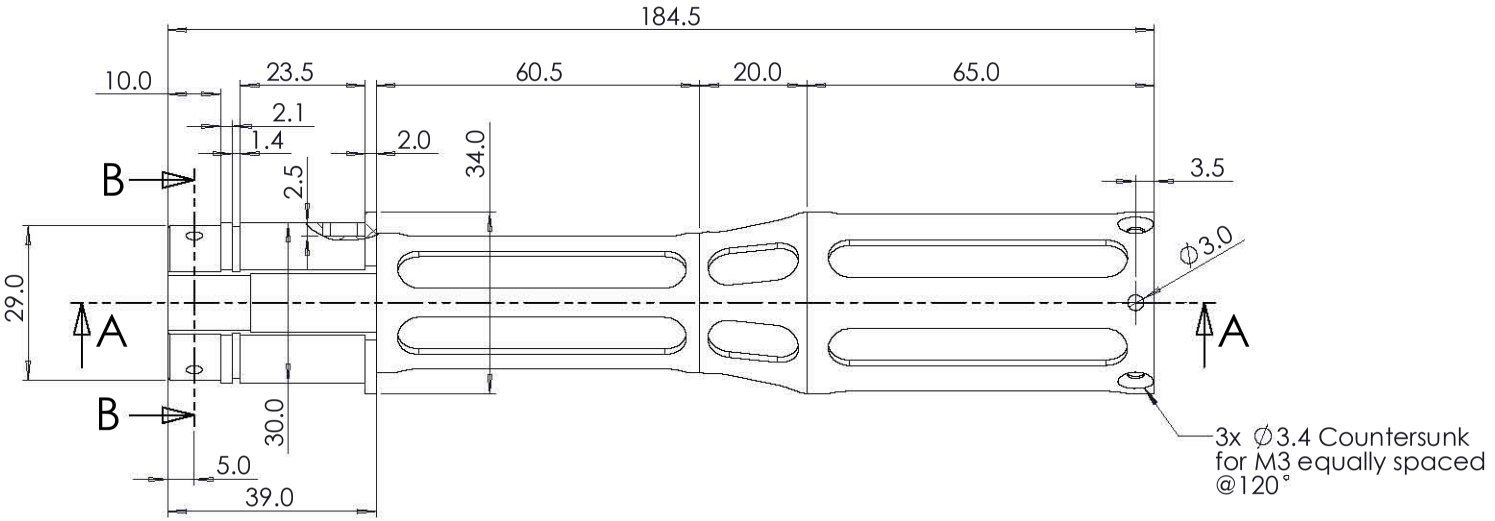

SECTION A-A
SCALE 1 : 1

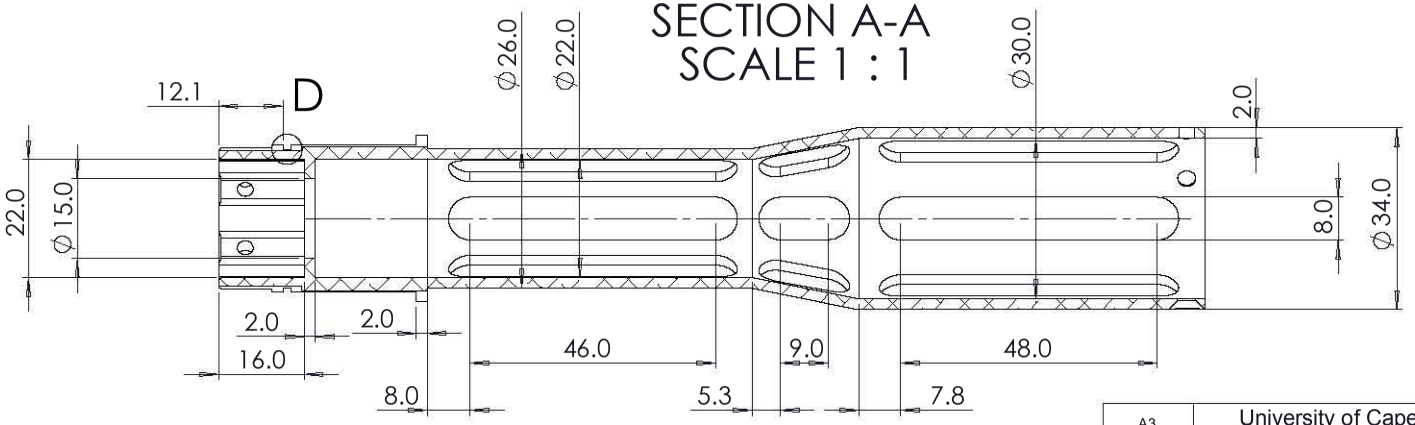

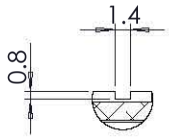

DETAIL D
SCALE 2 : 1

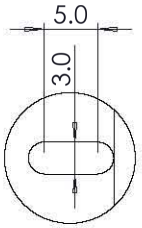

DETAIL G
SCALE 2 : 1

SolidWorks Student Edition.
For Academic Use Only.

A3 Landscape	University of Cape Town Department of Mechanical Engineering				
	Title: Wrist_Gripper_Motor_Holder				
Quantity: 1	Part Finish	Date: 2013/02/06	Scale: 1:1	Sheet1	of 1
Material: 6061 Alloy	Drawn By: Michael Rieger Robotics Lab			Drawing Number W-12	

Appendix C

Detailed Testing

Table of Contents

List of Figures

List of Tables

C-1. Introduction

In the main report, a list of detailed specifications was generated based on certain identified and estimated requirements for a fully functional end-effector system. The testing procedures detailed in this appendix will reference these specifications in order to gauge certain end-user performance characteristics and to ascertain if these specifications have been met.

Every test has been conducted utilising the same standard testing procedures and are presented in a modified format of the testing methods found in the American Society for Testing and Materials (ASTM) Blue Book [1]. This was to ensure that the reader would be provided with a structured and standardised reference guide in order to make testing methods easy to follow, comparable and repeatable if necessary.

Each test has been set up with the following general structure:

- Detailed title
- Indicate significance or importance of the test and its intended use; describe usefulness to predict end-user characteristics and performance
- Clarify terminology and definitions used in test
- List types of apparatuses and measuring instruments required to conduct the test
- Declare any safety precautions that were followed
- Indicate any calibrations to be performed before running the test
- Indicate if the test is repeatable and reproducible
- Detail measurement range over which test is valid
- Detail procedure on conducting the test (include sampling procedure and how sampled were attained)
- Present relevant data / samples
- Present relevant calculations and analysis of data
- Interpret test data output
- Describe any uncertainty in measurement results

C-2.1 Testing – Overall System

C-2.1.1 Mass Measurement Tests

Test Overview

One of the primary specifications for the end-effector was related to the overall mass as it could have a significant impact on the performance of the manipulator arm as a whole. As a result, future designs could be optimised based on the test results.

The aim of the following tests was to determine individual component masses, subsystem masses and the largest mass contributors of each system.

Apparatus and Measuring Equipment

1x Mettler PM30-K Scale

Calibration Requirements / Important Test Information

Care was taken to perform the tests on a flat, even surface to ensure accurate readings. Although anodising was performed before conducting this test, the mass changes should be insignificant in comparison to the original part masses.

Test Procedure

This test focussed on three specific mass areas:

1. Individual Component Masses
2. Subsystem Masses
3. Overall System Mass

The first step in conducting the test was to set up the scale on a flat surface. Parts and subsystems were placed on the scale one by one and the masses were recorded. SolidWorks Mass Analysis, which proved to be highly accurate, was also used to provide masses on some parts that were already assembled and could not be disassembled easily. The final test was the overall system mass.

From the recorded readings, pie charts were created indicating the highest mass contributors for each subsystem as well as the overall system.

Test Results

1. Gripper Subsystem

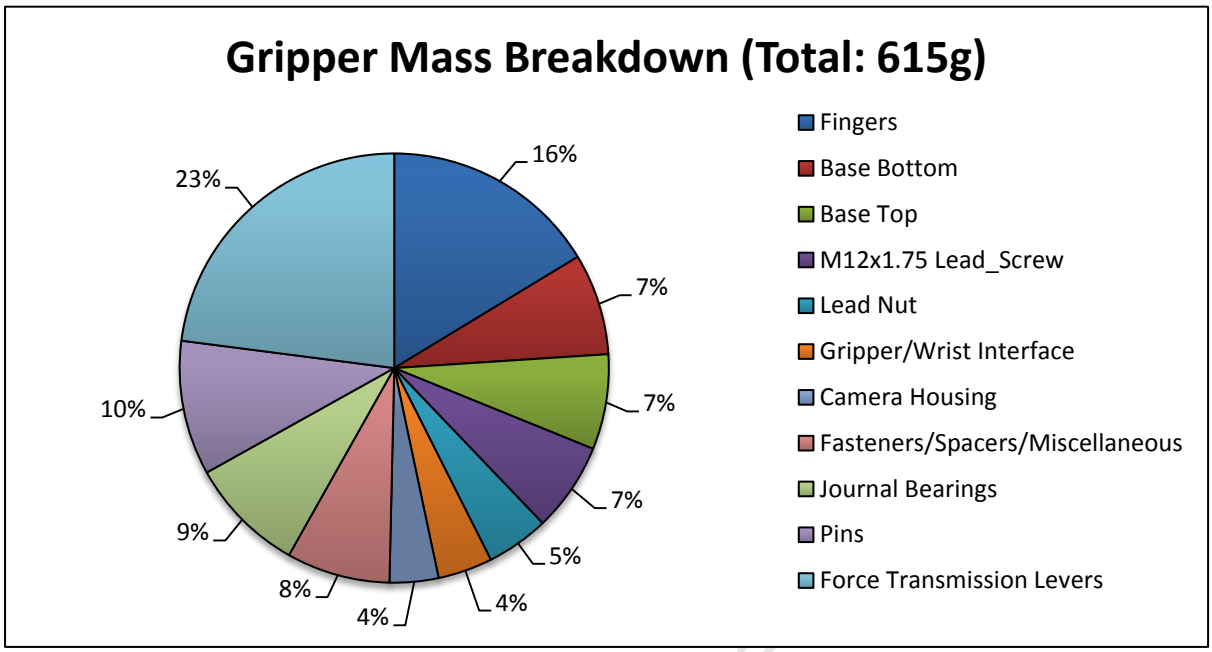

Figure C- 1: Pi Chart of Gripper Primary Mass Contributors

Figure C- 1 shows the mass breakdown of the gripper subsystem. As can be seen from the chart, the greatest mass contributors were the force transmission levels at 23% and the gripper fingers at 16%. The various pins holding together the linkages made up about 10% of the total, with each subsequent component group contributing 5% - 9%.

2. Wrist Subsystem

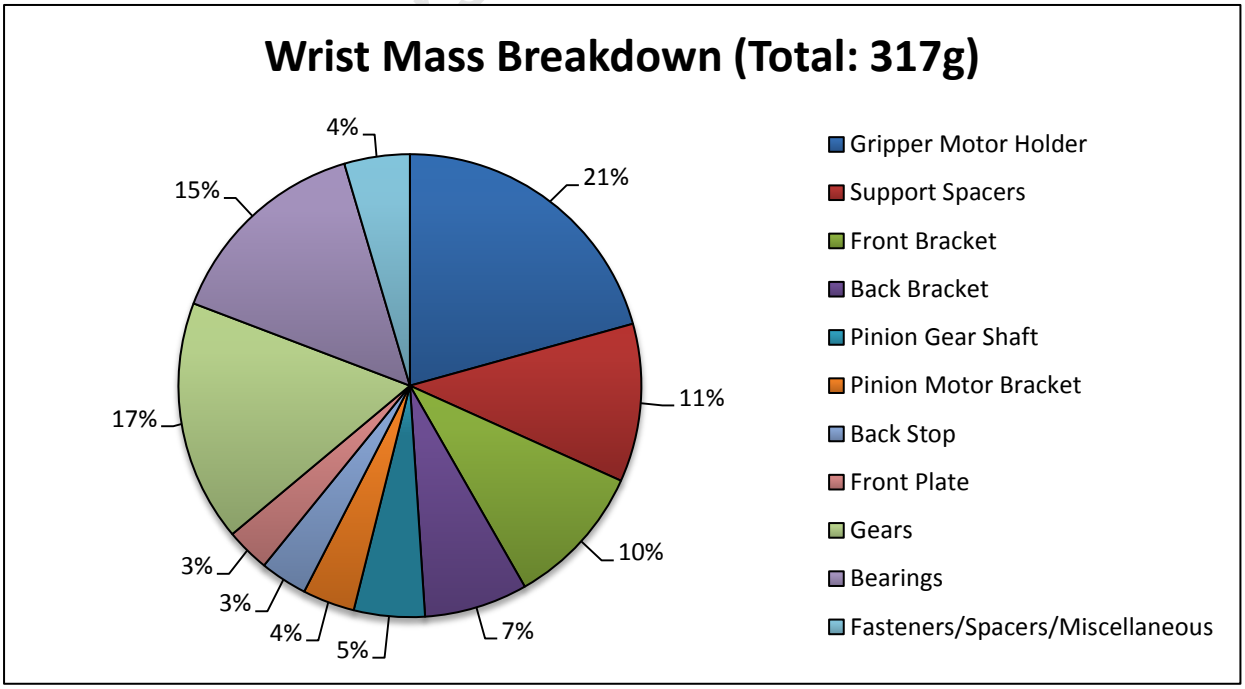

Figure C- 2: Pi Chart of Wrist Primary Mass Contributors

The wrist mass breakdown is shown in Figure C- 2. Of the 317g total, the gripper motor holder was the largest mass contributor at 21%, followed by the gear train at 17% and the bearings at 15%.

3. Electronics

A mass breakdown was not performed for the electronics module due to the large variety of components that were involved, including wires, connectors and sensors. The final mass was determined to be roughly 200g, including two Maxon DEC24/3 speed controllers, an LM3S8962 embedded controller, one current sensor board, a 30-way slip-ring as well as temperature and Hall Effect sensors.

4. Subsystem Mass Distributions

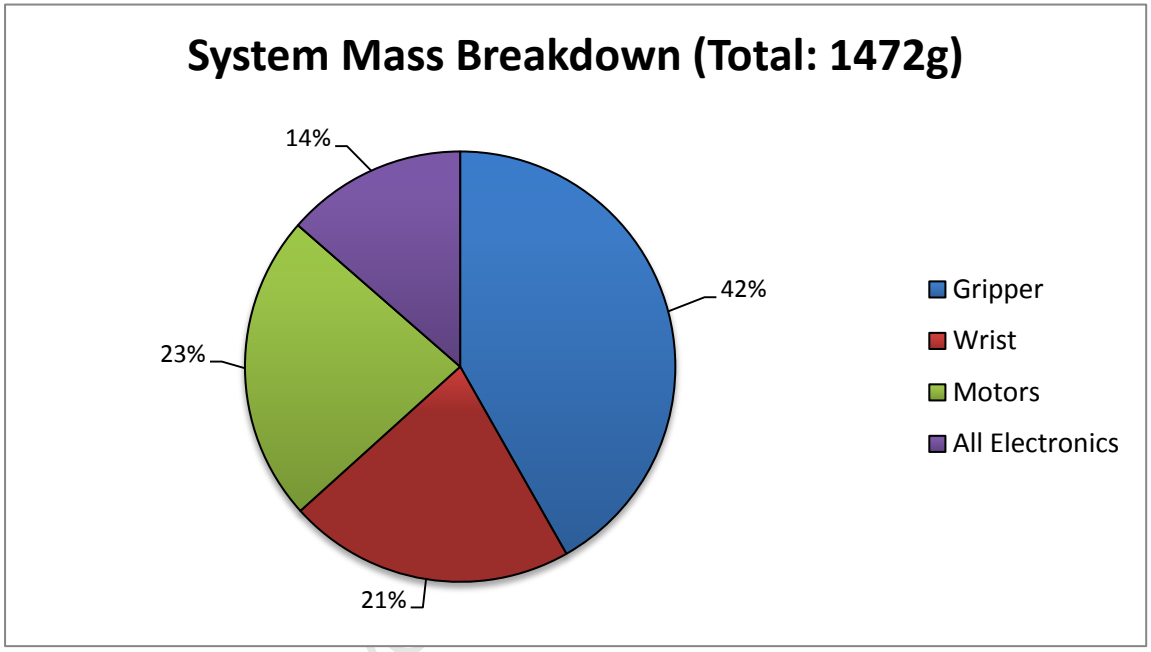

Figure C- 3: Pi Chart of End-Effector Subsystem Mass Contributors

The total mass of the end-effector was determined to be 1472g. As was expected, the gripper module was the largest mass contributor at 615g followed by the two Maxon motors at 23% and the wrist section at 21%. Surprisingly, the electronics subsystem also made a significant contribution at 14%.

Conclusions

The original target mass set by Peter Henson was 800g for the gripper and the wrist sections excluding the motors and electronics systems. Together, the final mass for these two systems was 932g, 16.5% more than was originally specified. The total for the entire end-effector system was 1472g. Significant weight reductions were implemented throughout the mechanical design of the system, but further reductions may be possible with a deeper strength to weight process analysis. With lower power motors, the total weight could also be reduced further due to the requirement for lower stress capable components.

C-2.1.2 Overall System Power Consumption Test

Test Overview

As the rescue robot is powered off six Makita 18V 3Ah batteries, the power consumption of every subsystem is important to the overall efficiency of the platform. For this test, the power consumption of the end-effector system was to be determined. This involved isolating each subsystem and measuring the current drawn and respective voltage for each.

A breakdown of individual contributors was then assembled to pinpoint high power usage subsystems.

Apparatus and Measuring Equipment

1x	End-effector mounting fixture	
1x	End-effector system	
1x	Agilent Multi-meter (U1242B)	[2]
1x	Manson HCS-3302 15A Power Supply	[3]

Figure C- 4: Power Measurement Test Setup

Test Procedure

The tests were performed by isolating every subsystem in turn and measuring the current on the 18V line. These systems included the gripper and wrist motor controllers and quadrature encoders, an LM3S8962 µP, a dual current sensor, the gripper integrated controller with LED lighting and a gripper camera.

Test Results and Analysis of Test Data

Table C- 1 and Figure C- 5 below present the data that was collected from the individual power tests.

Table C- 1: Power Measurement Data

Component	Voltage (V)	Current (mA)	Power (W)
Gripper Motor Controller	18	25	0.45
Wrist Motor Controller	18	25	0.45
LM3S8962 Microprocessor	18	84	1.51
Current Sensor	18	13	0.23
Gripper Integrated Controller	18	35	0.63
Quadrature Encoders	18	10	0.18
Total	18V	192mA	**3.45W**
LED Lighting (Max. Brightness)	18	34	0.61
Gripper Camera	18	68	1.22
Total	18V	294mA	**5.28W**

As can be seen from the table above, the end-effector drew roughly 3.5W in an idle state, peaking at 5.3W with the LED lights and gripper camera enabled. With both the gripper and wrist motors under full load, a peak power draw of approximately 85W may be approximated.

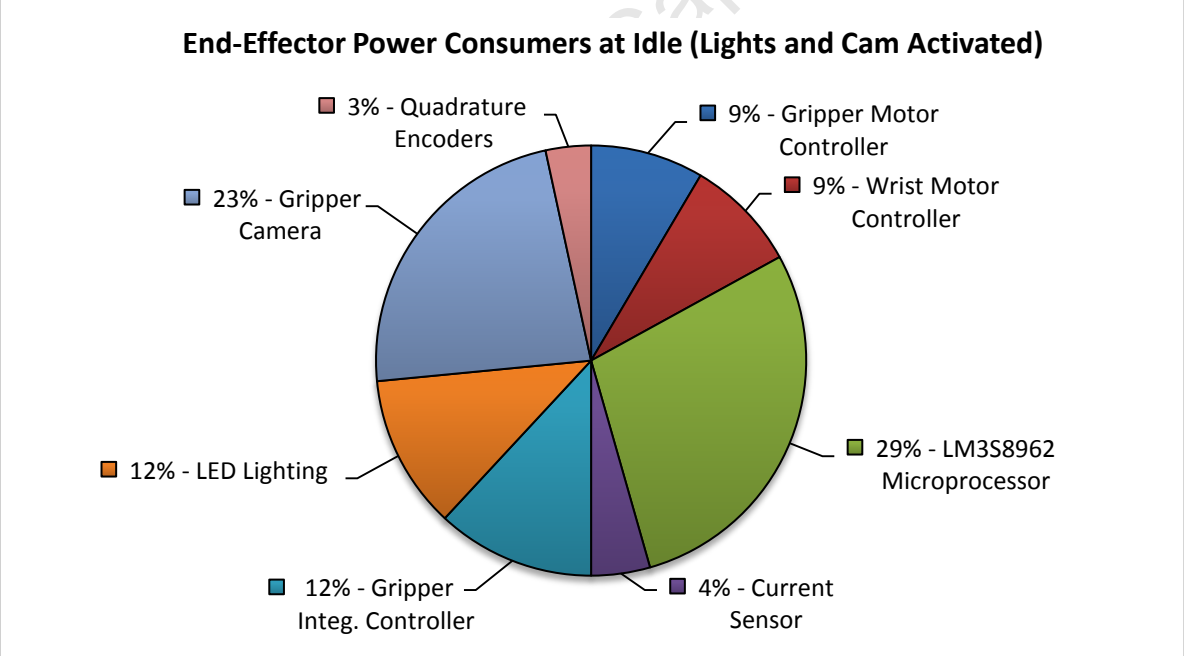

Figure C- 5: Pie chart showing the individual power consumers

From the chart above, it can be seen that the LM3S8962 primary controller was the largest power consumer at 29%, with the gripper camera next at 23%. The LED lighting and integrated gripper controller each made up 12% of the total usage.

Conclusions

From the tests above, it may be concluded that the end-effector used roughly 3.5W in an idle state and 5.3W with the LED lights and the gripper camera activated. Under full mechanical load, this would provide a peak power usage of not more than 85W. The tests also identified that the LM3S8962 was the highest power consumer and utilised about 44% of the overall power during idle operation. This is significant and may, in part, be due to the LabView ARM Embedded software running on the processor. During testing it was noted that using the LabView suite increased power usage on the processor by up to 100% compared to running regular C-code. If power consumption should be minimised further, this should be the first subsystem to be re-evaluated.

C-2.1.3 System Usability Testing

Test Overview

The usability and intuitiveness of an electro-mechanical system is of vital importance to a remote operator, both in terms of optimising movements and making a system simple to operate. In order to test for these criteria, nine inexperienced people were selected to each perform the simple task of gripping a bottle and placing it on a specified target. Each person was then requested to fill out a short questionnaire (see attached DVD) in order to rate individual sub-functions (out of five) as well as to judge the overall system performance. This was done separately for the end-effector system and the manipulator arm. These tests were performed in collaboration with Bradley Springer, an MSc student working on the inverse kinematic control of the Ratel manipulator arm.

Apparatus and Measuring Equipment

1x Powered Ratel Manipulator with End-Effector Installed
1x End-Effector Control Box with Bosch VIPX2
1x Graphical User Interface

Calibration Requirements / Important Test Information

After initial system power-up, the manipulator arm was recalibrated by B. Springer link by link using a predetermined calibration routine. Thereafter, the gripper and the wrist systems were calibrated using the auto- calibration routines provided on the graphical user interface.

Test Procedure

The tests were started by placing the arm in its standard pose with all control aids locked. A predetermined description of the system elements, as found on the graphical user interface, was then communicated to the user.

Two test runs were then performed where the user had to relocate a bottle from one position to another. During these practice runs the user could ask for assistance if needed. A final unassisted run was then performed for each user, after which a short questionnaire was given out for them to provide feedback on their experience. This test run was timed and the precision of the placement measured with a ruler. Figure C- 6, below, shows a test run in progress. The arrow indicates the relocation of the bottle from one location to the next.

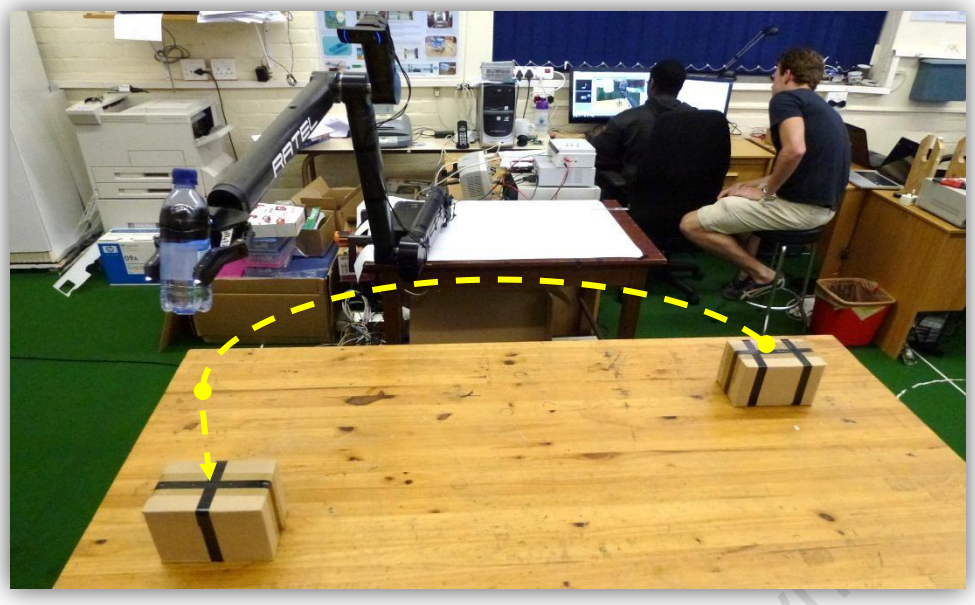

Figure C- 6: An Active Test Run in Progress

Test Results and Analysis of Test Data

In total, nine users were tested and provided feedback on their experience with the system. Figure C- 7 illustrates the averages that were recorded for each relevant sub-function of the end-effector.

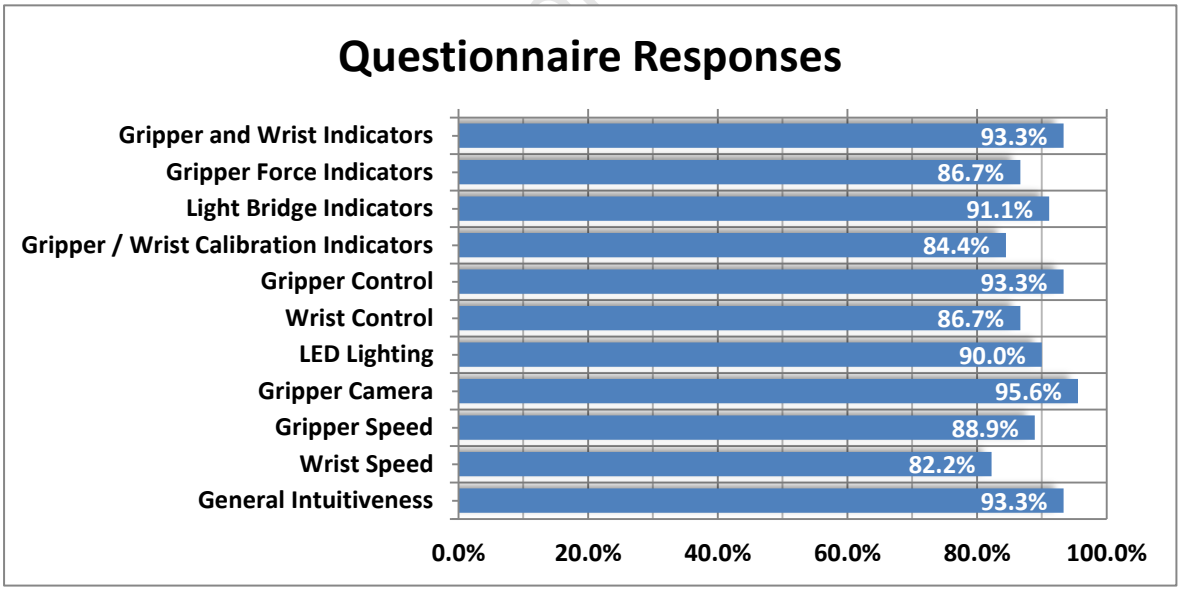

Figure C- 7: Summary of Responses to Usability Testing

From the distribution, it may be concluded that all sub-systems performed satisfactorily and as intended. As was indicated by the additional comments that were provided by users, the wrist speed, wrist control and gripper/wrist calibration indicators should potentially be re-evaluated.

In addition, the time to complete the main task was measured against the placement accuracy of the water bottle to the specified target. The following graph illustrates this data.

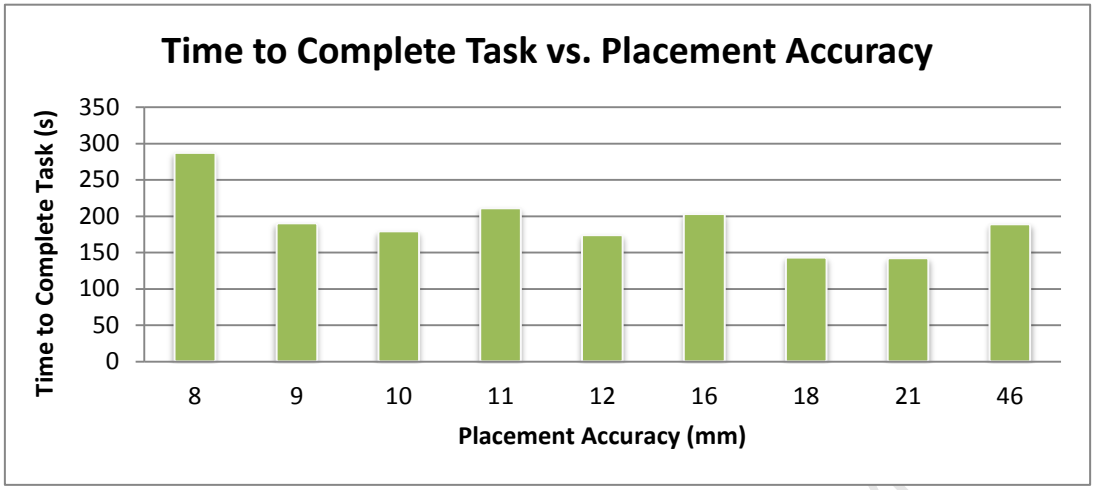

Figure C- 8: Time to Complete Task vs. Placement Accuracy

Although definitive conclusions cannot be drawn from data above due to the relatively small sampling size (nine users), it would appear that an inexperienced user could, on average, perform the set task in about 3 minutes with an accuracy of roughly 15mm.

The following is a short summary of the additional comments that were recorded on the user feedback questionnaires:

- Commendation on the operation of the force indicator
- Commendation on the assistance of the light bridges
- Wrist speed too sensitive and fast
- Gripper too slow
- A home position for the wrist would be advantageous
- Speed of wrist and gripper should be adjustable
- Gripper camera not effective during an actual gripping operation (too close)
- Addition of a cross-hair on the camera feed could be advantageous
- Possible show light bridges as moveable LEDs on the gripper graphic image

Conclusions

The tests above presented a positive outcome in terms of the usability and intuitiveness of the overall manipulation system. The comments and recommendations that were made by users reflected the data that was collected (Figure C- 7) and should be evaluated further for possible implementation in the system. The overall feedback for the end-effector was good, with most sub-functions receiving high ratings.

For the set task the average test time was roughly 3 minutes with an approximate accuracy of 15mm. For an inexperienced user this was remarkably good and these values may certainly be improved upon with additional practice and training.

C-2.1.4 Dual Current Sensor Board

Test Overview

Current sensing fulfils an important end-effector system function as it may be directly related to the force or torque being exerted by a motor link. For this reason, a custom current sensing board was developed. The board was produced in a 20A and a 5A configuration and can be used to sense positive and/or negative currents. The following tests will attempt to validate their use on the manipulator arm and the end-effector system.

Apparatus and Measuring Equipment

1x	Agilent Multi-meter (U1242B)	[2]
1x	Manson HCS-3302 15A Power Supply	[3]
1x	Agilent DSO1002A Oscilloscope	[4]
1x	Current Sensor Board (5A)	
1x	Current Sensor Board (20A)	

The test setup is shown in Figure C- 9 below:

Figure C- 9: Current Sensor Test Setup and Connections

Calibration Requirements / Important Test Information

5A Current Sensor Board: This version of the current sensor was configured using an Allegro ACS712 5A chip with a differential amplifier referenced to 2.5V and a gain of 5.6.

20A Current Sensor Board: This version of the current sensor was configured using an Allegro ACS712 20A chip with a differential amplifier referenced to ground and a gain of 0.67.

Test Procedure

The tests were conducted by shorting the Manson power supply through one of the modules on a dual sensor board. The built-in current limit of the power supply was used to restrict the amount of current to the board, but was not used to actually measure the current. This was done using an Agilent multi-meter in series with the sensor. The output voltage was then recorded for each current reading using an oscilloscope. For the 20A sensor the current range was limited to+-15A by the power supply. The 5A sensor was tested along its full current range of +-5A.

Test Results and Analysis of Test Data

The graph below shows a plot of the 5A configuration sensor with a 2.5V reference on the inverting input of the differential amplifier. This sensor configuration can be found in the end-effector and is used to measure the currents for both the wrist and gripper motors. The gain and inverting voltage reference were selected to give an improved output resolution up to 3A (stall current for the Maxon EC22 40W motors), as the potential for force derivation from current draw was a priority.

As can be seen in the plot below, negative currents up to -5A give an output of 0V as expected. On the positive current side, the linear relationship of voltage vs. current is visible up to roughly 2.7A. After this, the installed Schottky protection diode starts to conduct (to protect the µP ADC) and the voltage linearly tapers off.

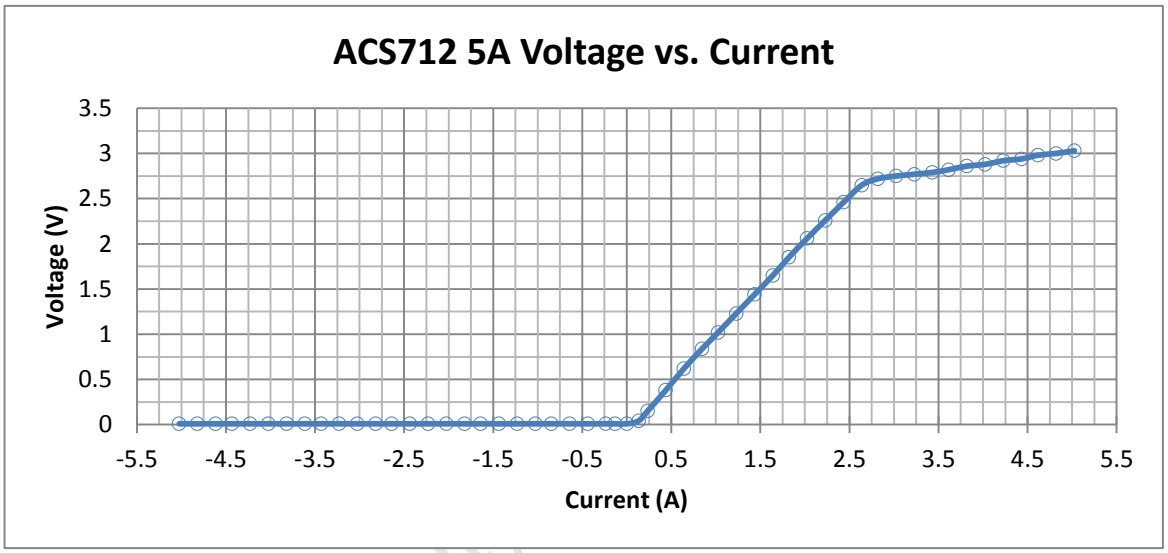

Figure C- 10: Graph Showing Output Voltage of 5A Current Sensor vs. Measured Current

The following graph is an extract of Figure C- 10, above, showing the expected operating region of the sensor.

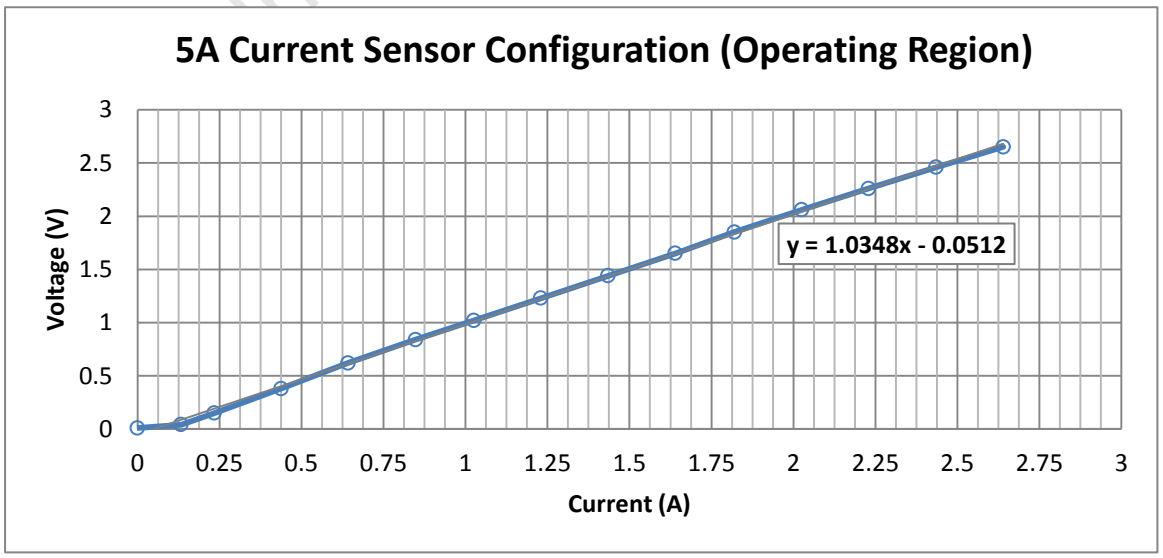

Figure C- 11: 5A Current Sensor Configuration (Operating Region)

From this graph, the following relationship was derived:

$$Current\ Sensor\ Output\ (V) = 1.0348 * Current\ (A) - 0.0512$$

$$for\ 0A \leq Current\ (A) \leq 2.7A$$

It should be noted that operation in the range $0A \leq Current\ (A) \leq 0.1A$ may provide slightly non-linear results as can be seen in Figure C- 11.

The second current sensor that was tested was configured for 20A operation with a ground reference on the inverting input of the differential amplifier. This type of sensor is located throughout the manipulator arm and the base of the robot platform. As can be seen from the plot below, a linear relationship is clearly visible when operating within a +-15A range.

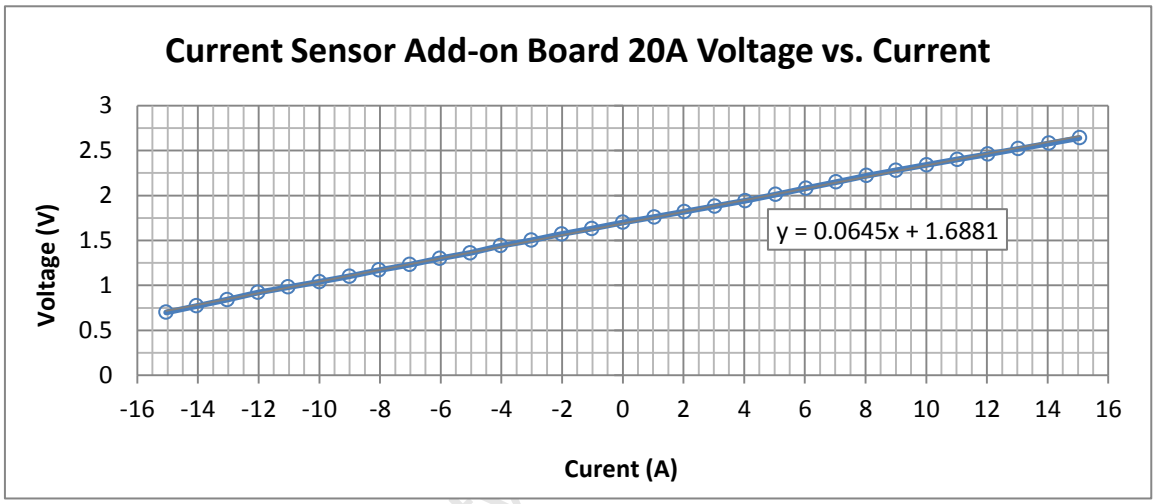

Figure C- 12: Graph Showing Output Voltage of 20A Current Sensor vs. Measured Current

From this plot, the following relationship was derived:

$$Current\ Sensor\ Output\ (V) = 0.0645 * Current\ (A) + 1.6881$$

$$for -15A \leq Current\ (A) \leq 15A$$

Conclusions

From the results above, it may be concluded that the sensors performed within the required specifications as detailed in the **Primary Specifications**, although the 5A current sensor only demonstrated a useful operating range up to 2.7A, not 3A as desired. This should not be an issue though as it was found that the Maxon DEC 24/3 speed controllers would not actually allow this amount of constant current draw. Utilising the 10bit ADC on the LM3S8962 microprocessor this should provide a current accuracy of 3mA/bit, which should be more than sufficient resolution if force derivation is to be attempted.

In summary, the derived equations for the two current sensor configurations were:

$$\mathbf{5A\ Current\ Sensor\ Output\ (V) = 1.0348 * Current\ (A) - 0.0512}$$

$$\mathbf{20A\ Current\ Sensor\ Output\ (V) = 0.0645 * Current\ (A) + 1.6881}$$

C-2.1.5 Temperature Monitoring During Operation

Test Overview

In rescue robot operations, temperatures may often be extreme and the ability for the MRP to continue operating in such harsh environments is vital. In the end-effector system, two temperature sensors were available for monitoring. One of these sensors was an LM35 placed in close proximity to the drive motors. The second, was an internal sensor located on the LM3S8962 microprocessor and should provide a reasonable indication of the state of the electronics subsystem due to heat dissipation through the PCB.

Calibration Requirements / Important Test Information

The ambient temperature read from the LM35 sensor was verified using a Lutron LM-8000 Series meter. According to the datasheet, the LM35 should provide a minimum accuracy ±0.75°C for the full sensor range. The LM3S8962 internal temperature sensor, on the other hand, is rated to a worst case error of 5°C. As the temperature readings were acquired using the LM3S8962 10bit ADC, the following conversions needed to be performed to calculate the actual temperatures in °C:

Ambient Actuator Temperature: $$T_{Amb} = ADC_{reading} * \frac{3V}{1023} * 100 \quad [5]$$

LM3S8962 internal sensor: $$T_{\mu P} = 147.5 - 0.22 * ADC_{reading} \quad [6]$$

Test Procedure

Two sets of tests were conducted. The ambient actuator temperature test was run over approximately 18 minutes and the LM3S8962 over 30 minutes. The tests were performed by running the system under loaded operating conditions and automatically logging temperature readings at 1s intervals. Figure C- 13 and Figure C- 14 present plots of the acquired data. The tests were performed in ambient air conditions of 24°C.

Test Results and Analysis of Data

The following graphs illustrate the temperature increases over time as measured by the aforementioned temperature sensors. The measured actuator temperature sensor increases from 24°C (ambient) to a maximum of approximately 32°C. An additional test was also performed outdoors in direct sunlight with an ambient temperature of 33°C. During this test, the temperature rose to approximately 45°C.

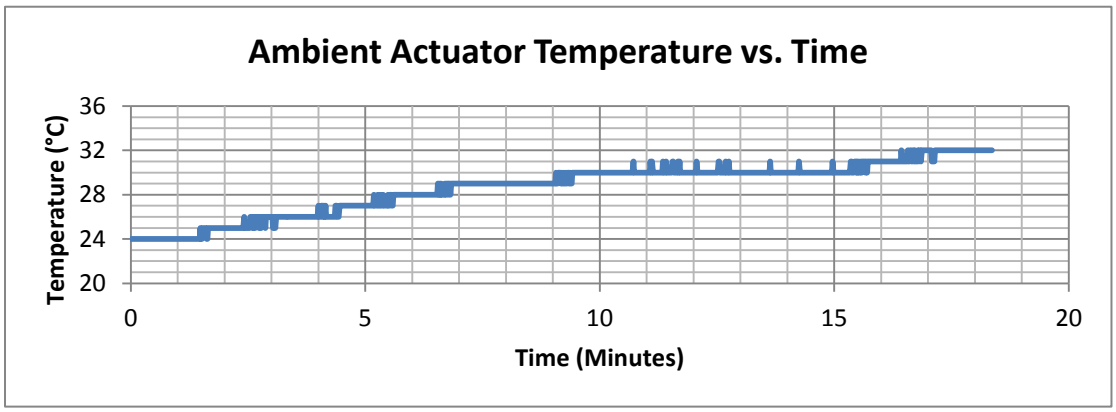

Figure C- 13: Actuator Compartment Ambient Temperature vs. Time

However, the LM3S8962 temperature test proved a bit more troubling. As can be seen in Figure C- 14 below, the temperature rose quickly to well above ambient within a couple of minutes. After 30 minutes, the microcontroller temperature was roughly 65°C. During the same outdoor test as above, the temperature rose to a maximum of 75°C.

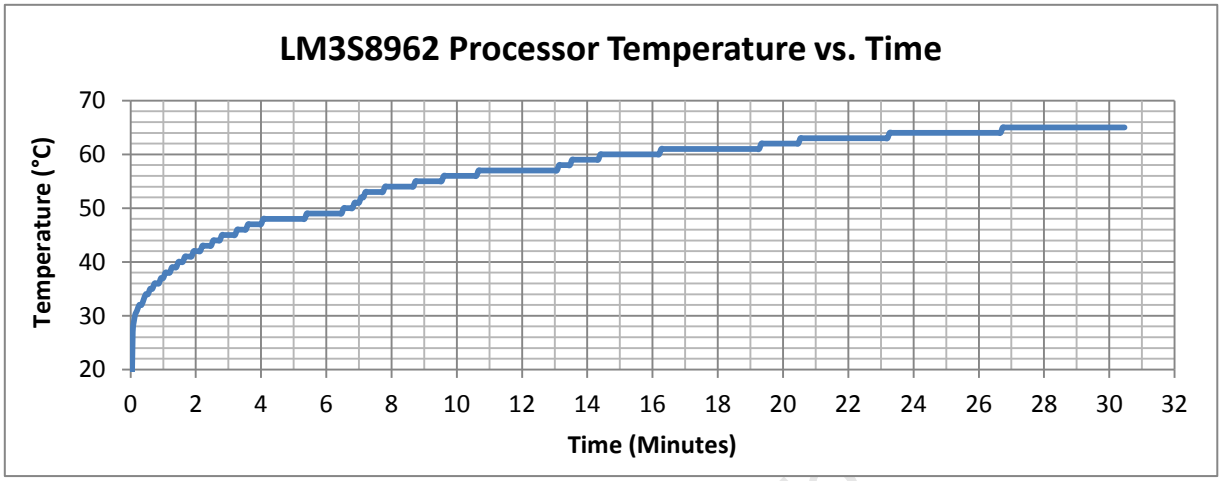

Figure C- 14: LM3S8962 Processor Temperature vs. Time

Conclusions

The operating temperatures of critical components play a large role in ensuring a robust and reliable system. The actuator compartment temperatures that were recorded in the test above proved to be well within the range of the Maxon EC22 motor's ambient operating temperature of -20°C to 100°C [7] and should provide sufficient headroom for extreme temperature conditions.

However, the LM3S8962 processor temperatures were significantly higher than expected. The maximum temperature that was recorded in the outdoor test was 75°C. The LM3S8962, in its current package, has an industrial temperature rating of -40°C to 85°C. This leaves little headroom for any additional ambient temperature rise. To ensure continued reliability of this sub-system, a heat sink should be installed to lower the maximum temperature to a more acceptable range.

C-2.2 Testing – Gripper Subsystem

C-2.2.1 Gripper Open/Close Times

Test Overview

One of the specifications of the gripper subsystem was a minimum open/close time of 5s. This is an important performance characteristic as it affects the usability and operability of the system. Both the open and close times were tested as these may be different due to the characteristics of the Maxon motor and any friction that may have been present in the system.

Calibration Requirements / Important Test Information

For every test the gripper was set to 5% speed until either the front or rear hall-effect limit switch was triggered. This ensured that the test times were always measured from the same starting points.

Test Procedure

LabView test code was created to measure the time until a hall-effect limit switch was reached at increasing speed settings. The results of every open and close run were then plotted on chart to graphically illustrate the responsiveness of the gripper at these speeds.

Test Results and Analysis of Test Data

Figure C- 15, below, illustrates the data that was captured during the tests. As can be seen from the graph, both the open and closing times of the gripper were very consistent. At the slowest speed settings, the open and close times were established at 185s. At the maximum operating speed the times were about 4.4s. It should be noted that the optimal opening and closing speeds where reached at about 65% speed setting. This was due to the jumper settings on the Maxon DEC 24/3 speed controllers, which already provided full speed at approximately 2V input.

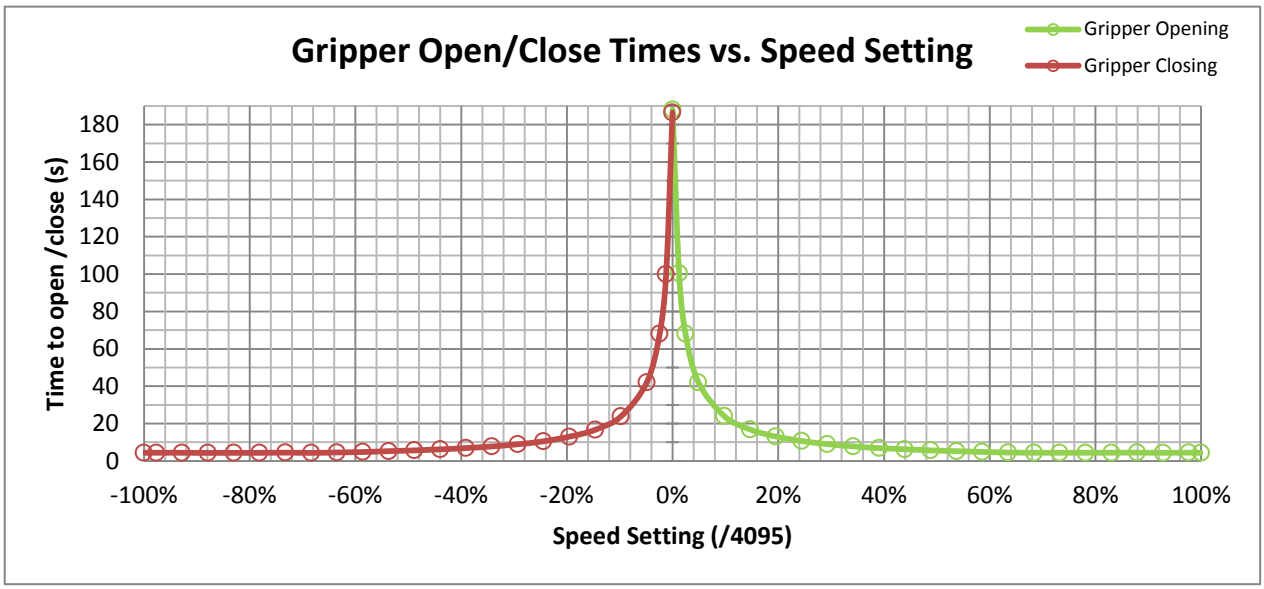

Figure C- 15: Plot Showing Open/Close Times versus Speed Setting

Conclusions

A minimum opening and closing time of 5s was specified as optimal in the **Primary Specifications**. From the tests that were conducted, the fastest open/close time was found to be 4.4s. This is well within the boundaries of the specification that was set and should provide an operator with a responsive and intuitive system. The maximum open/close time was found to be approximately 185s at 0% speed. This was due to the fact that the Maxon DEC 24/3 speed controller has no zero speed unless the brake function is activated.

C-2.2.2 Gripper Backlash Test

Test Overview

Backlash is an undesirable physical characteristic of a system and should be minimised as far as possible. The parallel arrangement of the gripper fingers reduced the amount of backlash compared with other types of systems, but could not eliminate it entirely.

The following test was conducted to establish the amount of backlash at various gripper positions and to determine if some type of relationship could be identified.

Calibration Requirements / Important Test Information

The first test run that was performed was conducted after approximately three months of running in the system. It was expected that the backlash for this test would demonstrate the worst backlash characteristics of the system. The second test was performed after a small overhaul of the gripper system, indicating minimum backlash.

Apparatus and Measuring Equipment

1x Powered End-Effector System
1x Vernier Calliper

Test Procedure

The tests were conducted by setting the gripper to various positions and measuring the backlash at these points using a Vernier Calliper. The backlash was measured by manually extending and contracting the gripping fingers by hand and measuring the maximum and minimum parallel distances between them.

Test Results and Analysis of Test Data

Figure C- 16 illustrates the data that was captured from the backlash tests. As can be seen from the graph, the maximum backlash after three months of running in was approximately 5mm at 10mm grip stroke. This is relatively high and would make accurate position control difficult. Particularly evident in the first test (blue) was a somewhat parabolic type relationship between the gripper stroke and the backlash.

The second graph (red) indicates the backlash after a brief overhaul of the gripper. As can be seen on the graph, the backlash has been reduced with a new maximum of approximately 4mm.

The parabolic relationship that was established in the first test was far less pronounced, but still apparent. The minimum backlash of both tests occurred at the maximum grip stroke and was roughly 1.5mm for both tests.

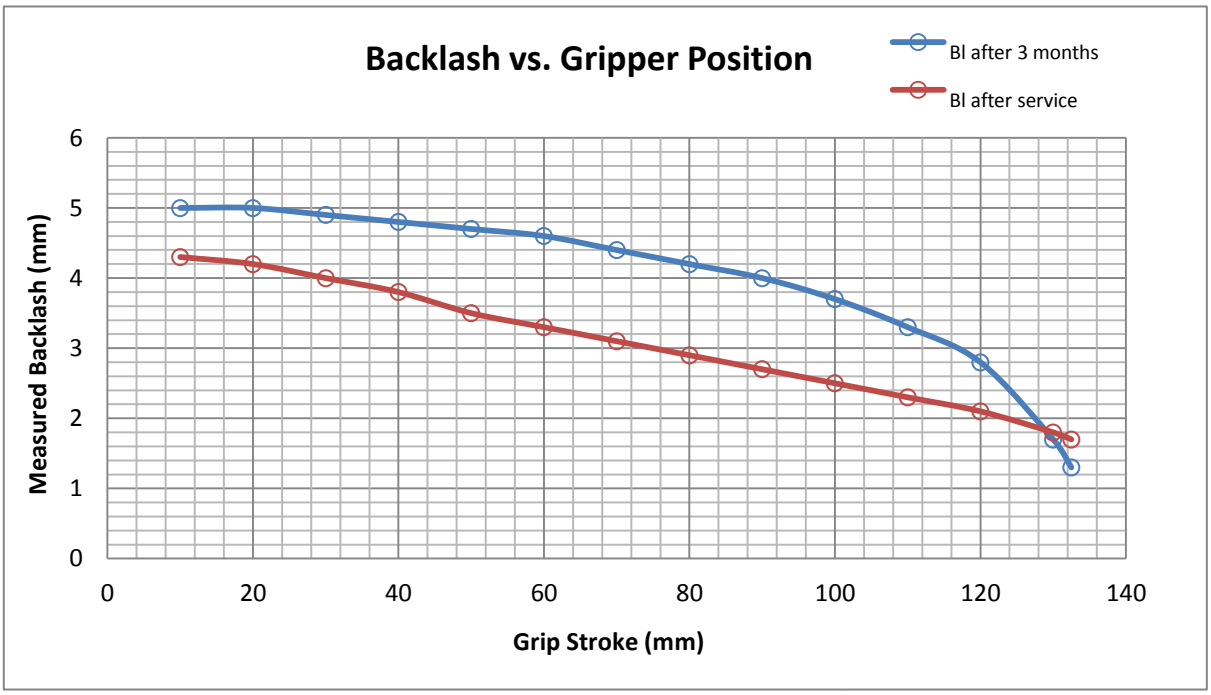

Figure C- 16: Gripper Backlash at Various Grip Strokes

Conclusions

The maximum backlash for the first test (three month run-in) was approximately 5mm, whereas the maximum after a short system overhaul was roughly 4mm. These values occurred at the minimum grip stroke. As the grip stroke increased, the backlash appeared to decrease in a parabolic manner, indicating that there was a significant relationship between the grip stroke and the backlash of the system. The maximum backlash of the system was significantly higher than expected and should be reduced further where possible by identifying high backlash components and either modifying or replacing them.

C-2.2.3 Gripper Prehension Tests

Test Overview

Gripper operations in rescue scenarios may be wide ranging with a variety of objects having to be manipulated. This may require the operator to know the force with which an object is being handled. For example, a glass bottle would be held with a lot more care than a plastic bottle.

The following tests will attempt to quantify the force being exerted on a gripped object by monitoring current and force sensing resistor readings and measuring the actual force being exerted through a compression spring gauge. Once this data has been captured, conclusions will be made on whether the current and FSR readings could be used to accurately gauge the prehension force being exerted on an object.

Apparatus and Measuring Equipment

1x Powered End-effector System with FSR Sensors Installed
1x Manson HCS-3302 15A Power Supply
1x Mettler PM30-K Scale
1x Vernier Calliper

The test rig is illustrated here:

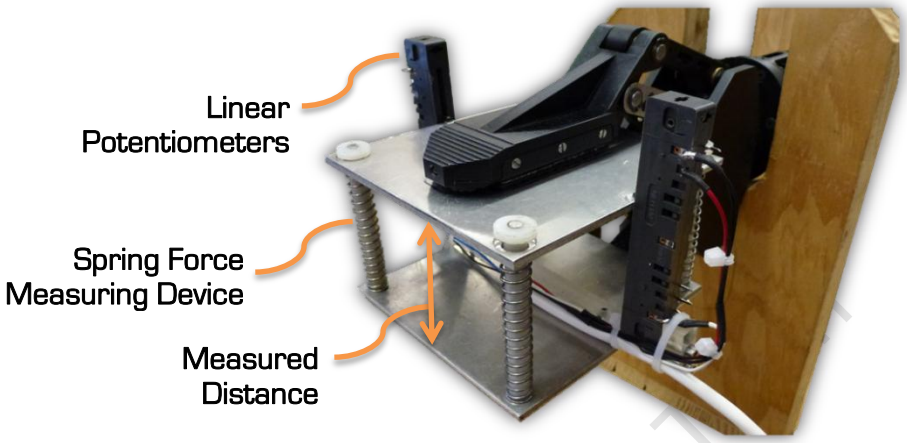

Figure C- 17: Prehension Force Test Apparatus with Linear Potentiometers Installed

Calibration Requirements / Additional Test Information

As seen in Figure C- 17, linear potentiometers attached to the spring device were used to verify the correct distances that the spring force measuring device was compressed by. This 'correct' distance was calculated using the current quadrature encoder value and its physical relationship to the gripping fingers (Refer to main body for a detailed derivation).

In order to determine the equivalent spring constant of the spring compression device, the spring device was placed on a scale and a G-clamp was used to compress the device (Figure C- 18). The weight was read then off the scale and plotted on a graph against the compressed distance measured with a Vernier calliper (Figure C- 19). From the graph, the equivalent spring constant was determined to be 3658.5$^{N}/_{m}$.

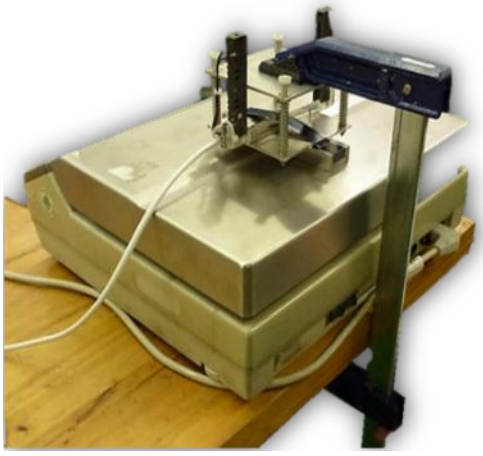

Figure C- 18: Measuring the Spring Constant with a Scale and a G-clamp

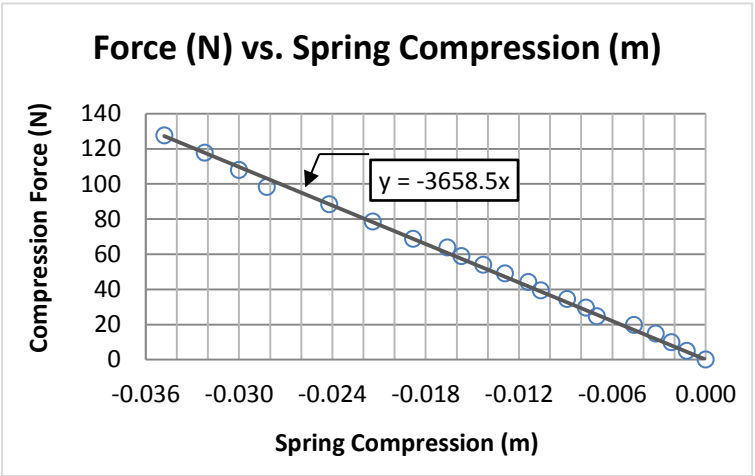

Figure C- 19: Compression Force (N) Plotted Against Spring Compression (m)

Safety Precautions

The following tests involved the physical operation of the end-effector, including the gripper and wrist subsystems and care should be taken when operating these systems.

As full power tests were run, the end-effector and its mounting fixture were secured onto a table with G-clamps to avoid sudden movements and injuries.

Test Procedure

The tests were conducted by first initiating an auto-calibration sequence of the gripper to zero the quadrature encoder register. The spring force compression device was then inserted into the gripping fingers the gripper was manually closed to just hold it in place.

Then, an auto close sequence was initiated at incrementally increased speed settings. The FSR readings and the current were then recorded and graphs plotted.

Test Results

The following graphs illustrate the data that was captured. A trend-line of the expected relationship has been superimposed on the graph.

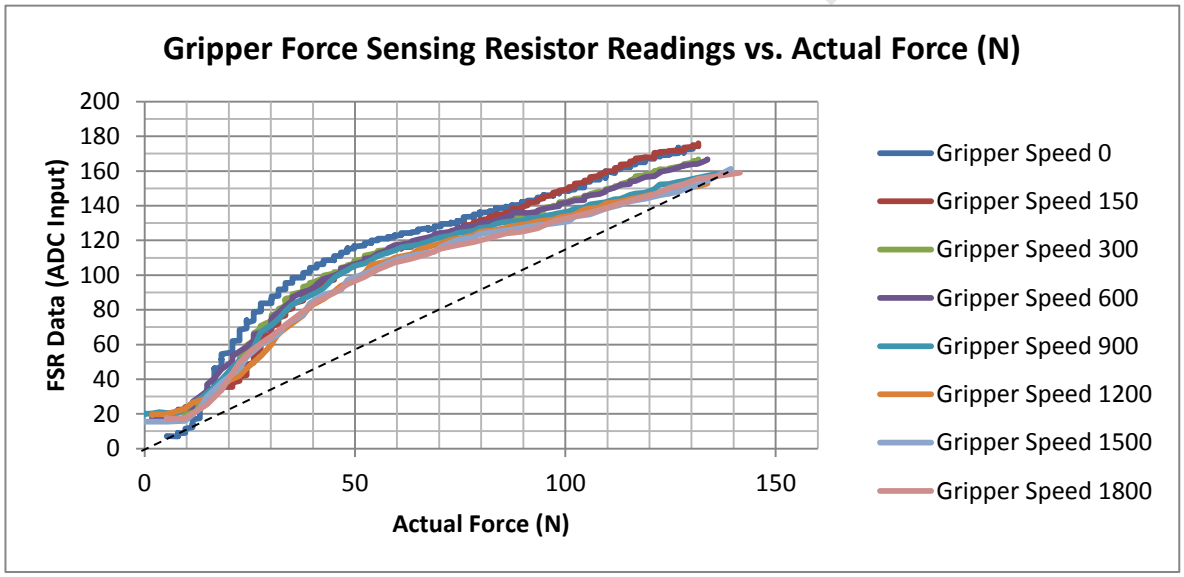

Figure C- 20: Graph Showing the Gripper FSR Readings vs. Actual Force

Figure C- 20, above, presents the FSR data that was collected over the various test runs. As can be seen from the graph, the relationship appears non-linear but fairly consistent between the various test runs. Potentially, a lookup table may be used, in combination with the gripper speed setting, to deduce the actual force from the FSR reading.

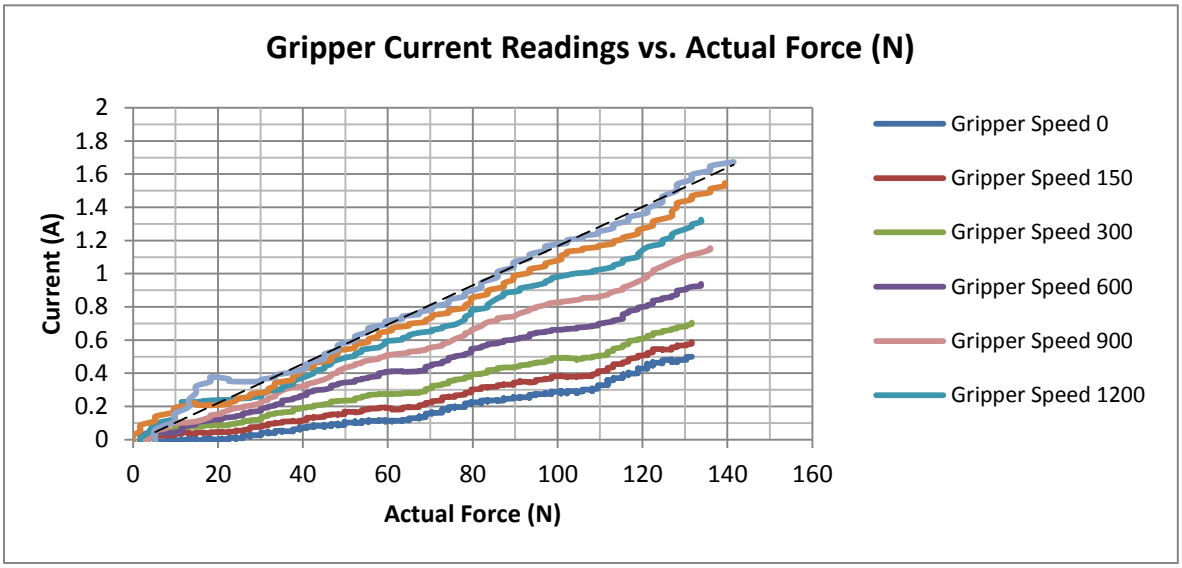

Figure C- 21: Graph Showing the Gripper Current vs. Actual Force (N)

Figure C- 21, above, shows a plot of the current readings and the respective actual forces for various speeds. The graph suggests that a linear realtionship may exist between the force and the current for the specific speeds being tested. It may be possible that this is only the somewhat linear region of the sinusoidal relationship between the gripper force and the lead screw travel that was deduced in Chapter 5, however it will be considered linear for this region.

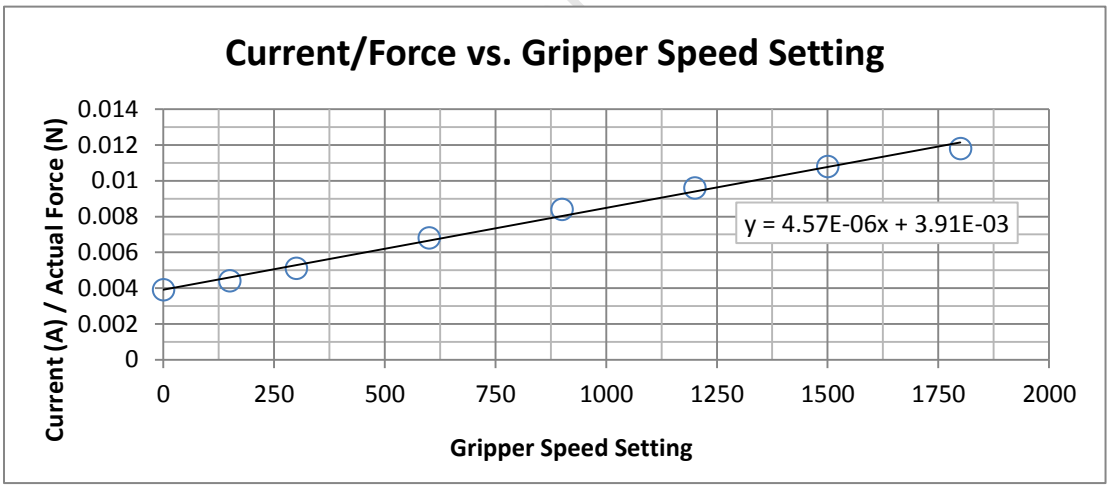

Figure C- 22: Graph Showing the Current/Force Relationship Dependant on Gripper Speed

The figure above provides a potential method of deducing the actual force using the gripper speed and the instantaneous current draw. The following formula was established from the graph:

$$Force(N) = \frac{Current(A)}{4.57 * 10^{-6} * Speed\ (/4095) + 3.91 * 10^{-3}}$$

Conclusions

Based on the data of the various tests, the following conclusions may be drawn.

Using the equation established above, the current may prove to be a useful method to determine the actual force being exerted on an object. However, the tests were all performed using the spring force device and further testing may need to be performed, using a variety of objects at different grip strokes, to verify this equation.

The recorded FSR readings appeared to indicate a non-linear relationship between the measured force and the sensors. However, the relationship appeared to remain the same under various speed settings. By setting up a lookup table based on the data that was recorded, a rough reading for the force may certainly be established.

In summary, utilising a combination of current sensing and FSR sensors or 9205i tactile sensing arrays, a good indication for the actual force exerted on an object may be determined.

C-2.2.4 Tactile Sensor Array Object Identification Test

Test Overview

As mentioned in the prehension force tests conducted previously, it could be of great advantage to an operator to know the force with which an object is being handled. However, of even more benefit would be to not only know the force, but the actual pressure distribution across the face of the gripped area. This could provide information on the actual geometry of an object being manipulated and may indicate to the operator if the object is moving (or slipping) in the gripper. The following test will demonstrate the outputs of two Weiss Robotics 9205i 84 cell tactile sensing arrays gripping a variety of objects.

Apparatus and Measuring Equipment

1x Powered End-effector System with WR 9205i tactile sensor arrays installed
1x Manson HCS-3302 15A Power Supply (End-Effector)
1x Topward Dual-Tracking 6303D 3A Power Supply (Tactile Sensors)
1x Custom RS232 – UART LVTTL and Sensor Power Extension Board

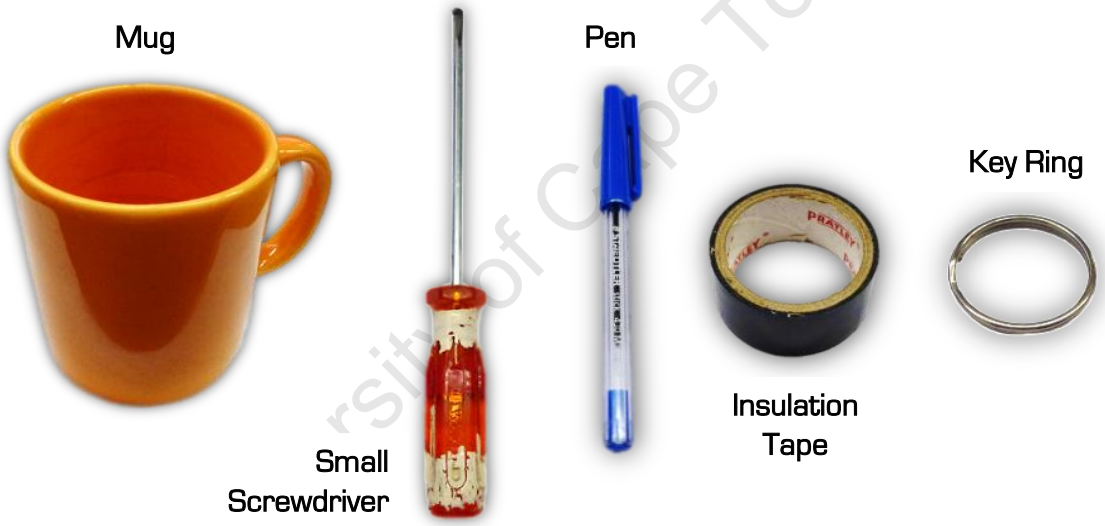

Figure C- 23: Various Items for Testing Object Verification with the Tactile Sensor Arrays

Test Procedure

The objective of these tests was to verify if any type of geometry identification could be performed using the Weiss Robotics 9205i tactile sensor arrays. The sensors were not interfaced with the gripper embedded controller directly (as described in the **Gripper Subsystem** chapter), but were rather powered by an isolated custom etched controller board.

This method was used due to time constraints of interfacing the sensors with the rest of the end-effector systems, but particularly due to the intricacies of programming the extended communications protocol for RS485 communication with the manipulator arm. The board was then interfaced with the Weiss Robotics DSA-Explorer software (included with the sensors) running on a PC via RS232.

The tests were conducted by gripping a variety of objects and recording the tactile sensor profile for each item. The prehension force was increased over three stages to illustrate pressure distributions during soft, medium and hard grips on both sensor pads. Based on the acquired images, conclusions were then drawn as to whether object geometries could potentially be identified and if the sensors could aid an operator during manipulation operations. Some videos of the gripper operations have been included on the accompanying DVD.

Figure C- 24: End-Effector with Tactile Sensors Installed Gripping a Screwdriver

Test Results

The first item that was selected for testing was a standard coffee mug. The objective was to determine if some type of curved distribution would present itself, as would be expected when gripping such an object. As seen in Figure C- 25, over the three frames a definite arced shape becomes visible, particularly as the pressure increases towards the right.

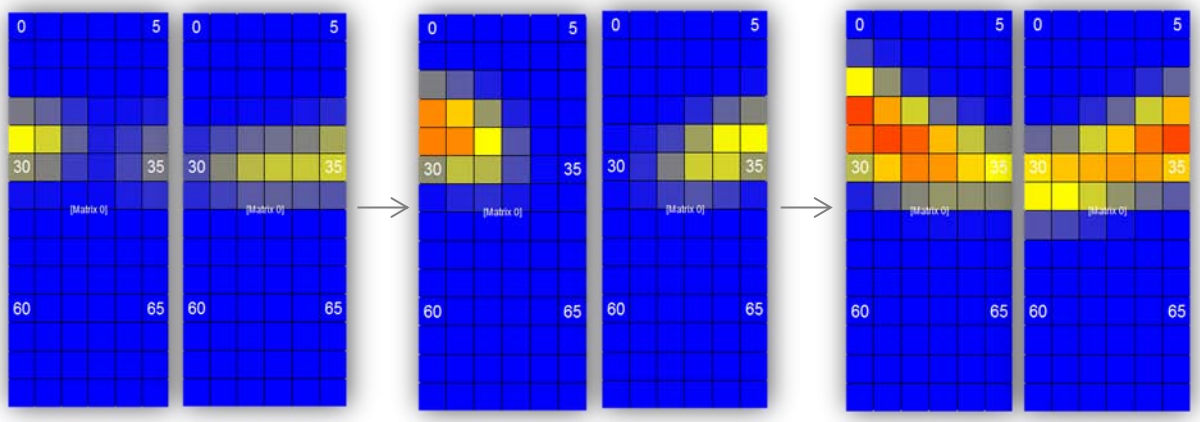

Figure C- 25: Tactile Sensor Pressure Distribution When Gripping a Mug Handle

Figure C- 26 and Figure C- 27 present the pressure distributions for a small screwdriver (roughly 17mm in diameter) and a vertical pen respectively. For both items, the first frames do not provide much information relating to the geometry of the objects, but as the pressure increases longitudinal force distributions become apparent.

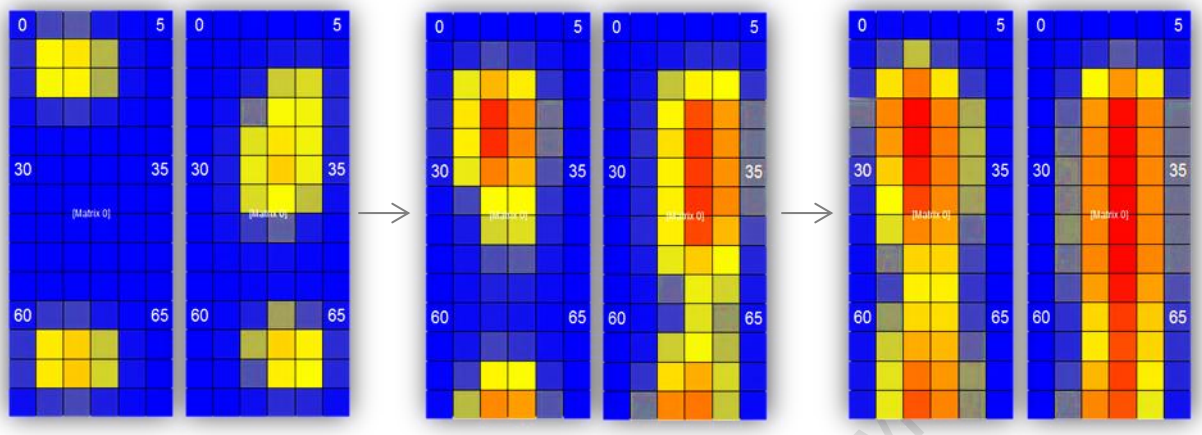

Figure C- 26: Tactile Sensor Pressure Distribution When Gripping a Screwdriver Lengthwise

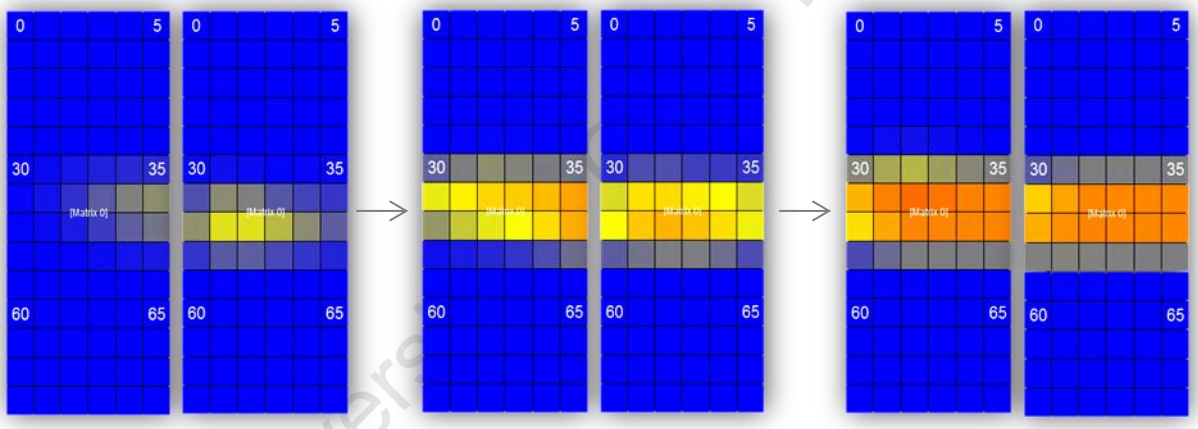

Figure C- 27: Tactile Sensor Pressure Distribution When Gripping a Vertical Pen

To test if the sensor pads could identify objects with circular geometries a roll of insulation tape (Figure C- 28) and a key ring (Figure C- 29) were tested.

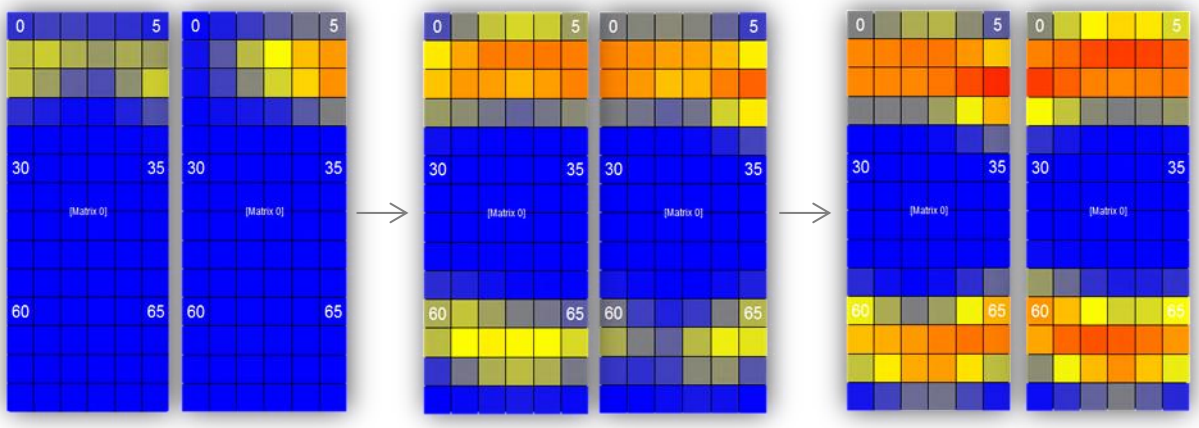

Figure C- 28: Tactile Sensor Pressure Distribution When Gripping a Roll of Insulation Tape

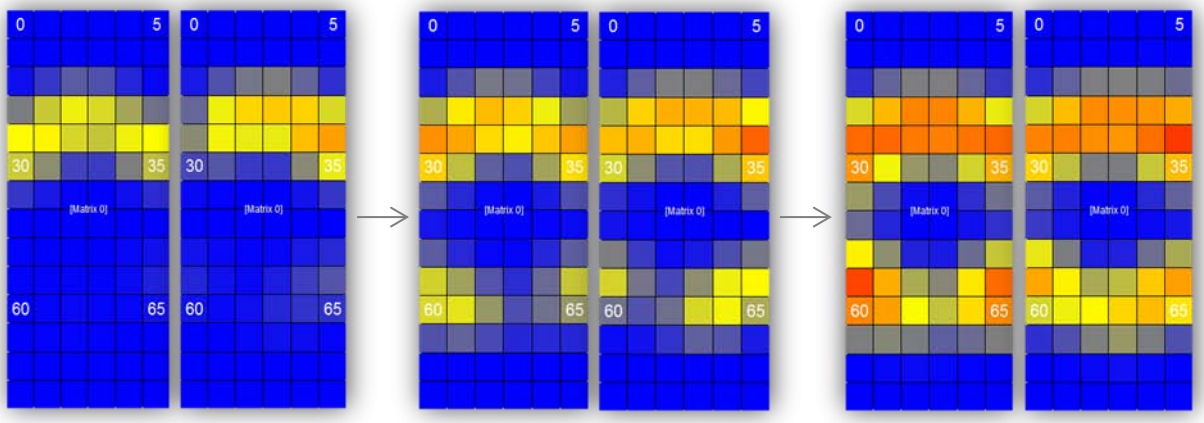

Figure C- 29: Tactile Sensor Pressure Distribution When Gripping a Key Ring

As seen in the figures, distinct circular patterns emerged for both the roll of tape and the key ring, with the key ring features being slightly more distinct due to the smaller diameter.

Conclusions

From the results above, the conclusion may be drawn that object geometries can definitely be identified using the Weiss Robotics 9205i tactile sensor arrays. Compared with standard FSR sensors, the high resolution pressure distributions provide insight into what type of objects are being gripped, how much pressure is being exerted and if there is any movement of the item within the fingers (possible due to slippage).

Once these sensors are fully interfaced with the control station, a remote operator will have far more control and an excellent overview when performing gripping operations.

C-2.2.5 Gripper CAM Range and Visual Acuity Performance

Test Overview

In USAR robotics, the ability to visually inspect an environment with a camera is of primary importance to responders. The quality of the acquired images is directly related to the performance of the camera system including the image sensor, lens, electronic circuitry, lighting and transmission medium. The camera installed in the end-effector is a cost effective KX-1 Micro Colour PAL 1/3 CMOS Camera (9.5mmx9.5mmx12mm).

The following tests will be performed based, in part, on the USAR robot standards report prepared by J.M. Evans for NIST on a set of recommended tests for visual acuity [8]. These tests include a Snellen chart, an EIA Resolution Chart 1956 and a grid distortion matrix test chart, which will be used to determine image distortion and Field of View capability.

Apparatus and Measuring Equipment

1x Powered End-Effector System
1x Tape Measure
1x Bosch VIP X2 Video Encoder

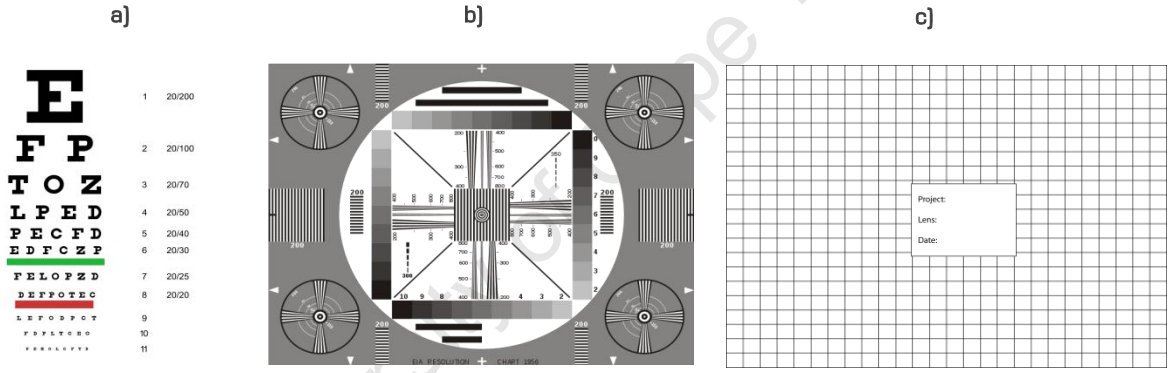

Figure C- 30: a) Snellen Chart [9], b) EIA Resolution Chart [8], c) Distortion Grid Matrix [10]

Calibration Requirements

In preparation for each test, the KX-1 camera was manually focussed to achieve the best possible result at each chart distance. This was done as the tests were designed to ascertain the optimal camera performance and not necessarily demonstrate the performance of the camera at the operational focal point of ≈200mm.

Test Procedure

Ambient Light Conditions: 400 Lux Vertical, 320 Lux at 45°, 160 Lux Horizontal

Snellen Chart: The standard distance for a Snellen chart with the largest letter being 88mm high is 6m. The test that was printed onto A4 paper (with the largest letter 48mm) therefore had to be 3.27m from the camera. At this distance the camera quality proved too low to attain a reasonable image for analysis. For

this reason the chart was placed at 1.5m, at which letters were more easily identified. The letter rows were then read from the Bosch VIP X2 RTSP feed via LabView by an operator. Figure C- 31, below, presents the end-effector setup during the test.

EIA Resolution Chart: The Electronic Industries Association 1956 Resolution chart was primarily designed to determine the limiting horizontal resolution of a camera feed. In order to establish this, the four linear sets of wedge patterns around the centre need to be visually inspected. When individual lines start to blur into one, the scanned resolution can be read off the wedge legend. The test was performed at 385mm distance to fully fill the camera image. Figure C- 34 shows a still image taken from the live camera video stream for inspection.

Distortion Grid Chart: The distortion grid matrix chart was designed to ascertain if a camera distorts an image. Distortion may occur for a variety of reason including low-quality imaging sensors or due to physical characteristics of the lens. Figure C- 32 illustrates the grid matrix that was placed perpendicularly to, and 385mm from, the camera (in order to saturate the FOV). By accurately measuring the vertical and horizontal distances of the image, the horizontal and vertical FOVs could be calculated as well as the aspect ratio.

Figure C- 31: Snellen chart Test From the View of the Gripper

Figure C- 32: Distortion Matrix Viewed from the End-Effector

Test Results and Analysis of Data

Snellen Chart: Figure C- 33, below, presents still images of the A4 Snellen chart at 1.5m distance (Left - Digital zoom, Right - No zoom) with gripper lighting turned on. From the image, the first three lines can be read relatively easily (E | F P | T O Z). The

fourth line (L P E D) is a lot more difficult to recognize. As the chart was not placed at the required 3.27m distance, a difinitive value for visual acuity was not established, although it can be said that the camera quality appears good enough to perform basic visual inspections.

Figure C- 33: Snellen chart still images at 1.5m with and without zoom

EIA Resolution (1956):

Figure C- 34, below, shows a still image captured from the RTSP camera feed. By visual inspection, it would appear that the limiting horizontal resolution of the camera is approximately 350 lines as the converging wedge lines become indistinguishable at this value.

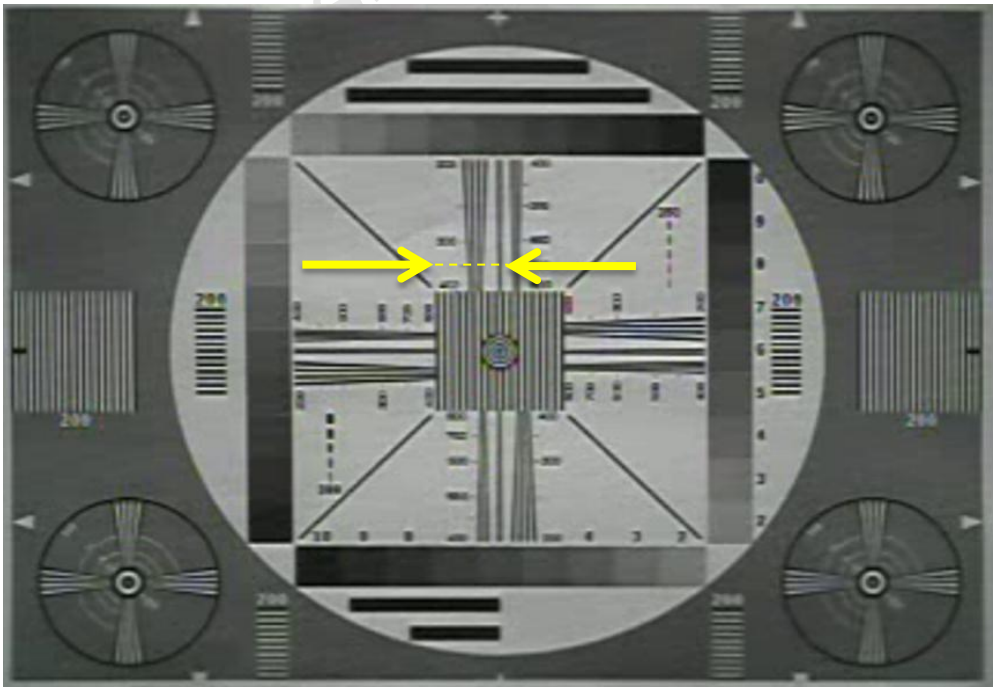

Figure C- 34: EIA Resolution Chart 1956 Still Image by KX-1 Camera

Distortion Grid Chart:

Figure C- 35 shows an image of the distortion grid matrix that was extracted from the camera feed. A rectangle (yellow) was superimposed on the image to determine if there was any indication of distortion (primarily barrel or pincushion types). As can be seen in the acquired image, there is almost no visible distortion and the matrix grid matches up well with the superimposed rectangle.

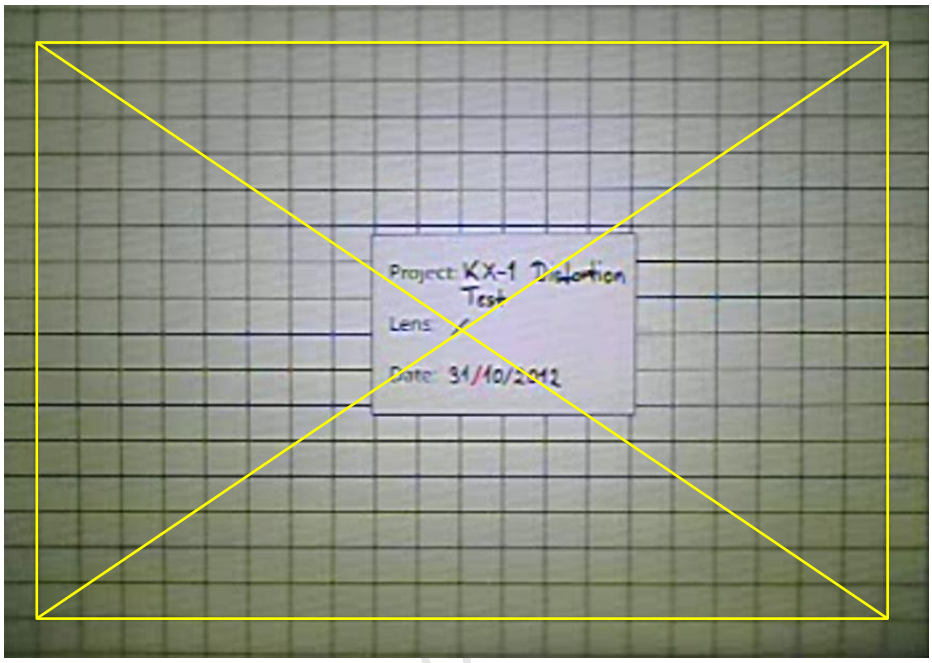

Figure C- 35: Still Image of Distortion Grid Chart

Conclusions

The tests that were performed were by no means exhaustive, but rather tested basic performance characteristics to verify if the KX-1 CMOS camera could be effectively deployed in an USAR end-effector system. The Snellen test established that the camera could be used to read basic text at relatively close range (+-1.5m). At this distance, warning or HazMat signs could certainly be detected and analysed. The EIA Resolution 1956 Chart established that the limiting horizontal resolution of the camera was approximately 350 scanned lines. The distortion matrix test verified that the camera exhibited no distortion of the acquired images.

The KX-1 CMOS camera was chosen for its compact size, low cost and low power consumption. Based on the image quality assessments that were conducted, the camera performance was on par with what one would expect from such a device. As such, it would be well suited as an end-effector camera for basic visual inspection with the option to implement basic image and motion detection capabilities.

C-2.2.6 Gripper CAM Lighting Test

Test Overview

In USAR disaster environments, response robots will often be deployed to areas that are dark and isolated. Without artificial lighting, cameras would not be able to operate effectively in such conditions. Although UCTs MRP has powerful LED lighting installed in the sensor payload and robot base, additional lighting has been implemented in the gripper body and fingers to aid the gripper CAM and the operator when performing close up operations. The following tests will evaluate the gripper camera in combination with various brightness settings and will attempt to define the relationship between distance and brightness. This is expected to present itself in the form of the inverse square law.

Apparatus and Measuring Equipment

1x Lutron LM-8000 Series Light Meter (ISO-9001, IEC1010)
1x Powered End-Effector System

Figure C- 36, below, presents the setup that was used to test the lighting capability of the end-effector system. The left side of the image illustrates the LM-8000 light meter mounted onto a section of plywood with a cable tie.

Figure C- 36: Gripper Lighting Testing

Test Procedure

As seen in

Figure C- 36, the system was set up with the end-effector directly illuminating the light meter. Additionally, a Snellen chart was placed next to the light meter to establish the camera image quality at various brightness and distance intervals.

The tests were performed in complete darkness which was verified by the lux meter to be 0 Lux. At every distance interval the brightness level of the gripper lights was increased incrementally and the lux reading on the light meter recorded. Furthermore, a still image

from the KX-1 camera was extracted at every distance and brightness setting to illustrate real world lighting situations. Figure C- 37 shows a still image of the light meter at 0.25m and ≈25% illumination.

Figure C- 37: Gripper Lighting Test at 0.25m and ≈25% Illumination

Test Results and Analysis of Data

Table C- 2, below, presents the data that was collected during the brightness versus distance test.

Table C- 2: Luminous Intensities in Lux at Various Distances/Brightness Settings

			Distance From End-Effector					
	/255	%	0.15m	0.25m	0.4m	0.5m	1m	1.5m
Brightness Setting	0	0.0%	*0*	*0*	*0*	*0*	*0*	*0*
	20	7.8%	*47*	*13*	*6*	*4*	*1*	*0*
	40	15.7%	*95*	*27*	*14*	*9*	*2*	*1*
	60	23.5%	*146*	*42*	*22*	*13*	*4*	*2*
	80	31.4%	*193*	*56*	*29*	*18*	*5*	*2*
	100	39.2%	*245*	*71*	*36*	*23*	*6*	*3*
	120	47.1%	*293*	*85*	*44*	*29*	*7*	*3*
	140	54.9%	*340*	*99*	*51*	*32*	*9*	*4*
	160	62.7%	*392*	*113*	*59*	*37*	*11*	*5*
	180	70.6%	*440*	*127*	*66*	*42*	*12*	*5*
	200	78.4%	*493*	*142*	*74*	*47*	*13*	*6*
	220	86.3%	*538*	*156*	*81*	*51*	*14*	*6*
	240	94.1%	*586*	*170*	*89*	*55*	*15*	*7*
	255	100.0%	*625*	*182*	*95*	*60*	*17*	*7*

As was to be expected, the measured luminance was a linear function of the brightness of the gripper lights (Figure C- 38). The larger the distance to the end-effector the smaller the increased lux per unit distance. This relationship is verified in Figure C- 39, below.

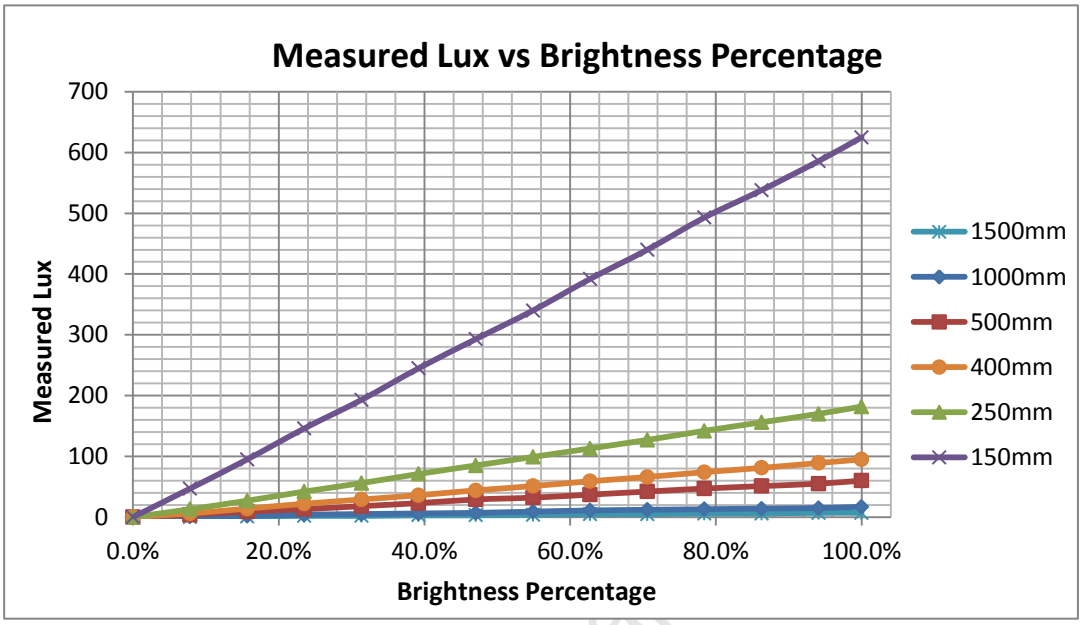

Figure C- 38: Measured Lux vs. Brightness Percentage

In theory, the luminance in a given area is inversely proportional to the square of the distance to that area. Figure C- 39 presents a plot of the maximum luminance per measurement against the distance at which the reading was taken. A trendline is superimposed on the plot in order to establish the equation of the graph. As can be seen below, the derived equation suggests a resemblance to an inverse square relationship with an R-squared coefficient of 1.00 indicating a very good trendline fit.

$$Luminance = 15.86 * distance^{-1.89}$$

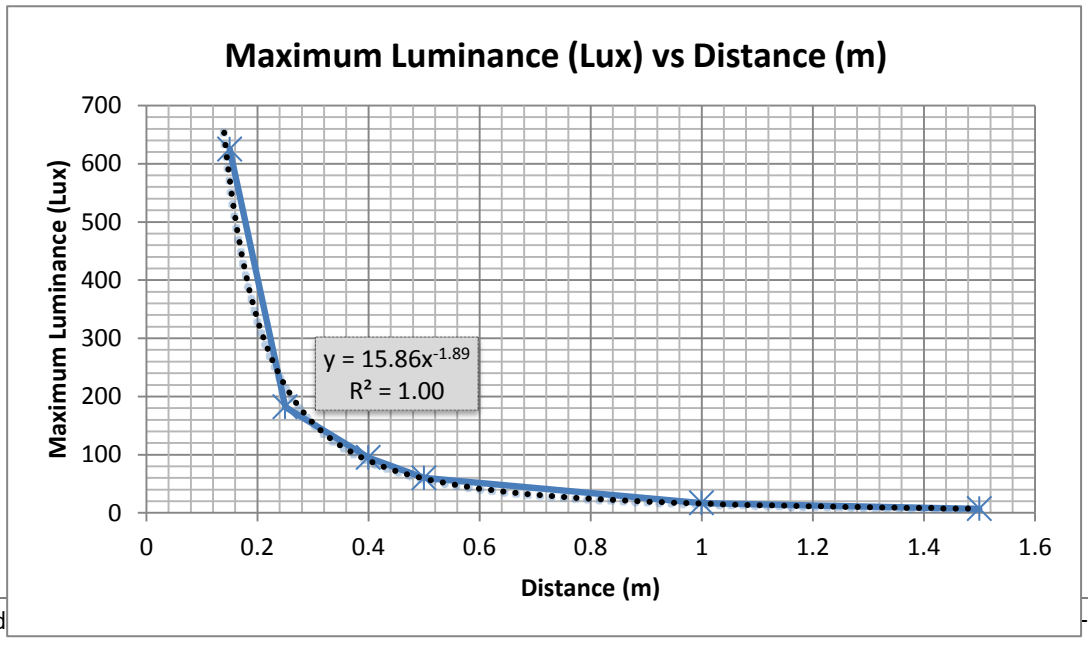

Figure C- 39: Maximum Luminance vs. Distance

Conclusions

Based on the datasheet and the camera's still images recorded during the tests, a Lux value of approximately 5 (which is often compared to typical side road lighting [11]) is sufficient to provide an acceptable image in a completely dark environment. From Figure C-39, it can therefore be concluded that the camera will perform capably at distances exceeding 1.5m with a brightness setting of 100% with an ideal operating range between 0 and 1.5m.

C-2.2.7 Gripper Cam Data Throughput

Test Overview

USAR MRPs are often operated wirelessly and the bandwidth available for video transmissions is therefore severely limited, particularly during long range missions. The aim of the following test is to determine the bandwidth that is consumed by the gripper camera during no motion and high motion scenes.

Apparatus and Measurement Equipment

1x Powered End-Effector System
1x Laptop connected to Bosch VIP X2 via 100Mbits Ethernet

Test Procedure

Within the manipulator arm, the gripper camera is connected to a Bosch VIP X2 that converts the analogue PAL signal to IP packets which get transmitted over WiFi. In order to determine the bandwidth required to view a video stream, the Bosch VIP X2 was connected to a laptop over wired Ethernet. The, the bandwidth was measured during no motion and high motion scenes and plotted on a Windows generated graph.

Test Results and Analysis of Data

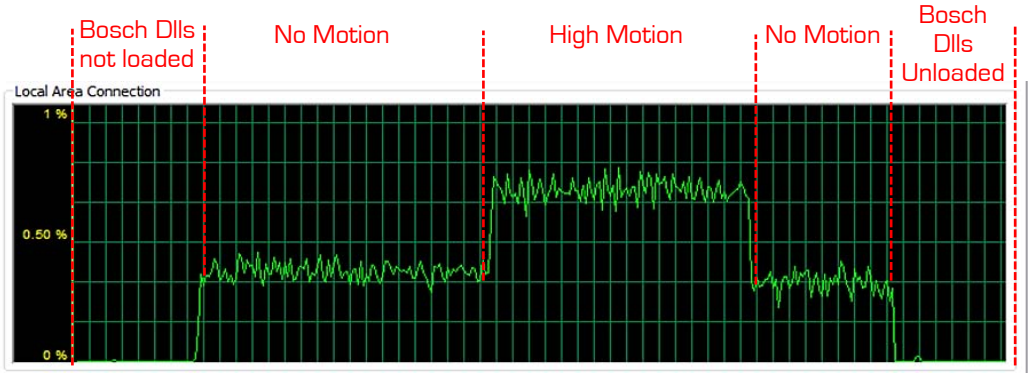

Figure C- 40: Plot of Bandwidth Usage vs. Time with Variable Motion Scenes (100Mbit)

The graph in Figure C- 40 illustrates the various bandwidth requirements during different motion scenes. When the Bosch Dlls were not loaded, 0% network traffic was measured. After the Dlls were loaded and the video stream became active, but there was no active motion in front of the camera, the network usage jumped to approximately 0.35% (i.e. 350kbps). During high motion scenes this usage increased to approximately 0.75% (i.e. 750kbps). High motion was achieved by setting the wrist of the end-effector to continuous rotation.

Conclusions

Many modern n-type WiFi systems promise speeds of up to 300Mbit/s, with traditional speeds limiting at 54Mbit/s. Even during high motion scenes, a data rate of 750kbps should be sustainable at close to medium ranges. With degradation of the wireless signal during long range missions, this might prove slightly more difficult on a slow connection as four active video streams are used during robot operation. This is in addition to control and system monitoring operations that occur in the background and which should have higher priority.

C-2.2.8 Gripper CAM QR Code and Signs of Life Detection

Test Overview

In real-world rescue scenarios, the ability of a vision system to detect victims autonomously is of great advantage. One method of achieving this is to perform motion detection analysis on a live video stream to trigger at a certain motion level. Another feature that is helpful, and which has been newly implemented at RoboCupRescue, is the automatic detection of QR codes. The following tests demonstrate the capabilities of the end-effector to perform both of these functions autonomously.

Apparatus and Measurement Equipment

1x Powered End-Effector System
1x Laptop connected to Bosch VIP X2 via 100Mbit/s Ethernet
1x Small DC motor with attached flag
1x Tape Measure

Calibration Requirements

The focal point of the camera was set to approximately 200mm to simulate standard operating conditions. Both the *CAM Sensitivity* and *Motion Trigger Level* controls were set to 30 providing good noise to motion results with the *Record on Motion* button enabled.

Test Procedure

Sign of Life Detection: In order to test if the end-effector could detect motion autonomously, a set of tests were performed utilising a small DC motor (Figure C- 41) with an attached rotating flag at various speeds and distances (0.5m, 1.5m, 3m and 5m) from the setup. When motion was detected, the video stream was

saved to an AVI file with an overlay indicating when the motion occurred and where in the image the motion was located.

QR Code Detection: QR code detection was performed by holding various Version 4 QR codes (45x45mm) in front of the end-effector camera at increasing distances and brightness levels (Figure C- 42). The ability to detect the QR at the specified distance was then recorded in a table.

Figure C- 41: Test Rig showing Rotating Flag Mounted to a DC Motor

Figure C- 42: QR Code Detection Testing

Test Results and Analysis of Data

Sign of Life Detection:

The following figure shows a print screen of the test code that was run with the test rig at 1.5m from the end-effector. On the left is the live video stream as acquired from the Bosch VIP X2 and on the right is an image illustrating the difference in subsequent image frames. The red area indicates any movement that has occurred with a green circle overlaid onto both images to indicate to the operator where motion has taken place.

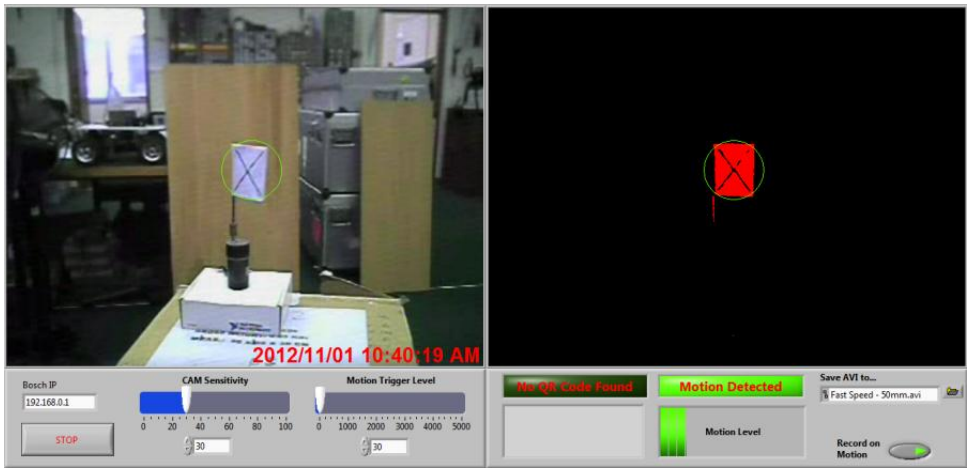

Figure C- 43: Original Image (Left) with Motion Detected Image (Right) at 1.5m

The figure below presents a screenshot of the test rig at 5m distance. Even at this distance, motion was consistently detected and the motion video was accurately captured.

Figure C- 44: Original Image (Left) with Motion Detected Image (Right) at 5m

QR Code Detection:

Table C- 3 and Table C- 4 present a summary of the QR code detection capabilities of the end-effector vision system operating autonomously.

Table C- 3: QR Code Detection Summary

Distance (mm)	QR Detected? (No Lighting)	QR Detected? (Full Lighting)
40	No	No
60	No	No
80	Yes	Yes
100	Yes	Yes
120	Yes	Yes
140	Yes	Yes
160	Yes	Yes
180	Yes	Yes
200	Yes	Yes
220	Yes	Yes
240	Yes	Yes
260	Yes	Yes
280	Yes	Yes
300	Yes	Yes
320	No	Yes
340	No	Yes
360	No	No
380	No	No

As can be seen in the table above, the ideal detection range for QR codes with no lighting is between 80 -> 300mm. With the lights activated, this may be extended another 40mm.

Table C- 4: QR Code Detection at Various Rotation Angles

Rotation (Deg)	Code Detected?
0	Yes
90	Yes
180	Yes
270	Yes

Figure C- 45, below, illustrates a successful QR code detection at 300mm. As can be seen in the image, a green rectangle overlay was created to encompass the QR code. The data of the code is displayed in the bottom right section.

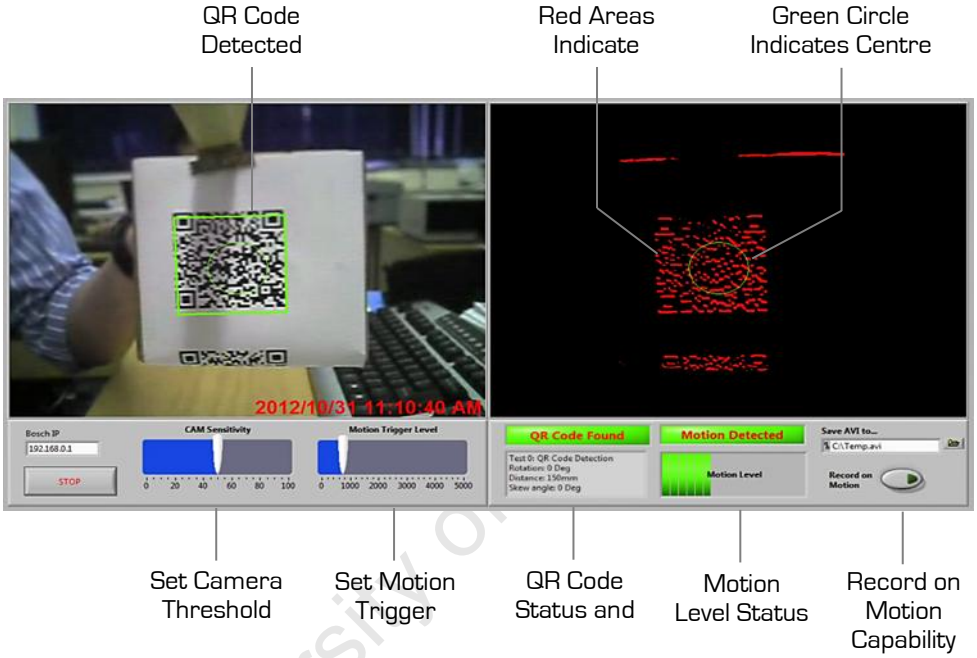

Figure C- 45: QR Code Autonomous Detection Test Program

Conclusions

For all motion detection tests at distances up to 5m, the end-effector consistently identified motion and captured video to AVI files. Almost no false triggering was detected during any of the tests. Further detailed testing information, including motion detection videos, can be found on the accompanied DVD.

QR tests were successfully detected from 80 to 300mm with an extra 40mm gained with activated lighting. For use in RoboCupRescue and real-life rescue scenarios, this should prove to be more than adequate. With an auto-focus camera this distance should be extendable to a meter or more.

C-2.2.9 Gripper Light Bridge Performance Test

Test Overview

When performing gripping operations remotely through an operator control station, it is very difficult to judge the depth of objects based solely on a camera feed. For this reason the end-effector has been fitted with two light bridges in order to inform the operator where an object is currently located relative to the gripper. The following tests demonstrate the performance of the light bridges in various lighting conditions and environments.

Apparatus and Measurement Equipment

1x Powered End-Effector System

1x 500ml Clear Plastic Water Bottle

1x 750ml Opaque Green Water Bottle

1x 500ml Clear Glass Bottle

1x 100mm Wooden Cube

1x Portable Phone

Calibration Requirements / Important Test Information

The light bridges consist of a phototransistor and an infrared LED that is pulsed in order to reject any ambient light that may be present in the environment. Utilising this method, a trigger threshold needs to be set in order to make the sensors more or less sensitive. For this test a value of 15 was chosen for the sensitivity. Please see the main report for a detailed explanation of how this variable thresholds the sensors.

Test Procedure

The first test to be performed was a base performance test to determine if any false triggering would occur during various lighting conditions. The results of this test are shown in Table C- 5, below.

The next test involved measuring the performance of the light bridges by placing various objects between the gripper fingers and recording:

1. If the sensors could detect items of varying materials and transparency
2. If any false triggering of the sensors occurred
3. If the light bridges could assist a remote operator in a gripping operation

Test Results and Analysis of Data

The following table illustrates the light bridges' performance with a rotating wrist and no objects within the sensing region.

Table C- 5: Light Bridge Test in Various Environments

Lighting Condition	Light Bridges Observations
No ambient light (0 Lux Vertical)	No false triggering
Fluorescent lighting (400 Lux Vertical)	No false triggering
Outside (Sunny Conditions)	Some false triggering when light shone directly into the phototransistor opening
Outside (No Direct Sunlight)	No false triggering
Incandescent light (Close Range)	Some false triggering at small angles with light falling directly into the phototransistor opening

As illustrated above, some false triggering was evident during direct lighting tests. It should be noted, however, that these false triggers occurred when the gripper was positioned at 90° and 270° with the phototransistors being directly exposed to the ambient light. During normal gripping operations (were the gripper would usually be horizontal), no false triggering was evident, even in extreme lighting conditions.

The next set of tests that involved using a multitude of objects to determine which could be detected successfully. The tests were conducted with the gripper set to half-open and full open positions to ascertain if this had any influence on the functionality of the sensors.

Table C- 6: Light Bridge Test for Various Objects

Object to be manipulated	Gripper Half Closed	Gripper Full Open
Clear Plastic Bottle 500ml (Empty)	Intermittent triggering	Consistent Triggering
Clear Plastic Bottle 500ml (Full)	Intermittent triggering – better than with an empty bottle	Consistent Triggering
Clear Glass Bottle 500ml	Some false triggering	Consistent Triggering
Opaque Green Plastic Bottle (750ml)	Consistent Triggering	Consistent Triggering
Wood Block 100mm Cube	n/a	Consistent Triggering
Portable Phone	Consistent Triggering	Consistent Triggering

From these tests it was made evident that the transparency of the object being detected has a significant impact on the performance of the light bridges causing occasional false triggering. However, during the tests this proved to be more of an irritation than an alright failure of the sensors, as objects could still be detected with a high level of certainty.

Conclusions

The tests above have demonstrated that objects could be effectively detected between the gripper fingers of the end-effector, with some false triggering occurring during specific lighting conditions and when detecting transparent objects. In an attempt to remedy these issues, the openings of the phototransistors were reduced to allow less ambient light to fall onto the sensing area. This greatly reduced the amount of false triggering whilst still allowing the sensors to trigger effectively. The modification is illustrated in Figure C- 46 below.

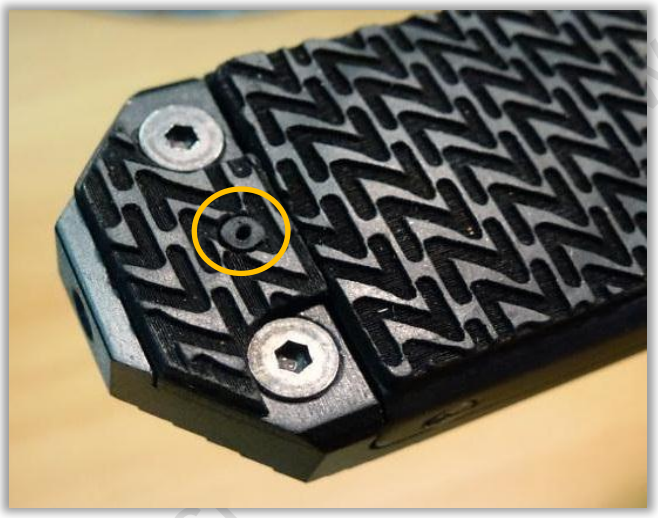

Figure C- 46: Light Bridge Phototransistor Opening Modifications

It is the opinion of the author that the sensors were invaluable during remote gripping operations and assisted greatly in performing successful manipulations. Without them, and relying only on a camera feed, the operator would have to be significantly more cautious and make small corrections far more frequently.

C-2.3 Testing – Wrist Subsystem

C-2.3.1 Wrist Rotational Speed Test

Test Overview

The rotational speed of the wrist affects the performance and responsiveness of the overall system, particularly when performing manipulation tasks such as drilling, opening doors or undoing screws. The following tests demonstrate the various speeds of the wrist for different DAC outputs.

Apparatus and Measuring Equipment

1x Powered End-Effector System

Test Procedure

A LabView test program was created to incrementally increase the speed setting of the wrist, whilst continuously logging the latest speed reading of the velocity register of the quadrature encoder. The speed setting was increased by 2 units (/4095 to the DAC) at 75ms intervals. The average speed reading over this period was then calculated and recorded on the graph below.

Test Results and Analysis of Data

Figure C- 47, below, illustrates the speed ramp that was recorded from during the test. As can be seen from the plot, the maximum speed reached was approximately 84rpm at a speed setting of 2650.

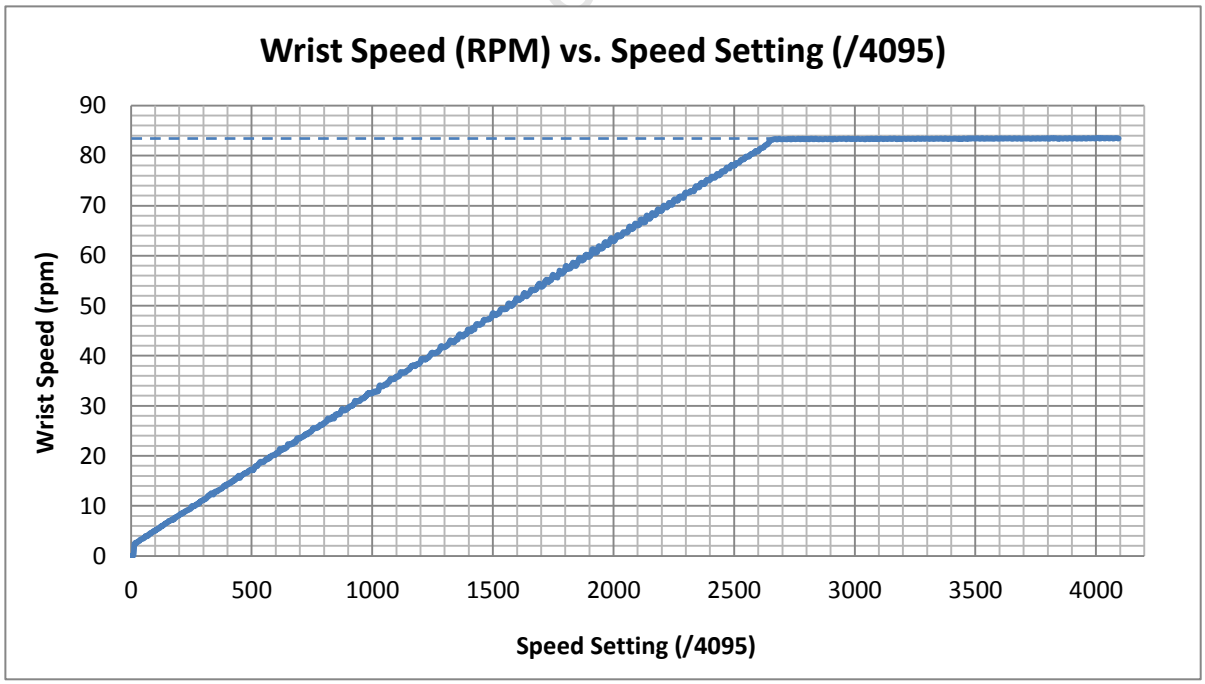

Figure C- 47: Wrist Rotational Speed Test

Conclusions

The wrist speed affects various performance characteristics of the end-effector system and its capability to accomplish certain tasks. The minimum achievable wrist rotation was initially specified at 60rpm. As demonstrated above, the achieved rotational speed was approximately 84rpm. It should be noted that some vibrations were identified in the system, particularly between 30rpm and 80rpm. This was most likely due to the misalignment of the spur gear set driving the wrist section and would need to be corrected in subsequent gripper revisions.

C-2.3.2 Wrist Torque and Current Draw Tests

Test Overview

Wrist operations in disaster areas are wide-ranging and may include activities like using tools (Screwdrivers, drills etc.) or moving objects such as bottles or rubble. The amount of torque and the torque characteristics of the end-effector wrist are important factors to consider for a remote operator undertaking such tasks. The following tests will present torque and current draw characteristics for various speed settings of the wrist and will attempt to validate if they meet the minimum requirements detailed in the specifications list.

Apparatus and Measuring Equipment

1x Powered End-effector System
1x Logitech HD Webcam
1x Mettler PM30-K Scale
1x Manson HCS-3302 15A Power Supply

Figure C- 48: Apparatus for Measuring the Wrist Torque

Safety Precautions

The following tests involved the physical operation of the end-effector including the gripper and wrist subsystems and care should be taken when operating these systems. As full power tests were run, the end-effector and its mounting fixture were secured onto a table with G-clamps and cable ties to avoid sudden movements and injuries.

Test Procedure

As seen in Figure C- 48 above, the tests were conducted by securing a piece of wood in the gripper at 220mm from the scale. Using this fixed distance, the torque could be determined by simply measuring the weight indicated on the scale.

$$Wrist\ Torque = 0.22 * 9.81 * Mass\ (kg)$$

As the scale had no simple way to provide a data stream of the current mass being applied, a program was written in LabView utilising the Machine Vision Module with Optical Character Recognition algorithms and a Logitech HD webcam pointed at the digital display. After training the program with some sample images, this provided an effective method for extracting the required data at sufficient speeds to perform the tests.

Each test was performed at a different wrist speed with the current and mass values being recorded at regular intervals. The torque was applied for approximately 2s with the piece of wood touching the scale (i.e. the wrist was stationary during the tests). Figure C-49, below, illustrates the webcam setup and the LabView VI (right) that was generated.

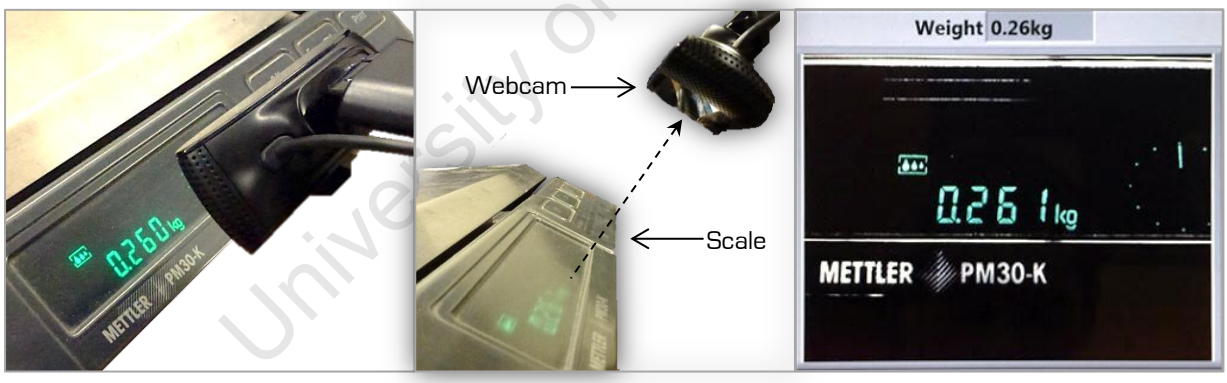

Figure C- 49: LabView Machine Vision (OCR) and a Webcam to 'Read' the Mass on the Scale

Test Results and Analysis of Data

The following graphs present the data that was captured from the eight tests that were performed. Figure C- 50 shows the wrist torque values that were captured for the various speed settings. As can be seen from the graph, the maximum peak torque achieved at any speed was approximately 5Nm (5.5Nm – 0.5Nm of the wrist at rest), 1Nm less that the theoretical maximum of 6Nm. A rough estimate is that a normal human can exert about 5-10Nm of torque using a screwdriver [12].

The graph shows some interesting results and seems to indicate that the speed setting has almost no effect on the maximum torque at that setting. This would make sense as the speed controller is a digital closed loop controller and the maximum torque should not be limited by the speed setpoint.

It would however appear that the Maxon speed controller limits the torque at speeds below 1000 to roughly 4Nm and 5Nm above 1000, which would indicate that the controller has distinct current limits for certain speed ranges. It should be noted that the torque appears to be relatively constant over the measured time interval, which is ideal for applications related to rescue scenarios.

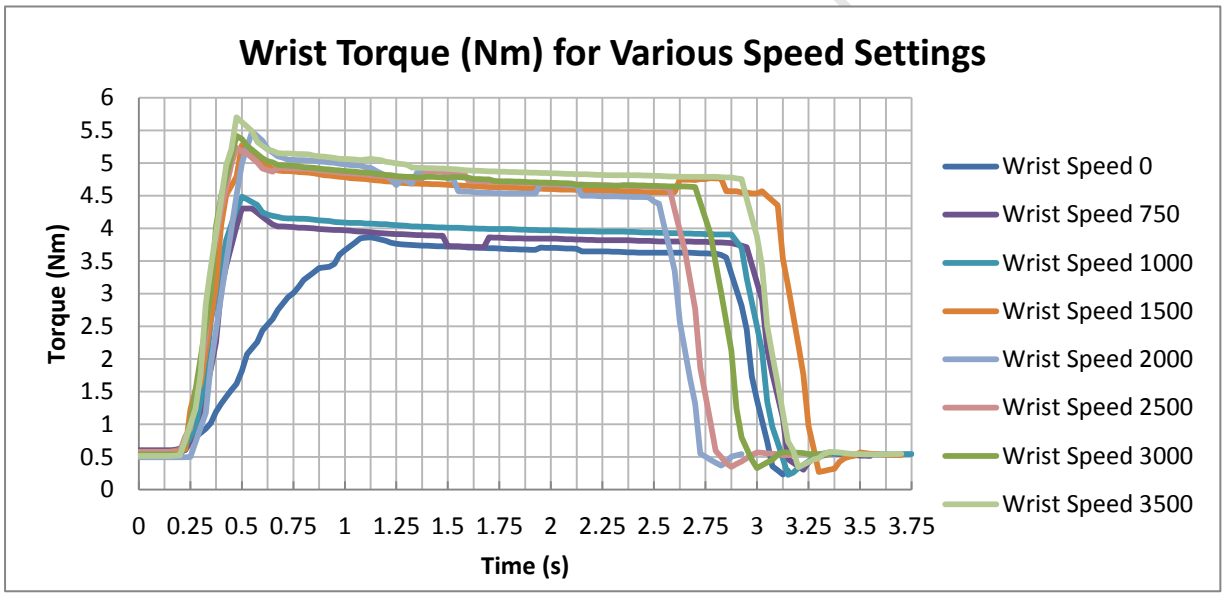

Figure C- 50: Wrist Torque (Nm) Plotted Against Time (s) for Various Speed Settings

Figure C- 51 presents the current values that were recorded simultaneously with the torque values from above. It is here that the nature of the Maxon DEC24/3 speed controller becomes apparent. As can be seen from the graph, there are distinct peaks that are visible for roughly 1s before the controller drops current output considerably to approximately 250mA. At this stage the controller indicates a "Shaft Blocked" error message. However, from Figure C- 50 it would seem that the torque is maintained during these instances, although clicking sounds are audible from the wrist motor when attempts are made to restart. For all tests it would appear that the maximum current was in the range of 0.5A to 0.8A, with maintained maximums around 0.5A.

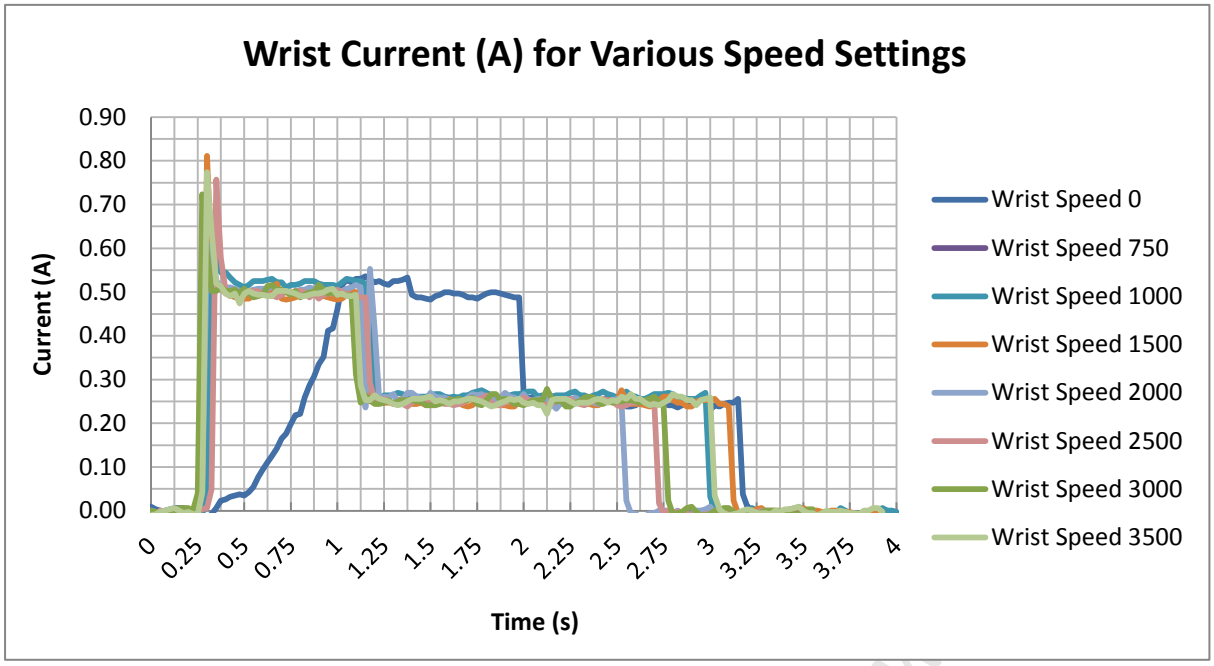

Figure C- 51: Wrist Current (A) Plotted Against Time (s) for Various Speed Settings

Conclusions

From the data that was captured, it may be concluded that the maximum torque that the wrist can constantly generate is approximately 5Nm @ 0.5A with peaks of 5.5Nm @ 0.8A. For comparative purposed, a Metabo 400Watt DRILLBE4006 has a rated torque of 6Nm [13]. It was also determined that the speed setting of the wrist had little effect on the amount of torque that the wrist motor could produce. This made sense as the wrist controller is a digital closed loop controller and the wrist started from rest and was never able to accelerate to the given setpoint.

From the graphs above it may also be concluded that the current is not an effective way to measure the wrist torque, unless only peak currents are used as torque indicators. This is due to the nature of the Maxon DEC24/3 speed controller and the sudden current drop-off under stall conditions.

From these tests, an operator should have enough information to know how much torque can be exerted by the end-effector wrist. Although an actual applied torque indicator would be difficult to implement, it would not be impossible by only monitoring peak current draws. In conclusion, the amount of torque that can be generated by the wrist should be sufficient for most tasks in rescue scenarios, which may include tool operations.

C-2.3.3 Wrist Position Accuracy

Test Overview

In using the end-effector more regularly, it became apparent that some form of wrist position control would be needed to assist a remote operator in controlling this subsystem. Due to its simplicity, straight proportional control was selected as the control method. The following test will illustrate the positional accuracy of using such a control technique on the wrist subsystem and will evaluate if the positional accuracy achieved is acceptable. It should be noted that the tests were run under no load conditions due to the nature of the Maxon speed controllers (refer to the main body for a more detailed explanation as to why the a load test could not be performed).

Apparatus and Measuring Equipment

1x Powered End-Effector System
1x Topward Dual-Tracking 6303D 3A Power Supply
1x Unbranded Laser Pointer (Adjustable Focus)
1x Tape Measure and a Ruler

The test setup is illustrated in the Figure C- 52 below:

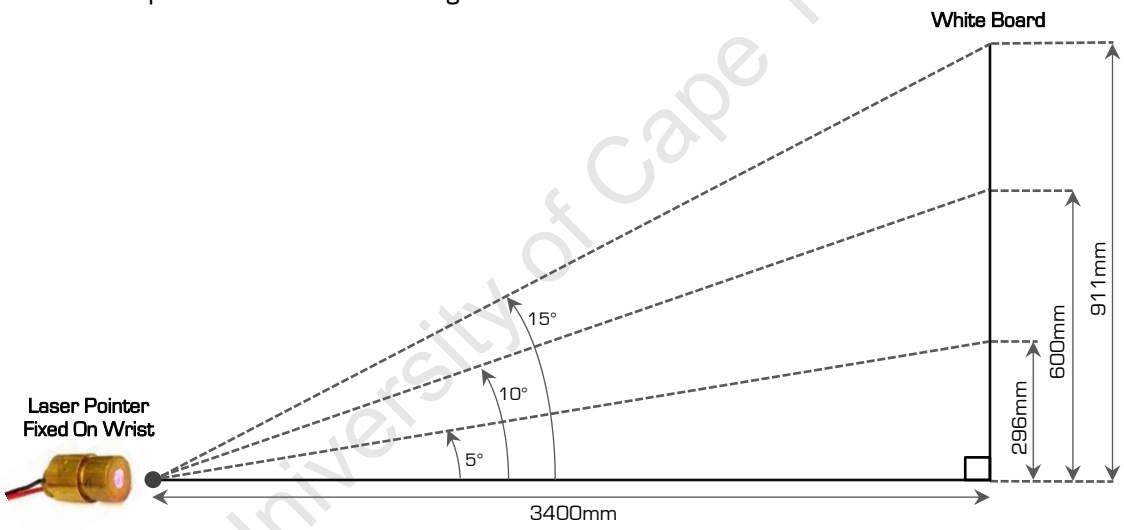

Figure C- 52: Test Rig Setup with Laser Focussed on a White Board

Figure C- 53 and Figure C- 54, below, show the laser pointer mounted onto the wrist and the laser pointer projected on the white board:

Figure C- 53: End-Effector with Mounted Laser Pointer

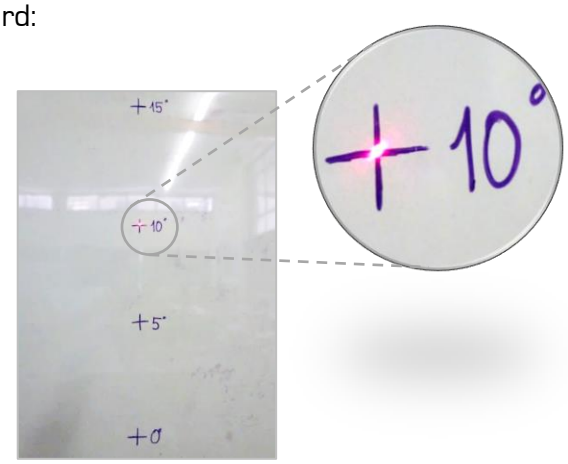

Figure C- 54: White Board with a Measurement Area Highlighted

Safety Precautions

The following tests involved the physical operation of the end-effector wrist subsystems and care should be taken when operating such systems. For all tests the end-effector and its mounting fixture were secured onto a table with G-clamps and cable ties to avoid sudden movements and injuries.

Test Procedure

In this test, a laser pointer mounted on the end-effector was used to determine the positional accuracy of the proportional control algorithm that was implemented. The laser was mounted onto the gripper at a distance of 3400mm from a white board and the wrist was re-calibrated to a zero position using an auto calibration routine. Marks were then made on the white board at 0°, 5°, 10° and 15° projected angles (See Figure C- 52).

The test was then run by setting the wrist to these angles sequentially over eight runs. For every position change, the vertical error from the exact position was recorded using a ruler. A positive error indicated an error above the desired value with a negative error indicating an error below. Although this is by no means an extensive position accuracy test, it should at least provide an indication of the maximum error that can be expected.

Test Results and Analysis of Data

The following graph presents the data that was recorded over all the test runs. The maximum error that was recorded was approximately 14mm and the calculated average over all readings was 7mm. The following deductions can be made from these values:

$$PosError_{max} = \arctan\left({}^{14mm}/_{3400mm}\right) = 0.24°$$

$$PosError_{avg} = \arctan\left({}^{7mm}/_{3400mm}\right) = 0.12°$$

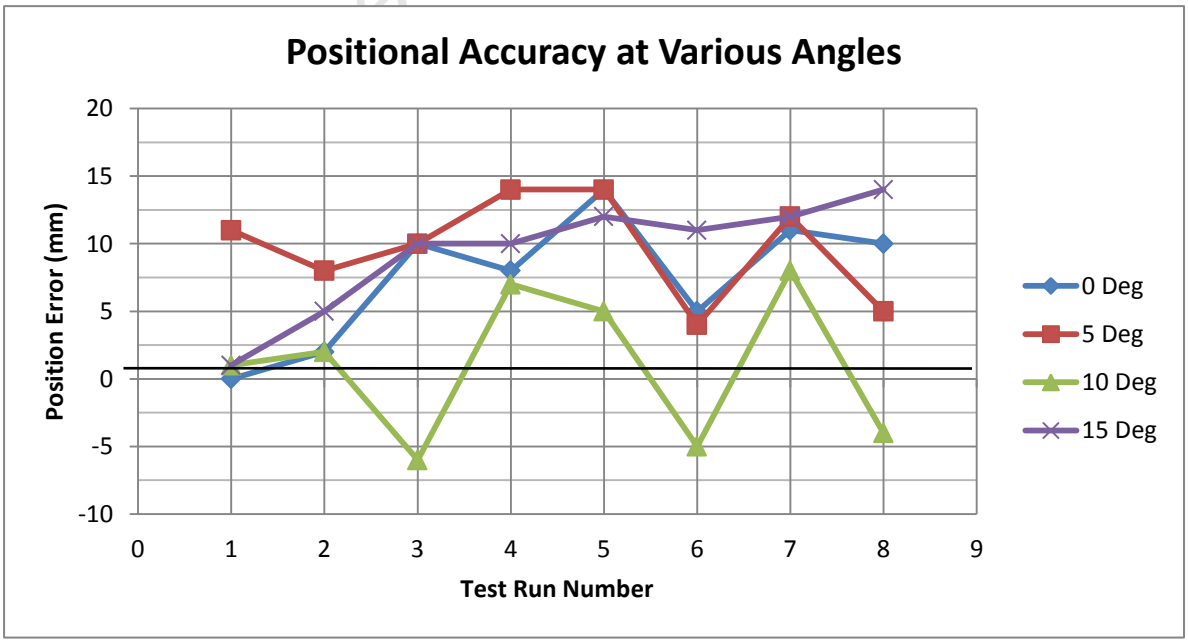

Figure C- 55: Positional Errors over 8 Test Runs

Conclusions

The positional accuracy of the wrist was specified as 1° in the wrist detailed specifications. From the tests above, it may be concluded that the maximum error over all the runs was 0.24° with an average error of 0.12°. This should prove more than sufficient for positioning the wrist under no load conditions during standard operation. It should be noted that there were some oscillations on rare occasions, which may indicate that the proportional control should be optimised further or a new control method should be adopted.

List of References

[1] ASTM. *Form and Style for ASTM Standards*, 2012.

[2] Hensley Technologies. "Agilent U1242B Handheld Digital Multimeter," 2009. Online: http://www.hensleytech.com/agilent-u1242b-handheld-digital-multimeter-4-digit [Accessed: December 12, 2012].

[3] Atlantec. "Manson HCS-3300," 2012. Online: http://www.atlantec.pl/zasilacz-laboratoryjny-15v-60a-manson-hcs3300-p-323.html [Accessed: December 12, 2012].

[4] Farnell Element 14. "Agilent Technologies - DSO1002A Oscilloscope," 2010. Online: http://uk.farnell.com/agilent-technologies/dso1002a/oscilloscope-2-ch-60-mhz/dp/1704738 [Accessed: December 12, 2012].

[5] Texas Instruments. *LM35 Precision Centigrade Temperature Sensors*, 2000.

[6] Texas Instruments. *Stellaris LM3S8962 Microcontroller Datasheet*, 2011.

[7] Maxon Motors. "Maxon EC22 40W Datasheet," 2012. p. 149 Online: http://www.maxonmotor.com/medias/sys_master/8800982827038/12_149_EN.pdf.

[8] J.M. Evans. *Standards for Visual Acuity*, Newtown: 2006.

[9] J. Dahl. "Snellen chart," 2008. Online: http://en.wikipedia.org/wiki/File:Snellen_chart.svg [Accessed: November 5, 2012].

[10] The RealVision KnowledgeBase. "Stereoscopic QC and the corner pin," 2012. Online: http://realvision.ae/blog/2011/10/stereoscopic-qc-and-the-corner-pin/ [Accessed: November 5, 2012].

[11] use-IP Ltd. "Lux Light Level Chart," 2008. Online: http://www.use-ip.co.uk/datasheets/lux_light_level_chart.pdf [Accessed: November 6, 2012].

[12] Biomech-L Forum. "Summary: max. torque with a screwdriver," 2012. Online: http://biomch-l.isbweb.org/threads/7457-Summary-max-torque-with-a-screwdriver [Accessed: December 18, 2012].

[13] Metabo. "Product Catalogue - DrillBE4006," 2012. Online: http://www.metabo.co.za/Product-catalogue-handheld-powertools.23996+M52e83dffa59.0.html [Accessed: December 21, 2012].